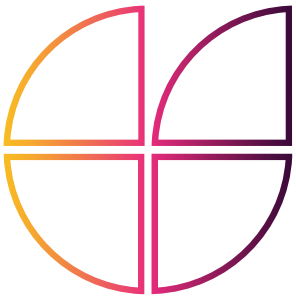

DEPARTMENT OF
ENGINEERING
SCIENCE

Materials Testing for Heatshield Applications during CubeSat Re-entry with Passive Demise

Claudio Vestini, Fizza Naqvi, Hani Moussa, Alex Berresford

May 27, 2025

1 Abstract - Claudio Vestini

The development of reliable heat shield materials for commercial re-entry vehicles requires experimental validation under real-world hypersonic conditions, a challenge that traditional ground-based testing cannot adequately address. This report presents the innovative design of an 8U CubeSat intended to serve as an experimental testing platform for heat shield materials in commercial applications. The satellite deploys from a RocketLab launch vehicle at 400 km altitude, performs semi-controlled re-entry using cold gas thrusters and a reaction wheel system. Beginning at an altitude of 150 km, integrated thermocouples, recession sensors, and a spectrometer capture material performance and atmospheric impact data, while a novel phased array bidirectional communication system indirectly transmits through the CubeSat's wake to a ground station via the Iridium network. Comprehensive numerical modelling validates mission feasibility and predicts thermal-aerodynamic loading throughout re-entry phases. At an estimated cost of £700,000, each mission provides the customer with otherwise inaccessible experimental data on material behaviour under extreme hypersonic conditions, directly addressing the current scarcity of validated re-entry design data and advancing design-for-demise methodologies.

Contents

2 Introduction

2.1 Preface - Claudio Vestini

Since the first successful deployment of a human-made object into Earth's orbit with Sputnik in 1957, over 10,000 satellites have been placed in orbit around our planet [1]. Of these, over 84% are in low Earth orbit (LEO), of which only a relatively small percentage is still operational. The increasing accumulation of orbital space debris poses a significant threat to current and future space missions, leading to a growing emphasis on effective end-of-life disposal strategies for spacecraft and ground impact mitigation techniques after their demise. To this scope, the European Space Agency (ESA) issued a report in 2014 [2] (later revised in 2023 [3]), stipulating that the casualty risk for any re-entry event should be no greater than 1 in 10,000. Several other space agencies, including NASA, the Inter-Agency Space Debris Coordination Committee (IADC) [4] and the European Space Agency (ESA) [5], have since agreed with the prescription.

Accurately assessing casualty risk requires a detailed understanding of fragmentation dynamics, the geometries of surviving components, impact locations, and geographical population density. One of the main sources of uncertainty in these assessments is the prediction of aerothermal heating across the different stages of re-entry. Unlike typical re-entry capsules, satellites often feature geometric discontinuities such as sharp edges and facets. This results in unique flow behaviours - particularly around corners - leading to increased local heat fluxes due to boundary layer thinning caused by strong expansions. This is a ripe field of research, as there is great concern associated with the Kessler syndrome [6]: in short, a scenario where the density of debris in Earth orbit is such that catastrophic collisions are inevitable. Existing demise prediction tools employ various approaches to simulate these re-entry conditions. Object-oriented tools, such as ORSAT and DRAMA, utilise tumble-averaged heating rates for basic shapes [7, 8], whereas spacecraft-oriented models, like SCARAB, relate stagnation-point heating to a characteristic radius of curvature [9]. Newer tools such as FOSTRAD and PAMPERO employ local radius-of-curvature methods [10, 11]. None of these tools, however, relies on high-fidelity data for hypersonic aerothermal flow distributions around complex geometries, and a scarce number of studies are available on the topic in the literature. The primary objective of this 3YP project is to establish a testing platform that bridges the gap in scientific understanding.

2.2 Motivation & Overview - Alex Berresford

The space industry plays a key role in modern society, driving technological innovation, supporting global communications and addressing challenges such as climate monitoring and disaster management. Satellites in orbit enable GPS navigation, weather forecasting and internet connectivity, all of which are deeply ingrained in daily life. Looking ahead, the industry is expected to grow rapidly, with projections estimating the market to reach nearly $2 trillion USD by 2035 [12]. Much of this growth is being fuelled by increasing involvement from the private sector and new markets in areas such as space tourism and asteroid mining. We've already seen some of this growth come to fruition, with SpaceX having launched over 7,000 satellites in the past seven

years for their Starlink Satellite constellation [13]. Furthermore,the worlds first Space Hotel is expected in the not-too-distant future – Voyager station is expected to open in 2027. With all this new interest Earth's Orbit is going to become a much busier place.

However, this comes with its own set of issues. Global space agencies are already tracking over 25,000 objects in low earth orbit, with over half of it being classed as debris or rocket bodies [14]. However not all objects are being tracked, with the European space agency estimating there could be 130 million debris objects larger than 1mm in diameter [15]. The source of this debris is often collisions or explosions of defunct satellites or rocket bodies left in orbit. Given this level of debris is only from 70 years of the developing space industry, it's clear that the issue could compound uncontrollably if ignored– as described by the Kessler effect, where a chain reaction of colliding space debris leads to the accumulation of debris, eventually rendering low Earth orbits unusable for space missions due to the high risk of collisions with debris [6]. This has led to an increased interest in re-entry dynamics as de-orbiting spent satellites or using reusable vessels has become more of a priority. Being able to predict how an object will interact with the atmosphere during re-entry is key to designing vessels with efficient demise, or that will survive re-entry for reuse or recovery. In the long term, this understanding could also be crucial to protecting the environment from potentially harmful materials that are released during re-entry.

The current understanding of how any specific material or geometry behaves in the hypersonic environment of re-entry is limited, as ground testing facilities can't effectively replicate the high enthalpies and high speeds in conjunction with each other. Furthermore, facilities that are capable of high enthalpies are limited to short test times, meaning test models are limited to small sizes. The fixed nature of these tests does not allow for much or any change in orientation, so fails to accurately replicate tumbling that would be present during re-entry of a satellite of certain geometries.[16]

This project aims to develop a commercially available CubeSat platform that allows for the standardised testing of heatshield materials in the hypersonic conditions of re-entry. This enables companies to test their heatshield material in environment, overcoming the limitations of ground facilities. Furthermore, the environmental impact of the test material will also be examined, which is another factor that can help inform companies on heatshield material choice.

CubeSats are a modern standardised classification of microsatellites that make small space missions more cost effective through the use of standardised commercially available parts and services. Launch providers offer rideshare opportunities for different CubeSat geometries for a reasonable price, allowing many to be deployed in a single launch, often alongside the primary load. A CubeSats geometry is often described by its volume in the "U" unit, which roughly describes a 100mmx100mmx100mm cube, these units are then arranged in a variety of geometries, from the simplest 1U to the largest standard configuration, 12U.

For the purposes of this project, an 8U configuration in a 2x2x2 configuration is being proposed, as it provides a sufficient volume for the required hardware and heatshield materials whilst being symmetrical in 3 dimensions. This allows a tumbling condition to be assumed as there's no equilibrium point, allowing for even exposure of

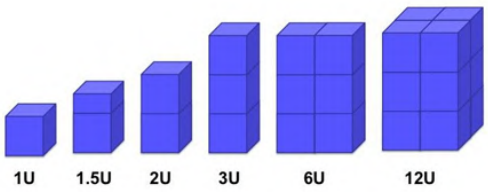

Figure 2.1: Diagram of some Standard Cubesat Geometries [17]

all faces of the CubeSat to the freestream. Even exposure degrades all sides evenly, keeping the internals within their operating region for as long as possible while allowing multiple materials to be tested simultaneously.

Recession sensors placed within the test material will be used to measure the degradation of the ablatives during re-entry alongside a set of thermocouples to track temperatures on the inside faces of the heatshield. The Environmental impact of the materials will be examined by an optical spectrometer which will observe the emission spectra of the demising species within the hypersonic shock layer to quantify the contamination of different species in the atmosphere. This data will be transmitted back to Earth via the Iridium Satellite network, using Constructive interference from multiple antennae to direct a strong signal through the thin plasma layer formed at the back of the CubeSat.

The proposed launch date is December 2026, when space weather is predicted to be ideal for our mission and conforms with RocketLab's - our chosen launch provider – timeline. The expected mission length is 20 days. The CubeSat will be deployed at approximately 400km altitude where it will perform a deorbit burn using cold gas thrusters. At 150km measurements will start to be taken and transmitted via Iridium which will continue until demise or complete power drain. To ensure demise and eliminate the risk of dangerous ground impact, the CubeSat is fitted with a set of carefully placed thermite charges. These will self-ignite at a specific design temperature of 635K independently of any other system, destroying the internal structure apart, allowing individual parts to demise on their own. Thermite ignition is expected at around 40km altitude.

Following introductory sections, this report continues into Section 3, where the role of a Launch provider is described and rideshare options compared. Section 4 - Trajectory - describes how our mission timeline was modelled with an analysis of space weather, atmospheric models and thrusters to calculate our expected mission time and ideal launch window. Section 5 – Structural Design - explains the analysis of the harsh launch environment to inform on frame design as well as the optimisation of internal component placement to protect key systems. Section 6 – Electronics - covers the communication and electronic systems within the CubeSat, focussing on solving the difficulties of communicating during re-entry and managing the power budget. Section 7 - Instrumentation - describes the various design choices that went into selecting components and sensors, before explaining their use. Most importantly, this section describes the altitude tracking system, attitude control system, and atmospheric composition analysis. Section 8 - Aerothermal – includes simulations of the aerothermal environment during the orbital and re-entry periods, informing the expected demise window and requirements to maintain the electronics within their operational window. Sections 9 and 10 discuss budget estimations and project risks respectively, before concluding statements are made in section 11.

3 Launch Provider

An obvious necessity of a CubeSat mission is the ability to launch it into orbit. Another obvious point is that its completely unfeasible to do this ourselves, necessitating the use of rideshare from a launch provider.

Ridesharing is when a single launch is used to transport multiple payloads into space. Whilst ridesharing has been occuring for over 50 years [18], its become prevalent in recent years with the development of reusable rockets, more frequent global launches and the growing interest in space for smaller companies.It works similarly to carpooling, where multiple passengers share a ride to save costs. Most importantly it gives access to space for smaller companies or educational institutions who wouldn't be able to afford a dedicated launch. The growth of commercial ridesharing has birthed the idea of CubeSats due to the benefit of standardising parameters of rideshare payloads - it helps if the bus doesn't need to be redesigned for every different passenger.

Requirements Table 3.1 below summarises the launch provider requirements with a qualitative rating of 1-5, with 5 meaning required and 1 indicating an unnecessary quality.

Table 3.1: Launch Requirements and their Necessity Ratings

Requirement	**Necessity Rating (1–5)**
Support for 8U deployment	5
Frequent launches	2
Reusable rocket	1
400 km or lower deployment	4
Low price	2

Obviously, the provider has to be able to facilitate the 8U 2x2x2 configuration. The next most important requirement is a 400km or lower deployment altitude. As the CubeSats purpose is to re-enter and demise, any excess time spent in orbit only increases risk of mission failure through either impact, radiation or thermal damage. As can be seen in figure 4.15 and section 4.6, orbital decay is much slower at higher altitudes due to the lesser effect of atmospheric drag as it thins out. The same simulation with nominal solar flux indicates that with a starting altitude of 500km, the mission would take 3569.3 hours, which is approximately 5 times the expected length when starting at 400km.

Should the initial test be successful, and repeat launches be required as customer materials are tested, having a partnership with a provider with frequent launches and low costs would be beneficial. This would allow missions to be run on tighter timescales and budgets, which both benefit business.

A reusable rocket would be ideal to reduce environmental damage from excess manufacture, but is not a requirement for any other reasons.

3.1 Options - Alex Berresford

Due to the 8U requirement, most launch providers were ruled out as the majority only offer rideshare to 1U or 1*X configurations. For example Nanoracks is a company that facilitates the deployment of 1*X CubeSats from the international space station.

The considered providers are SpaceX and RocketLab as other providers found could not offer rideshare to an 8U CubeSat.

SpaceX SpaceX is an American based space company owned by Elon Musk, with goals to improve humanity by making it more of a spacefaring society.Its well known due to its impressive Starlink and Starshield projects, which are vast constellations of communication satellites [19]. SpaceX's reusable rocket Falcon 9 is has currently has frequent launches to deploy these satellites [20], and provides a reliable rideshare option worth consideration [21]. The cost to deploy anything up to 50kg to a Sun-Synchronous orbit of 500km-600km with them is $325,000 or £240,500. Missions to other orbits are advertised at "affordable rates", which are assumed to be similar. Their rideshare launch schedule is advertised ahead of time on their website , but currently only display launches to a 500-600km altitude in a sun synchronous orbit[22].

RocketLab RocketLab is an American based space company, with facilities in both the US and New Zealand. They offer rideshare on their rocket the Electron, which due to its small size can be manufactured quickly for flexible and on-demand launch. The Electron also has the ability to provide staggered deployment, allowing precise deployment of payloads to custom altitudes, even when ridesharing [23]. Figure 3.1 shows the available deployment range of the Electron. RocketLab have not been open about their costs, and were not receptive to contact about a student project, so their launch cost is currently unknown.

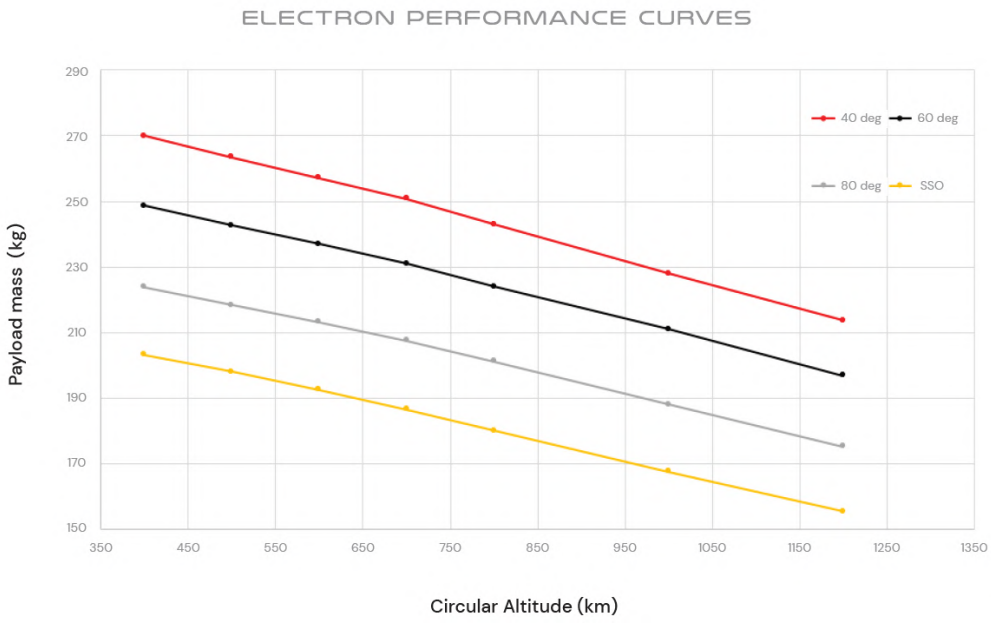

Figure 3.1: Graph showing the orbital performance of the electron [23]

3.2 Comparison

SpaceX offers a regular and reliable service at a fixed cost, however as previously mentioned, a 500km altitude for currently advertised launches has too great an affect on mission time. Furthermore, a Sun-synchronous orbit risks thermal damage to our CubeSat, as thermal analysis of our orbital phase in section 8.2 assumes a

cool phase as the CubeSat passes behind the earth. The staggered altitude deployment from the Electron and RocketLab makes both of these concerns a non-issue. From a business mindset, the flexibility of launch offered by RocketLab is more appealing than the regularly scheduled launches from SpaceX, as it allows missions to be launched as and when customers require tests.

From this information, RocketLab is the clear choice. However, should their launch cost prove unfeasible and SpaceX start offering more appropriate altitude deployments, this decision should be be reconsidered.

4 Trajectory

4.1 Overview - Fizza Naqvi

The satellite's mission begins with its launch into a circular Low Earth Orbit (LEO) at 400km, chosen for its advantages in terms of orbital dynamics and mission costs. LEO provides a natural environment for rapid orbital decay due to atmospheric drag, making it an ideal choice for missions involving semi-controlled re-entry. The proximity of LEO to Earth's surface ensures a shorter orbital lifetime, which reduces the time and energy required to bring the CubeSat to the desired re-entry altitude for testing purposes. In addition, the cost of launching into LEO is lower compared to other orbital regimes, due to the reduced energy required for launch and the greater availability of launch vehicles capable of reaching these altitudes. Furthermore, the selected launch altitude is less congested than higher altitudes, such as above 500 km, where spatial density increases and the risk of collision with other objects is greater.

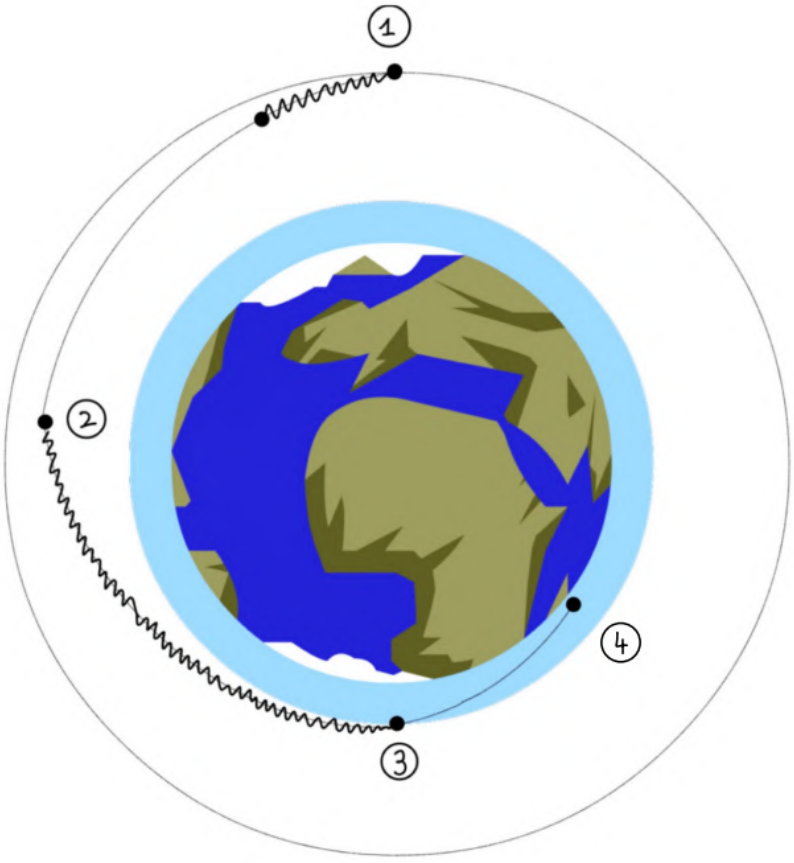

Figure 4.1: Trajectory Overview.

To facilitate re-entry, the satellite will perform a short de-orbit burn manoeuvre at 400km (stage 1, shown in Figure 4.1), where the CubeSat's propulsion system will be used to slow it down, change the orbit and initiate atmospheric re-entry. This controlled de-orbit burn accelerates the satellite's descent, ensuring a faster re-entry timeline. When the CubeSat's power is turned on at 150km (stage 2), reaction wheels will be employed to spin up the satellite until 130km (stage 3), using Model Predictive Control (MPC) to maintain the desired spin rate. This induced tumbling mechanism helps to evenly distribute heat across the satellite's surface during re-entry,

promoting uniform heating to limit structural failure and allow for more accurate measurements for materials testing. These measurements for the mission will also begin at 150km.

As the CubeSat descends through the atmosphere, it will undergo thermite breakup at an altitude of approximately 40 km (stage 4). This ensures that the satellite burns up completely, leaving minimal debris and significantly reducing the risk of reaching the Earth's surface.

While Low Earth Orbit (LEO) offers advantages like reduced launch costs and shorter re-entry times, it also introduces orbital perturbations that can influence the satellite's trajectory. However, the analysis presented in the following sections assumes a two-body problem and neglects these perturbations due to the short mission duration. Effects such as Earth's oblateness (which causes the J2 effect[1]), solar radiation pressure, and third-body gravitational influences from the Moon and Sun are considered negligible. Although the J2 effect can be significant in low orbits, it is assumed to have a minimal impact on the orbital decay rate over the short timescale considered [24]. Likewise, atmospheric winds and other small forces are not included in the model.

4.2 De-Orbit Burn for Semi-Controlled Re-entry - Fizza Naqvi

To ensure the CubeSat's semi-controlled re-entry, a retrograde impulse burn is performed using cold gas thrusters, with their instrumentation detailed in section 7.2. The burn works in conjunction with the MPC system for attitude control, discussed in section 7.6, ensuring that the CubeSat's attitude is maintained throughout the process. Proper attitude control is crucial to prevent misalignment during the burn, which could otherwise destabilise the descent and increase the risk of mission failure.

Without the de-orbit burn, the CubeSat would rely solely on atmospheric drag to gradually lower its altitude. At 400 km, drag is relatively weak, so orbital decay is slow, and it could take several months to reach the denser atmosphere needed for rapid re-entry. However, by performing the burn, the satellite transitions to an elliptical orbit with a perigee of 140 km. Instead of slowly spiralling down through multiple circular orbits, the CubeSat now descends directly to a region of high drag, dramatically accelerating the re-entry process.

The burn is modelled as an impulsive manoeuvre, occurring over a very short duration. As a result, the CubeSat's altitude during the burn remains nearly constant. The total burn time for the three MiPS (Micro Propulsion System) thrusters to achieve the required delta-v is 399 seconds, calculated using the following equation [25]:

$$T_b = \frac{m_{\text{propellant}}}{\dot{m}} = \frac{m_{\text{propellant}} \cdot I_{sp} \cdot g_0}{F_{\text{total}}} \tag{4.1}$$

where I_{sp} is the specific impulse in seconds, g_0 represents the standard gravitational acceleration, taken as $9.8\,\mathrm{m/s^2}$, and F_{total} is the total thrust produced by the thrusters.

[1]The J2 effect refers to the perturbation in a satellite's orbit caused by Earth's equatorial bulge. Due to the oblateness of the planet, the gravitational field is not perfectly spherical, leading to a gradual shift in the satellite's orbital elements.

The selection of 140 km as the perigee altitude reflects a deliberate balance between achieving timely re-entry and preserving sufficient time for experimentation during descent, as outlined in Table 4.1. At this altitude, the satellite begins encountering significant atmospheric drag, which initiates a rapid but not immediate descent. This allows it to spend more time within the critical altitude range where materials testing and data collection can be conducted effectively.

Table 4.1: Trade-offs of Different Perigee Altitudes for CubeSat Re-entry

Perigee Altitude	**Re-entry Behaviour**	**Impact on Experimentation**
120–130 km	Very rapid descent due to strong atmospheric drag; altitude drops sharply in a short time.	Minimal time for data collection; limited opportunity for meaningful experimentation before burn-up.
140–150 km	Moderate descent rate with significant drag effects; more time spent in denser atmospheric layers.	Allows more detailed materials testing and environmental data collection before major deceleration.
Above 150 km	Slower descent through thinner atmosphere; prolonged orbital decay phase.	Extended testing window, but risk of insufficient re-entry if altitude is too high.

For the de-orbit burn to be effective, it must be executed precisely at the correct orbital position and with perfect alignment. The thrusters must fire exactly opposite to the satellite's velocity vector (retrograde direction) to ensure that the reduction in velocity translates purely into a decrease in perigee, rather than introducing unwanted inclination changes or perturbations. Any misalignment could result in an inefficient burn, an incorrect perigee altitude, or an unstable trajectory, potentially compromising the mission objectives.

To mitigate these risks, the CubeSat's MPC system ensures proper attitude control during the burn. Before firing the thrusters, the satellite undergoes a precise orientation maneuver to align itself with the desired retrograde direction. Real-time feedback from onboard sensors is used to verify and correct alignment errors before ignition.

The initial orbit is circular, therefore the velocity before the burn is determined by the orbital velocity equation:

$$v_{\text{initial}} = \sqrt{\frac{\mu}{r_{\text{orbit}}}} = 7.67\,\text{km/s} \tag{4.2}$$

Where μ is the gravitational parameter for Earth ($3.986 \times 10^5\,\text{km}^3/\text{s}^2$) and r_{orbit} is the orbital radius at 400 km altitude ($r_{\text{orbit}} = 6778\,\text{km}$).

After the deorbit burn, the semi-major axis [26] of this orbit is calculated as:

$$a = \frac{r_{\text{orbit}} + r_{\text{perigee}}}{2} = 6648\,\text{km} \tag{4.3}$$

where $r_{\text{perigee}} = 6518\,\text{km}$.

Using this value, the final velocity at the apogee of the elliptical orbit is calculated to be:

$$v_{\text{final}} = \sqrt{\mu \left(\frac{2}{r_{\text{orbit}}} - \frac{1}{a} \right)} = 7.59\,\text{km/s} \tag{4.4}$$

The required delta-V for the deorbit burn is:

$$\Delta v = v_{\text{initial}} - v_{\text{final}} = 0.0767\,\text{km/s} \tag{4.5}$$

Thus, the CubeSat requires a delta-V of approximately 77 m/s to execute the deorbit burn and lower its perigee to 140 km. This delta-V is within practical limits for the propulsion system selected for our CubeSat, detailed in section 7.2, and ensures a controlled descent into the denser layers of the atmosphere.

4.3 Orbital Dynamics - Fizza Naqvi

Simulating the trajectory of the CubeSat involves understanding how its altitude changes over time, while accounting for the influence of atmospheric drag. An equation for the rate of change in altitude is derived by considering the total mechanical energy of the satellite in orbit [27].

The total mechanical energy of a satellite in orbit is the sum of its gravitational potential energy and kinetic energy:

$$E = -\frac{\mu m}{r} + \frac{1}{2} m v^2. \tag{4.6}$$

The velocity for the orbit, after the de-orbit burn, is given by:

$$v = \sqrt{\mu \left(\frac{2}{r} - \frac{1}{a} \right)} \tag{4.7}$$

The eccentricity of an orbit is given by:

$$e = \frac{r_{\text{apogee}} - r_{\text{perigee}}}{r_{\text{apogee}} + r_{\text{perigee}}} \tag{4.8}$$

Equation 4.9 can be used to calculate the instantaneous radial distance in an elliptical orbit:

$$r = \frac{a(1 - e^2)}{1 + e \cos\theta} \tag{4.9}$$

The eccentricity for our target trajectory, calculated using equation 4.8, is very small (< 0.1). Therefore, for simplicity in the simulation, equation 4.9 can be approximated as $a \approx r$.

After substituting equation 4.7 with the approximation into equation 4.6, we obtain:

$$E = -\frac{\mu m}{2r}. \tag{4.10}$$

In an LEO, atmospheric drag must be considered, as it leads to a continuous loss of mechanical energy over time, which results in a gradual decrease in altitude. The dissipated power due to drag can be expressed as:

$$P = F_D \cdot v, \tag{4.11}$$

where F_D is the drag force acting on the satellite. Using equation 4.10, the time derivative of the satellite's mechanical energy can thus be written as:

$$\frac{d}{dt}\left(-\frac{\mu m}{2r}\right) = F_D \cdot v. \tag{4.12}$$

The drag force acting on a body with drag coefficient C_D and reference area A moving at a velocity v through an atmosphere of density ρ is:

$$F_D = \frac{1}{2}\rho C_D A v^2, \tag{4.13}$$

Substituting equation 4.13 and equation 4.7 (with $a \approx r$) into equation 4.12, and differentiating the left hand side, gives the result:

$$\frac{\mu m}{2}\frac{\dot{r}}{r^2} = -\frac{1}{2}\rho(r) C_D A \left(\frac{\mu}{r}\right)^{\frac{3}{2}} \tag{4.14}$$

which simplifies to:

$$\dot{r} = -k\sqrt{r}\rho(r) \tag{4.15}$$

where:

$$k = \frac{C_D A \sqrt{\mu}}{m} \tag{4.16}$$

In this expression, k is treated as a constant based on the following assumptions:

- The spinning motion of the CubeSat promotes symmetrical heat distribution and allows the use of an average effective drag coefficient C_D, which is assumed to remain approximately constant throughout the descent.

- The effective cross-sectional area A remains nearly constant due to the uniform shape and stable geometry of the CubeSat.
- While ablation occurs, the relative mass loss is assumed to be small compared to the total mass of the CubeSat during the majority of the descent. This allows the mass m to be treated as constant for the purposes of the trajectory simulation.
- The gravitational parameter μ is constant for Earth.

These approximations are valid in the context of this analysis, especially for altitudes above 40 km, where the CubeSat remains largely intact and the primary variation in the system arises from changes in atmospheric density $\rho(r)$.

4.4 Atmospheric Model - Fizza Naqvi

The atmospheric density model used in the trajectory simulation accounts for the influence of solar activity on the exosphere and thermosphere, which significantly impacts the environmental conditions experienced by the CubeSat during re-entry. Solar radiation is a key factor in determining atmospheric density, as it interacts with atmospheric particles, ionising them and increasing their energy. This leads to an expansion of the thermosphere, resulting in variations in density depending on the solar cycle.

The solar cycle follows an 11-year periodic variation in solar activity, with solar maximums characterised by heightened radiation, increased thermospheric temperature, and subsequent expansion. As a result, atmospheric density decreases at higher altitudes, reducing the drag force experienced by the satellite. However, despite the lower density, the increased temperature and energy of atmospheric particles lead to higher momentum transfer, effectively increasing drag. Conversely, during solar minimums, solar radiation is weaker, causing thermospheric contraction and an increase in atmospheric density, which leads to lower overall drag and a slower orbital decay rate. These fluctuations can have a significant impact on satellite orbits and re-entry trajectories.

To account for these effects, the trajectory model incorporates solar flux ($F_{10.7}$) and geomagnetic activity (A_P) indices. The solar flux at a 10.7 cm wavelength is a widely used proxy for total solar X-ray flux, which strongly influences atmospheric density. The expected value for the planned launch period in December 2026 is 125 SFU[2], based on the solar cycle radio flux progression data determined by the Space Weather Prediction Center, as shown in Figure 4.2. The (A_P) geomagnetic index quantifies geomagnetic disturbances caused by interactions between solar wind and Earth's magnetosphere, particularly through the interplanetary magnetic field (IMF). Unlike the $F_{10.7}$ index, which follows a smooth solar cycle, the A_P index is highly variable due to its sensitivity to unpredictable solar events, such as coronal mass ejections or solar flares. However, outside of these solar events, the A_P index shows limited variation. For this study, a constant, averaged A_P value of 10.8 for 2024 [28] is used, providing a reasonable estimate of geomagnetic activity during this period.

The primary atmospheric density model employed is the Australian Space Weather Agency (ASWA) model [30],

[2]SFU (Solar Flux Unit) is a measure of solar radio flux density, where 1 SFU = 10^{-22} $\mathrm{W\,m^{-2}\,Hz^{-1}}$.

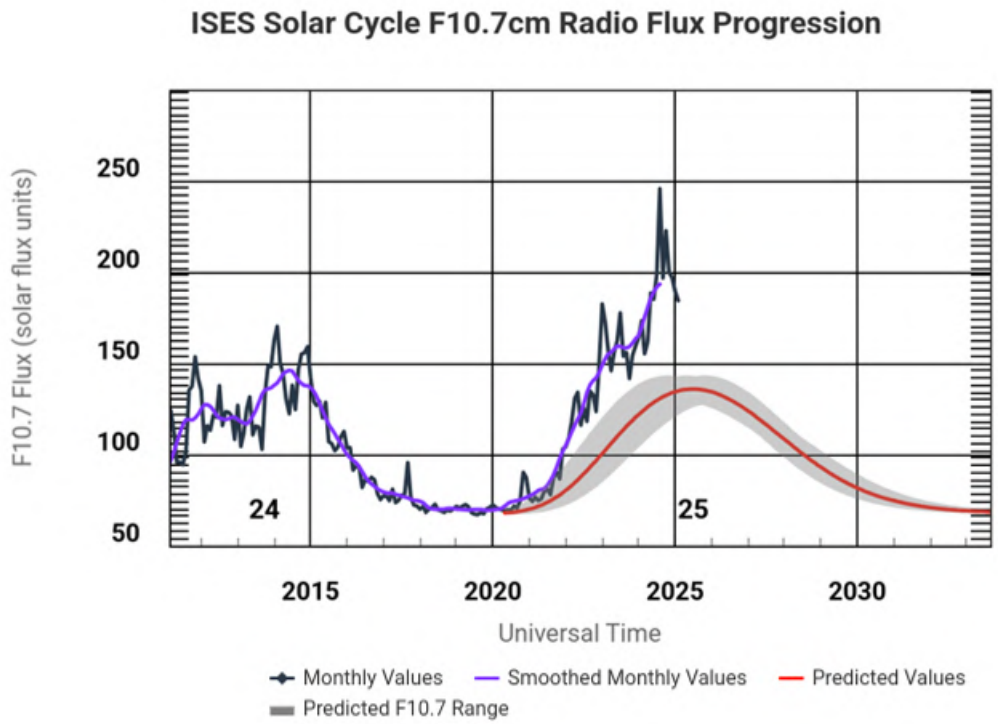

Figure 4.2: Solar cycle radio flux progression data determined by the Space Weather Prediction Center (SWPC) [29].

which defines density using an exponential formulation with a variable scale height. The model equations are as follows:

$$T = 900 + 2.5(F_{10.7} - 70) + 1.5Ap \tag{4.17}$$

$$m = 27 - 0.012(h - 200), \quad 180 < h < 500 \tag{4.18}$$

$$H = \frac{T}{m} \tag{4.19}$$

$$\rho = 6 \times 10^{-10} \exp\left(-\frac{h - 175}{H}\right) \tag{4.20}$$

where T is the temperature in Kelvin, m is the mass in kg, h is the altitude in km, H is the scale height[3] in km, and ρ is the atmospheric density with units kg/m^3. This model is valid for altitudes between 180 km and 500 km. The ASWA model's molecular mass equation is not valid below 180km, as it does not correctly account for variations in atmospheric composition. Therefore, a piecewise model has been developed to ensure smooth transitions between different atmospheric layers while maintaining consistency in density predictions, as shown in Figure 4.3.

For altitudes below 180 km, the modified model utilises NASA's Earth Atmosphere Model [31] to incorporate temperature and mass variations in the stratosphere and troposphere. The equations are defined as:

[3]The scale height represents the altitude over which the atmospheric density decreases by a factor of e.

For $100 < h \leq 180$ km (lower stratosphere):

$$T = 216.69\,\text{K} \tag{4.21}$$

$$m = 28.96 - 0.0076 \cdot (h - 100) \tag{4.22}$$

$$\rho(h) = \rho_{180} \cdot \exp\left(-\frac{h - 180}{H}\right) \tag{4.23}$$

For $h \leq 100$ km (trophosphere):

$$T = 288.19 - 0.00649 \cdot h \tag{4.24}$$

$$m = 28.96 \tag{4.25}$$

$$\rho(h) = \rho_{100} \cdot \exp\left(-\frac{h - 100}{H}\right) \tag{4.26}$$

In these equations, ρ_{180} and ρ_{100} refer to the reference densities at 180 km and 100 km, respectively.

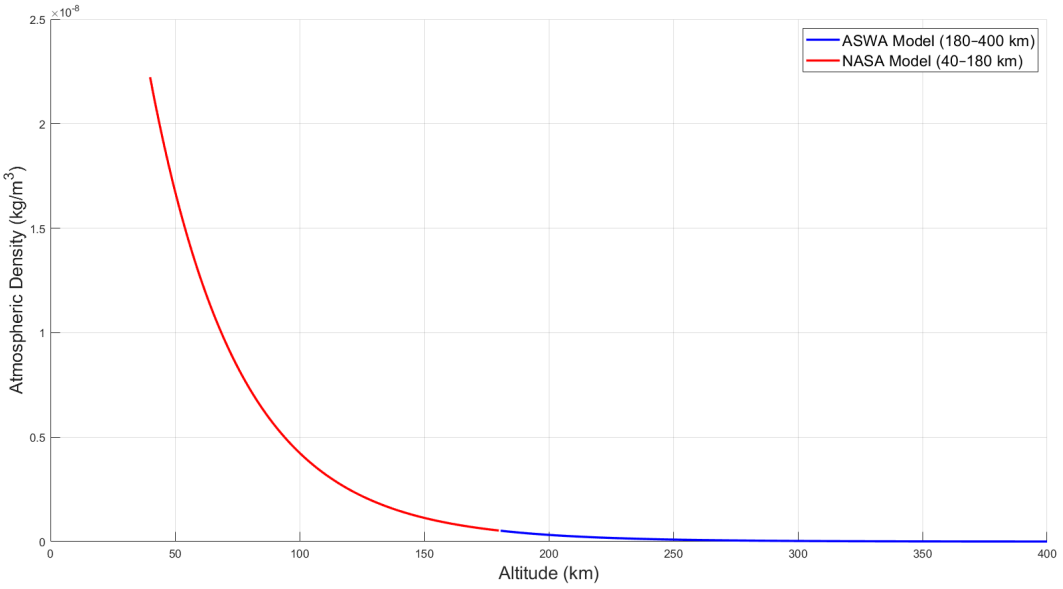

Figure 4.3: Atmospheric density vs altitude plot using a piecewise function that combines ASWA's Atmospheric Density Model and NASA's Earth Atmosphere Model.

This piecewise approach ensures continuity between atmospheric layers and improves the accuracy of density estimations for the CubeSat's re-entry trajectory. While more complex models exist, the combined models from ASWA and NASA provide a practical balance between accuracy and computational efficiency: the piecewise model provides sufficient accuracy for the scope of the simulation, while being computationally less demanding than higher-order models. This makes it a practical choice for the analysis, where computational efficiency is important for handling the extensive calculations involved in simulating the CubeSat's re-entry trajectory.

4.5 MATLAB Trajectory Model - Fizza Naqvi

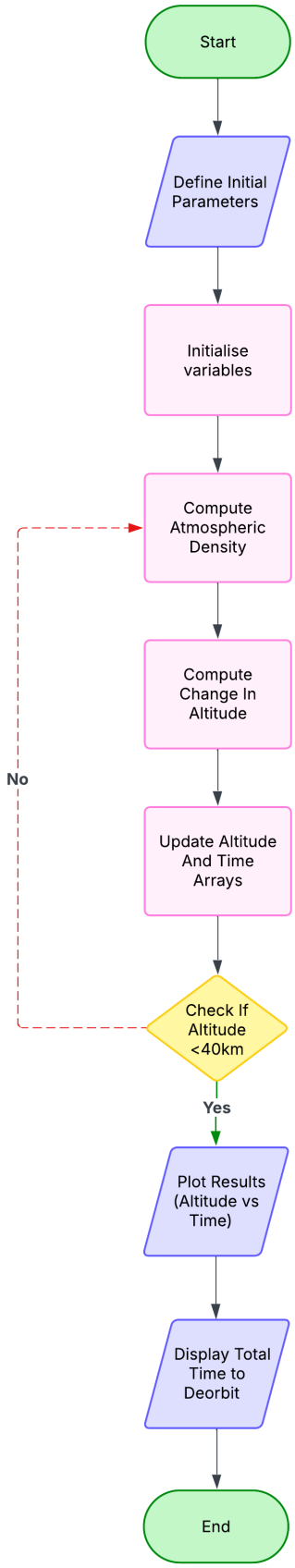

Figure 4.4: Algorithm flowchart for simulating the satellite re-entry trajectory.

Simulation Process The flowchart in Figure 4.4 visually illustrates the algorithm used to simulate the satellite's re-entry. The general process is outlined as follows:

1. **Initialisation:** The function begins by initialising the required variables and arrays, including those for storing altitude and time. Additionally, constants such as the Earth's radius and gravitational constant are defined, ensuring consistency throughout the simulation.
2. **Iteration:** In each iteration, the algorithm calculates the atmospheric density at the satellite's current altitude, solves equation 4.15 using Runge-Kutta 4[4], and updates the altitude and time arrays.
3. **Termination:** The simulation continues until the satellite reaches an altitude of 40 km, where thermite breakup is expected to occur, at which point the re-entry process is considered complete.

Input Parameters The simulation requires several input parameters, which are crucial for calculating the satellite's motion during atmospheric re-entry. These parameters are as follows:

- Altitude (h = 400 km): The initial altitude of the CubeSat above Earth's surface, positioned in Low Earth Orbit (LEO).
- Satellite Mass (m = 12 kg): The mass of the CubeSat, which influences the deceleration rate during re-entry.
- Reference Area ($A = 0.06 \times 10^{-6}\,\text{km}^2$): The averaged surface area of the CubeSat exposed to drag forces. This is not equivalent to the cross-sectional area of the 8U CubeSat[5].
- Drag Coefficient ($C_D = 2.2$): An approximate value for the dimensionless number representing the aerodynamic drag experienced by the CubeSat, based on typical values for similar small satellites [33].
- Solar Flux Index ($F_{107} = 125$): An average value representing solar activity for December 2026.
- Geomagnetic Index ($A_p = 10.8$): An average value representing geomagnetic activity over the course of a year.

Outputs of the Simulation The outputs of the simulation allow the CubeSat's descent to be tracked:

- Altitude: This is an array containing the satellite's altitude (in kilometers) at each time step, showing the change in altitude as the satellite descends towards the Earth's surface.
- Time: This is an array containing the corresponding time (in hours) for each altitude step.

[4]The Runge-Kutta 4th order (RK4) method [32] is a numerical integration technique commonly used to solve ordinary differential equations. It provides a good balance between accuracy and computational efficiency by evaluating the derivative at four points within each time step.

[5]This reference area differs from the geometric cross-sectional area of the 8U CubeSat because it represents an effective area averaged over all orientations and spin states during re-entry, accounting for the tumbling and rotation of the satellite.

4.6 Results - Fizza Naqvi

The simulation demonstrates the critical role of atmospheric drag in shaping the satellite's descent profile, shown in Figure 4.5. At altitudes above approximately 250–300 km, the satellite undergoes a gradual decline due to the relatively thin atmosphere. As it descends into denser atmospheric layers below 250 km, the drag force increases substantially, resulting in a rapid decrease in altitude as drag becomes the dominant factor in orbital decay. This transition from gradual to steep descent is consistent with expectations from the atmospheric drag model (Figure 4.3) and is typical for satellites in LEO. To further illustrate this, the re-entry profile of ESA's ERS-2 satellite is shown in Figure 4.6, demonstrating a similar observed descent pattern with a marked increase in decay rate after 250 km. This comparison confirms that the shape of the re-entry profile observed in the simulation aligns with established behaviour for re-entering satellites at these altitudes.

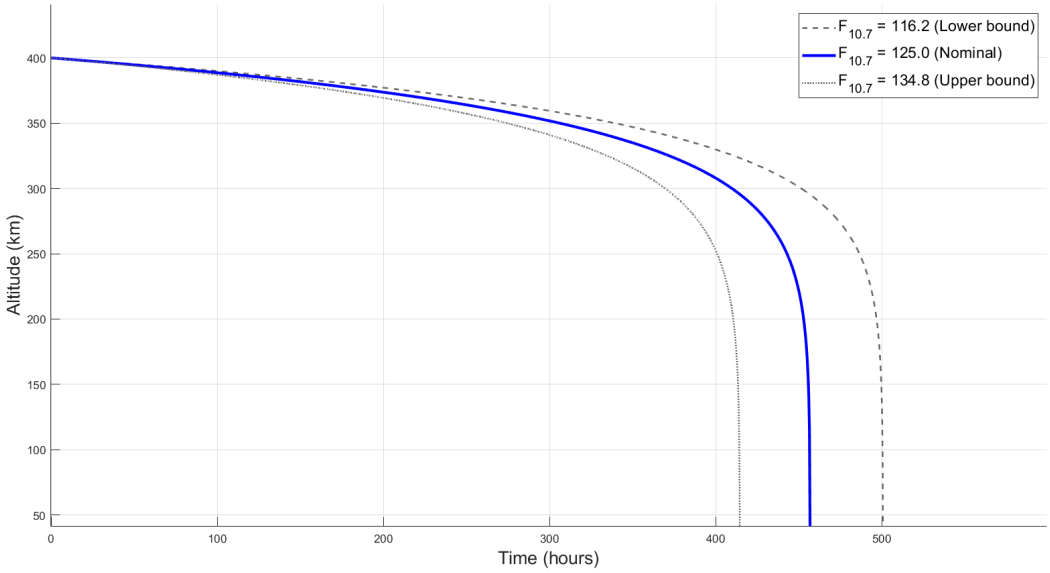

Figure 4.5: Altitude vs Time plot generated by the MATLAB trajectory simulation.

The simulation of the CubeSat's de-orbit trajectory predicts a total duration of 456.9 hours. This result provides insight into the timescale for re-entry, although the duration is highly dependent on several key parameters. One such parameter is $F_{10.7}$, which can exhibit significant variation throughout the year. While Ap is modelled as constant or averaged, the variability in $F_{10.7}$ introduces a level of uncertainty in predicting the exact de-orbit time. Therefore, the duration of the re-entry process can vary depending on the specific timing of the launch, as $F_{10.7}$ fluctuates with solar activity.

The average value of $F_{10.7}$ for December 2026 is forecasted to be 125, but the range of forecasted values for the month is $116.3 \leq F_{10.7} \leq 134.8$. Running the simulation for these values results in different de-orbit durations, as shown in Table 4.2.

This variation highlights the high sensitivity of the de-orbit duration to the solar flux index, with the predicted time varying by over 80 hours depending on the $F_{10.7}$ value, suggesting that the re-entry duration could vary

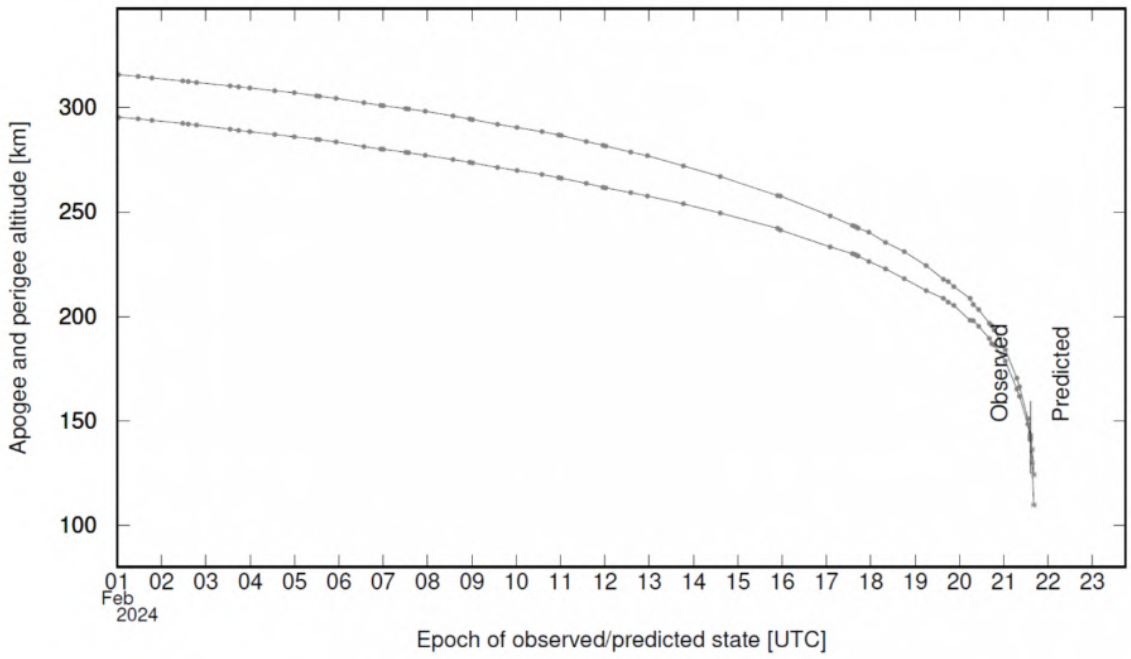

Figure 4.6: Re-entry profile of the ERS-2 satellite, showing high decay after 250 km [34].

Table 4.2: De-orbit duration for different forecasted $F_{10.7}$ values.

Forecasted F10.7	**De-orbit Duration (hours)**
116.3	500.3
125	457.9
134.8	414.6

even more if a different month is chosen for the launch date.

4.7 Verification - Fizza Naqvi

To verify the MATLAB trajectory model, a comparative simulation was conducted using NASA's General Mission Analysis Tool (GMAT) [35]. GMAT is an open-source, astrodynamics software widely used for mission design and trajectory analysis. It employs numerical integration techniques, including the Runge-Kutta 8(9) method, to propagate spacecraft motion under various force models, including atmospheric drag, gravity perturbations, and thrust events. By directly implementing the deorbit burn and subsequent atmospheric decay, GMAT provides a benchmark for assessing the accuracy of the MATLAB model.

As shown in Figure 4.7, the two predictions for nominal solar flux in December 2026 follow each other very closely, verifying the accuracy of the MATLAB model's implementation of the aerodynamic decay equation using the RK4 method. Overall, there is a 2.46% difference in the final time to reach an altitude of 40 km.

The GMAT simulation confirms that the assumption of neglecting the altitude change during the deorbit burn in the MATLAB model is reasonable. In GMAT, a retrograde burn is applied, and the results clearly show that the altitude change at 400 km is negligible. However, the applied delta-V effectively lowers the perigee, enabling a moderately fast re-entry time. This validates the use of the deorbit burn and the assumptions made, as the simulation confirms that the intended trajectory is achieved while maintaining a controlled descent.

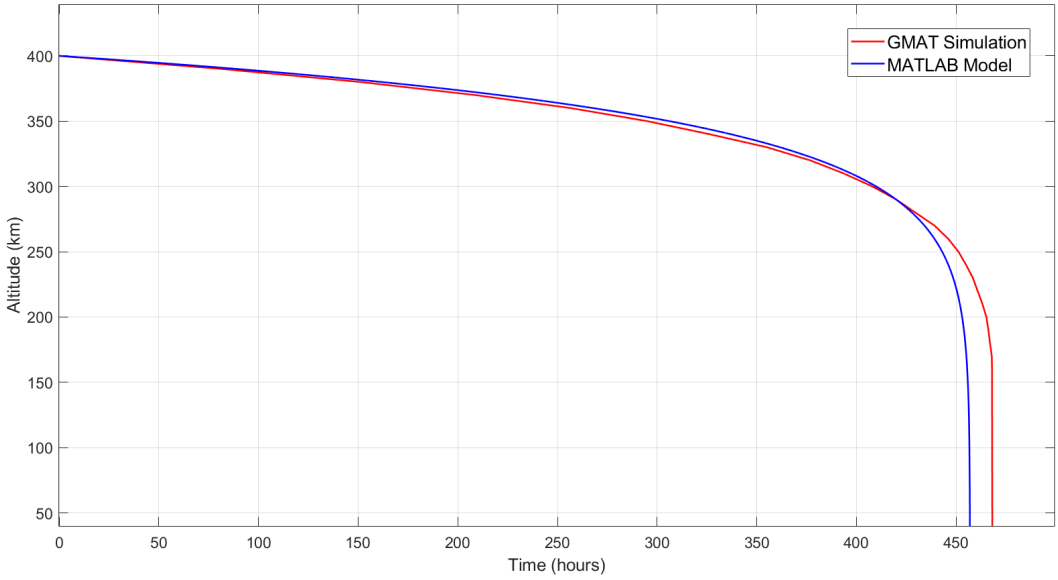

Figure 4.7: Comparison of MATLAB model and GMAT simulation.

The greatest deviation between the two models occurs below 300 km, where the effects of drag become dominant. This discrepancy likely stems from the MATLAB model's simplified drag approach, which combines a constant, averaged drag coefficient with a piecewise atmospheric density model. While sufficient at higher altitudes, this simplification becomes less accurate in denser regions of the atmosphere. In contrast, GMAT uses the MSISE90 atmospheric model, which integrates empirical data and responds dynamically to solar and geomagnetic activity, allowing for finer-grained updates to atmospheric density and resulting in more realistic behaviour at lower altitudes. Additionally, below 300 km, perturbative effects such as J2 and solar radiation pressure—though minor individually—may cumulatively influence the trajectory, and their inclusion could further reduce the observed 2.46% discrepancy.

The level of fidelity in the MATLAB model is appropriate for the short mission duration and the key assumptions made. Given that the satellite's orbital decay is primarily driven by atmospheric drag over a limited timescale, this simplified approach offers an effective and computationally efficient solution. While minor discrepancies—such as the 2.46% difference in re-entry time—emerge due to the exclusion of high-fidelity drag modelling and perturbative effects, these remain acceptable within the scope of the analysis. For longer-term simulations or missions subject to more variable environmental conditions, the inclusion of higher-order perturbations and a more detailed drag formulation would be necessary to ensure accuracy.

4.8 Collision Analysis - Fizza Naqvi

As the number of satellites launched into space continues to rise, along with the increasing amount of orbital debris, in-orbit collision analysis has become an essential aspect of satellite mission planning. With more objects in space, the risk of collisions grows, making it crucial to assess the potential for satellite impacts with other objects or debris. Table 4.3 shows the estimated space debris by numbers based on statistical

models (MASTER-8), taken from ESA's annual environmental statistics report for 2024 [36]. The table shows a significant number of smaller objects that pose a greater collision risk despite their small size. These numbers highlight the importance of including collision analysis in satellite simulations to ensure mission safety.

Table 4.3: Estimated Number of Space Debris Objects in Orbit in 2024.

Size Range	**Estimated Number of Objects**
Greater than 10 cm	40,500
1 cm to 10 cm	1,100,000
1 mm to 1 cm	130,000,000

One way to model the probability of collisions is through the Poisson probability distribution [37], which is commonly used in collision analysis in LEO to estimate the likelihood of events occurring in a given time or space. This model is based on a few key assumptions:

1. The probability of a collision occurring is independent of any prior events.
2. The rate of collisions is constant over time and space.
3. The probability of more than one collision occurring in a given time frame is negligible.

The Poisson probability distribution function is given by the following equation:

$$P(k) = \frac{\lambda^k e^{-\lambda}}{k!} \tag{4.27}$$

where P_k represents the probability of k events occurring, k is the number of events, and λ is the rate of occurrence parameter.

To determine the probability of no events occurring, we substitute $k = 0$ into Equation 4.27, yielding the expression:

$$P(0) = e^{-\lambda} \tag{4.28}$$

The Poisson distribution is typically used when the probability of two or more events occurring simultaneously is extremely small. If we assume that the likelihood of more than one event occurring is negligible, the probability of exactly one event occurring can be represented as:

$$P(1) = 1 - P(0) = 1 - e^{-\lambda} \tag{4.29}$$

The rate of occurrence parameter is derived from the kinetic theory of gases and represents the number of collisions that occur between one molecule and others within a given volume over a specified duration. This parameter is influenced by factors such as the molecule's size, the density of the gas, the relative speed of the molecules, and the length of the time period considered [38].

Applying this kinetic theory to orbital objects, the collision rate between a specified object and all others in a given volume can be determined. The rate of occurrence for orbital collisions is the product of the object's

cross-sectional area, the spatial density (the number of objects per unit volume) of other objects, the relative velocity between the object under consideration and other objects, and the time during which the object is exposed to the risk of collision (the time for de-orbit and decay) [39]. Substituting this analytic form of the rate of occurrence parameter into Equation 4.29, we obtain the probability of a collision occurring between a given object and any other object within a specified volume over a given time period:

$$P_C = 1 - e^{-A_C \cdot SPD \cdot V_R \cdot T} \tag{4.30}$$

where P_C represents the probability of a collision occurring during the time T, A_C is the cross-sectional area of the object (in square kilometers), SPD is the spatial density of objects (in objects per cubic kilometer), V_R is the relative velocity between the object and other objects (in kilometers per second), and T is time (in seconds).

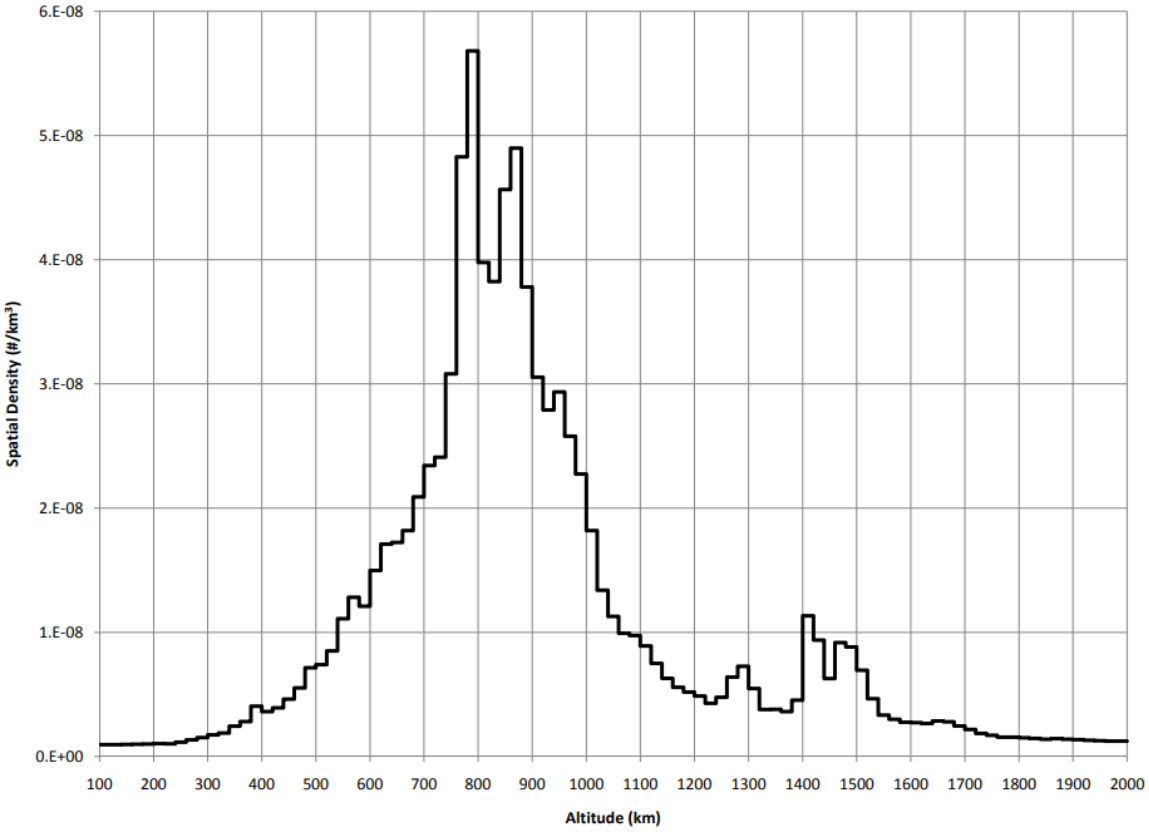

Figure 4.8: Spatial Density of Debris (SPD) in LEO [40].

The cross-sectional area of the satellite is $0.04\,\mathrm{m}^2$. The spatial density of debris (SPD) can be approximated using NASA's data on the current debris environment in Low Earth Orbit (LEO). This data is visually represented as a graph in Figure 4.8, providing a clearer depiction of how SPD varies with altitude. By averaging the SPD values over 100 km intervals, the resulting SPD value from 100 km to 400 km is $1.16 \times 10^{-9}\,\mathrm{objects/km}^3$. The relative velocity between objects in LEO can theoretically range from 0 m/s to twice the orbital velocity. For simplification, the average relative velocity is commonly estimated as $\sqrt{2}$ times the orbital velocity, which approximates to 10 km/s [41]. This assumption is based on the expectation of an average relative angle of 90 degrees between objects. The time duration considered for the analysis is 456.9 hours, as detailed in section

4.6.

NASA's collision risk threshold is 0.1% for robotic spaceflight, as defined in their orbital debris mitigation guidelines [39]. This threshold represents the maximum allowable probability of collision with space debris during a mission segment. If the risk is below this level, additional mitigation measures, such as manoeuvrability or shielding, are not required, indicating that the likelihood of collision is acceptably low. Using Equation 4.30, the probability of collision is calculated to be 0.0765%, indicating that the probability of collision is low enough for the CubeSat to not require manoeuvrability abilities. However, it's important to note that this calculation assumes a constant rate of collisions over time and space, which does not fully capture the dynamic nature of space debris. While this assumption is commonly used for simplicity, it may affect the accuracy of the collision probability, especially in regions of higher debris concentration. To further mitigate any potential risk, the CubeSat's cold gas thrusters and reaction wheels, which are used in conjunction with the MPC system, could be used. In addition to the delta-v used for the de-orbit burn, the cold gas thrusters provide 11 m/s of delta-V (detailed further in section 7.2) allowing the CubeSat to adjust its orientation and maintain the correct attitude for the mission. While the CubeSat cannot perform large-scale collision avoidance maneuvers, the combination of the MPC system, reaction wheels, and cold gas thrusters could be used to ensure that the CubeSat remains correctly oriented if a small-scale collision was to occur, enabling the mission to continue smoothly. These precautions, alongside the calculated low collision probability, minimise the risk to the mission while maintaining the ability to respond to unforeseen circumstances.

5 Mechanical and Structural Design

5.1 Design Goals - Alex Berresford

This iteration of the physical CubeSat was designed with several goals in mind. These goals are as follows:

1. Geometrically centralised centre of mass (COM)
2. Geometry that won't form a stable equilibrium point during re-entry
3. Critical electronics centralised
4. Reaction wheel centred on each major axis
5. All critical components included
   (a) On board computer (OBC)
   (b) Communications array
   (c) Power source
   (d) Reaction wheels
   (e) Thrusters
   (f) Sensors
   (g) Heatshield
   (h) Spectrometer
6. Sufficient volume left for secondary components

Both the geometrical central COM and no stable equilibrium conditions are necessary to assume the tumbling condition which gives even exposure to all faces. This is advantageous in two ways. Firstly, distributing the ablation across the entire CubeSat surface protects the internals for as long as possible, letting us collect more data. Secondly, the even distribution gives a more standardised test, making the experiment more repeatable, which is ideal given an overall goal is to provide a test that becomes industry standard. The centralisation of critical electronics keeps the communications system within it's thermal operation limit for as long as possible, again allowing the collection of more data. Centring a reaction wheel on each major axis is necessary for the control of attitude. This first iteration of the design is not fully complete, so its in our best interests to leave excess volume for unconsidered minor components, and the proper design of internal structure, rather than just internal component placement. Examples of secondary components include wiring and its routing, internal support structures, internal thermal control materials and minor circuit boards.

5.2 CubeSat Geometry - Alex Berresford

One of the major limitations of designing a CubeSat is the few geometries available to be chosen. To satisfy design goal 2 only two geometries were available, 1U and 8U (2*2*2 configuration) as they are the only reasonably sized options that form a cube. Ultimately an 8U design was decided on due to its significantly higher volume. Although a working 1U design would be superior in the long run due to much lower launch costs and more launch options (see Section 3) , an early design was shown to be unfeasible due to a lack of volume. This is largely because most CubeSat components on the market seemed to be designed with the extreme dimensions of a 1U CubeSat in mind. For example, our chosen OBC has dimensions 96mmx96mmx25mm [42], would just tuck into a 1U CubeSat, but doesn't leave enough room at the edges for a significant ablative heatshield to test. Figure 5.1 shows an earlier design of a 1U CubeSat containing only two reaction wheels, a battery and an OBC. This design determined the unfeasibility of a 1U design due to the lack of available volume for other key components e.g. a communications array, thrusters or a third reaction wheel. Furthermore, the excess volume of the 8U CubeSat allows the inclusion of a Spectrometer so that our secondary objective – observation of environmental impact on the atmosphere – can be completed.

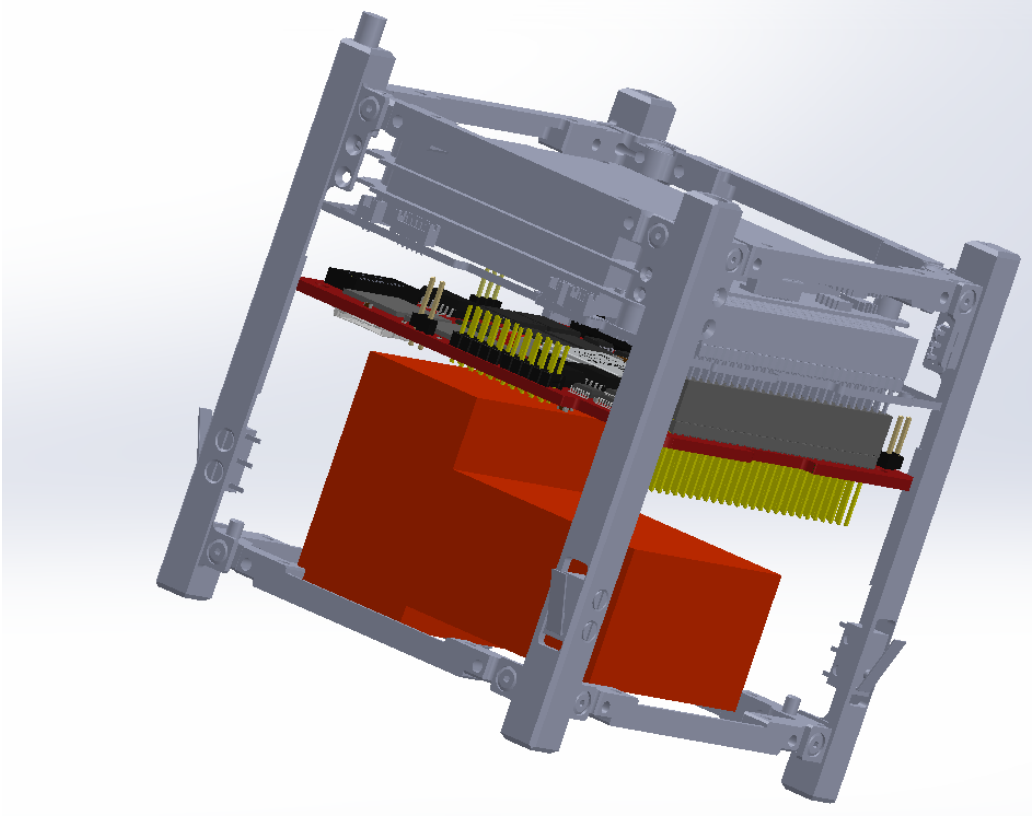

Figure 5.1: A CAD model of a concept design for a 1U CubeSat

5.3 Internal Design - Alex Berresford

The current design iteration is an 8U design containing the components listed in table 5.1, including an example heatshield and custom designed frame. The initial designs mass comes to 7kg, which is significantly lower than the estimated 12kg used for analysis throughout this report. However, secondary components and internal

structures were not considered on this iteration of the design, which is a significant omission that should make up close to the difference. Furthermore, the total mass is inherently variable as the heatshield material will vary with every mission.

Table 5.1: Component list with dimensions and mass details.

Component	**Count**	**L** (mm)	**W** (mm)	**H** (mm)	**Mass** (g)	**Total Mass (g)**
GS-RW10 Reaction wheel [43]	3	50	50	60	250	750
Vacco Cold Gas Thruster [44]	3	100	100	30	542	1626
AvaSpec-Mini2048CL Spectrometer [45]	1	95	68	20	175	175
ICEPS System Core (EPS/OBC/Radio) [46]	1	96	96	25	100	100
CC-UV/VIS/NIR-8MM Cosine Corrector [47]	6	12⌀	–	29	Unknown	–
BA06 A/S Battery [48]	1	90	96	9	209.45	209.45
HXDC16010-SA02 Iridium Certus [49]	4	14⌀	–	41.5	22	88
EPB-25PS-C20004 Transducer	6	6.98 ⌀	–	5.84	Unknown	–
MEAS 410 Thermocouple [50]	6	Negligible	Negligible	Negligible	Negligible	–
MM200 Magnetometer [51]	1	33	20	11.3	12	12
Thermite Charges	8	Arbitrary	Arbitrary	Arbitrary	Unknown	–
Frame	1	180	180	180	361.63	361.63
Central Plate	2	112	112	2	70.16	140.32
GE-223 Carbon Ablator Heatshield	1	200	200	200	3664.12	3664.12
					Total	**7000.47**

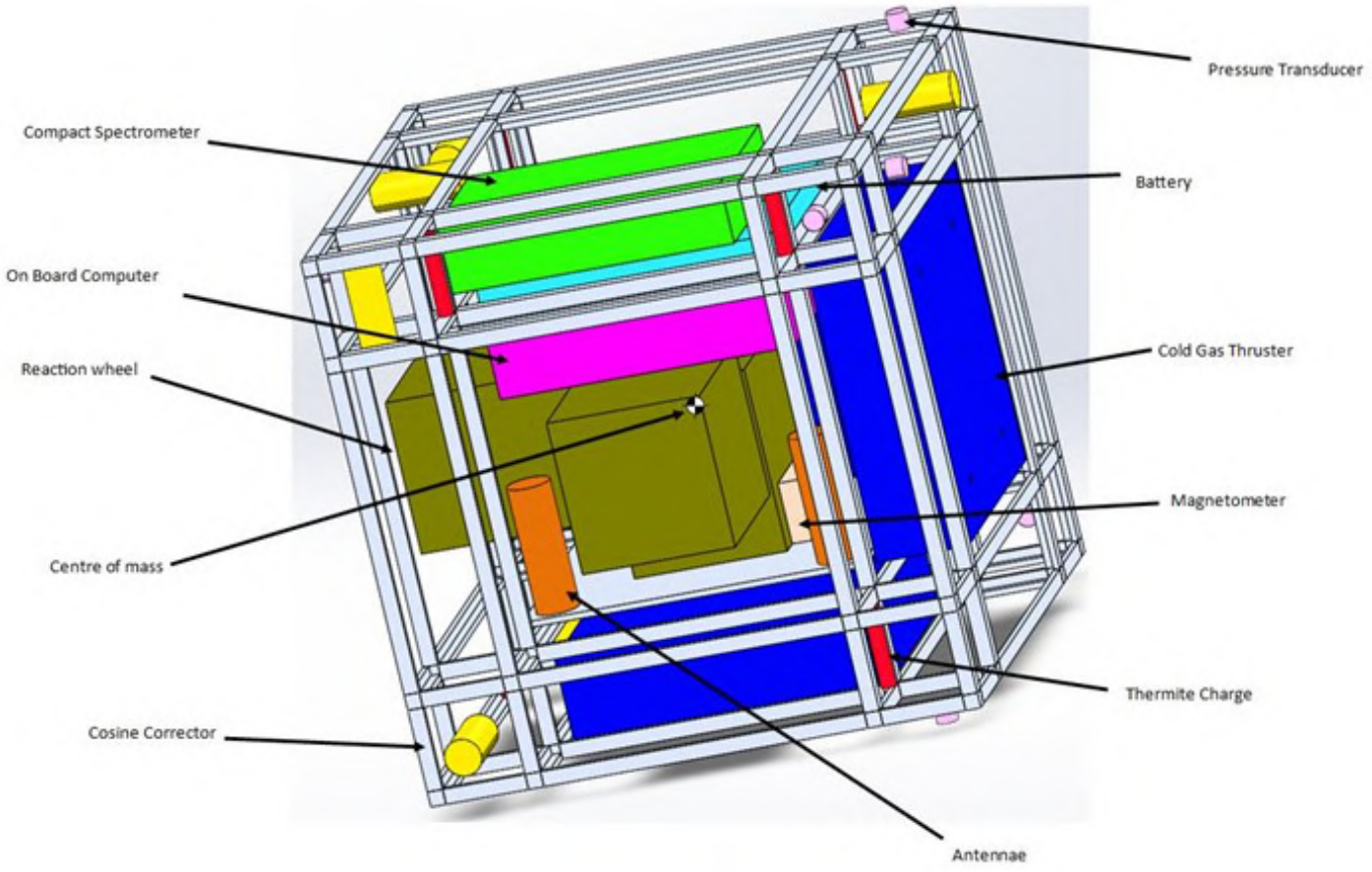

Figure 5.2: Current CAD model of CubeSat

The current CAD model is an abstraction of what the final design might look like, using rough volumes of components to show how the packing problem can be solved while fitting components into ideal places with

regard to the design goals. The sensors that seem to be floating are embedded partially within the heatshield on each face.

Thrusters are placed as such to minimise the routing required for propellant. Also, as their critical role is to perform a deorbit burn near the start of the mission, their increased thermal exposure during re-entry due to proximity to the CubeSat edge is not a problem. The communications array and OBC are placed as centrally as possible as they make up the critical electronic components, achieving the design goal to protect them as much as possible from the extreme thermal environment of re-entry. The antennae array is made up of four antennae placed in a two-by-two grid, 92mm apart. This is necessary to allow beamforming and therefore communication as described in section 6.1.3. The COM is successfully designed to be near the geometric centre and there's a reaction wheel centred on each central axis, satisfying the design goals 1 & 4.

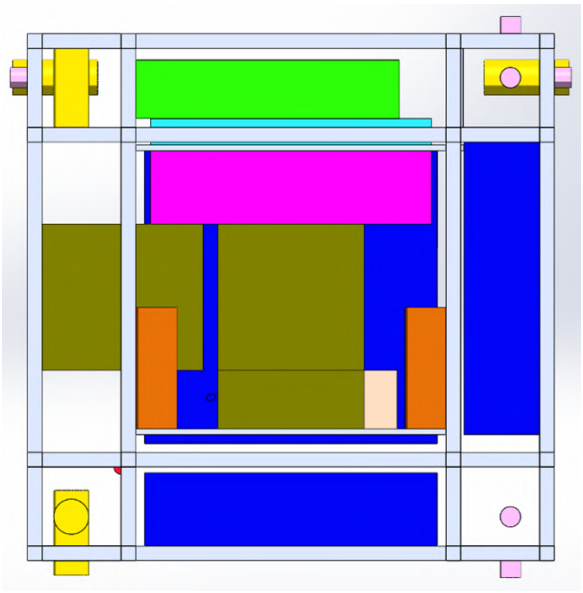

((a)) Front

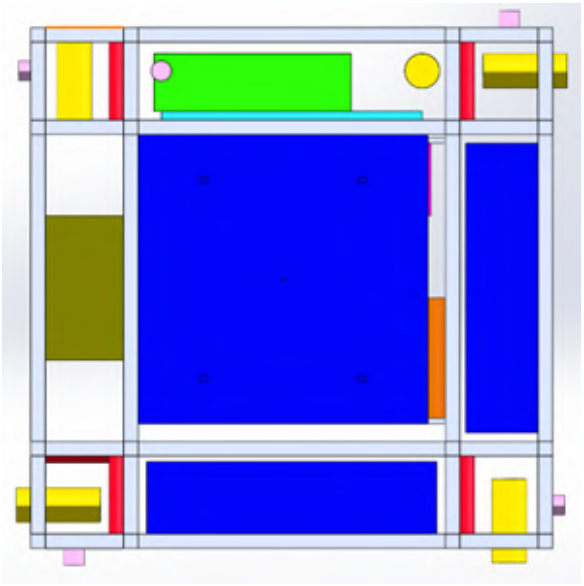

((b)) Side

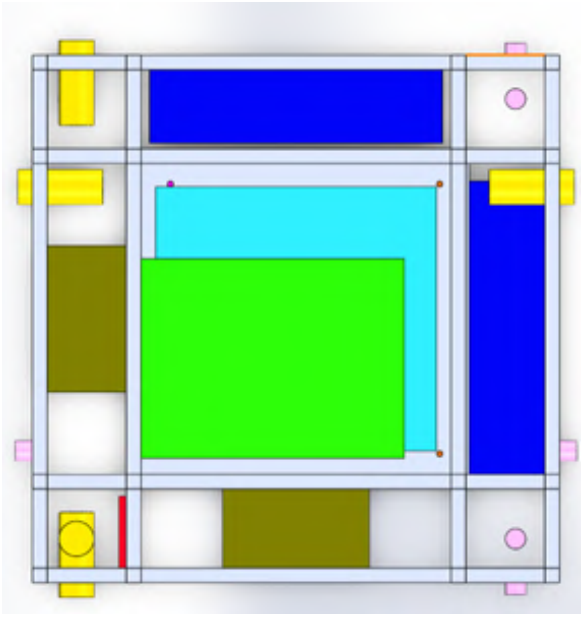

((c)) Top

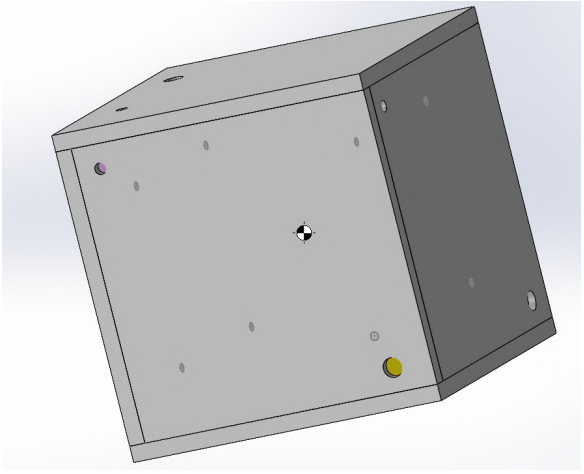

((d)) With ablative

Figure 5.3: Various views of CAD model

5.4 Frame Design - Alex Berresford

5.4.1 Material

Material selection is of high importance when designing a space frame. The material must satisfy physical, mechanical and thermal properties to be determined an appropriate fit. Often, the strength to weight ratio is the key factor when determining what material to use, as it's ideal to minimise payload mass for a cheaper launch, whilst maintaining the strength of the structure. Our case is no different. Aluminium alloys have some of the best strength to weight ratios of any readily available material, are highly machinable and have high corrosion resistance, making them an ideal material for space applications. A qualitative analysis on common aluminium alloys was conducted, with an emphasis on ease of manufacture, strength and low thermal conductivity. Low thermal conductivity is important to slow conduction through the CubeSat and keep the critical electronic systems within their operational window.

Table 5.2: Mechanical and physical properties of considered alloys [52].

Alloy	**Density** (kg/m^3)	**Thermal Cond.** ($W/m.K$	**Melting Pt** (K)	**Thermal Exp.** ($10^{-7}K^{-1}$	**Elastic Mod.** (GPa)	**Shear Str.**(MPa)	**Proof Str.** (MPa)	**Tensile Str.** (MPa)	**Notes**
1050 H14	2.71	222	923	24	71	60	85	100	Easy to weld, difficult to machine
2014	2.82	138	808	23	71	290	390	404	Ideal for cold arc welding and machining
3103-H14	2.73	1609	928	23.1	69.5	–	120	140–180	Easy to weld in most forms
5251-H22	2.69	134	898	25	70	125	165	210	Easily weldable, corrosion resistant
6005A	2.7	188	878	24	70	205	225	270	Difficult to produce thin-walled or complicated extrusions, easily weldable
6063	2.7	200	873	23.5	69.5	150	160	195	Welds easily, good in intricate extrusions
6082	2.7	180	828	24	70	210	310	340	Structural alloy with ok welding, great for high-stress applications
6060	2.7	210	928	24.5	69.5	–	120	160	
6061	2.7	195	923	23.4	70	190	270	310	
2024	2.78	121	775	24.7	73.1	283	324	469	Not suitable for welding

Ultimately, Al 2014 was the clear choice of frame material for our CubeSat. It had one of the highest Tensile and Proof stresses, one of the lowest thermal conductivities and remains easy to manufacture as it can be cold arc welded as well as machined easily. It's comparatively low melting point means it will demise easily from the thermite ignition, which is planned for when the internal temperature reaches 650K at approximately 40km altitude. It's one drawback is that it's the densest of the considered options, however at this stage in the design process we are happy with our current mass estimate, so this isn't a problem.

5.4.2 Structure

The current frame design is a cube frame with 180mm side length, which leaves 10mm on each side for ablative test materials to be fitted. It is formed entirely of of 2x5mm L sections. L sections are ideal as they have a high second moment of area for the volume of material used, giving the frame resistance to vibrations and bending. They do this whilst minimally limiting available volume for components, which is an advantage over hollow sections.

The frame features a central area with similar dimensions to a 1U CubeSat, which was specifically designed to house several components designed for that geometry, for example our OBC and battery. Although not placed

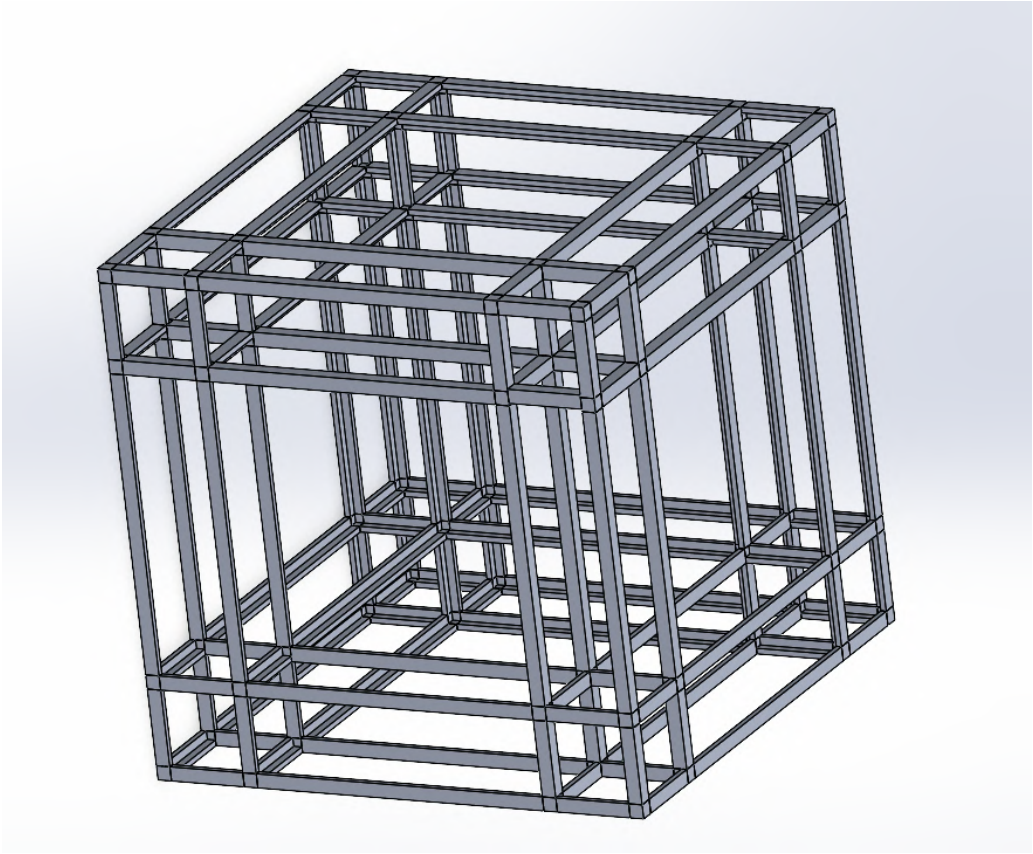

Figure 5.4: CAD model of frame

in the central section, the Cold Gas thrusters share this geometry and require a similarly sized opening.

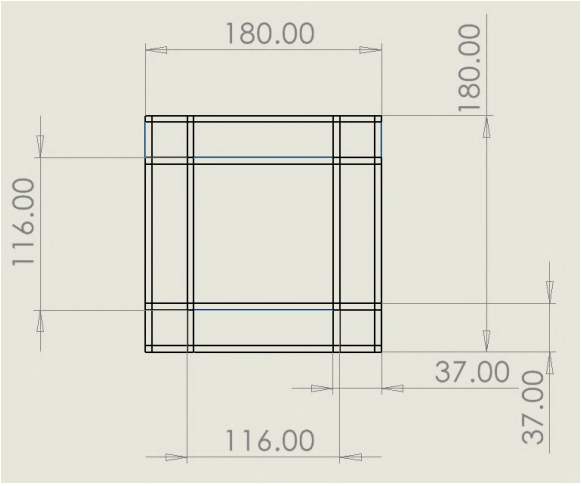

((a)) Drawing of frame

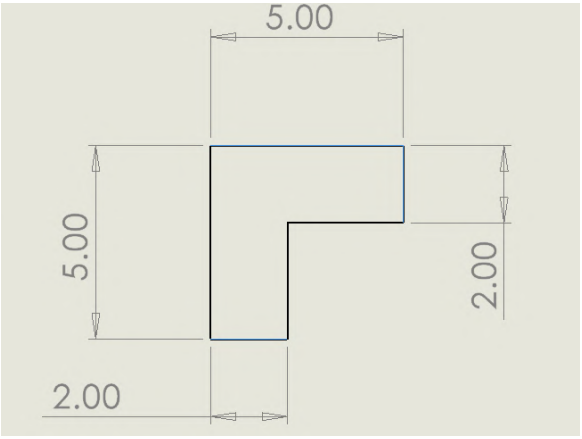

((b)) Drawing of L-section

Figure 5.5: Drawings of Frame and L-section (mm)

5.5 Launch environment analysis - Alex Berresford

While the thermal attributes of the CubeSat were designed to survive the harsh environment of space, it was necessary to design the mechanical aspects of the CubeSat to survive the launch phase. Two major causes of failure were considered. The first was resonance, which considers the random vibrations during launch and ensures they do not induce large enough vibrations in the CubeSat such that the frame fails. The second was acceleration loading, which considers the load through the CubeSat during launch due to its self-weight at the high g-forces it would experience during launch.

5.5.1 Vibrational analysis

Modelling Figure 5.6 shows how the CubeSat was modelled for vibrational analysis, a frame with n frames and m columns, whilst being symmetrical in the x and y axis. The bottom floor is fixed to the baseplate, where the vibrations enter the system. Each floor is assumed to hold an equal portion of the total CubeSat mass. It followed to model this as a horizontal mass-spring system, with the bending of the supports producing spring-like action. The spring constant was calculated from the support height, second moment of area and the Youngs modulus of material, as shown in Figure 2 and below. This analysis only considered horizontal vibrations as vertical vibrations are prevented by the fixed baseplate, and any elastic behaviour along the length of a strut is considered negligible when compared to the horizontal displacements of the floors.

$$x = \frac{FL^3}{3EI}[53] \tag{5.1}$$

The analysis point of figure 5.7 was taken as the midpoint between each floor such that $L = \frac{h}{2}$ and $x_f = 2x$ where h is floor height and x_f is the horizontal floor displacement. Substituting and rearranging into the form $F = kx$ to find the spring constant gave the following.

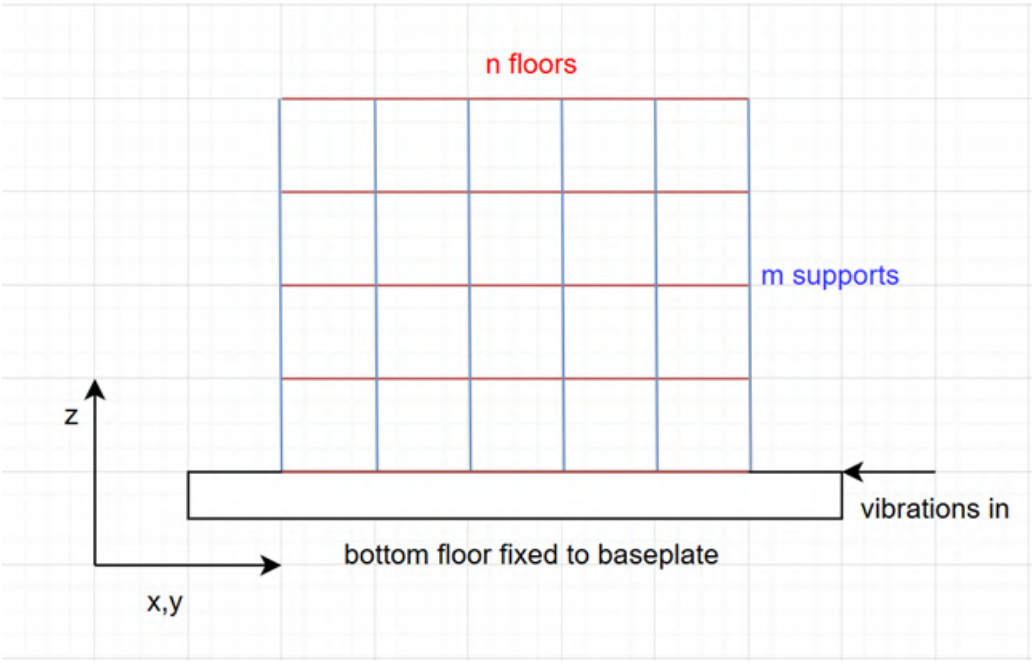

Figure 5.6: Simplified CubeSat Model

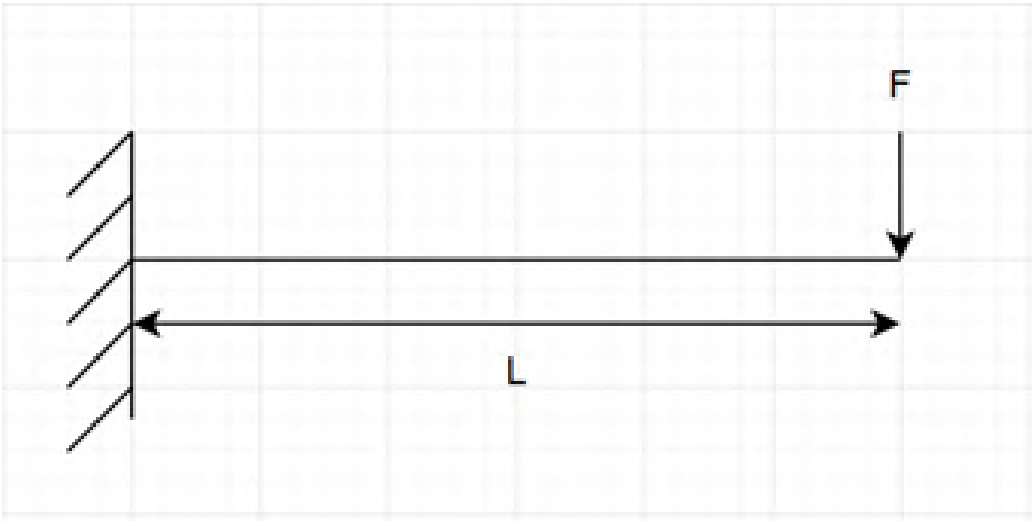

Figure 5.7: Fixed end cantilever diagram [53]

$$F = \frac{12EIx_f}{h^3}$$
$$k = \frac{12EI}{h^3} \tag{5.2}$$

The equations of motion of the modelled system can be expressed in matrix form as:

$$M\ddot{X} = KX \tag{5.3}$$

where

$$M = \begin{bmatrix} m_f & 0 & \dots \\ 0 & m_f & \dots \\ \vdots & \vdots & \ddots \end{bmatrix}$$

$$K = \begin{bmatrix} m^2k & -m^2k & 0 & \cdots \\ -m^2k & 2m^2k & \ddots & 0 \\ 0 & \ddots & \ddots & -m^2k \\ \vdots & 0 & -m^2k & m^2k \end{bmatrix} \tag{5.4}$$

and X is a vector of horizontal floor displacements, m_f is the floor mass. The m^2 comes from summing the spring constants of all supports within the square shape.

Assuming a sinusoidal solution for X with natural frequency ω_0 gives:

$$0 = \left(K - {\omega_0}^2 M\right) X$$

$${\omega_0}^2 = \frac{K}{M} \tag{5.5}$$

Solving for ω_0 gives us the natural frequencies of the system. Ideally, we design these frequencies to be in the low power areas of the vibrational power spectral density – shown in figure 3. It is important to note that this analysis assumes no damping, which means that the real system would have resonant peaks at slightly different frequencies to those calculated by this method.

Simulation Figure 5.8 shows the power spectral density (PSD) of random vibrations the CubeSat would experience during launch. Using MATLAB, the PSD was used to generate a set of sample signals to simulate the system vibrations. Summing these signals into the time domain produces a single signal. The flowcharts in Figures 5.9,5.10(a) and 5.10(b) describe the entire process.

With the PSD's maximum frequency being $2000Hz$, to avoid aliasing the signals, a dt of $\frac{1}{4000}$seconds was chosen, for a sampling rate of $4000Hz$, satisfying the Nyquist frequency limit. The natural frequencies are calculated using the process described in the modelling section prior.

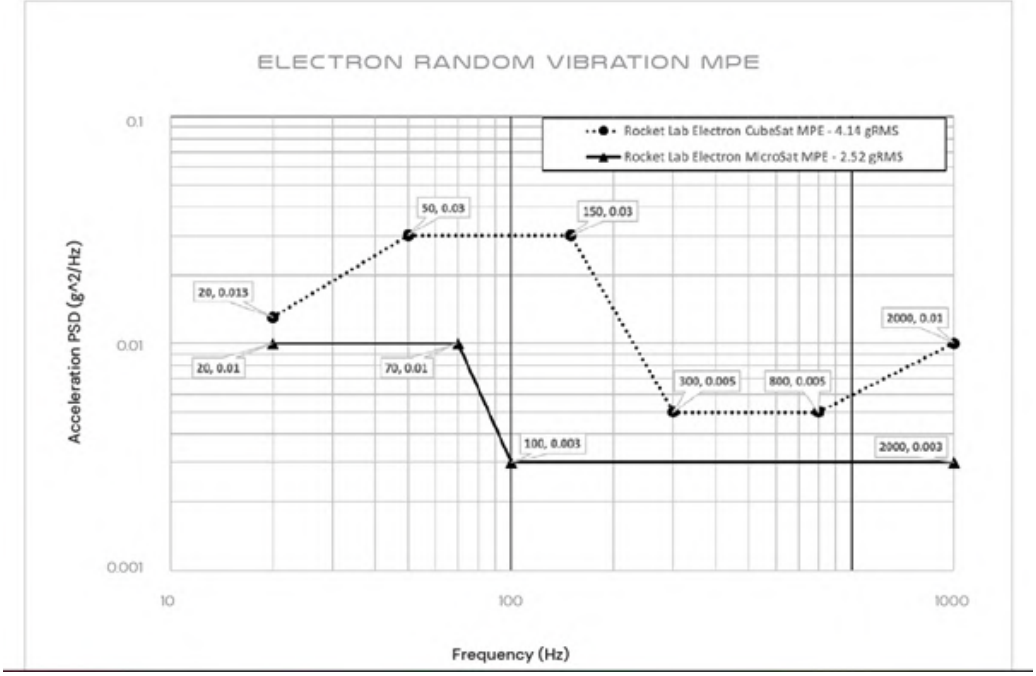

Figure 5.8: Power spectral density of expected vibrations during launch [23]

Validation Due to the relatively simple modelling approach, validation of this simulation was achieved by comparison of a solved base case – the single mass-spring system with a sinusoidal forcing function, for which the equation of motion for is:

$$\ddot{x}(t) \; + \; {\omega_0}^2 x(t) \; = \; F_0 cos(\omega t) \tag{5.6}$$

This has two different solutions depending on the value of ω. The first is where $\omega \neq \omega_0$ giving;

$$x(t) \; = \; d_1 cos(\omega t) \; + d_2 sin(\omega t) [54] \tag{5.7}$$

Which is simply a sum of coherent sinusoidal functions, which produces a single output sinusoid.
The second case is where $\omega \; = \omega_0$; which has the solution:

$$x(t) \; = \; t(d_1 cos(\omega t) \; + d_2 sin(\omega t)) [54] \tag{5.8}$$

Which produces a sinusoid which has a growing oscillatory response, bounded by the line $x \; = \; t$, showing resonance.

To test this base case, a two-floor model was used, with a single, manually generated sinusoidal input. The two-floor model matches the single spring-mass model due to the single set of supports between the base and the only unfixed floor. Firstly, the $\omega \neq \omega_0$ case was tested in a 1 second simulation, as shown in figure 5.11 .

Floor 1 is the fixed floor, which showed some movement as the displacements are all taken relative to the $n-1$

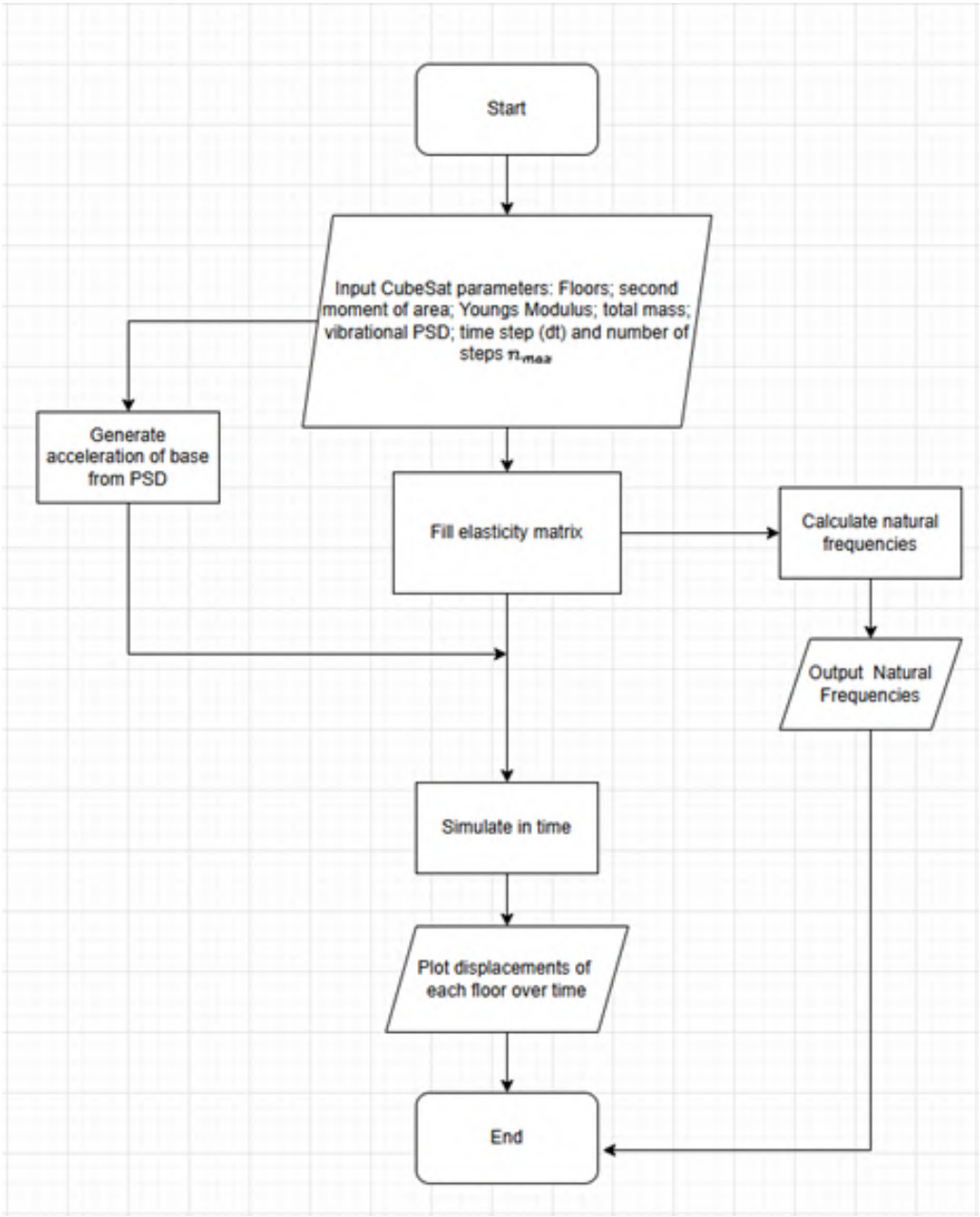

Figure 5.9: Overall flowchart of vibrational analysis code

displacement of the fixed base. Otherwise, the second floor behaved as expected, following a sinusoid of fixed amplitude.

The same parameters were tested again, using an input signal at to the systems natural frequency. This showed resonance as expected, with a sinusoid bounded by an $x = at$ curve reaching magnitude orders of magnitude above the non-resonant case.

In the case where $\omega \approx \omega_0$, and the simulation time is extended, a beating effect can be observed, which is again, expected in a real system.See 5.13

Results Simulations using this model on various frame geometries were ran to inform on which geometry showed the most promise for surviving launch. Standard runs were completed on varying numbers of floors,

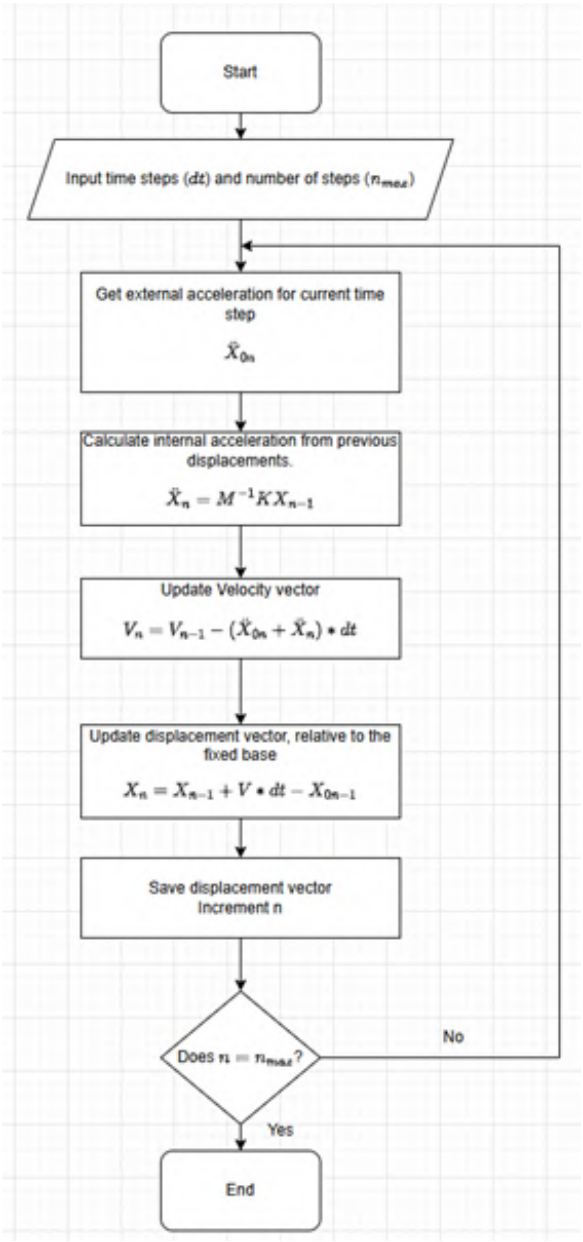

((a)) Flowchart describing simulation process

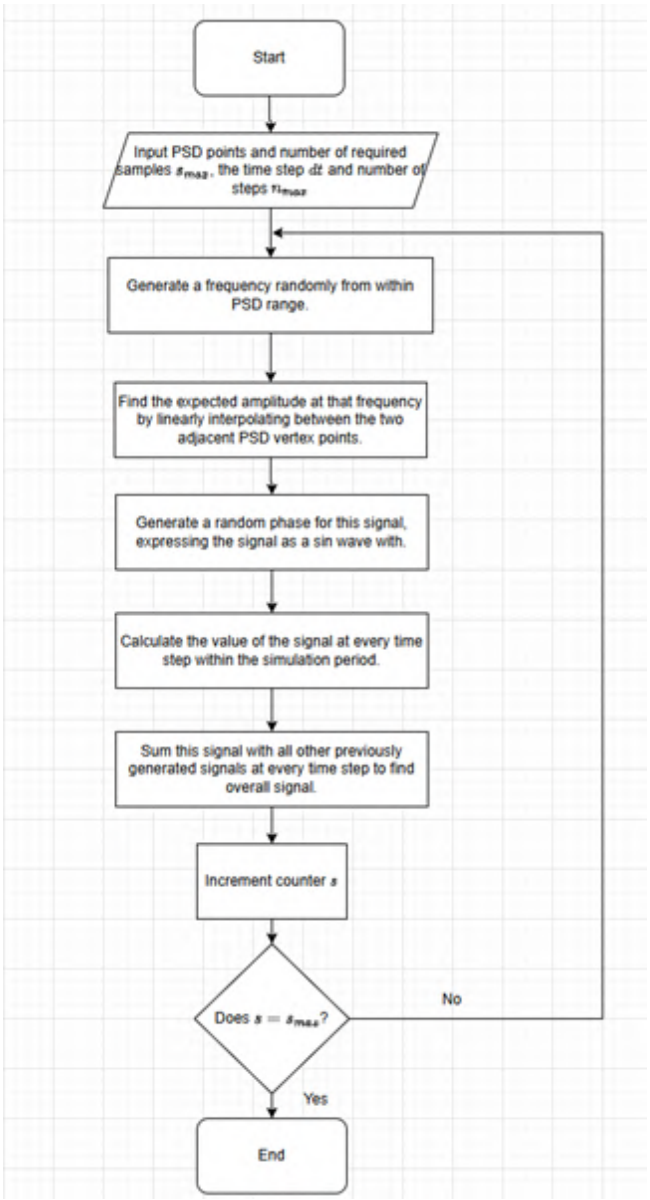

((b)) Flowchart describing sampling process

Figure 5.10: Simulation and Sampling Flowcharts

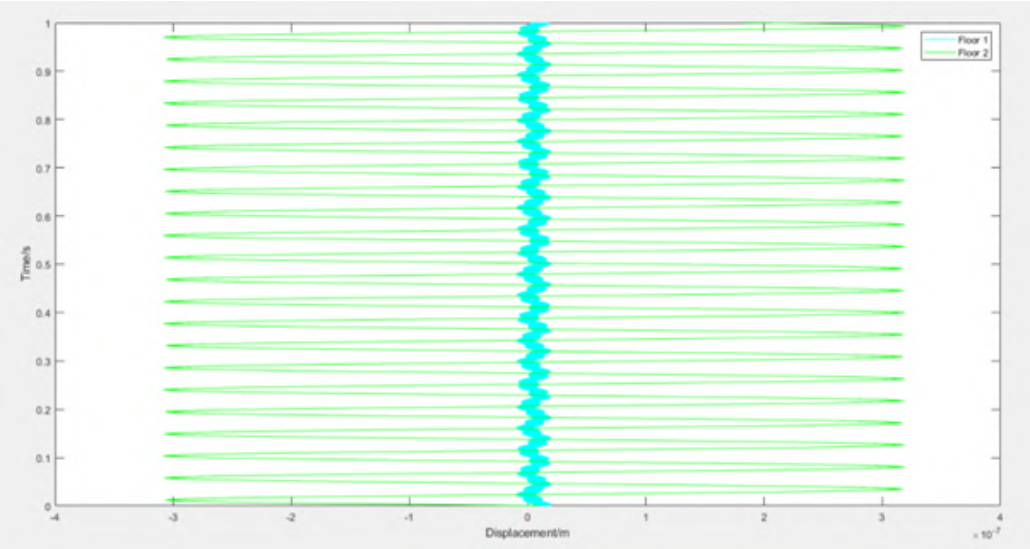

Figure 5.11: Non-resonant test case

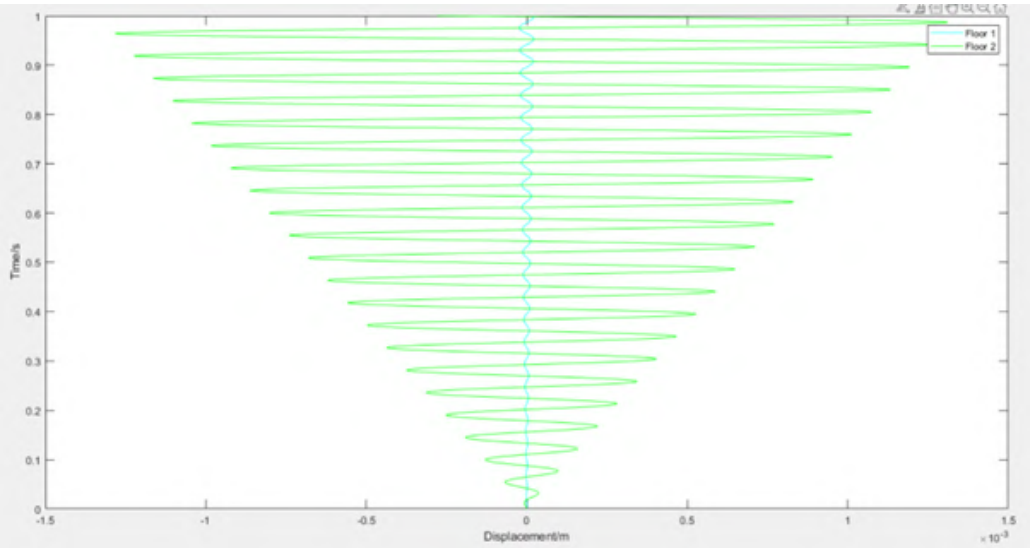

Figure 5.12: Resonant test case

with the same randomly generated signal and the parameters described as follows in 5.3:

Table 5.3: Frame Test Parameters

Mass (kg)	**Struts**	**Strut I (m^4)**	**Material**	**E (GPa)**	**Sim Time (s)**	**Signals**	**Length (mm)**
12	4	3.385×10^{-11}	Aluminium	70	50	1000	200

Whilst the simulation results may be pretty, there's limited useful data we can draw from them due to the absence of damping in the simulation. They serve as an upper bound for the potential of the vibrations in the extreme case of low damping. Therefore, we can only usefully use the maximum displacements and a check for a resonant response of each simulation for a comparison. The table below shows the mean maximum displacement of each CubeSat over three trials, with each geometry being tested with the same input signal.

It can be observed that the 7-floor geometry show the lowest mean maximum displacement over the set of trials,

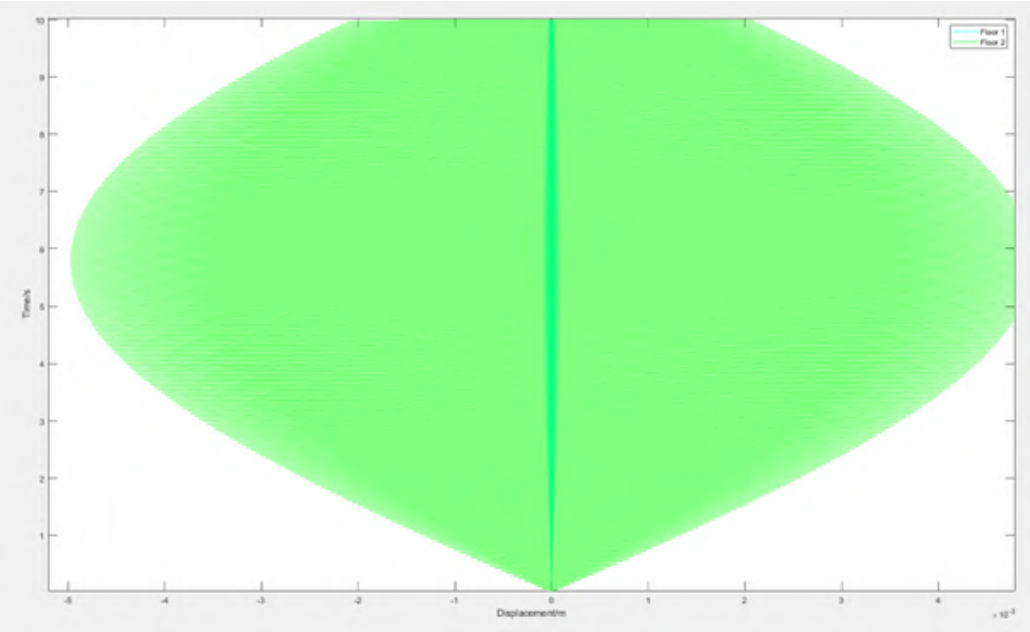

Figure 5.13: Extended test showing a beating effect

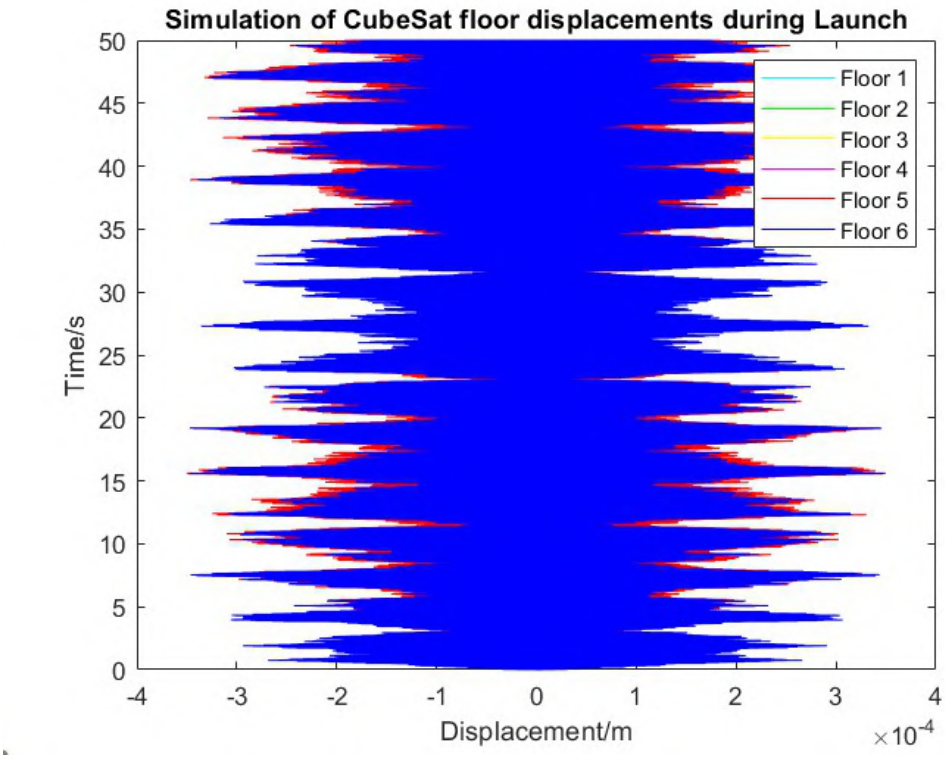

Figure 5.14: Example plot from a 6 floor test

indicating that a 7-floor design might be best suited to resist the vibrational environment during launch. More critically, no frame showed resonant behaviour.

Our frame design doesn't fall easily into any of these categories. Whilst having 4 floors, they aren't evenly spaced as the test runs were, instead featuring 2 floors close together at either end of the frame. This spacing most closely resembles that of a 7-floor design that's missing the middle 3 floors. The simulation was run with a modified parameters and elasticity matrix to mirror the frame design in section 5.4.

Table 5.4: Maximum Displacement Magnitude vs Number of Floors

Number of Floors	**Max Displacement (mm)**
2	1.046 507 88
3	2.188 738 00
4	0.392 875 00
5	0.925 319 00
6	0.323 091 00
7	0.102 572 00

Table 5.5: Actual Frame Test Parameters

Mass (kg)	**Struts**	**Strut I (m^4)**	**Material**	**E (GPa)**	**Sim Time (s)**	**Signals**	**Length (mm)**
12	4	3.385×10^{-11}	Al 2014	73	50	1000	180

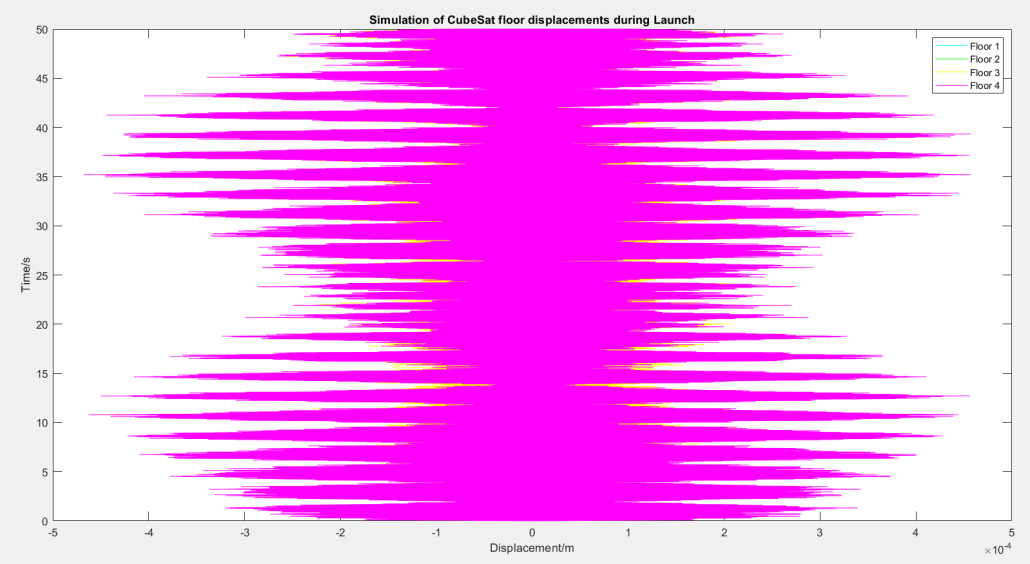

Figure 5.15: A simulated floor displacement plot of frame

Similarly, to before, three tests were performed and the mean maximum displacement calculated. This was found to be $0.262502mm$ and no resonance was observed. A simple static finite element analysis study was run in SolidWorks to observe the worst-case scenario of two adjacent floors undergoing this displacement in opposite directions, and the resulting stress on a support beam. FEA as a technique will be discussed in more depth in section 5.5.2.

This study shows the yield stress of material being exceeded by a factor of two, indicating the frame could fail due to the vibrational environment. However, there are several mitigations to this. As previously discussed, this analysis technique gives an upper bound, and this scenario in question is an absolute worst case. It's more likely that the close adjacent floors move in unison, and that the largest displacement will be observed between the top and bottom floors. When this analysis was applied to the central larger floor gap, the yield stress was not exceeded in any section of the beam.

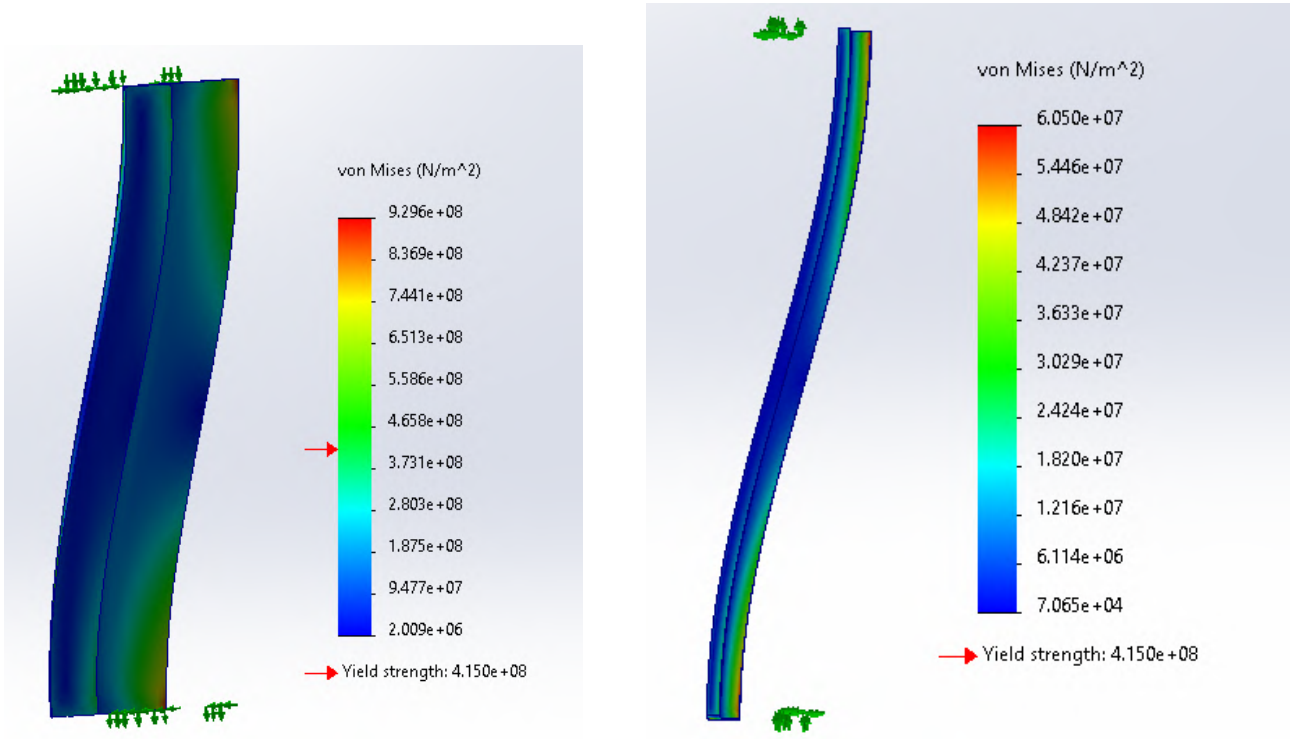

((a)) 27mm section ((b)) 106mm section

Figure 5.16: Stress heat diagrams from sections under extreme displacement

5.5.2 Acceleration Environment

During launch the CubeSat will be subject to large g-forces due to the rocket accelerating. Figure 5.17 below shows the typical envelope for which the electron accelerations lie. Lateral acceleration forces would be caused by manoeuvres whilst axial acceleration would be caused by thrust or drag.

To ensure the frame doesn't fail under these g-forces, the design was analysed using Finite element analysis (FEA) within SolidWorks to simulate the extreme load cases.

FEA is a numerical analysis technique that works by dividing an object up into a mesh of small elements, before a governing equation is applied across the mesh to simulate what might happen under different boundary and initial conditions. In this case, a static analysis was performed, meaning the stiffness matrix method was applied over the mesh to find displacements and stresses.

The frame was analysed with the estimated CubeSat mass of 12kg distributed across its top surface whilst the bottom face was fixed, under all the load pairs on the vertices of the Acceleration MPE.

Distributing the mass across the top surface simplifies the boundary conditions and provides slightly harsher conditions than shown by the MPE, as it overestimates the weight each top cross beam has to support. This upper bound simplification is valid as it only builds more confidence in the frame design.

As we can't assume the angle which the CubeSat will be at whilst the rocket makes lateral manoeuvres, it's necessary to simulate them at the two most extreme angles; perpendicular to and at 45 degrees to a flat face.

In no case is the highest stress within the order of magnitude as the yield stress of the frame, and the highest

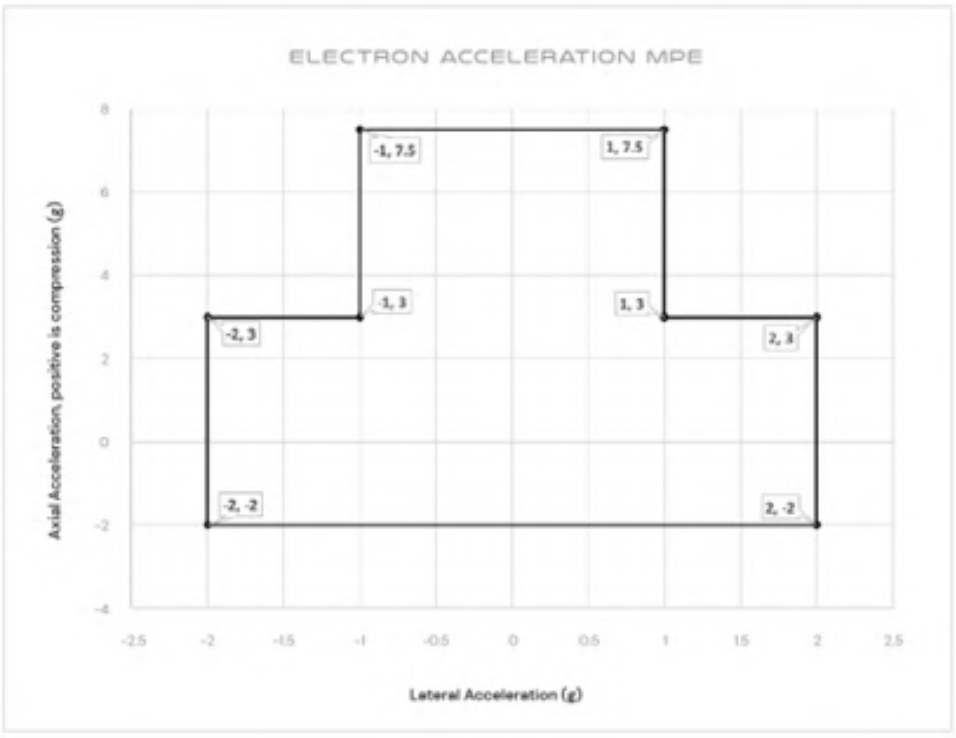

Figure 5.17: Plot showing expected bounds of acceleration during launch [23]

observed displacement across all cases was 0.606mm, which is observed in one of the top supporting beams that are taking several times the load they're expected to carry. Overall, this analysis shows that the frame is more than capable of surviving the g forces present during launch.

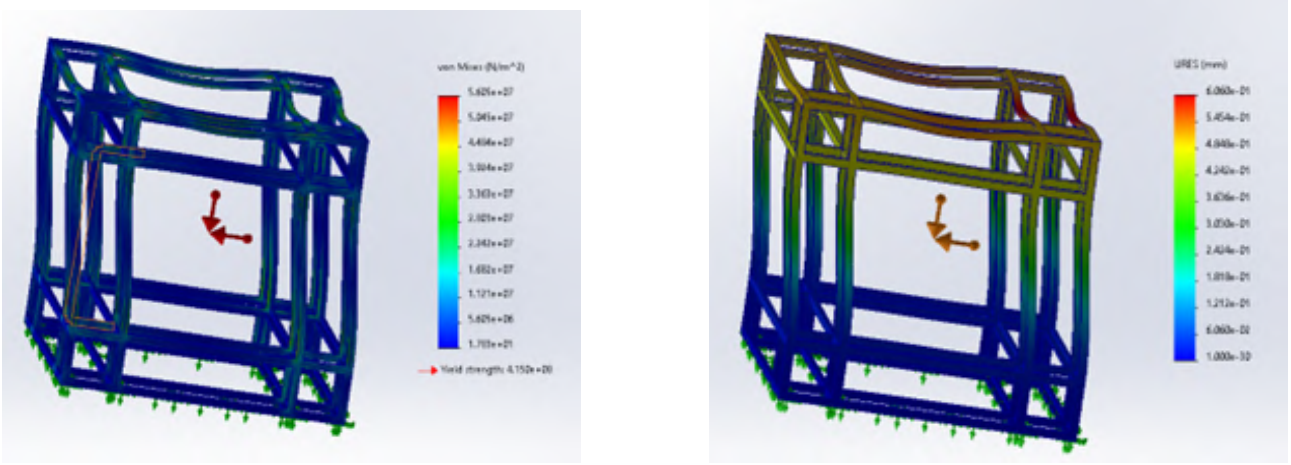

((a)) Stress ((b)) Displacement

Figure 5.18: Heat maps for a 7.5g axial load and 1.5g horizontal load perpendicular to face

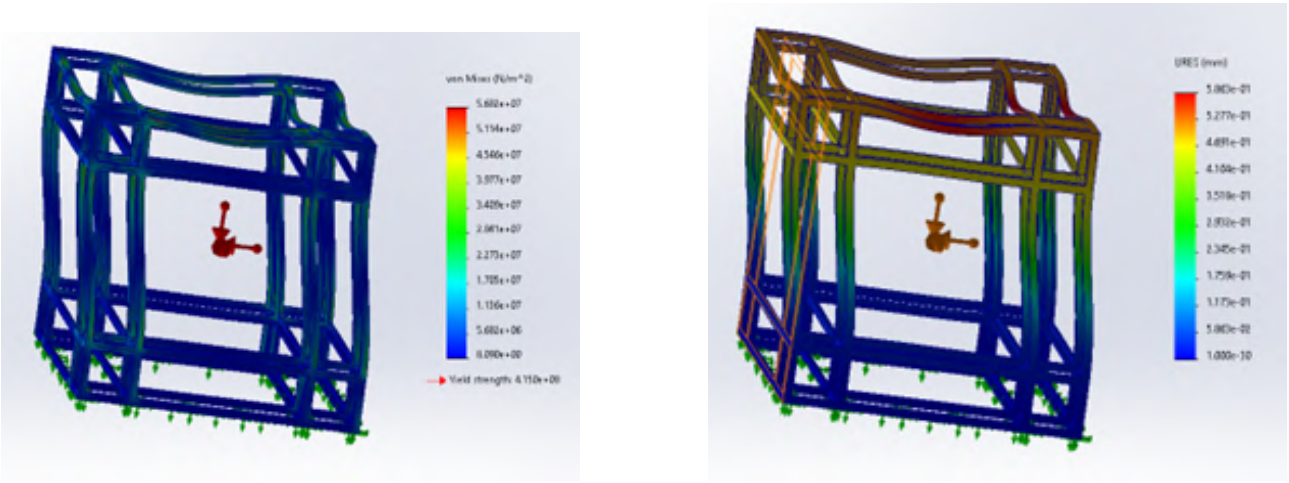

((a)) Stress ((b)) Displacement

Figure 5.19: Heat maps for a 7.5g axial load and 1.5g horizontal load 45 degrees to face

5.6 Thermite for Demise (T4D) - Claudio Vestini

This section presents the design-for-demise (D4D) strategy established for the CubeSat mission. Given the adoption of ablative materials, the exact passive demise altitude of the CubeSat cannot easily be predicted. To significantly lower the probability of ground impact, Thermites were implemented to ensure the complete demise of the spacecraft.

D4D is an increasingly important methodology within spacecraft design, aimed at reducing the probability of surviving debris reaching the ground during uncontrolled atmospheric re-entry. Within the context of D4D strategies, thermite-for-demise (T4D) is a promising approach that involves embedding thermite-based pyrotechnic charges within the spacecraft's structure to provide an internal heat source during re-entry. Thermites, composed of a metal and metal oxide powder (Al+Fe_2O_3 for this design), undergo highly exothermic redox reactions upon ignition, releasing intense localised heat. Their high energy density, chemical stability, and tunable ignition characteristics make them well-suited for passive integration in systems that enhance demise.

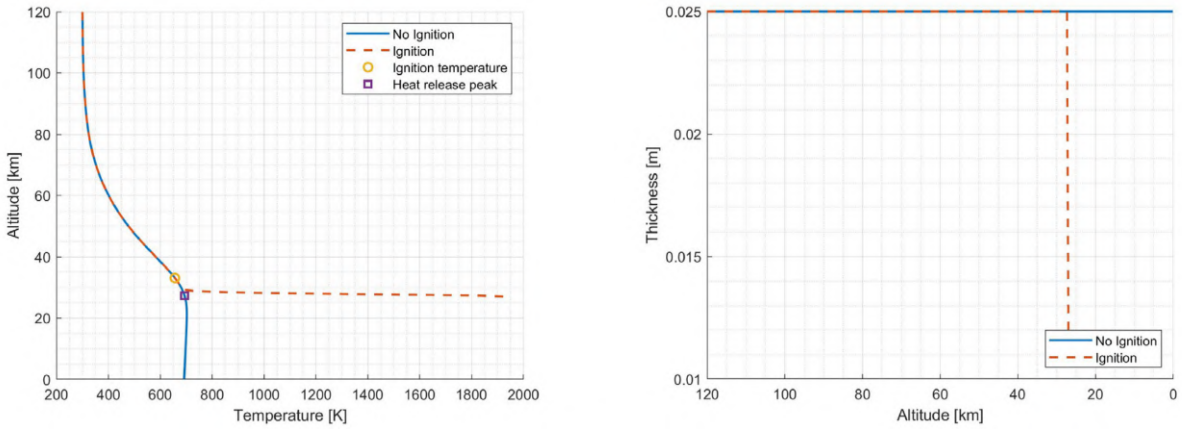

Figure 5.20: TRANSIT simulation results showing thermite-enhanced re-entry of a titanium 1000U CubeSat, with temperature (left) and wall thickness (right) plotted against altitude. Figure adapted from Finazzi et al. (2024).

Experimental studies at the *Politecnico di Milano* have shown that thermite confinement plays a key role in

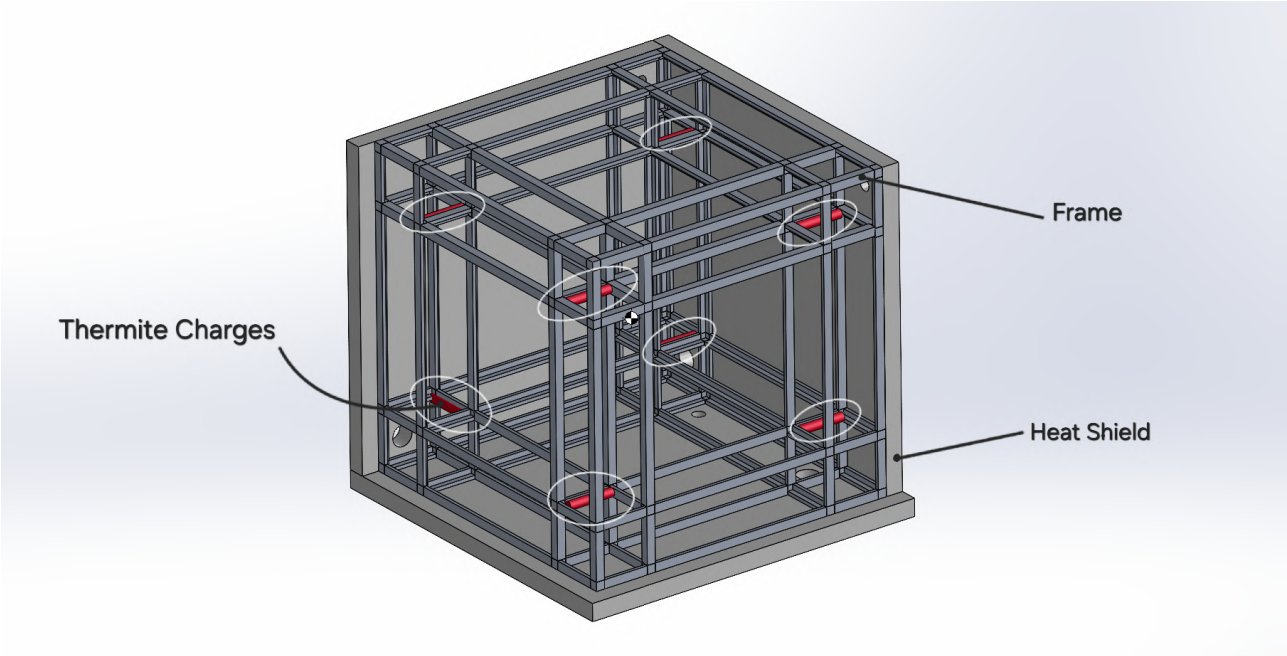

Figure 5.21: Labelled CAD model of CubeSat showing embedded thermite charge locations.

maximising heat transfer to surrounding materials, with measured efficiencies of up to 60% of the theoretical energy release [56]. These results support the potential of thermites to ablate high-melting-point components during re-entry. Simulations through the ad-hoc numerical tool TRANSIT [57] have further demonstrated the utility of thermites in enhancing the demise profile of metallic CubeSat structures. Figure 5.20 presents a reference case showing temperature and wall thickness evolution under thermite-assisted re-entry conditions for a titanium 1000U CubeSat.

In the design presented in this report, thermite charges were positioned at structural joints to induce fragmentation and break apart load paths as the structure weakens, promoting targeted failure and increasing the surface area-to-mass ratio of disintegrating components. The placement location of these charges is illustrated in Figure 5.21. Further thermite powder is embedded within the heat shield's inner surface to mitigate the risk of incomplete ablation (not shown as a separate entity in Figure 5.21). These are expected to activate during the later stages of descent (below 40 km), breaching any surviving ablative layer and exposing the internal structure to direct heating. This configuration is designed to maximise the probability of complete disintegration of the CubeSat within the upper atmosphere. With the proposed demise plan described in this section, the CubeSat is expected to completely disintegrate at an altitude of approximately 20 km, ensuring minimal probability of ground impact.

6 Electronics

Electronic hardware plays a vital role in the CubeSat, facilitating everything from thruster control to the acquisition and transmission of mission data. The onboard computer executes the mission's procedures and guides data flow between subsystems to enable reliable retrieval at a ground station. This section explores the communications architecture, addressing challenges such as the re-entry blackout and phased array beamforming method. It then examines the power systems and strategies, including the orbital shut-off period, power budgeting, and distribution design. Together, these elements form the electronic infrastructure that underpins the mission's success.

6.1 Interfacing and Communications - Hani Moussa

A critical aspect of the mission's success is the CubeSat's ability to reliably transfer data from the sensor arrays to clients on the ground. To achieve this, the sensors are carefully selected to ensure integration with the onboard computer (OBC), while a reliable communications array is featured in the CubeSat design. The redundancy built into this data transmission process is crucial. Without the successful acquisition and transfer of this data to the ground, the mission would fail to yield results, eliminating the purpose of its investment.

6.1.1 Data System Architecture

The CubeSat generates data through measurements taken by the sensor arrays, which include the thermocouple, pressure sensor, and recession sensor, as outlined in Section 7.1. This sensor data is relayed to the onboard computer (OBC), where it is processed, organised into data packets, and modulated for transmission through the communications array. A visual overview of the system's data flow is shown in Figure 6.1.

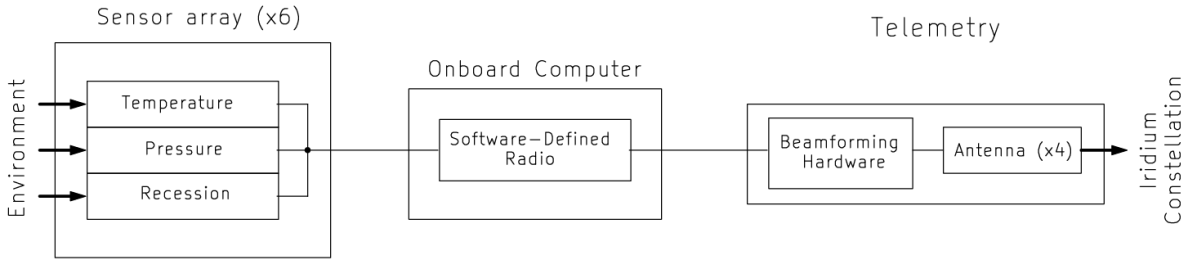

Figure 6.1: System architecture overview illustrating data flow

One of the onboard computer's main purposes within the context of this mission is to collect, collate and dispatch data. The selected OBC is the Ecuadorian Space Agency's ICEPS Spacecraft System Core, which offers a selection of desirable features, simplifying the CubeSat's design and ensuring a smooth flow of data.

Figure 6.2: ICEPS Spacecraft System Core

This OBC features an Inter-Integrated Circuit (I^2C) slave network, a serial communication protocol well-suited for compact embedded systems like in the CubeSat. I^2C operates on a simple two-wire interface: a Serial Data Line (SDA) and a Serial Clock Line (SCL). This allows multiple slave devices (in this case, the analogue-to-digital converters corresponding to each sensor) to communicate with a single master, the OBC. Each slave device is assigned a unique address, enabling the OBC to selectively query and receive data from individual components without the need for extensive wiring. This significantly reduces system complexity and volume (important considerations in a CubeSat) while ensuring synchronised data acquisition across the sensor arrays. This topology and the ease of its integration make I^2C an ideal choice for managing the CubeSat's internal communication efficiently. The network topology is illustrated in Figure 6.3, highlighting the connection between the OBC and slave devices.

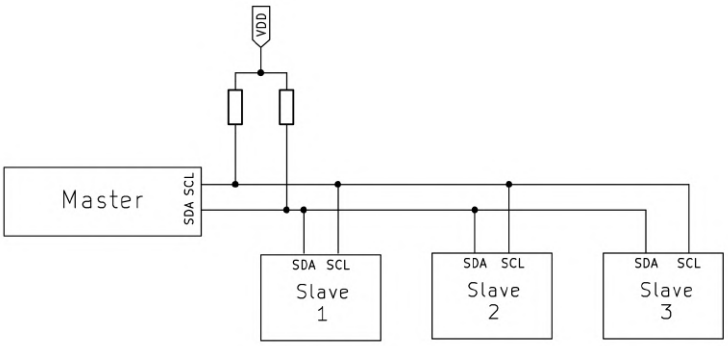

Figure 6.3: I2C network configuration, with pull-up resistors (in OBC) to set HIGH signal as default

Communication over I^2C begins when the OBC, acting as the master, sends the address of the component whose response is needed. If a device on the bus recognizes its address, it responds with an acknowledgement bit (ACK), allowing the OBC to verify that a device is present before proceeding. Once acknowledged, the OBC can initiate data transfer from the sensor, one byte (8 bits) at a time. After each byte, the OBC sends an ACK to confirm successful reception of the byte. The I^2C protocol allows for sequential bytes to be sent in a single interaction, meaning that a device can return multiple bytes of data with consecutive messages and ACKs. This process ends when the master (OBC) ends the interaction and sends a new address. This approach makes I^2C highly scalable, allowing the OBC to poll each sensor for its data as required.

Table 6.1: ICEPS OBC configuration options and corresponding prices[42]

Option	**Price (€)**
FULL EPS ONLY (I^2C INTERFACE) + 25W BATTERY	20,500
FULL EPS (USB/I^2C) + OBC/SDR RADIO/32GB SSD	36,000
FULL EPS (USB/I^2C) + OBC/SDR RADIO/256GB SSD + LASER COMMS	45,000
FULL EPS (USB/I^2C) + OBC/SDR RADIO/256GB SSD + LASER COMMS + D/R CONTROL	50,000
FULL EPS (USB/I^2C) + OBC/SDR RADIO/512GB SSD + LASER COMMS + D/R CONTROL + 25W BATTERY	55,000
FULL EPS (USB/I^2C) + OBC/SDR RADIO/512GB SSD + LASER COMMS + D/R CONTROL + 50W BATTERY	58,000
FULL EPS (USB/I^2C) + OBC/SDR RADIO/512GB SSD + LASER COMMS + D/R CONTROL + 100W BATTERY	66,000

Additionally, ICEPS can be provided with a Software-Defined Radio (SDR), which plays an important part in the CubeSat's communication system. The SDR is integrated within the OBC, enabling it to handle both the transmission and reception of data in a flexible, reconfigurable manner. Using software control, the SDR can be dynamically adjusted to work across different communication frequencies, modulation schemes, and protocols, making it adaptable for a variety of mission requirements. Once the OBC collects sensor data and processes it into packets, the SDR modulates the data for transmission over the L-Band.

ICEPS is designed for modularity, offering flexible configurations for a range of mission requirements, as outlined in Table 6.1.

The second configuration was selected as it consolidates the OBC, SDR, and EPS into a proven, integrated system with flight heritage. This reduces design complexity and integration risk compared to sourcing and validating separate modules, offering greater reliability and faster development. Additionally, the laser communications option is not chosen here since it does not provide the beamforming capabilities detailed in Section 6.1.3.

It is pertinent, when discussing a data collection and transmission process, to account data collection rates. This allows for acquisition and transmission design (including overheads), and accurate advertising to clients of the design's final deliverables. The total data rates can be deduced by reviewing the components listed in Sections 7.1 and 7.7.1, and has been surmised below in Table 6.2.

Table 6.2: Data rates from various sources in the CubeSat

Sensor System	**Data rate (bps each)**	**Number of Sensors**	**Total Data Rate (bps)**
Temperature	2880	6	17 280
Pressure	13760	6	82 560
Recession	13760	6	82 560
Spectrometer	98304	1	98 304
Total			280 884

The communication system uses the Iridium Certus 350 service, chosen over the higher-rate Certus 700 to maintain a strong signal to noise ratio (SNR) and therefore link margin. While Certus 700 offers more bandwidth, its higher data rate reduces the link margin to around 4dB, which is too low for reliable communication, making Certus 350 the preferred choice.

The ablation sensor data rates comfortably fit within Certus 350's maximum capacity of 352 kilobits per second. The spectrometer originally samples at 217 sps (samples per second), generating around 7.1 MBps, far exceeding available bandwidth.

To balance data quality and communication reliability, the spectrometer sampling rate is limited to 3 samples per second. This produces a data rate of approximately 98 kbps, bringing the total data rate to about 281 kbps. This leaves about 71 kbps, or 20% overhead, to cover communication protocol framing, error correction, retransmission if needed, and periodic reception of signals from Iridium to assist with beamforming (see Section 6.1.4).

This data system architecture represents a trade-off among complexity, cost, and performance, forming a reliable platform for data acquisition and communication within the CubeSat's operational constraints.

6.1.2 Re-entry Communications Blackout

A vital component of the data return process is the communications system. The chosen strategy involves crosslinking mission data to the Iridium satellite constellation, which then relays the data to a ground-based station. This approach has been effective in previous missions, such as the QARMAN CubeSat developed by the Von Karman Institute, for the European Space Agency [58].

The Iridium constellation consists of 66 active satellites at an altitude of 780 km, significantly lower than alternatives such as Globalstar (1,414 km) or Inmarsat (∼36,000km). This reduces free space path loss (FSPL), resulting in more reliable communication. While Kepler operates at similar altitudes, Iridium provides global coverage and uses the L-band, which is less susceptible to atmospheric attenuation than the Ku-band used by Kepler [59]. Additionally, L-band transmission requires less power, making it more suitable for a small CubeSat with limited energy resources. By transmitting signals upward and away from the CubeSat's trajectory, the satellite system can help overcome communication blackout caused by the plasma sheath formed during atmospheric reentry.

In this period, the CubeSat travels at hypersonic speeds, heating surrounding air to very high temperatures. This ionises the gases around the satellite, forming a plasma sheath: a layer of charged particles. This sheath can interfere with or completely block radio frequency signals, a circumstance known as a communication blackout. Given the mission centres around the collection of data during reentry, and that the CubeSat will not survive the process, communication despite the blackout becomes necessary.

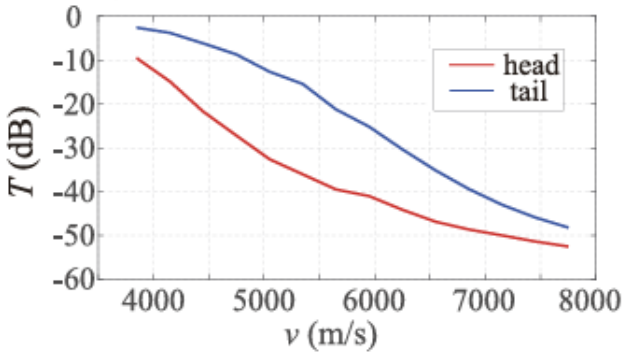

Figure 6.4: Transmission Coefficient through plasma sheath with velocity [60]

According to the study by Mao et al. (2023) [60], transmission through the plasma sheath becomes increasingly difficult at higher spacecraft velocities or communication frequencies, as signal absorption and reflection intensify under these conditions. Accordingly,transmission is directed through the CubeSat's wake, where attenuation due to the plasma sheath is lower, but not zero.

Evaluation of signal attenuation through the wake begins with the calculation of the attenuation coefficient α, which appears in the expression for electromagnetic wave propagation through plasma:

$$\mathbf{E}(x) = \mathbf{E}_0 e^{-\alpha x} \tag{6.1}$$

where $\mathbf{E}(x)$ is the electric field vector at distance x into the plasma and $\mathbf{E}_0$ is the initial field amplitude.

This coefficient is determined by the plasma's complex permittivity ($\epsilon_r + j\epsilon_i$), which itself depends on the plasma frequency ω_p and the collision frequency ν of charged particles [61]. The following calculation proceeds by first establishing the plasma frequency, followed by the real and imaginary components of permittivity, and finally the attenuation coefficient.

The electron density in the wake of a re-entering spacecraft in the ionosphere has been observed to reach an upper limit of $10^4\,\mathrm{e^-cm^{-3}}$, as reported in the measurements taken by the TAIYO probe [62]. For the purposes of this analysis, this value is converted to SI units, yielding $n_e = 10^{10}\,\mathrm{e^-m^{-3}}$. The collision frequency within this wake region is relatively well-defined. In the case of hypersonic flight at an altitude of approximately 50 km, a collision frequency of 0.1 GHz is adopted as an upper bound in the attenuation model [63].

The plasma frequency is the natural oscillation frequency of electrons in a plasma when displaced from their equilibrium positions, and is a relevant quantity to consider when assessing a signal's attenuation. When wave frequency is smaller than plasma frequency, the signal is significantly attenuated, and a larger disparity typically results in the signal being unable to propagate. Around this state, as the values become comparable, attenuation occurs to some degree. The plasma frequency is dependant on the electron density of the plasma:

$$\omega_p = \sqrt{\frac{n_e q_e^2}{\epsilon_0 m_e}} = \sqrt{\frac{(10^{10}) \cdot (-1.6 \times 10^{-19})^2}{(8.85 \times 10^{-12}) \cdot (9.11 \times 10^{-31})}} \approx 5.63 \times 10^6 \,\text{rad/s}. \tag{6.2}$$

where

- n_e is the electron density ($\text{e}^{-}\text{m}^{-3}$)
- q_e is the charge of an electron ($\approx -1.6 \times 10^{-19}$ Coulombs)
- ϵ_0 is the permittivity of free space ($\approx 8.85 \times 10^{-12}\text{Fm}^{-1}$)
- m_e is the mass of an electron ($\approx 9.11 \times 10^{-31}\text{kg}$)

The real and imaginary parts of the effective permittivity (ϵ) are calculated using

$$\epsilon_r = 1 - \frac{\omega_p^2}{\omega^2 + \nu^2} \approx 1 - (1.20 \times 10^{-5}) \tag{6.3}$$

$$\epsilon_i = \frac{\omega_p^2 \nu}{\omega(\omega^2 + \nu^2)} \approx 7.36 \times 10^{-7} \tag{6.4}$$

where

- ω is the wave frequency (rad/s)
- ν is the collision frequency (= 0.1 GHz)

Finally, the attenuation coefficient (α) can be derived from these values of permittivity.

$$\alpha = k_0 \sqrt{\frac{\sqrt{\epsilon_r^2 + \epsilon_i^2} - \epsilon_r}{2}} \approx 5.70 \tag{6.5}$$

where $k_0 = \frac{\omega}{c} \approx 5.42$ is the free space number (m^{-1})

The attenuation coefficient is the pertinent variable to consider when aiming to calculate attenuation through the wake, but the calculated value does not directly represent the attenuation factor. When seen in the context of Equation 6.1, the attenuation is the negative exponential of the coefficient.

$$L_p = -20 \log_{10}(e^{-\alpha x}) \tag{6.6}$$

$$\frac{L_p}{x} = 20\alpha \log_{10}(e) = 1.73 \times 10^{-5} \,\text{dB/m} \tag{6.7}$$

where

- L_p is the attenuation due to the plasma (dB)

- x is the distance through the plasma the signal travels (m)

This suggests that, theoretically, up to 405 km of signal propagation through the wake is possible when considering the link margin, as detailed in Section 6.1.5. In practice, however, the plasma wake is significantly shorter and is generally understood to extend less than 100m for a small spacecraft, even under extreme hypersonic conditions [64]. Consequently, the expected attenuation is negligible, on the order of 10^{-3} dB or less. This is consistent with successful data transmissions from previous missions, such as QARMAN, to the Iridium satellite constellation [58]. Signal attenuation through the wake is therefore not a limiting factor for reliable communication beyond the plasma sheath.

6.1.3 Beamforming Strategy

Reliable communication in space requires overcoming radio signal attenuation, primarily due to free-space path loss. Conventional high-gain antennae are impractical due to their large size and narrow beamwidth, which cannot accommodate the tumbling motion of the CubeSat. Omnidirectional antennas, while tolerant of attitude changes, lack sufficient gain. Beamforming offers a compromise by synthesising a directional antenna pattern from an array of smaller elements. This technique achieves high gain without mechanical steering and adapts dynamically to the satellite's changing orientation.

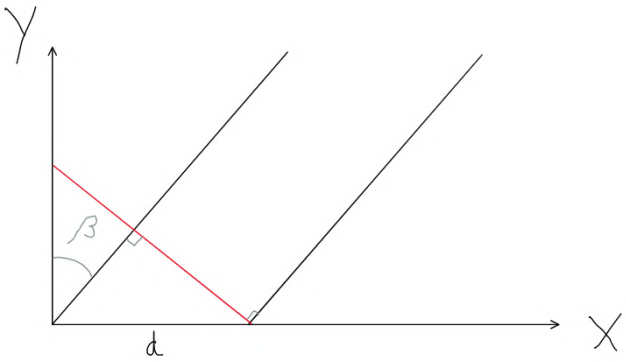

Figure 6.5: Diagram illustrating change in distance travelled between signals from different beamforming elements

Consider the case of a linear array of antennae. In the above diagram, the electromagnetic wave formed from the element on the left (of distance d from the right element) travels another $d\sin(\beta)$. Therefore, in an array of M elements, signals arriving from a direction β cause different time delays based on the angle of arrival. These delays are determined by:

$$\tau = \frac{d\sin(\beta)}{c} \tag{6.8}$$

where d is the spacing between elements, and c is the speed of light.

To compensate for these delays (and allow parallel signals to be congruent), a steering vector $\mathbf{a}(\beta)$ is applied.

$$\mathbf{a}(\beta) = \begin{bmatrix} 1 & e^{-j\frac{2\pi d \sin(\beta)}{\lambda}} & \dots & e^{-j\frac{2\pi(M-1)d \sin(\beta)}{\lambda}} \end{bmatrix}^T, \tag{6.9}$$

where λ is the signal wavelength. Each term represents the phase offset needed at a given element to align the signals in the desired direction. This steering vector is used to generate weights with which to multiply the input signal, allowing every antenna to transmit its corresponding signal.

The following section outlines the hardware implementation of this beamforming approach within the CubeSat.

6.1.4 Phased Array Signal Chain

The phased array signal chain generates and conditions a transmission signal for directional emission from an antenna array. A single RF signal is split into four equal paths, each undergoing individual phase shifts and amplification to create a coherent beam in a specified direction. This section outlines the signal conditioning architecture and its implementation.

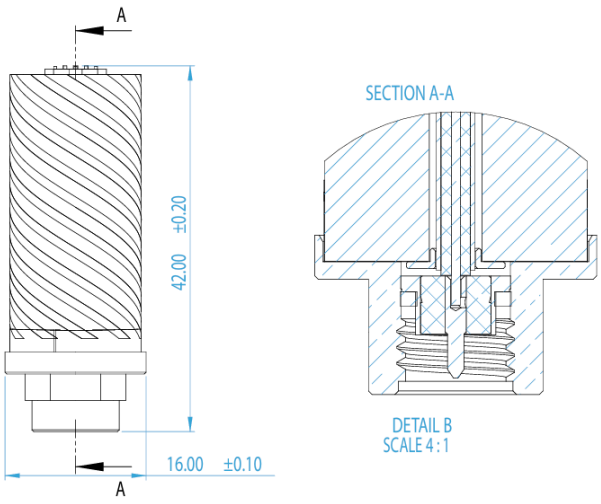

Figure 6.6: HXDC16010-SA02 Iridium Certus 9704 antenna dimensions [49]

The antenna used is the HXDC16010-SA02 seen in Figure 6.6, designed for the Iridium satellite network and operating within the 1616–1626 MHz band. With a peak gain of 2 dBic and compact dimensions (42 mm × 16 mm) [49], it is suitable for dense array configurations within the limited volume of a CubeSat. The antenna maintains performance in close proximity to other antenna elements and supports reliable operation in harsh environments. The CubeSat employs the Iridium Certus 350 1 GB plan [65], exceeding the mission's estimated data requirement of approximately 600 MB over 1 hour (see Section 6.1.1).

MATLAB's Phased Array System Toolbox was used to simulate and visualise the radiation pattern of a uniform rectangular antenna array. A custom antenna element was defined using a cardioid-like magnitude pattern to model the chosen antenna. The element spacing was set to half the wavelength (92.2mm) to minimise grating lobes but still maintain constructive interference. The toolbox was used to visualise the array geometry and

compute beamforming weights using a steering vector corresponding to azimuth and elevation angles from user input. The resulting directional gain pattern is shown in Figure 6.7

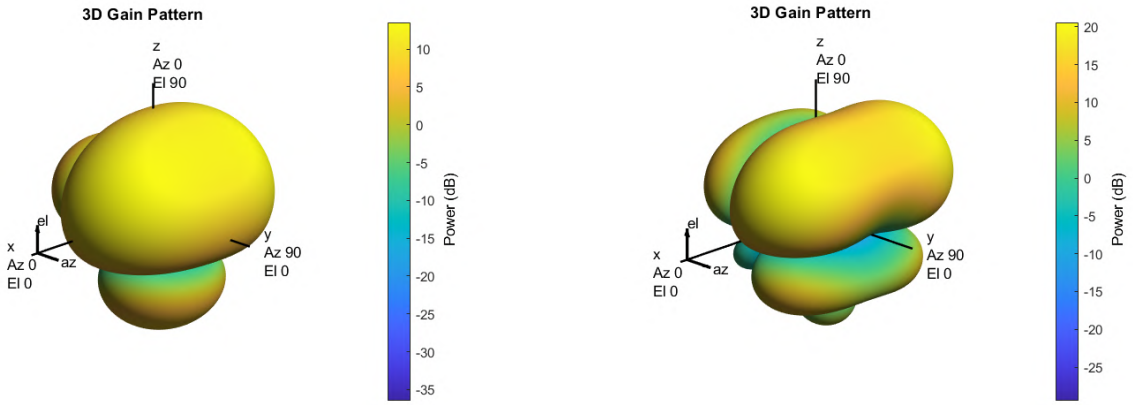

((a)) 2x2 arrangement ((b)) 3x3 arrangement

Figure 6.7: Radiation patterns at azimuth and elevation angles of 30 degrees for (a) 2x2 and (b) 3x3 arrangements

Subfigure 6.7(a) corresponds to a 2x2 array, which achieves a peak gain of 13.52 dB, while subfigure 6.7(b) is for a 3x3 array, providing a peak gain of 20.56 dB. The 3x3 configuration requires a larger physical area but offers the advantage of a higher peak gain.

The 2x2 arrangement was selected as the ideal compromise between design complexity and antenna gain. Even with the severely decreased peak gain, the link margin is sufficiently high (as seen in Section 6.1.5). This option simplifies component needs, reduces complexity (thereby increasing reliability) and, crucially, fits more effectively in the CubeSat's limited volume.

The onboard computer includes an Epik Z2 module, combining a Linux-based system and RF transceiver. Only one Tx/Rx SMA interface is available, preventing direct connection to each antenna. Dedicated beamforming ICs (e.g. ADAR1000) are unsuitable due to their design for Ka-band signals. Consequently, a splitter and four identical custom PCBs are used to accommodate the system's 2x2 antenna design.

The Epik Z2's output is initially divided by a Mini-Circuits ZX10-4A-19+ splitter, which provides four output paths with uniform amplitude and phase, and supports operation in the 1425–1900 MHz range.

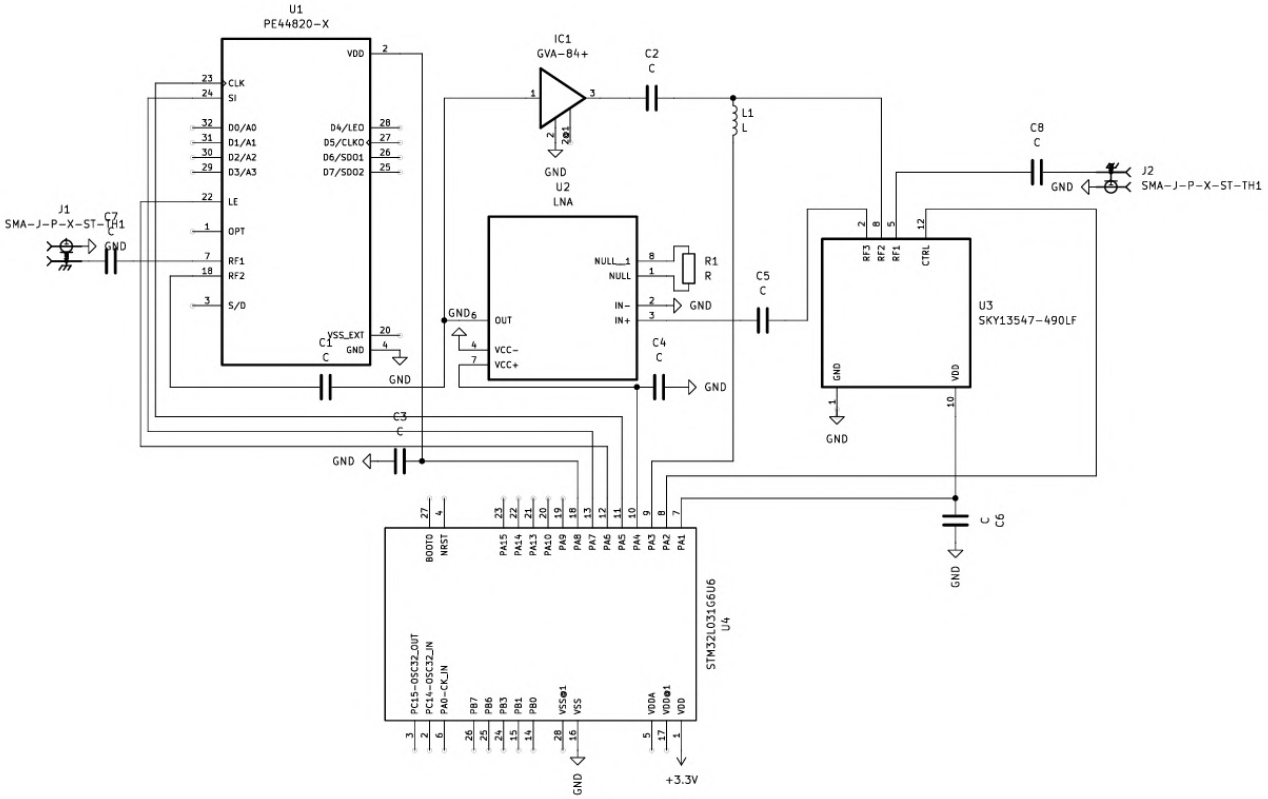

Figure 6.8: Phase-shift control PCB design

Each output is routed to a custom phase-shift control PCB (Figure 6.8). The signal enters the PCB via a PCB-mounted male SMA port connected to a standard 50Ω trace to allow for efficient power transfer. A PSemi PE44820 digital phase shifter applies a defined delay to each signal. Though rated for frequencies above what is desired, the component supports narrowband operation from 1.1–3.0 GHz, allowing effective control at 1.625 GHz.

Amplitude control is not implemented in this design, but future versions may include digital attenuators (e.g. Analog Devices HMC1119) for side-lobe suppression or adaptive beamforming (altering signals to suit the environment). The current configuration provides sufficient directivity with reduced complexity.

Insertion loss from the splitter and phase shifter is compensated by a Mini-Circuits GVA-84+ amplifier, which provides up to 20 dB of gain. Placing the amplifier after phase-shifting avoids distortion that could occur otherwise. This configuration also reduces overall power consumption compared to alternatives such as omnidirectional antennas, which require higher transmission power to achieve comparable effective isotropic radiated power (EIRP), or more software-defined radios (SDRs), which typically consume approximately 2W per channel (see Section 6.2.2) and add complexity.

A Skyworks SKY13547-490LF RF switch allows half-duplex operation by routing transmission or reception paths. The transmit signal passes through the power amplifier to the antenna. In receive mode, the switch diverts the incoming signal to an ADL8122 low-noise amplifier, offering a 2 dB noise figure suitable for weak signal acquisition. Both amplifiers share the bidirectional splitter and phase shifter route.

An STM32L031C6T6 microcontroller uses SPI and DAC to control the phase shifter and switch according to instructions received via the OBC's I^2C interface.

Beamforming provides the CubeSat a higher gain, but assumes knowledge of the direction of the plasma sheath's wake. The CubeSat uses its communications array once per second to read an incoming signal from the nearest iridium satellite, suitable for the radiation pattern and low tumbling frequency. It does this by reading signals sent to it from the nearest Iridium constellation, checking the most likely position first based on the OBC's internal model of its orientation and changing the receiving direction until received power is maximised. At this point, an acknowledgement transmission is sent and data is communicated.

Once the direction of transmission is known, the communications array is once again used to transmit data. Until the next occurrence of the direction-measuring process, the onboard computer's in-built IMU is used to make slight adjustments to the array's directionality, recalculating the phase shifts for each antenna at every time-step (after every transmission frame). This allows for a reliable system due to the relatively low tumbling frequency and cardioid-based radiation pattern from the antennae, granting the CubeSat flexibility in the direction of transmission.

6.1.5 Link Budget

Link budget analysis is an important element of communications systems design, allowing engineers to decide both the efficacy and performance of a particular set-up. It involves the consideration of several different factors affecting the gain or attenuation of a signal from transmission to reception. An equation of the following format is typically used for this analysis [66].

$$P_{rx} = P_{tx} + G_{tx} - L_{tx} - L_{fs} - L_{prop} + G_{rx} - L_{rx} \tag{6.10}$$

where

- P_{rx} is the received power (dBm)
- P_{tx} is the transmitter power amplifier output power (dBm)
- G_{tx} is the transmitter antenna gain (dBi)
- L_{tx} is the transmitter losses (dB)
- L_{fs} is the free space path loss (dB)
- L_{prop} is other propagation losses (dB)
- G_{rx} is the receiver antenna gain (dBi)
- L_{rx} is the receiver losses (dB)

This takes into account multiple aspects of the data link, from the more anticipated components like the

free space path loss L_{fs}, to more inconspicuous elements like the losses due to components in the receiver L_{rx}. Another significant detail in this context is the transmitter gain, G_{tx}, being measured in units of dBi, or decibels relative to an isotropic (3-dimension omnidirectional) antenna. This means the high directionality produced by the beamforming technique (described in Section 6.1.3) is considered in the calculation.

Of additional interest is the Link Margin, a variable directly measuring the feasibility of a data link. It in effect, conveys how much stronger the received signal is than it must be to be secured by the receiver and is given by the following relatively simple equation:

$$LM = P_{rx} - RS \tag{6.11}$$

where

- LM is the link margin (dB)
- P_{rx}, as defined above, is the received power (dBm)
- RS is the receiver sensitivity (dBm)

MATLAB's Link Budget Analyser application, part of the Satellite Communications toolbox, was used to appraise both data links: both directions between the CubeSat and Iridium satellites.

CubeSat to Iridium The required energy per bit to noise power density ($\frac{E_b}{N_0}$) represents how much energy is needed for each bit of data to overcome the noise present in the system. With a lower ratio, less energy is required to successfully transmit one bit. This value is derived from the bit error rate (BER) - for which a typical value chosen for a similar application is 10^{-5} [67]. This leads to $\frac{E_b}{N_0} = 9.1\text{dB}$.

The ratio $\frac{G}{T}$, defined below by Equation 6.12, describes the performance of the Iridium satellite receiver

$$\frac{G}{T} = G_r - 10\log_{10}(T_{\text{sys}}). \tag{6.12}$$

Assuming a system noise temperature $T_{\text{sys}} = 350\text{K}$ and receiver gain $G_r = 24.9dB$ [67], results in $\frac{G}{T} = -0.54\text{dB/K}$.

Table 6.3: Link Analysis results of CubeSat Tx to Iridium Rx crosslink as seen in MATLAB, altitude of CubeSat = 50km

Tag	Name	L3
N1	Distance (km)	2.0620e+03
N2	Elevation (deg)	12.3353
N3	Tx EIRP (dBW)	10
N4	Polarization loss (dB)	3.0103
N5	FSPL (dB)	162.9506
N6	Rain attenuation (dB)	0
N7	Total atmospheric losses (dB)	0.4670
N8	Total propagation losses (dB)	163.4176
N9	Received isotropic power (dBW)	-156.4279
N10	C/No (dB-Hz)	71.6312
N11	C/N (dB)	-3.8094
N12	Received Eb/No (dB)	16.1658
N13	Margin (dB)	7.0658

These values were applied, and an example communications link was assembled in the Link Budget Analyser tool. As seen in Table 6.3, this results in a link margin of about 7.07dB, a comfortable margin allowing for adverse conditions.

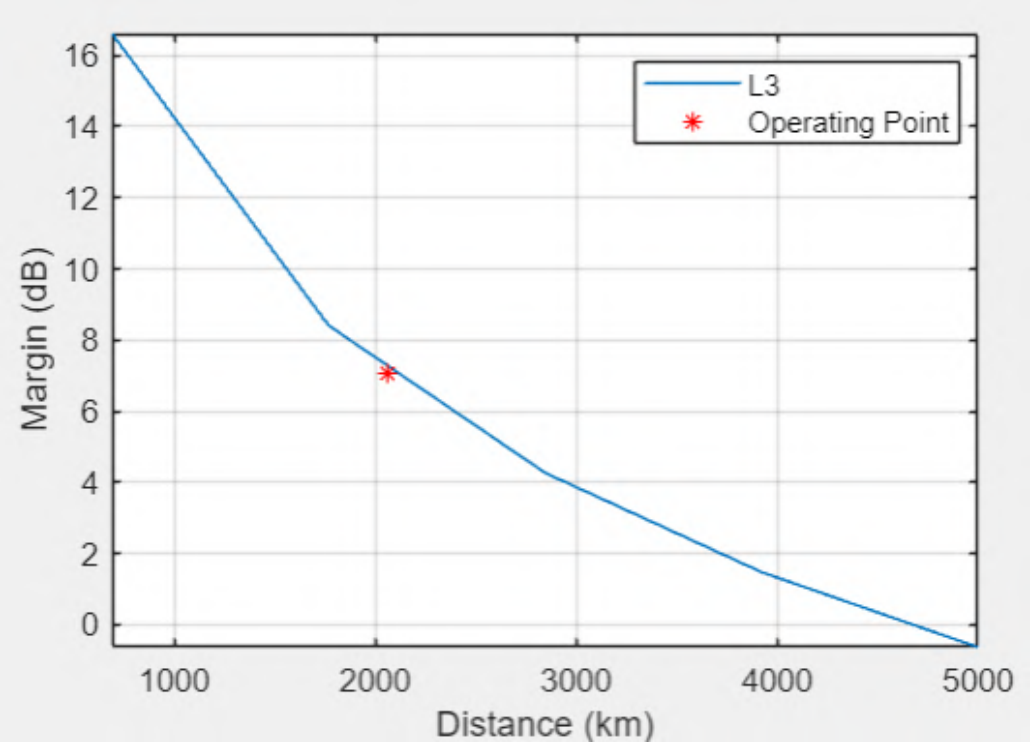

Figure 6.9: Effect of changing distance between the CubeSat and Iridium satellite on link margin

Two thousand kilometres is a typical value for such a crosslink with Iridium [67], but Figure 6.9 shows a positive margin (and therefore a successful transmission) to Iridium until around 4600 km. Practically, the horizontal distance between the ground station and the nearest Iridium satellite, considering only longitude and latitude, does not exceed 2000 km [68]. Accounting for the difference in altitude, the true distance does not surpass 2200

km, confirming a positive link margin regardless of location.

Iridium to CubeSat The communications protocol and modulation are identical bidirectionally, and therefore the required bit to noise power density is unchanged when considering the Iridium satellite's transmission back to the CubeSat. The $\frac{G}{T}$, however, is specific to the receiver design. Equation 6.12 is used to measure the performance of the CubeSat receiver system. Due to the principle of reciprocity [69], the transmission radiation pattern of the beafmorming array is the same as the receiver sensitivity. The noise temperature, however, is as of yet undefined for the CubeSat. System noise can be considered as a summation of the noise from multiple elements, described by the Friis formula for cascaded noise [70]:

$$T_{\text{sys}} = T_{\text{ant}} + T_{\text{LNA}} + \frac{T_{\text{phase}}}{G_{\text{LNA}}} + \frac{T_{\text{comb}}}{G_{\text{LNA}} \cdot G_{\text{phase}}} \tag{6.13}$$

where

- T_{LNA} is the Low Noise Amplifier Noise Temperature (K)
- G_{LNA} is the Low Noise Amplifier Gain (linear scale, not dB)
- T_{phase} is the Phase Shifter Noise Temperature (K)
- G_{phase} is the Phase Shifter Gain (linear scale, not dB)
- T_{comb} is the combiner Noise Temperature (K)

The gains are simply referenced from the relevant datasheets: $G_{\text{LNA}} = 39.8$ and $G_{phase} = 0.251$. The noise temperatures, however, are calculated from the noise figure of the devices using the following standard relation [71]:

$$NF = 10 \log_{10}(\frac{T_{\text{noise}}}{290} + 1) \tag{6.14}$$

Once the result is again converted into decibels, the results are $T_{\text{LNA}} = 138\text{K}$, $T_{\text{phase}} = 871\text{K}$ and $T_{\text{comb}} = 1070\text{K}$. The antenna temperature noise is not as simple, varying on the contextual information of the CubeSat's telemetry.

MATLAB was used to estimate the antenna noise temperature based on the radiation pattern seen in Figure 6.7(a) and the integral of the noise temperature over the range of the array weighted by the radiation pattern [72]:

$$T_{ant} = \frac{1}{4\pi} \int_0^{2\pi} \int_0^{\pi} G(\theta, \phi)\, T(\theta, \phi) \sin\theta \, d\theta \, d\phi = 53.78\text{K} \tag{6.15}$$

Using Equation 6.13, the system temperature noise is given by $T_{\text{sys}} = 220\text{K}$ and therefore the CubeSat's total

$\frac{G}{T} = -9.90$. Though much lower than the performance of the high-budget Iridium satellite (designed to receive signals through the atmosphere), the power and gain is far higher than in the CubeSat's transmission.

Table 6.4: Link Analysis results of Iridium Tx to CubeSat Rx crosslink as seen in MATLAB, altitude of CubeSat = 50km

Tag	Name	L3
N1	Distance (km)	1.8288e+03
N2	Elevation (deg)	-30.4348
N3	Tx EIRP (dBW)	30.8700
N4	Polarization loss (dB)	3.0103
N5	FSPL (dB)	161.9084
N6	Rain attenuation (dB)	-
N7	Total atmospheric losses (dB)	-
N8	Total propagation losses (dB)	161.9084
N9	Received isotropic power (dBW)	-134.0487
N10	C/No (dB-Hz)	84.6505
N11	C/N (dB)	9.2098
N12	Received Eb/No (dB)	29.1851
N13	Margin (dB)	20.0851

The back-transmission link margin from the Iridium satellite to the CubeSat was found to be approximately 20.1 dB, as shown in Figure 6.4. This is far higher than even the CubeSat transmission's link budget, assuring that the process of finding the Iridium satellite's direction (as described near the end of Section 6.1.4) is possible even with fluctuations in permittivity or unintended attenuation in components.

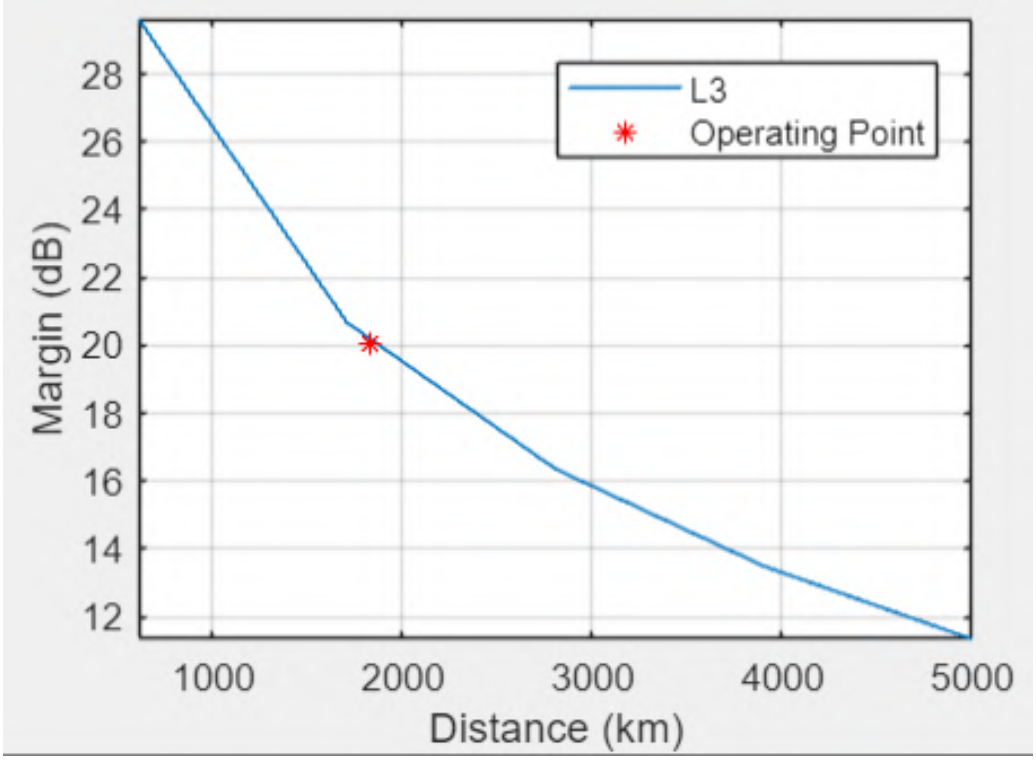

Figure 6.10: Effect of changing distance between the Iridium satellite and CubeSat on link margin

The plot in Figure 6.10 shows a similar outcome to that of Figure 6.9. The communications link, in both directions, provides a strong and reliable method of obtaining data from the CubeSat as it demises.

6.2 Electrical Systems and Power - Hani Moussa

Power is a critical constraint in CubeSat missions, requiring efficient generation, storage, and distribution. This CubeSat uses the ICEPS (Irvine-Class Electrical Power System), which integrates power management and an SDR into a compact onboard computer. The CubeSat does not require power generation, instead rationing its stored power for the duration for which it is needed. This section outlines the use of each power rail on the OBC, the overall power budget, and battery selection, as well as the CubeSat's orbital power-down strategy for energy conservation.

6.2.1 Orbital Shut-off Period

One of the primary challenges in designing the power system for this CubeSat is managing energy consumption during the long-duration orbital phase, which is expected to last approximately 19 days. During this period, the spacecraft is inactive until the start of atmospheric re-entry. Even if the onboard computer (OBC) alone were to remain powered throughout this duration, the energy demands would be extreme. It draws an average 4 watts of power, which would lead to an energy requirement exceeding 2,000 watt-hours over the shut-off period. Therefore, an alternative mechanism is required to reliably reactivate the satellite in time for reentry while ensuring it is not drained of its energy before the mission is complete.

A considered approach involved using a GPS module to determine the altitude of the spacecraft. Various space-specific GPS receivers were considered. Although many of these modules would provide the required information, GPS modules demand significant power and volume. For example, the Hexagon OEM719 consumes 1.8W (translating to hundreds of watt-hours over the course of the mission) and is sized at 46 x 71 x 11 mm. Altitude, therefore, is measured through sensor fusion of a (small) magnetometer and the onboard computer's integrated IMU, as discussed in Section 7.5.

These components, however, still have a high power draw, especially when considering the IMU's integration into the OBC. A more viable solution emerges through the use of a low-power Real-Time Clock (RTC) module that remains active throughout the orbital period.

The Seiko Epson RA8000CE was chosen for its high temperature range, low power draw, and alarm feature. The latter quality allows the user to provide a specified date and time at which a high digital signal is outputted from the device. It operates with a typical power consumption of 1.8μW, resulting in a negligible energy requirement during the orbital shut-off period. This is a highly efficient solution for ensuring the CubeSat can reactivate prior to re-entry. The minimal energy requirement also grants room for redundancy.

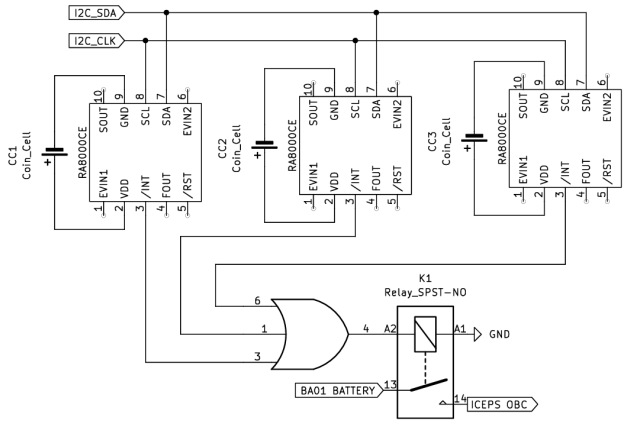

Figure 6.11: Simplified representation of OBC reactivation mechanism

Three RTC components are placed into an OR gate (as seen in Figure 6.11)reaarrangement within the CubeSat, lessening the capacity for a single-point failure in reactivation. Additionally, each is powered with a separate Sony CR2032 coin cell battery (theoretically capable of powering them for several years), simplifying and diversifying their power provisions.

Due to the OR gate, once one of the RTCs' alarms outputs a high signal, the onboard computer is activated, assesses the current altitude, and acts according to Table 6.5.

Table 6.5: OBC protocol upon wake-up depending on altitude

Altitude	**OBC Actions**
$>$ 150km	Compare position and velocity/acceleration to internal model, reschedule system to reactivate at 150km, and shut off again
150-120km	Verify connection to Iridium network, and start collecting and transmitting sensor data
$< 120km$	Error has occurred. Verify connection with Iridium network, communicate error state, and start collecting and transmitting sensor data

Additionally, the OBC undertakes a procedure to reassess the reliability of each RTC. Upon boot-up, the RTCs are queried over the I^2C network for their current time and alarm status. According to the component's datasheet, the time variation is expected to be within 130 seconds per month. If any one RTC deviates beyond this threshold (allowing for a margin due to the shorter mission length) relative to the median, it is logged as likely faulty in the OBC's solid-state drive (SSD), and its alarm function is disabled. If the two remaining RTCs disagree beyond the allowed margin, the true time is requested through Iridium and the further RTC is also marked as faulty.

6.2.2 Operation Power Budget

Following reactivation, the CubeSat's systems are powered and operational. The components are activated, and the process of data acquisition and transmission begins. The power budget for this operational phase of the mission is described below in Table **??**.

Table 6.6: Power budget during operation (re-entry) phase of CubeSat

Subsystem	**Average Power (W)**	**Peak Power (W)**	**Duty Cycle (%)**	**Avg. Power Usage (W)**
ICEPS-integrated Epik Sidekiq Z2	2	2	100%	2
6 x Analog Devices TMP36	0.00099	0.00099	100%	0.00099
6 x Microchip MCP3421 ADC	0.00307	0.00376	100%	0.00307
6 x TE connectivity EPB-25PS-C20004 Pressure Sensor	0.498	0.498	100%	0.498
6 x Texas Instruments TLV9062 Amplifier	0.0107	0.0107	100%	0.0107
12 x Texas Instruments ADS1115 ADC	0.0108	0.0108	100%	0.0108
6 x Recession Sensor Custom Mesh	0.0675	0.0675	100%	0.0675
6 x Recession Sensor Custom Foil	0.0432	0.0432	100%	0.0432
12 x ON Semiconductor CAT4101 Constant-Current LED Driver	0.0048	0.0048	100%	0.0048
AAC Clyde Space MM200 Magentometer	0.033	0.033	100%	0.033
3 x Granstal GS-RW10 Reaction Wheel	11.7	11.7	50%	5.85
Avantes AvaSpec-Mini2048CL Spectrometer	2.5	2.5	100%	2.5
4 x PSemi PE44820 Digital Phase Shifter	0.00172	0.00264	100%	0.00172
4 x Mini Circuits GVA-84+ Amplifier	2.16	2.704	80%	1.728
4 x Analog Devices ADL8122 Low Noise Amplifier	1.9	1.9	20%	0.38
4 x ST Electronics STM32L031C6T6 Microcontroller	0.03209	0.03209	100%	0.03209
Total		**9.81**		**13.16**

The recession sensor mesh and foil seen in Table 6.6 have matching average and peak power, despite having variable resistance. The intention of the primary objective is to record the ablation, and so the resistance for

a large period of time is unpredictable without the data output of the mission. As such, a worst-case scenario is assumed where the sensor ablates to near-maximum: enough to increase power use, but not enough to cause shut-off of the sensor

The reaction wheels source power from 3.3V rails (see Section 6.2.3). Therefore, a boost converter is employed to attain a suitable 12V input for these components. Table 6.6 assumes a 90% efficiency for the converter and works on the basis of 0.5 hrs of reaction wheel usage during re-entry (in the 150-130km altitude range specified in Section 4.1).

The majority of power consumption during the operational phase following reactivation is seen in three key areas. First, the ICEPS onboard computer's integrated Sidekiq Z2 consumes up to 2W of power. This is a vital demand: it organises the CubeSat's running through the I^2C network and includes the software-defined radio that acts as the satellite's modem. The second is the spectrometer requiring 2.5W. It provides the necessary data for the secondary objective, but represents a large portion of the power budget. While the current design comfortably accommodates this consumption, future projects could explore lower-power alternatives. The third large sink of power is the communications array - namely, the amplifiers (2.18W). This is typically a high power draw in satellite designs, allowing successful transmission and a strongly positive link margin (see Section 6.1.5).

The post-reactivation section of the mission is planned to last a maximum of 1 hour from an altitude of 150km. The total energy requirement for this phase is calculated as the sum of the energy consumed during the operational period and the initial deorbit burn stage.

$$E_{\text{total}} = P_{\text{avg}} t_{\text{operation}} + (P_{\text{thrust}} + P_{\text{wheels}}) t_{\text{deorbit}} \tag{6.16}$$

Where:

- E_{total} is the total minimum energy capacity required (Wh)
- P_{avg} is the average power consumption during operation (W)
- $t_{\text{operation}}$ is the duration of this phase (hrs)
- P_{thrust} is the summed average power consumption of the cold gas thrusters (W)
- P_{wheels} is the summed average power consumption of the reaction wheels (W)
- t_{deorbit} is the duration of initial deorbit (hrs)

With given values, the minimum energy provision for the OBC-connected system is given as

$$E_{\text{total}} = (13.16 \cdot 1) + ((33 + 10.5) \cdot 0.111) = \mathbf{17.993}\text{Wh} \tag{6.17}$$

A typical margin for CubeSat power budgets is 20% [73]. This allows for degradation in power storage over

the mission length, as well as fluctuations in power from components. The Pegasus Class BA01/S battery was selected for its flight heritage and compatibility with the ICEPS OBC, for which the battery was designed by the Ecuadorian Space Agency. It offers a 22Whr energy storage (providing a 22.2% margin) and can come with an integrated carbon nanotube option for thermal management. Additionally, it is only 7mm thick, suitable for the limited volume in the CubeSat.

6.2.3 Power Distribution and System Design

The ICEPS OBC is a compact platform offering a well-developed electrical power system (EPS), multiple accesses to power for connected components and (given with some purchase options) a designed-to-be-compatible battery. The provided power rails include [46]:

- one 5V rail up to 3A
- one 12V rail up to 3A
- two 3.3V rails up to 3.6A each
- one unregulated 4.2 - 3.6V rail up to 12A

The CubeSat's components (excepting the separated reactivation instrumentation) are generally powered through these rails. The 3.3V rails are not at current capacity with the listed components, so are used simultaneously for increased in-built redundancy.

Table 6.7: Direct power rail assignments and current draw per component

Component	**Voltage (V)**	**Rail(s)**	**Current (A)**	**Qty**	**Total Current (A)**
TMP36 Temperature Sensor	3.3	3.3V Rails	0.00005	6	0.0003
MCP3421 ADC	3.3	3.3V Rails	0.000155	6	0.00093
TLV9062 Operational Amplifier	3.3	3.3V Rails	0.000538	6	0.00323
STM32L031 Microcontroller	3.3	3.3V Rails	0.0024	4	0.0096
MM200 Magnetometer	3.3	3.3V Rails	0.01	1	0.01
Granstal GS-RW10 reaction wheel	12	3.3V Rails	1.18	3	3.54
CAT4101 LED Driver	3 - 5.5V	3.3V Rail	1.0008	1	1.0008
CAT4101 LED Driver	3 - 5.5V	4.2 - 3.6V Rail	1.0008	11	11.0088
ADS1115 ADC	5.0	5V Rail	0.00018	12	0.00216

Component	Voltage (V)	Rail(s)	Current (A)	Qty	Total Current (A)
EPB-25PS-C20004 Pressure Sensor	5.0	5V Rail	0.0083	6	0.0498
VACCO CuSP Micro Propulsion System	12.0	12V Rail	0.917	3	2.751
					Total Current per Rail (A)
3.3V Rails (Combined)					**4.56486**
4.2 – 3.6V Rail					**11.0088**
5V Rail					**0.05196**
12V Rail					**2.751**

The advantage of the ICEPS EPS can be observed in Table 6.7. It provides several high-power rails with various voltage ratings that are convenient for this application. The 3.3V and 5V rails are widely applicable in CubeSat contexts, being used to power most sensors and analogue-to-digital converters. The 12V rail as well, however, is practical for providing power to the propulsion system, and the LED drivers (used as recession sensor current sources) can nearly entirely subsist on the unregulated 4.2 - 3.6V rail alone. The remaining CAT4101 driver is placed on the 3.3V rail due to the small quiescent current (0.8mA each) consumed by the drivers themselves, as well as to account for possible fluctuations in power usage. The reaction wheels are distributed across the two 3.3V rails, with two connected to one rail and the third sharing the second rail with other components. This ensures a wide margin to the maximum current rating for each rail.

Some components are not directly connected to any rails, but are powered through interfaces from other components. These are listed below for completion.

Component	Power Connection Path
ICEPS Epik Sidekiq Z2	Powered directly from the ICEPS OBC (pre-integrated)
PE44820 Phase Shifter	Powered via STM32L031 Microcontroller
Custom Recession Sensor Mesh	Powered by CAT4101 LED driver
Custom Recession Sensor Foil	Powered by CAT4101 LED driver
GVA-84+ Amplifier	Powered via STM32L031 Microcontroller
ADL8122 LNA	Powered via STM32L031 Microcontroller
AvaSpec Spectrometer	Powered via USB connection to ICEPS OBC

Table 6.8: Components powered indirectly via subsystem interfaces

7 Instrumentation

The following subsections describe the onboard instrumentation used for sensing and control throughout the duration of the mission.

7.1 Ablation Sensing - Hani Moussa

The CubeSat is designed to test a different ablative material on each of its six exterior faces. To produce meaningful data for client use, each material sample will be equipped with its own dedicated sensor array. These arrays will measure temperature, pressure, and material recession through a combination of sensors and analogue-to-digital converters. All components were selected to be compatible with the I^2C communication protocol, allowing for integration with the satellite's onboard computer.

7.1.1 Temperature

Several methods exist for the evaluation of temperature. The options are described below in Table 7.1.

Table 7.1: Temperature measurement device types and their advantages/disadvantages

Measurement Type	**Advantages**	**Disadvantages**
Infrared Camera	Provides a detailed view of temperature distribution over material surfaces	Expensive, difficult to position, and low frequency of measurement
Heat Flux Sensor	Directly measures heat transfer, suitable for use on ablative material surface	Limited temperature range, and do not measure temperature directly
Thermocouple	Can possess a wide temperature range, offer rapid response time, and is cost-effective	Only provides relative temperature difference (i.e. requires reference)

Given the constraints of the CubeSat context, infrared cameras are unsuitable due to their size, complexity, and limited practicality in space applications. Similarly, heat flux sensors do not directly provide the specific data required for this mission - that being the ablative material's temperature.

Thermocouples, by contrast, are well-established in aerospace applications. They offer high-frequency temperature measurements, are relatively simple to apply, and are highly reliable in harsh environments. Operating based on the Seebeck effect, thermocouples generate an analogue voltage in response to a temperature gradient between two junctions. Among the available types, Type K thermocouples are best suited to this application due to their wide operating temperature range, durability, and extensive flight heritage.

The TE Connectivity MEAS 410 Type K thermocouple was selected for its wide operating range of -200°C to 1,250°C, suitable for the thermal conditions expected in re-entry. It provides adequate measurement precision

Table 7.2: ADC options for use with the MEAS 410 Thermocouple

Product	**Voltage Range**	**Operating Temperature**	**Resolution**	**Interface**	**CJC**
Texas Instruments ADS1118IDGST	0V to 4.096V	-40°C to 125°C	12 bit	I^2C	No
ST Electronics RHFAD128	-0.3 V to 4.8 V	-55°C to 125 °C	12 bit	SPI	No
Maxim MAX31856	-0.3V to +4.0V	-55°C to 125°C	19 bit	SPI	Yes
Microchip MCP3421	-0.3V to 0.3V	-55°C to 125°C	18 bit	I^2C	No
Texas Instruments ADS1115	-0.3V to 0.3V	-40°C to 125°C	16 bit	I^2C	No

and is compatible with satellite integration due to its simple electrical interface and robustness in extreme environments. This makes it a practical and reliable choice for temperature monitoring in the system.

This thermocouple requires an analogue-to-digital converter to be able to communicate its measurements. With standard type K thermocouple potential difference and temperature relations in mind [74], the operating voltage for the chosen thermocouple is likely to range between $-5891\ \mu V$ and $50644\ \mu V$. Additionally, the thermocouple requires a cold junction (reference temperature) in order to measure the temperature of the test material. Many ADCs designed for use with thermocouples are made with CJC (Cold Junction Compensation). This feature creates a junction of known temperature for the thermocouple to use as a reference, simplifying the sensor array's design. A list of compatible ADCs is described below in Table 7.2.

None of the listed ADCs offer a perfect match for the application. They either do not feature CJC or have an incompatible interface protocol. Each limitation may be addressed in a different manner:

- **No CJC** - The feature can be externalised from the ADC by incorporating a dedicated temperature sensor to monitor the reference junction. Texas Instruments outlines such an approach [75], which enables accurate compensation through post-processing of the thermocouple signal.
- **No I^2C interface** - SPI-enabled devices may be paired with an SPI-to-I^2C bridge, such as the SC18IS602B. This may lead to a decreased data throughput, increased designed complexity and a higher power draw.

Prioritising simplicity in the interfacing mechanism, and therefore reliable data acquisition, the Microchip MCP3421 (no CJC) was selected and the cold junction is externalised and measured seperately using the TMP36. With an operating temperature range of -40°C to 125°C and a history in thermocouple applications, it is a dependable choice for monitoring the cold junction temperature. By integrating the TMP36 alongside the MCP3421 ADC, Cold Junction Compensation can be implemented without relying on native ADC support.

7.1.2 Pressure

Pressure sensors used in aerospace applications can vary significantly in size. However, the constraints of CubeSat engineering demand care to volume and mass minimisation. With these limitations in mind, the sensor options listed in Table **??** have been selected for their compact size and practicality for integration within a CubeSat.

Table 7.3: Suitably compact pressure sensor options

Product	**Pressure Range**	**Temperature Range**	**Interface**
Honeywell MPR Series	60 mbar to 2.5 bar	0°C to 50°C	I^2C/SPI
TE Connectivity EPB-25PS-C20004	0 - 1.5 bar	-40°C to 120°C	Requires ADC
Sensata PTE7300-14AM-1B010SN	0 - 10 bar	-40°C to 100°C	I^2C

The pressure range offered by TE Connectivity's EPB-25PS-C20004 is suitable relative to the pressures considered in Section **??**, and it functions in a wide temperature range. It does not, however, include an integrated ADC.

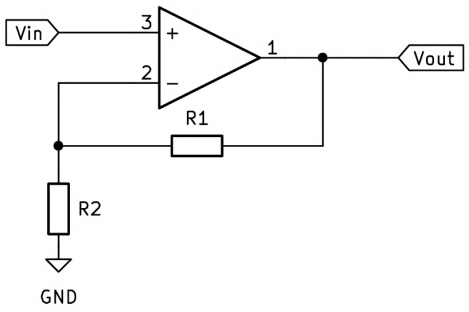

Figure 7.1: Non-inverting Operational Amplifier Layout

The component features a maximum analogue output of 50mV. This output is amplified through the use of a non-inverting operational amplifier. The Texas Instruments TLV9062 operational amplifier is used as seen in Figure 7.1, with an intended closed-loop gain for the circuit of 100. The true value, however, is governed by the ratio of the two resistances[76].

$$A = 1 + \frac{R_1}{R_2} \tag{7.1}$$

With standard resistor values $R_1 = 1\text{k}\Omega$ and $R_2 = 100\text{k}\Omega$, a gain of 101 is achievable with minimal current draw. Coupled with the pressure transducer input, the result is a 5.05V maximum analogue signal. The Texas Instruments ADS1115 ADC is selected to quantify and communicate this value through the OBC's I^2C network. Due to the limitation by the ADC's 5V supply from the ADC, it is unable to measure beyond this value. Therefore, the maximum pressure detectable decreases to 1.485bar, an acceptably small loss of range.

7.1.3 Recession

Recession sensors are critical for measuring the ablation that occurs when the CubeSat surface is exposed to extreme conditions during reentry. These sensors are designed to quantify the rate at which a material is eroded over time, providing valuable data on its durability and performance under thermal stress. By tracking the changes in the material's thickness, the recession sensors will allow for a greater understanding of the ablative

properties of test materials.

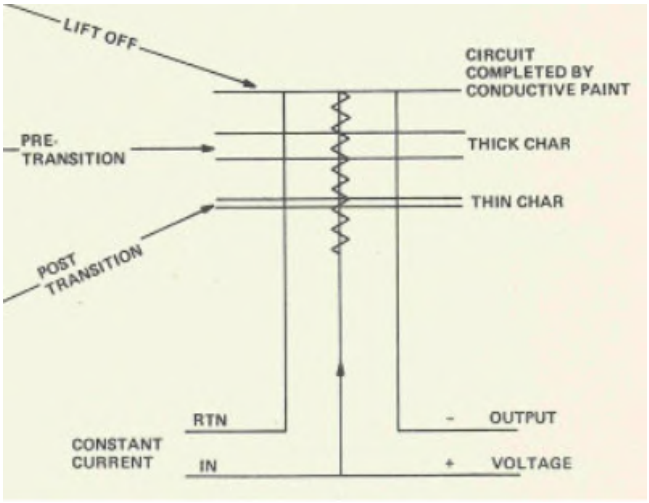

Figure 7.2: ARAD sensor electrical scheme [77]

Capacitive Sensors Material recession can be measured using two main strategies. One widely adopted approach utilises capacitive-based sensors, such as NASA's Analog Resistance Ablation Detector (ARAD) sensor [77]. These sensors are positioned perpendicular to the ablation direction and consist of layered capacitive elements, comprising a dielectric material held between conductive plates. As the ablative material undergoes erosion, the effective area of the capacitor decreases, leading to a measurable reduction in capacitance. This reduction can be directly correlated with the extent of material recession, providing a real-time assessment of the length of remaining ablative material.

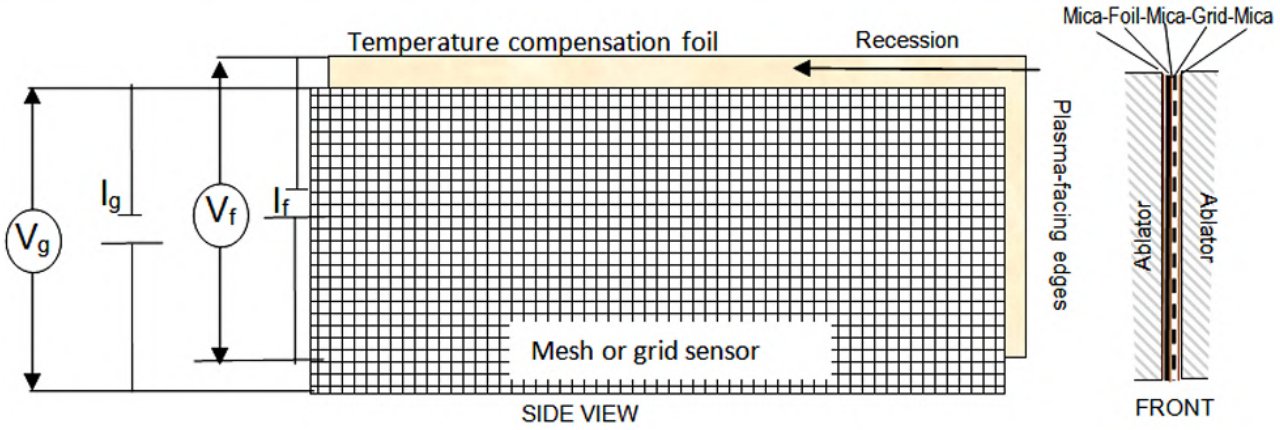

Figure 7.3: ReWiG Sensor as seen in ESA report [78]

Resistive Sensors Another approach to measuring material recession is employed by ESA's ReWiG sensor [78]. This system includes a nickel wire mesh within the ablative surface perpendicular to the erosion direction. As the material ablates during reentry, the mesh progressively ablates at the same rate. Direct measurement of the mesh resistance can then be used to determine the remaining thickness of the ablative material.

A key component of this system is the nickel temperature compensation foil, which helps to account for

temperature-induced changes in the resistance of the mesh. As the temperature fluctuates during reentry, both the mesh and the foil experience changes in their resistance. By comparing the resistance of the foil to that of the mesh, the sensor can isolate and correct for any temperature-related effects on the nickel mesh's resistance. This ensures that the readings more accurately represent the erosion rate, accounting for thermal error to the resistance of the mesh.

Comparison NASA's ARAD and HEAT sensors are widely documented approaches. However, these have significant limitations. As noted by the European Space Agency, both sensors measure recession indirectly through thermal gradients and rely on assumptions regarding conductor melting and pyrolysis. Their precision has been reported at approximately 6 mm when calibrated with PICA, and they have been described as "unsatisfactory and unreliable" by NASA personnel during IPPW12 [78]. In contrast, the ReWiG sensor was developed by ESA to address these limitations directly. It provides direct recession measurement, built-in temperature compensation, and simpler electrical integration. Therefore, it was selected as the most suitable option for accurate erosion monitoring in this mission context.

The initial resistance of the Nickel foil can be calculated with the standard resistivity equation and the mesh dimensions provided in the ESA proposal [78]. For a sensor of width 3mm and length through the material 6mm,

$$R_{foil} = \frac{\rho_{Ni} L}{A} = 0.0011875\,\mu\Omega \text{ (3sf)} \tag{7.2}$$

where

- $\rho_{Ni} = 9.500 \times 10^{-8}\Omega$m is the resistivity of Nickel 200 [79]
- L is the width of the sensor (as the length of the equivalent wire)
- A is the area of the equivalent wire

Figure 7.4 was generated using MATLAB, extending Equation 7.2 for a range of 1-6 mm of remaining ablative material. Due to the reciprocal relationship, measurement below 1 mm is impractical. The recession sensor is embedded from 1 mm behind the ablative material to suitably align the effective "zero" value.

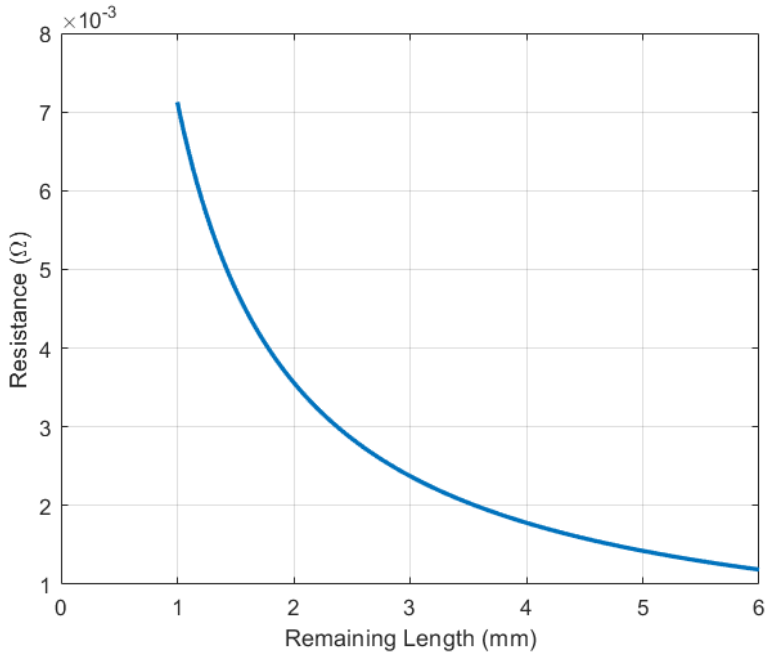

Figure 7.4: Calculated resistance of recession foil as a function of remaining ablative material thickness

A simplified model shows the mesh to have a comparable resistance (greater than that of the foil by a factor of 1.25). As the foil and grid erode, the resistance of each increases, allowing recession to be measured through the application of a fixed current.

The desired current is decided by a compromise complicated due to the low resistance of the mesh and foil. A higher current results in a higher, more easily readable voltage, but also a higher power requirement and increased self-heating of the recession sensor. This self-heating may potentially disturb the temperature condition if of significant magnitude.

The selection of the operating current involved a trade-off influenced by the low resistance of the mesh and foil. While a higher current improves measurement resolution, it also increases power consumption and induces greater heating within the recession sensor. If significant, this self-heating could disrupt thermal conditions and potentially affect measurement accuracy.

Current options, their extremes in generated output voltages, and their maximum power use are shown below in Table 7.4. These were derived with values from Figure 7.4 and Ohm's law.

Table 7.4: Voltage drop and power consumption across recession sensor foil (1.2 - 7.2mΩ) at various currents

Current (A)	**Initial Voltage (mV)**	**Final Voltage (mV)**	**Max Power (mW)**
0.1	0.12	0.72	0.072
0.5	0.60	3.60	1.80
1.0	1.20	7.20	7.20
2.0	2.40	14.40	28.80
3.0	3.60	21.60	64.80
5.0	6.00	36.00	180.00

Each the mesh and the foil require the same current, and a recession sensor is placed on each of the CubeSat's six faces. This means the power requirement for only the main sections of the recession sensors is twelve times as high as seen in Table 7.4. 1A is chosen for its ability to produce initial voltages greater than one millivolt whilst keeping power usage low.

This current is provided with the ON Semiconductor CAT4101 Constant-Current LED Driver. Designed for the purpose of delivering a stable, constant current to a low resistance LED, the component is suitable for the purposes of the recession sensor. It can output up to 1A of current and consumes approximately 42.6mW of power; this is high relative to the sensor but not for typical drivers that can reach a 1A output.

The potential difference output, as detailed in the ReWiG design [78], is between the high potential sides of each the mesh and the foil. This allows for temperature compensation, as the resistive differences between the mesh and foil shapes are the significant factor in forming the varied voltage between the two, temperature affecting both equally. The potential difference spans between approximately 1.20 - 7.20 mV for the foil (described in Table **??**), and 1.5 - 9 mV for the grid. The resulting potential difference is a range of 0.3 - 1.8 mV, far too low to be practically sensed by an analogue-to-digital converter.

To bring the sensor output within the ADS1115 ADC's measurable range, the signal is amplified using a non-inverting configuration. This ADC's lowest upper bound on measurable voltage (with the highest resolution) is 256mV, and therefore the ideal gain for an amplifier would be 142. Using a similar design to Figure 7.1, the closest simple design (minimising the error caused by tolerances) would include values of $R_1 = 1\text{k}\Omega$ and $R_2 = 140\text{k}\Omega$ for a gain of 141. The latter resistor, while uncommon, is offered at a low tolerance of 1% by Yageo as the RC0603FR-07140KL model.

The range used (as in Figure **??**) is 1mm to 6mm due to the operating limits of the recession sensor and to keep the system within safe electrical parameter ranges. As the ablative material erodes and the resistance of the sensor increases beyond the upper limit of 7.2mΩ, the voltage drop across the sensor increases too (proportionally given the constant current source and Ohm's law). If this voltage becomes too high, it can exceed the safe operating voltage or power dissipation limits of the LED driver, risking overheating or damage to the electrical system as a whole.

To prevent this, a comparator circuit is used to monitor the voltage across the sensor's amplifier. When this voltage exceeds 256mV (indicating 1mm of the sensor remaining), the comparator output triggers a shutdown mechanism. This can disable the current driver directly by opening a MOSFET in the sensor circuit, concluding recession measurement on the corresponding side of the CubeSat. This safeguard avoids unnecessary power draw or potential component damage.

The ReWiG-based sensor system provides a reliable, low-power method for direct recession measurement with built-in temperature compensation and overvoltage protection, suitable for the mission context.

7.2 Cold Gas Thrusters - Fizza Naqvi

The CubeSat will use three of VACCO's CubeSat Propulsion System (CuSP) [44] units, each of which integrates a Cold Gas Micro Propulsion System (MiPS), to achieve the required attitude control. The MiPS is specifically designed for small spacecraft such as CubeSats, providing precise thrust for orbital adjustments and de-orbit burns.

Figure 7.5: VACCO's CubeSat Propulsion System unit [44].

Each CuSP unit, shown in Figure 7.5, is approximately 0.3U in volume, keeping the propulsion system compact and space-efficient. The system uses four 25 mN cold gas thrusters per unit, and collectively, these thrusters generate a specific impulse[6] (I_{sp}) of 69s.

Each propulsion system has an allowed propellant mass of 177g, providing the necessary fuel for the CubeSat to perform the required manoeuvers. The total delta-V of the CubeSat is calculated using the Tsiolkovsky rocket equation [80]:

$$\Delta v = I_{sp} \cdot g_0 \cdot \ln\left(\frac{m_i}{m_f}\right) \tag{7.3}$$

In the equation, the terms m_i and m_f correspond to the CubeSat's mass before and after the de-orbit burn respectively.

[6]Specific impulse is the ratio of impulse to the mass of propellant consumed.

The three CuSP units provide a combined delta-V capability of 88 m/s, offering sufficient propulsion power to achieve the CubeSat's mission objectives. Since the required delta-V for the de-orbit burn is about 77 m/s (as detailed in section 4.2), this gives the CubeSat an additional 11 m/s of delta-V margin, allowing flexibility in mission planning and manoeuvring if necessary.

7.3 Reaction wheels - Alex Berresford

Reaction wheels are essential components within space vehicles and satellites during their orbital life. They use a spinning flywheel and the conservation of angular momentum to allow for the control of a vehicles attitude, which can be necessary for angling the vehicle for directional communications or thrusters. They are simple devices. In principle, a flywheel spins in one direction with a certain torque. To satisfy conservation laws, the rest of the CubeSat rotates in the opposite direction, but with the same magnitude of torque. The relative speeds of these rotations depend on the ratio of the moment of inertia between the flywheel, and the rest of the CubeSat.

$$\begin{aligned} L_{sat} + L_{wheel} &= 0 \\ J_{sat}\omega_{sat} &= -J_{wheel}\omega_{wheel} \\ \omega_{sat} &= \frac{-J_{wheel}}{J_{sat}}\omega_{wheel} \end{aligned} \tag{7.4}$$

In this project, reaction wheels serve two purposes. The first is attitude control of the CubeSat to allow for a successful de-orbit burn and efficient re-entry, requiring a reaction wheel ready on 3 separate axes. The second is as spin up manoevre to encourage the CubeSat to tumble through the atmosphere rather than stagnate, ensuring that the heatshield material is tested evenly on all faces.

When selecting a reaction wheel, several factors were considered. Size was the most crucial aspect, as they needed to be small enough to reasonably fit three reaction wheels within the CubeSat. Ideally, the length, width and heights will be similar values as a singular significantly larger dimension makes internal component placement more difficult. A high maximum momentum is desirable to make manoeuvres in a shorter time frame, as well as giving the CubeSat a higher maximum spin rate during the spin up during the re-entry phase. A low mass was looked upon favourably but was not a critical factor in decision making.

Maximum angular velocities were estimated by assuming the CubeSat has a mass of 12kg (1.5kg per U) and that mass is evenly distributed. This yields an inertia of $1kgm^2$. Maximum angular velocity can then be calculated

Company	**Product**	l (mm)	w (mm)	h (mm)	Max momentum (mNms)	Max Torque (mNm)	Mass (g)	Max 8U rotational speed (rad/s)
Comat	RW60	65.6	65.6	44.8	60	6	270	0.06
Space Inventor	WHL-1000	109	109	42.5	1000	50	1200	1
AA Clyde Space	RW402	50	50	27	50	8	375	0.05
GranStal	GS-RW10	50	50	60	100	10	250	0.1

Table 7.5: An abridged comparison of CubeSat specifications [81] [82] [43] [83]

directly from the equation below.

$$\omega_{sat} = \frac{-L_{wheelmax}}{J_{sat}} \tag{7.5}$$

The Granstal GS-RW10 was the clear choice. It has the lowest mass, and the highest resulting CubeSat angular velocity whilst having reasonable dimensions.

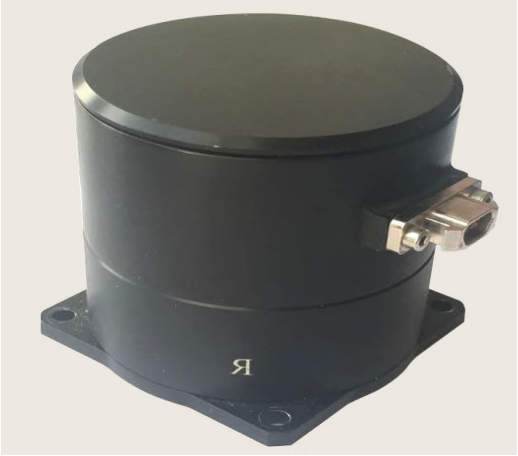

Figure 7.6: GS-RW10 Reaction wheel

7.4 Magnetometer - Alex Berresford

A magnetometer is a device that measures magnetic fields. The simplest case of a magnetometer is a compass, which was first invented in 206 BC China and initially used for geomancy and divination [84]. It took over a millennium after this for the development and use of a navigational compass [85]. As we know, they measure the directionality of the earths magnetic field to give the user their orientation, which can be used in conjunction with known geographical data (maps) to allow for navigation. Magnetometers used in satellites work similarly. Field direction and magnitude are both measured but are then instead compared to known magnetic field data to help determine position and orientation – for example the World Magnetic Model. [86]

The World Magnetic Model (WMM) is the standard model for navigation systems which use the geomagnetic

field [86]. Its developed jointly by the British Geological survey and the National Centers for Environmental Information, of the US. The model is accurate up to 850km in altitude and track's location using seven geomagnetic readings [86], which can be thoroughly decoded at a ground station once the readings have been received. Onboard, the measured magnitude of the magnetic field can be compared to an uploaded sample of the WMM to aid in altitude estimation. The measured magnetic field direction can be used to help determine CubeSat orientation, which is critical for performing a successful deorbit burn.

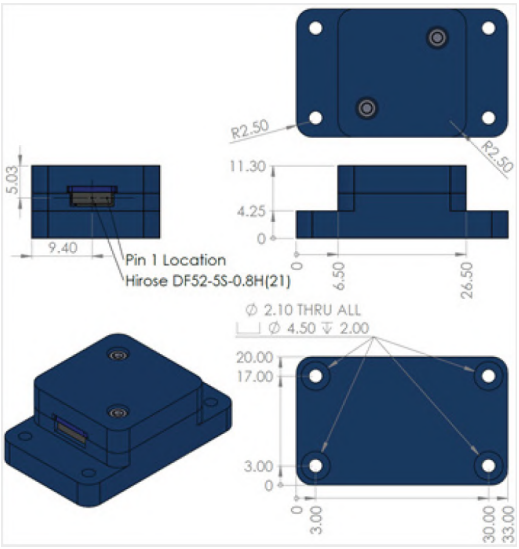

Figure 7.7: MM200 Magnetometer [51]

Use of a magnetometer has limitations. During re-entry, the plasma layer formed can affect local magnetic fields due to the high density of charged particles within it [87]. This disruption interferes with all readings taken by the magnetometer, limiting its use to earlier stages of the mission. Furthermore, the WMM can be affected by solar wind at higher altitudes, which needs to be accounted for prior to launch to prevent inaccuracies in altitude estimation [86]. Blackout zones exist around the poles where the WMM shouldn't be relied upon, and the orientation measured from the magnetometer will be significantly different to anywhere else in orbit. Therefore, polar orbits will be avoided. [86] The MM200 magnetometer from AAC Clyde Space was chosen for our CubeSat. It is extremely light weight and low volume, making it ideal for a CubeSat mission. Its high precision of $1.18nT\sqrt{Hz}$ and sampling rate of up to $500Hz$ [51] allows for high accuracy measurements to be made, aiding in altitude and orientation estimation. The measurement range of +/- $800m\mu T$ far exceeds the expected magnetic field intensities of up to $28\mu T$, courtesy of the WMM. [86]

Company	**Sensor**	l (mm)	w (mm)	h (mm)	Mass (g)	Max sampling rate (Hz)	Min power (mA)	Max power (mA)	Range (μT)
AAC Clyde Space	MM200	33	20	11.3	12	500	0.5	10	±800

Table 7.6: Specifications of MM200 magnetic sensor from AAC Clyde Space [51]

7.5 Attitude and Altitude Tracking via Sensor Fusion - Fizza Naqvi

7.5.1 Overview

Accurate altitude and attitude tracking are essential for the CubeSat re-entry experiment to correlate material ablation data with atmospheric conditions throughout re-entry. The hypersonic environment presents challenges such as sensor noise, bias, and drift [88], which degrade measurement accuracy. Conventional sensors alone often struggle due to high thermal loads, rapid attitude changes, and fluctuating atmospheric densities, resulting in noisy and uncertain readings. To overcome these challenges, a Kalman filter with sensor fusion[7] combines measurements from an Inertial Measurement Unit (IMU) and a magnetometer. This method is proposed and adapted from established sensor fusion techniques to suit the specific requirements of the CubeSat re-entry experiment. This fusion exploits the IMU's ability to capture high-frequency inertial dynamics and the magnetometer's role as a long-term orientation reference, especially for stabilising yaw. The filter framework compensates for individual sensor weaknesses, enhancing reliability and precision in attitude determination, which is vital for controlling the retrograde burn and maintaining the desired re-entry trajectory. Figure 7.8 illustrates the sensor fusion structure.

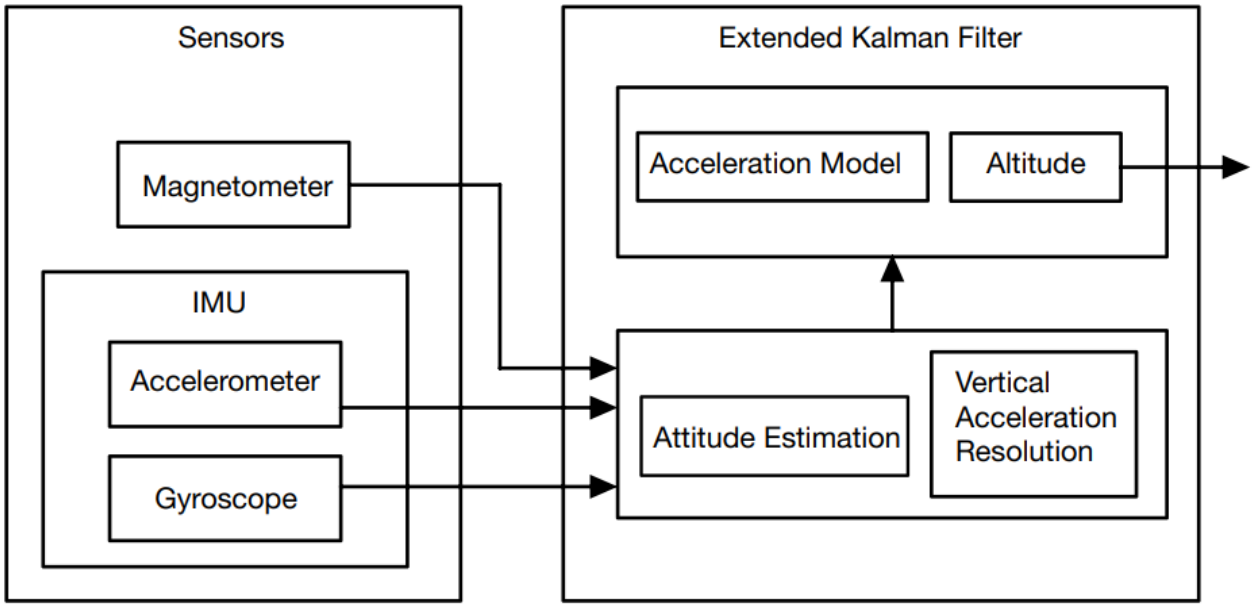

Figure 7.8: Sensor fusion algorithm to determine altitude, adapted from Bashir et al. [90].

7.5.2 Instrumentation Models

An IMU consists of two primary components: a tri-axis accelerometer and a tri-axis gyroscope. The accelerometer measures linear acceleration components along three orthogonal axes, denoted as a_x, a_y, a_z, and detects changes in velocity due to external forces [91]. However, since it also senses gravitational acceleration, it cannot inherently separate gravity from motion-induced acceleration. When accelerometer readings are integrated over time to estimate position or velocity, this ambiguity accumulates, resulting in drift. The gyroscope measures

[7]Sensor fusion integrates data from multiple sensors to provide a comprehensive and accurate understanding of the environment or system being monitored or controlled [89].

angular velocity $(\omega_x, \omega_y, \omega_z)$ about three perpendicular axes (roll, pitch, and yaw) [92], providing information on the CubeSat's orientation. The magnetometer measures the CubeSat's magnetic field components m_x, m_y, and m_z relative to the Earth's magnetic field, provides an absolute reference aligned with Earth's magnetic field, helping to correct orientation errors. By fusing data from the IMU and magnetometer within a Kalman filter, gravitational components can be modelled and subtracted, and accumulated drift errors are continually corrected, resulting in more accurate and stable altitude and attitude estimates even under dynamic re-entry conditions.

Gyroscope Gyroscopes measure angular velocity in the body frame, but to obtain the time derivatives of the roll (ϕ), pitch (θ), and yaw (ψ) angles in the inertial frame, a transformation is required. This transformation accounts for the non-linearity in Euler angle kinematics and ensures proper mapping between the measured angular rates and the actual rotational dynamics of the CubeSat.

The relationship between the time derivatives of Euler angles, shown in Figure 7.9, and the body-frame angular velocity components $\boldsymbol{\omega}_b = (\omega_x, \omega_y, \omega_z)^T$ is given by [93]:

$$\begin{bmatrix} \dot{\phi} \\ \dot{\theta} \\ \dot{\psi} \end{bmatrix} = \begin{bmatrix} 1 & \sin\phi\tan\theta & \cos\phi\tan\theta \\ 0 & \cos\phi & -\sin\phi \\ 0 & \frac{\sin\phi}{\cos\theta} & \frac{\cos\phi}{\cos\theta} \end{bmatrix} \begin{bmatrix} \omega_x \\ \omega_y \\ \omega_z \end{bmatrix} \tag{7.6}$$

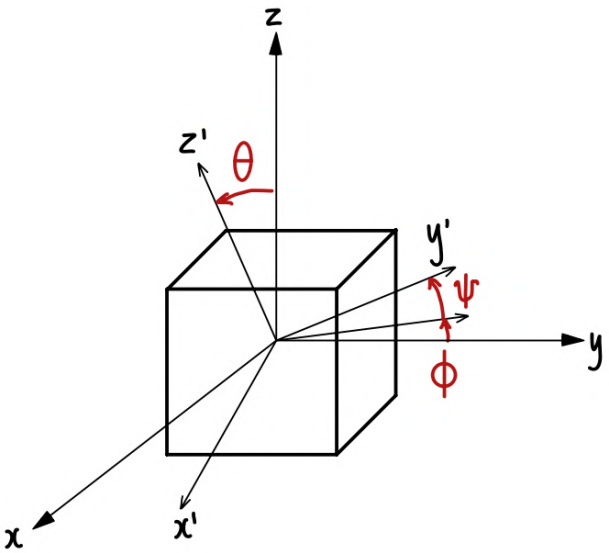

Figure 7.9: Representation of Euler angles: roll, pitch, and yaw, illustrating the CubeSat's orientation relative to its body axes.

Accelerometer The accelerometer measures gravitational acceleration along the CubeSat's body axes. By resolving these measurements through trigonometric relationships, estimates of roll and pitch can be obtained. The orientation angles are derived as [94]:

$$\phi = \arctan\left(\frac{a_y}{\sqrt{a_x^2 + a_z^2}}\right) \tag{7.7}$$

$$\theta = \arctan\left(\frac{a_x}{\sqrt{a_y^2 + a_z^2}}\right) \tag{7.8}$$

Magnetometer The magnetometer measures the Earth's magnetic field vector in the CubeSat's body frame. By combining this measurement with the estimated roll and pitch angles from the accelerometer, the yaw angle can be determined. This provides an absolute heading reference and corrects for gyroscopic drift over time. The tilt-compensated yaw angle is computed as [95]:

$$\psi = \arctan\left(\frac{m_x \cos\phi - m_y \sin\phi}{-m_x \sin\phi \sin\theta - m_y \cos\phi \sin\theta - m_z \cos\theta}\right) \tag{7.9}$$

7.5.3 System Dynamics

The system dynamics are crucial because they define the physical model that the attitude estimation will be based on. By understanding how the attitude state evolves, a better estimate of the vehicle's orientation can be determined at any given time.

In discrete-time form, a causal linear time-invariant system in state-space form [96] is given by:

$$\bar{x}_{k+1} = A_d \bar{x}_k + B_d \bar{u}_k + \bar{w}_k, \tag{7.10}$$

$$\bar{y}_k = C_d \bar{x}_k + \bar{v}_k. \tag{7.11}$$

where $\bar{w}_k \in \mathbb{R}$ and $\bar{v}_k \in \mathbb{R}$ represent the process noise and measurement noise that enters the system at $t = kT$ respectively. Here, $k \in \mathbb{Z}_{\geq 0}$ is the discrete time-step index, and T is the sampling period (in seconds) that defines the time interval between successive updates.

Both sources of noise enter at the sample time. It is reasonable to assume that the measurement noise is uncorrelated in time, since $\bar{y}_k$ is sampled at $t = kT$, meaning each measurement is only affected by noise at that specific time instant. On the other hand, the state equation is derived from the evolution of the state over the period $t = kT$, so $\bar{w}_k$ represents the accumulation of the effect of the process noise over this interval.

It is assumed that the process and measurement noises are uncorrelated, zero-mean, white noise random processes with covariance matrices Q and R:

$$E[\bar{w}_k \bar{w}_k^T] = Q, \quad E[\bar{v}_k \bar{v}_k^T] = R. \tag{7.12}$$

Additionally, we assume that there is no correlation between the two noise processes:

$$E[\bar{w}_k \bar{v}_k^T] = 0. \tag{7.13}$$

The state vector for the system (adapted from Bashir et al. [90]) is given as:

$$\hat{\mathbf{x}}_k = \begin{bmatrix} \hat{\phi}_k \\ b_{\hat{\phi}_k} \\ \hat{\theta}_k \\ b_{\hat{\theta}_k} \\ \hat{\psi}_k \\ b_{\hat{\psi}_k} \end{bmatrix} \tag{7.14}$$

In this extended state vector, $\hat{\phi}_k$, $\hat{\theta}_k$, and $\hat{\psi}_k$ represent the roll, pitch, and yaw angles, respectively, at time k. The variables $b_{\hat{\phi}_k}$, $b_{\hat{\theta}_k}$, and $b_{\hat{\psi}_k}$ denote the biases in the measurements of the roll, pitch, and yaw angles, respectively, at time k.

The input vector is:

$$\mathbf{u}_k = \begin{bmatrix} \dot{\phi}_{Gk} \\ \dot{\theta}_{Gk} \\ \dot{\psi}_{Gk} \end{bmatrix} \tag{7.15}$$

In this input vector, $\dot{\phi}_{Gk}$, $\dot{\theta}_{Gk}$, and $\dot{\psi}_{Gk}$ represent the angular velocities of the CubeSat around the roll, pitch, and yaw axes, respectively, at time k, measured in the ground frame of reference, G. This means that they are referenced to the Earth's frame.

The measurement vector is:

$$\mathbf{z}_k = \begin{bmatrix} \hat{\phi}_{Ak} \\ \hat{\theta}_{Ak} \\ \hat{\psi}_{Ak} \end{bmatrix} \tag{7.16}$$

In this measurement vector, $\hat{\phi}_{Ak}$, $\hat{\theta}_{Ak}$, and $\hat{\psi}_{Ak}$ represent the roll, pitch, and yaw angles of the CubeSat at time k. These angles are computed from onboard sensors and are expressed with respect to the Earth-fixed frame, while the measurements originate from the CubeSat's body frame, denoted by A.

Varying gyroscope bias causes drift in the angular position estimates. To eliminate this drift, the biases are estimated and subtracted from the gyroscope's measured angular rates. This correction provides updated and more accurate estimates of the CubeSat's angular position.

The general state space form for the system [90] is:

$$\mathbf{x}_{k+1} = \begin{bmatrix} 1 & -\Delta t & 0 & 0 & 0 & 0 \\ 0 & 1 & 0 & 0 & 0 & 0 \\ 0 & 0 & 1 & -\Delta t & 0 & 0 \\ 0 & 0 & 0 & 1 & 0 & 0 \\ 0 & 0 & 0 & 0 & 1 & -\Delta t \\ 0 & 0 & 0 & 0 & 0 & 1 \end{bmatrix} \mathbf{x}_k + \begin{bmatrix} \Delta t & 0 & 0 \\ 0 & 0 & 0 \\ 0 & \Delta t & 0 \\ 0 & 0 & 0 \\ 0 & 0 & \Delta t \\ 0 & 0 & 0 \end{bmatrix} \mathbf{u}_k + \mathbf{w}_k \tag{7.17}$$

$$\mathbf{y}_k = \begin{bmatrix} 1 & 0 & 0 & 0 & 0 & 0 \\ 0 & 0 & 1 & 0 & 0 & 0 \\ 0 & 0 & 0 & 0 & 1 & 0 \end{bmatrix} \mathbf{x}_k + \mathbf{v}_k \tag{7.18}$$

The Kalman filter algorithm used to estimate the CubeSat's attitude based on this state-space model is described in Appendix A.2.

The current lack of flight data from tumbling re-entry vehicles limits direct testing and validation of the model under representative conditions. Despite this, a synthetic dataset was used to test the model under simplified and controlled conditions. The process and measurement noise covariance matrices, Q and R, were tuned in MATLAB through iterative trial and error.

To approximate realistic sensor behaviour, simulated sensor measurements were generated by adding noise and bias consistent with typical CubeSat gyroscope, accelerometer, and magnetometer characteristics. These synthetic sensor inputs enabled evaluation of the Kalman filter's ability to estimate the CubeSat's roll, pitch and yaw angles. The filter's performance was assessed by comparing the estimated attitude against the known synthetic 'true' states, shown in Figure 7.10. This method, while limited in representing complex tumbling dynamics fully, provides a useful baseline for confirming filter stability and convergence over small to moderate angular variations.

Future improvements include extending validation to larger angle ranges, incorporating more complex tumbling motion profiles, and ultimately testing with real flight data once available. Such validation steps are critical to ensuring the robustness and reliability of the attitude determination system under the dynamic and harsh conditions of atmospheric re-entry.

7.5.4 Altitude Estimation

Altitude estimation is carried out by integrating measurements from the IMU and magnetometer. The acceleration vector is resolved into its vertical component, which is then used to estimate the vertical velocity and subsequently the altitude of the CubeSat throughout re-entry.

The system is modelled using the following state vector [90]:

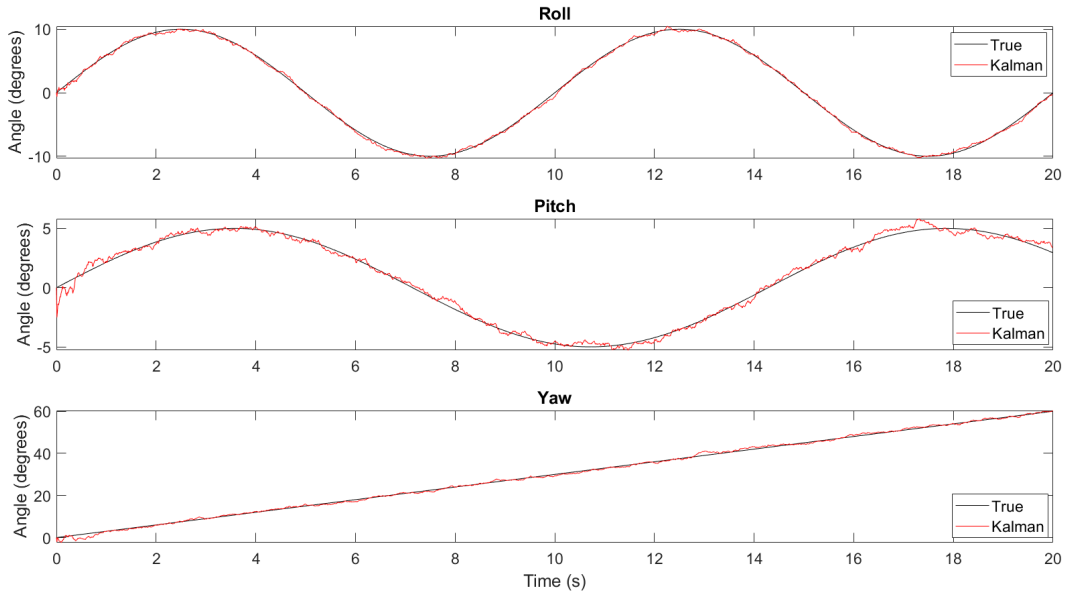

Figure 7.10: Comparison of true Euler angles for roll, pitch and yaw with estimates obtained from the Kalman filter using simulated sensor data.

$$x_k = \begin{bmatrix} h_k \\ v_k \\ b_k \\ s_k \end{bmatrix}, \quad x_k \in \mathbb{R}^{4\times 1} \tag{7.19}$$

Here, h_k is the altitude, v_k the vertical velocity, b_k the accelerometer bias, and s_k the scale factor that accounts for non-ideal accelerometer behaviour.

The accelerometer measurements are related to the acceleration inputs α_k by [97]:

$$a_k = s_k \alpha_k + b_k + n_k \tag{7.20}$$

where n_k represents additive noise.

The system dynamics used to update the state and output the altitude are:

$$\dot{h}_k = v_k \tag{7.21}$$

$$\dot{v}_k = r_k \left(\text{diag}(s_k)^{-1}(a_k - b_k)\right) + g \tag{7.22}$$

In this formulation, $\dot{h}_k$ gives the rate of change of altitude (i.e. velocity), while $\dot{v}_k$ is the vertical acceleration.

The term r_k denotes the third row[8] of the rotation matrix, R_k, which transforms vectors from the CubeSat's body frame to the inertial frame. This is equation 7.23 [98]. g is the gravitational acceleration vector.

$$R_k = R_z(\psi)R_y(\theta)R_x(\phi) \tag{7.23}$$

where

$$R_x(\phi) = \begin{bmatrix} 1 & 0 & 0 \\ 0 & \cos\phi & -\sin\phi \\ 0 & \sin\phi & \cos\phi \end{bmatrix}, \quad R_y(\theta) = \begin{bmatrix} \cos\theta & 0 & \sin\theta \\ 0 & 1 & 0 \\ -\sin\theta & 0 & \cos\theta \end{bmatrix}, \quad R_z(\psi) = \begin{bmatrix} \cos\psi & -\sin\psi & 0 \\ \sin\psi & \cos\psi & 0 \\ 0 & 0 & 1 \end{bmatrix}$$

7.6 Attitude Control System - Claudio Vestini

To achieve the mission objectives of performing a de-orbit burn and inducing tumbling of the CubeSat prior to re-entry through the upper atmosphere, it is necessary to control the CubeSat's orientation through a robust attitude controller. This section presents the implementation of a Model Predictive Control (MPC) architecture to achieve this objective. MPC differs from feedback control techniques such as proportional–integral–derivative (PID) control by explicitly predicting the future behaviour of the system over a finite time horizon. Instead of reacting solely to current errors, MPC optimises a series of control inputs at each timestep by solving a constrained optimisation problem based on a dynamic system model. This strategy is well-suited to the CubeSat control problem due to its capability to process Multiple-Input, Multiple-Output (MIMO) dynamics and capacity to explicitly handle actuator constraints, which are present due to maximum torque restrictions of the reaction wheels: using a constraint-aware MPC architecture (over traditional control strategies), the CubeSat is ensured to remain within safe operational limits throughout critical mission phases.

7.6.1 Dynamics

The CubeSat can be modelled as a rigid body with inertia matrix $\boldsymbol{J} \in \mathbb{R}^{3\times3}$, whose entries are found from the CAD model of the spacecraft. The motion of the CubeSat in space is governed by kinematic equations that describe attitude evolution and dynamic equations that reflect the rotational response to applied torques. The torques provided by each of the three reaction wheels are packaged into torque vector $\boldsymbol{\tau} \in \mathbb{R}^3$, where $\boldsymbol{\tau} = \boldsymbol{\tau}_a + \boldsymbol{\tau}_d$, combining actuator torque $\boldsymbol{\tau}_a$ and disturbance torque $\boldsymbol{\tau}_d$ (due to environmental effects like kinetic particle interactions or geomagnetic fields). The rotational response dynamics of the CubeSat follow Euler's equation (7.24), where ω is Euler angular velocity $\boldsymbol{\omega} := [\omega_i, \omega_j, \omega_k]^\mathsf{T} \in \mathbb{R}^3$. See Figure 7.11 (left) for the definition of axes.

$$\boldsymbol{J}\,\dot{\boldsymbol{\omega}} = -\boldsymbol{\omega} \times (\boldsymbol{J}\,\boldsymbol{\omega}) + \boldsymbol{\tau}, \tag{7.24}$$

[8]Only the third row of the rotation matrix R_k is used because it corresponds to the vertical (Z-axis) direction in the inertial frame. Since altitude estimation requires only the vertical component of acceleration, projecting the body-frame acceleration vector onto this row isolates the vertical inertial acceleration without computing the full transformation.

7.6.2 Kinematics: Quaternion Representation

While sufficient for computing Kalman Filter state estimates, the Euler angle representation described in Section 7.5 is not suitable for attitude control due to the potential presence of the kinematic singularity known as gimbal lock. This occurs when two of the three rotation axes in an Euler angle sequence become aligned, resulting in a loss of one degree of rotational freedom and rendering it impossible to uniquely determine the spacecraft's orientation. To overcome this limitation, the spacecraft's attitude is represented using unit quaternions for the MPC architecture. A quaternion is a four-dimensional vector that encodes rotation with equation (7.25).

$$\boldsymbol{q} = \begin{bmatrix} \eta \\ \boldsymbol{\epsilon} \end{bmatrix} = \eta + \epsilon_i\,\mathbf{i} + \epsilon_j\,\mathbf{j} + \epsilon_k\,\mathbf{k} \equiv \cos\left(\frac{\alpha}{2}\right) + \sin\left(\frac{\alpha}{2}\right)(\epsilon_i \boldsymbol{i} + \epsilon_j \boldsymbol{j} + \epsilon_k \boldsymbol{k})\,; \quad \eta^2 + \|\boldsymbol{\epsilon}\|^2 = 1, \tag{7.25}$$

In this representation, a rotation angle α about axis $\boldsymbol{\epsilon}$ (imaginary part) is encoded as half angle $\eta = \alpha/2$ (scalar part), as illustrated in Figure 7.11 (right), as opposed to the yaw-pitch-roll representation of Figure 7.11 (left).

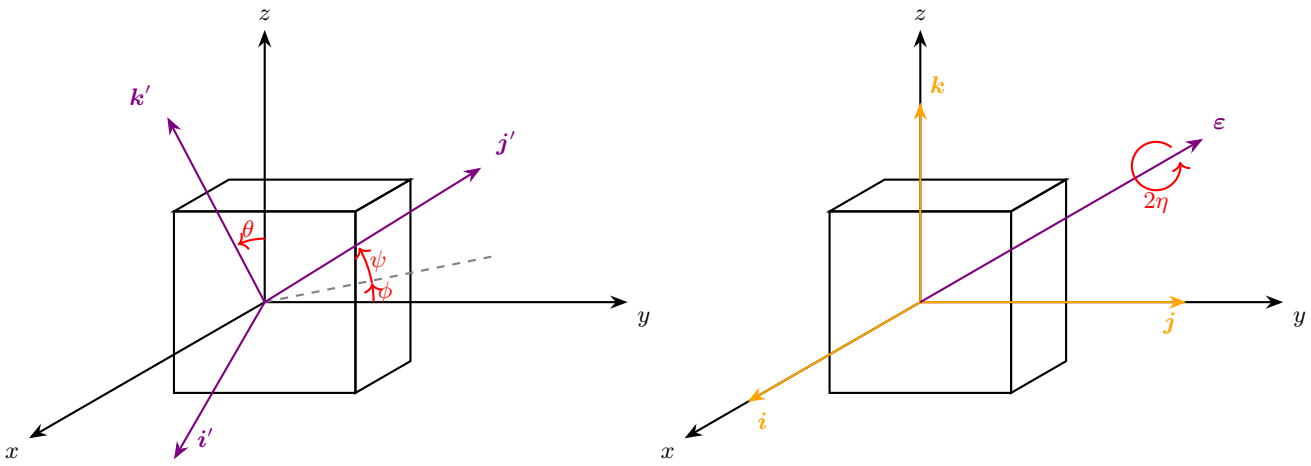

Figure 7.11: Comparison of Euler (roll ϕ, pitch θ, and yaw ψ) (left) to quaternion (right) rotation representation.

A rigid body rotation of any vector $\boldsymbol{p}$ can be represented as: $\boldsymbol{p}' = \boldsymbol{q}\boldsymbol{p}\bar{\boldsymbol{q}}$. Angular velocity $\boldsymbol{\omega}$ is mapped into quaternion space by the 4×4 skew-symmetric matrix [99]:

$$\boldsymbol{\Omega}(\boldsymbol{\omega}) = \begin{bmatrix} 0 & -\omega_i & -\omega_j & -\omega_k \\ \omega_i & 0 & \omega_k & -\omega_j \\ \omega_j & -\omega_k & 0 & \omega_i \\ \omega_k & \omega_j & -\omega_i & 0 \end{bmatrix}. \tag{7.26}$$

The system's kinematic update is then given by equation (7.27):

$$\dot{\boldsymbol{q}} = \frac{1}{2}\boldsymbol{\Omega}(\boldsymbol{\omega})\boldsymbol{q}; \tag{7.27}$$

7.6.3 Control Architecture

To implement the controller digitally, the continuous-time dynamics and kinematics given in equations (7.24), (7.27) are discretised under a zero-order hold assumption on the actuator torque with sampling interval T_s. The state vector $\boldsymbol{x}_k = \boldsymbol{x}(kT_s)$ and control input vector $\boldsymbol{u}_k = \boldsymbol{u}(kT_s)$ are constructed from quaternion attitudes, angular velocity components, and actuator torques, respectively, as:

$$\boldsymbol{x}_k = \begin{bmatrix} \boldsymbol{q}_k \\ \boldsymbol{\omega}_k \end{bmatrix} \in \mathbb{R}^7 \quad \text{and} \quad \boldsymbol{u}_k = \boldsymbol{\tau}_{a,k} \tag{7.28}$$

Hence, the nonlinear discrete-time state dynamics become:

$$\boldsymbol{x}_{k+1} = f(\boldsymbol{x}_k, \boldsymbol{u}_k) = \begin{bmatrix} \boldsymbol{q}_k + \frac{1}{2}\, T_s\, \boldsymbol{\Omega}(\boldsymbol{\omega}_k)\, \boldsymbol{q}_k \\ \boldsymbol{\omega}_k + T_s\, \boldsymbol{J}^{-1}\Big(-\boldsymbol{\omega}_k \times (\boldsymbol{J}\, \boldsymbol{\omega}_k) + \boldsymbol{\tau}_{a,k} + \boldsymbol{\tau}_{d,k} \Big) \end{bmatrix}; \quad f : \mathbb{R}^7 \times \mathbb{R}^3 \to \mathbb{R}^7 \tag{7.29}$$

$$\boldsymbol{y}_k = C_d\, \boldsymbol{x}_k; \quad C_d = \begin{bmatrix} I_4 & \mathbf{0}_{4\times 3} \\ \mathbf{0}_{3\times 4} & \mathbf{0}_{3\times 3} \end{bmatrix} \in \mathbb{R}^{7\times 7} \tag{7.30}$$

Note that angular velocity is only used to internally update the quaternion state, and does not appear in the output $\boldsymbol{y}_k$. Given the nonlinearity in (7.29), the system must be linearised online for implementation within the MPC framework. With a sample time selected as $T_s = 0.05\,\mathrm{s}$[9], at step k, this is computed as:

$$\boldsymbol{x}_{k+1} \approx A_k\, \boldsymbol{x}_k + B_k\, \boldsymbol{u}_k + \hat{\boldsymbol{d}}_k, \tag{7.31}$$

where $A_k = \partial f/\partial \boldsymbol{x}\big|_{(\hat{x}_k, \hat{u}_{k-1})}$, $B_k = \partial f/\partial \boldsymbol{u}\big|_{(\hat{x}_k, \hat{u}_{k-1})}$. This local, linear, time-varying approximation is updated at each sampling instant to maintain operability. The MPC controller relies on the discrete-time Kalman filter disturbance estimate $\hat{\boldsymbol{d}}_k$ and state estimate $\hat{\boldsymbol{x}}_k$ for this update. At each step, the matrices A_k and B_k are therefore:

$$A_k = \begin{bmatrix} I_4 + \frac{1}{2}\, T_s\, \Omega(\boldsymbol{\omega}) & \frac{1}{2}\, T_s\, [\, \Omega_1\, \boldsymbol{q},\ \Omega_2\, \boldsymbol{q},\ \Omega_3\, \boldsymbol{q}\,] \\ \mathbf{0}_{3\times 4} & I_3 - T_s\, J^{-1}\big([J\, \boldsymbol{\omega}]_\times + [\boldsymbol{\omega}]_\times\, J \big) \end{bmatrix}\Bigg|_{(\hat{\boldsymbol{x}}_k,\ \hat{\boldsymbol{u}}_{k-1})} \qquad B_k = \begin{bmatrix} \mathbf{0}_{4\times 3} \\ T_s\, J^{-1} \end{bmatrix}\Bigg|_{(\hat{\boldsymbol{x}}_k,\ \hat{\boldsymbol{u}}_{k-1})}$$

where $[v]_\times = \begin{bmatrix} 0 & -v_3 & v_2 \\ v_3 & 0 & -v_1 \\ -v_2 & v_1 & 0 \end{bmatrix}$ is the skew-symmetric cross product matrix, and $\Omega_j = \frac{\partial \Omega(\omega)}{\partial \omega_j}$.

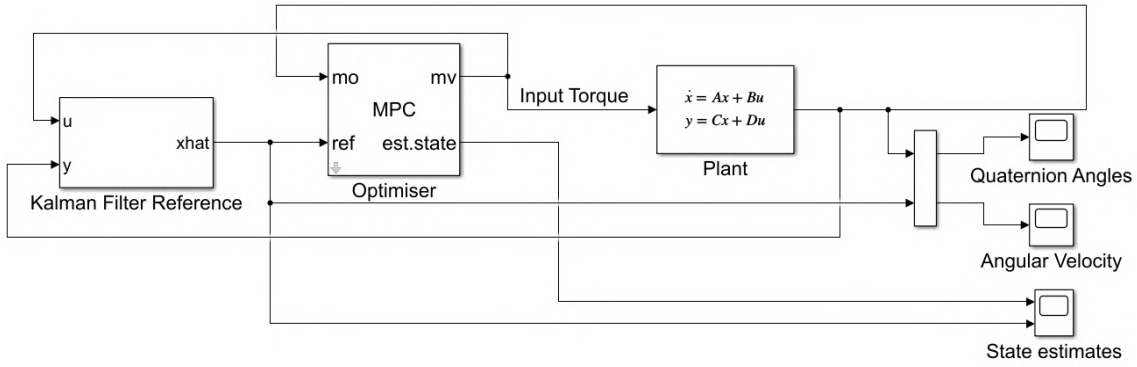

Figure 7.12: SIMULINK implementation of the Model Predictive Control controller.

7.6.4 MPC Problem Formulation

Model Predictive Control optimises future control actions by solving a finite-horizon Constrained Quadratic Programming problem (CQP). Figure 7.12 shows the `SIMULINK` implementation of the controller, which makes use of the `Model Predictive Control Toolbox`. At step k, the optimiser minimises the cost function $\boldsymbol{J}(\cdot)$ online:

$$\begin{aligned}\min_{\{\boldsymbol{u}_{k|i}\}} \boldsymbol{J}(\boldsymbol{u}_{k|i}) =& \|\boldsymbol{x}_{k|N} - \overline{\boldsymbol{x}}\|_P^2 + \sum_{i=0}^{N-1} \left(\|\boldsymbol{x}_{k|i} - \overline{\boldsymbol{x}}\|_Q^2 + \|\boldsymbol{u}_{k|i} - \overline{\boldsymbol{u}}\|_R^2\right) \\ \text{s.t.} \quad & \boldsymbol{x}_{k|i+1} = A_k\, \boldsymbol{x}_{k|i} + B_k\, \boldsymbol{u}_{k|i} + \hat{\boldsymbol{d}}_k, \\ & |\boldsymbol{u}_{k|i}| \leq \boldsymbol{u}_{\max}, \\ & |\boldsymbol{u}_{k|i} - \boldsymbol{u}_{k|i-1}| \leq \boldsymbol{\rho}_{\max}, \\ & \boldsymbol{x}_{k|0} = \hat{\boldsymbol{x}}_k, \quad \boldsymbol{u}_{k|-1} = \boldsymbol{u}^*_{k-1}.\end{aligned} \tag{7.32}$$

Here, $Q, R, P \succeq 0$ are the weighting matrices penalising tracking error, actuator effort, and terminal error, respectively. The first constraint ensures $\boldsymbol{J}(\cdot)$ is a function of $\boldsymbol{u}_{k|i}$ only. The remaining constraints enforce actuator amplitude $\boldsymbol{u}_{\max}$ and slew-rate $\boldsymbol{\rho}_{\max}$ limits, dictated by the physical limits of the reaction wheels: $\boldsymbol{u}_{\max} = 10\text{mN m}$, $\boldsymbol{\rho}_{\max} = 1\text{mN m s}^{-1}$ [43]. The last line represents initialisation of the state using Kalman Filter estimate $\hat{\boldsymbol{x}}_k$, and actuation via the first entry in the control sequence $\boldsymbol{u}^*_{k-1}$. Input and output horizons are given by N_m and N_p, respectively. A visual explanation of the MPC controller's algorithm is given in Figure 7.13.

7.6.5 Proposed Embedded Implementation

It can be shown [100] via elimination of state variables that the CQP can be reduced to:

$$\min_{\boldsymbol{u}} \ \tfrac{1}{2}\, \boldsymbol{u}^\mathsf{T} H\, \boldsymbol{u} + g^\mathsf{T}\, \boldsymbol{u} \quad \text{s.t. } \boldsymbol{u} \in \mathcal{U}, \tag{7.33}$$

with Hessian H and gradient term g dependent on the current state and disturbance. The above MPC architecture is proposed to be implemented using the Fast Gradient Method (FGM), an efficient first-order solver for

[9] The choice of sampling time $T_s = 0.05\,\text{s}$ (20 Hz) balances control performance with computational constraints: sufficiently low so the bandwidth is enough to capture the CubeSat's attitude dynamics, while at the same time allowing the full MPC optimisation to execute within the 50 ms sampling period.

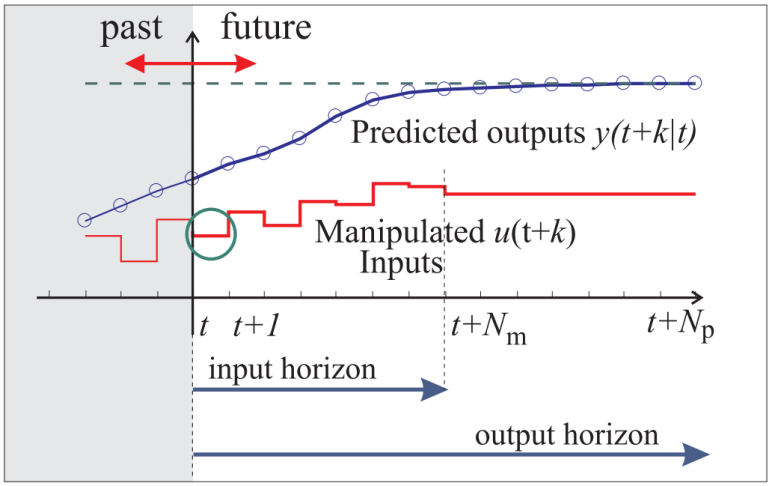

Figure 7.13: Evolution of predicted outputs $\boldsymbol{y}_{k|i-1}$ (blue line) as effect of manipulated control inputs $\boldsymbol{u}_{k|i-1}$ (red line). The controller minimises actuator effort and tracking error as quadratic cost function $\boldsymbol{J}(\cdot)$ over input horizon N_m and output horizon N_p. Image and nomenclature from C21 Lecture Notes by Cannon (2023).

CQPs with simple constraints [101]. The FGM is particularly well-suited for embedded MPC applications due to its computational simplicity, deterministic iteration bounds, and ability to handle box constraints efficiently. Unlike interior point methods, which require complex matrix factorisations and have unpredictable iteration counts, FGM provides a priori guarantees on the maximum number of iterations needed to achieve a specified accuracy. The FGM iterations combine gradient steps with momentum:

$$v^{(i)} = (I - \alpha H)v^{(i-1)} - \alpha g, \tag{7.34}$$

$$u^{(i)} = \Pi_{\mathcal{U}}(v^{(i)}), \tag{7.35}$$

where $\Pi_{\mathcal{U}}$ represents the Euclidean projection onto the convex control constraints. Hessian conditioning is managed through terminal cost design [101]:

$$\begin{aligned} P &= A_d^\mathsf{T} P A_d - A_d^\mathsf{T} P B_d (B_d^\mathsf{T} P B_d + R)^{-1} B_d^\mathsf{T} P A_d + Q, \\ \kappa(H) &\leq \gamma, \end{aligned} \tag{7.36}$$

where γ bounds the condition number $\kappa(H) = \lambda_{\max}(H)/\lambda_{\min}(H)$ to ensure convergence within sampling time T_s. The pseudocode for the proposed FGM implementation is provided in Algorithm 1.

Algorithm 1 Fast Gradient Method for CubeSat MPC Quadratic Program

Input: Previous control input u_{k-1}, Hessian H, gradient g, iteration count M
Output: Control update u_k

$\alpha \leftarrow 1/\lambda_{\max}(H)$ {Step size inverse to dominant eigenvalue}
$\beta \leftarrow (\sqrt{\lambda_{\max}(H)} - \sqrt{\lambda_{\min}(H)})/(\sqrt{\lambda_{\max}(H)} + \sqrt{\lambda_{\min}(H)})$ {Acceleration step}
Initialise $v_0 \leftarrow u_{k-1}$, $p_0 \leftarrow v_0$
for $i = 0$ **to** $M - 1$ **do**
  $z_{i+1} \leftarrow v_i - \alpha(Hv_i + g)$ {Gradient descent step}
  $p_{i+1} \leftarrow \Pi_{\mathcal{U}}(z_{i+1})$ {Projection to feasible set}
  $v_{i+1} \leftarrow p_{i+1} + \beta(p_{i+1} - p_i)$ {Momentum update for acceleration}
end for
$u_k \leftarrow p_M$ {Return final projected solution}

On line 1, we set $\alpha = 1/\lambda_{\max}(H)$ as the gradient descent step size. Line 2 computes $\beta = (\sqrt{\lambda_{\max}(H)} - \sqrt{\lambda_{\min}(H)})/(\sqrt{\lambda_{\max}(H)}+\sqrt{\lambda_{\min}(H)})$, which balances aggressive acceleration (when the Hessian is well-conditioned) against stability (when it is ill-conditioned). Line 3 starts both v_0 and p_0 at the last control setting u_{k-1}. Inside the loop (lines 4–8), line 5 takes a simple gradient step $z_{i+1} = v_i - \alpha\,(H\,v_i + g)$, to pull the iterate towards the global minimum (which is guaranteed to be unique since the quadratic function is convex). Line 6 then "clips" z_{i+1} back into our allowed range $\mathcal{U}$, making sure we never request more torque or faster changes than the hardware can handle. Line 7 introduces momentum via $v_{i+1} = p_{i+1} + \beta(p_{i+1} - p_i)$, which carries over inertia from previous updates (this is a typical feature of most modern gradient descent methods). After M iterations, line 9 returns the optimal and constraint-bound control input, $u_k^* = p_M$, which represents the torque vector applied to the reaction wheels.

This quaternion-based MPC scheme delivers robust, constraint-aware attitude control under tight onboard resource constraints. The proposed FGM algorithm can be implemented on a TI C2000 dual-core microcontroller (or similar). Future testing is required to ensure that the MPC control iteration can run within one clock cycle of the board adopted in the mission-ready design.

7.7 Optical Spectroscopy Hardware - Fizza Naqvi

7.7.1 Spectrometer

During re-entry, the spectrometer records the emission spectra of species undergoing transitions between energy states in the shock layer. The spectrometer used for this experiment is the AvaSpec-Mini2048CL [45], shown in Figure 7.14(a), a compact ($95 \times 68 \times 20$ mm) spectrometer with a spectral resolution of 2 nm. This spectrometer operates within a temperature range of 0–55°C, so it will be placed inside the CubeSat, beneath the ablative materials, to ensure that its temperature remains within operational limits.

The detectable wavelength range of the AvaSpec-Mini2048CL is 200–1100 nm, making it suitable for capturing emissions from various material classes. Metals typically emit in the UV range (200–400 nm), silica-based materials emit in the UV and visible range (200–500 nm), and carbon-based composites emit emissions in the UV and visible regions, with some near-infrared (IR) signatures. Although some carbon-based materials may have emissions extending beyond 1100 nm, the majority fall within the spectrometer's detection range, ensuring useful data collection for the study.

7.7.2 Fibre Optic Cable

To guide the light from the shock layer to the spectrometer, a multi-furcated fibre optic cable, the FC6-UVIR400-2 [102] from Avantes, shown in Figure 7.14(b), was selected. This cable features six 400µm fibres and has a total length of 2 meters. The fibres are evenly split from a central point, significantly increasing light throughput compared to single-fibre setups. This configuration allows simultaneous collection of light from multiple locations around the shock layer, enhancing spatial coverage. The selection of the 400µm core

diameter provides an effective compromise between light collection efficiency and spectral resolution, which is beneficial in the dynamic and high-temperature environment of hypersonic re-entry.

The spectrometer, positioned within the CubeSat, collects light from the shock layer through this optical fibre, which is aligned with a small hole in the outer materials layer. The fibre is set back 5mm from the edge of the hole to shield it from excessive heat exposure, reducing degradation and prolonging its operational lifespan. This design ensures that the spectrometer can reliably capture emission data while minimising thermal damage, which is essential for maintaining data continuity throughout re-entry.

7.7.3 Cosine Corrector

To enhance the accuracy of the spectral intensity measurements, a cosine corrector is used. Without this component, optical fibres may preferentially collect light from certain angles, leading to biased intensity measurements. The cosine corrector ensures that the collected light intensity follows a Lambertian response [103], meaning it is proportional to the cosine of the incident angle. This improves radiometric accuracy, enabling more reliable spectral data collection from the re-entry plasma, which emits radiation in multiple directions.

The selected cosine corrector is the CC-UV/VIS/NIR-8MM from Avantes [47]. This corrector is compatible with the FC6-UVIR400-2 fibre optic cable and offers a 180° field of view (FOV), which is well-suited for collecting light over a broad area. The broader FOV complements the multiple fibres in the FC6-UVIR400-2 cable, ensuring that light is collected from multiple points around the shock layer during re-entry. This configuration will optimise the accuracy of the measurements and ensure that the spectrometer captures the full range of radiation emitted during the re-entry process.

((a)) Spectrometer ((b)) Multi-Furcated Fibre Optic ((c)) Cosine Corrector

Figure 7.14: Main 3 components of the spectroscopy system.

7.8 Instrumentation and Data Analysis - Fizza Naqvi

7.8.1 Overview

This section provides an analysis of the atmospheric composition during the re-entry of a CubeSat, focusing on the processes of emission spectroscopy, calibration, and post-mission data analysis. The core objective is to quantify the concentrations of various species in the region surrounding the CubeSat as it interacts with the atmosphere during its re-entry phase. Spectroscopic data is crucial for identifying the species present in the shock layer, as well as understanding their emission characteristics and distribution.

While detailed studies on CubeSat re-entry and its environmental impact are limited, this analysis proposes a framework for quantifying ablation products during satellite demise. The assumptions made in this analysis (detailed in section 7.8.4), while simplifying the complex nature of re-entry dynamics, are necessary for the feasibility of the study. While the exact outcomes cannot be determined due to uncertainties arising from the assumptions made, the approach still offers valuable insights into species concentrations and their potential environmental impact. This can serve as a foundation for further research, particularly in understanding and quantifying the environmental consequences of satellite demise in the upper atmosphere.

7.8.2 Pre-flight calibration

As light travels through a spectrometer, the optical properties of the components inside affect the raw data signal recieved by the spectrometer. Figure 7.15 displays the difference between the spectrum found in literature and the actual, distorted spectrometer output for a Tungsten halogen light bulb [104]. Based on the raw data, the intensity of the signal at 1000nm appears to be lower than the signal at 620nm. However, in reality, the intensity is about twice as high. Therefore, before launch, the spectrometer must be calibrated to correct for variations in instrument response, ensuring accurate in-flight measurements that may be affected by optical depth effects and local plasma conditions.

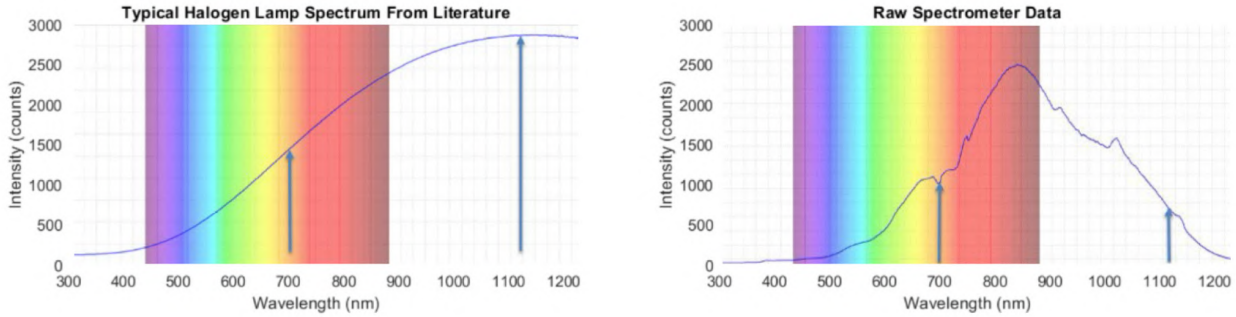

Figure 7.15: Left image shows the typical halogen spectrum. Right shows the raw data provided by the spectrometer [104].

Calibration is performed using an integrating sphere and standard calibration lamps [105] that emit light at well-characterised intensities and wavelengths. The spectrometer records light from a known calibration lamp under controlled conditions to set baseline spectral intensities and gain factors. The actual spectral intensity of the calibration lamp at each wavelength is known from the manufacturers data or reference bases. The measured intensity is then used to compute a calibration factor using equation (7.37), which is applied to all subsequent in-flight data to ensure that the measured intensities accurately reflect the true emission intensities of species within the shock layer.

$$I_{ij} = I_{\text{corrected}}(\lambda) = c(\lambda) \cdot I_{\text{measured}}(\lambda) \tag{7.37}$$

7.8.3 Post-mission data analysis

The spectrometer records the emission spectra of species undergoing transitions between energy states in the shock layer during re-entry. Measurements will be limited to the shock layer, where particles are heated enough to excite species and generate measurable radiation. The optical fibre's acceptance angle defines a cone-shaped measurement region, shown in Figure 7.16, limiting the spatial resolution but ensuring that light from a specific region of the shock layer is effectively captured. Key emission lines corresponding to species of interest from the ablation products can be identified using spectral databases like the NIST Atomic Spectra Database [106]. Each emission line's wavelength is measured and can be used to identify the specific energy transitions corresponding to the measured emission lines. The NIST Atomic Spectra Database can be used to find the energy levels E_j and E_i to calculate the difference between the excited and ground states for each species using equation (7.38).

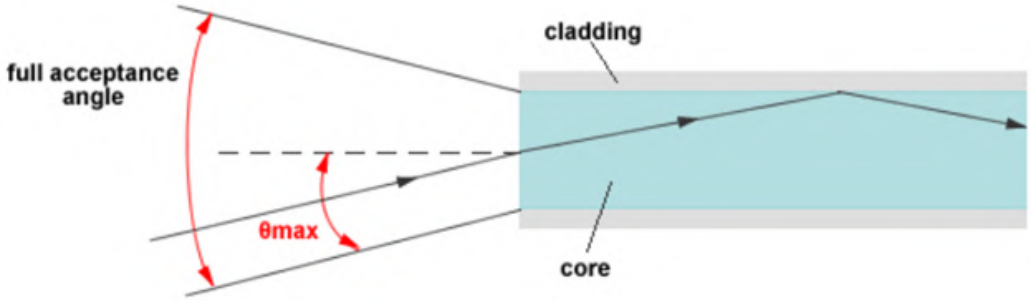

Figure 7.16: Cone-shaped measurement region for the optical fibre [107].

$$E_j - E_i = \frac{hc}{\lambda} \tag{7.38}$$

Where h is Planck's constant, c is the speed of light, and λ is the wavelength of the emission line.

Temperature variations during re-entry influence the population of species in excited states. A temperature sensor onboard the CubeSat provides direct measurements of the shock layer temperature. The temperature and particle densities vary between the free stream and the wake region. To account for this, the onboard IMU will track the CubeSat's orientation and position, enabling the distinction between measurements taken in each region.

The relative concentration of species in excited states follows the Boltzmann distribution [108] (equation (7.39)), which describes how the fraction of atoms or molecules in a given energy state depends on temperature. Using this relationship, the population of different energy states can be estimated.

$$\frac{N_i}{N} = \frac{g_i e^{-E_i/k_B T}}{q} \tag{7.39}$$

Where N_i is the population in the i-th energy state, N is the total population, g_i is the degeneracy[10] of the

[10]Degeneracy refers to the number of available quantum states for a given energy level i; this can be found in atomic or molecular databases for the species in question.

i-th energy state, q is the partition function, E_i is the energy of the state, k_B is the Boltzmann constant ($k_B = 1.380649 \times 10^{-23}$ J/K [53]), and T is the temperature at the current altitude.

The raw, measured intensity values need to be multiplied by the calibration factor using equation (7.37) to obtain the absolute intensity values. Equation (7.40) [109] relates the emission intensity at a given wavelength to the population difference between energy levels, using the Einstein coefficient A_{ji} for spontaneous emission. This can be solved simultaneously with a rearrangement of the Boltzmann equation in equation (7.41) to find N_j and N_i. A_{ji}

$$N_j - N_i = \frac{I_{ji}}{A_{ji}} \tag{7.40}$$

$$\frac{N_i}{N_j} = \frac{g_i}{g_j} e^{-(E_i - E_j)/k_B T} \tag{7.41}$$

Determining the total number density allows for an estimate of the overall species abundance in the sampled region. Once numerical values for N_j and N_i have been obtained, equation (7.42) is used to calculate the total number density of particles in all energy states within the cone-shaped volume shown in Figure 7.16. By integrating the estimated number densities across the expected extent of the shock layer, a broader understanding of species distribution during re-entry can be developed.

$$n_{\text{total}} = \sum_i N_i + \sum_j N_j \tag{7.42}$$

Species concentrations are tracked throughout re-entry by timestamping the emission spectra and correlating the data with altitude data, as detailed in section 7.5. This enables the creation of species concentration profiles, illustrating how the chemical composition of the shock layer evolves with altitude. Variations in species concentrations with altitude can indicate the onset of ablation, as different materials begin to vaporise and emit characteristic spectral lines.

The environmental impact is evaluated by integrating species concentration data over time and converting it to mass using conservation principles. Comparing this with baseline atmospheric models, such as the US Standard Atmosphere Model, highlights deviations due to CubeSat material ablation, offering a foundation for assessing long-term atmospheric effects amid growing small satellite deployments.

7.8.4 Assumptions

Several assumptions are made in this analysis to simplify calculations while maintaining accuracy.

High-speed re-entry can cause a slight shift in emission wavelengths due to the Doppler effect. However, assuming a re-entry velocity of approximately 8 km/s and considering a characteristic emission line for SiO at 250 nm, the resulting Doppler shift is on the order of 10^{-12} m, calculated by equation (7.43). Given that the resolution of the spectrometer detailed in section 7.7.1 is 2nm, this shift is negligible in the context of this study.

Additionally, ablated species are assumed to be distributed around the CubeSat rather than being ejected in a single direction. This leads to a roughly symmetric emission pattern, where some emission sources experience a small positive Doppler shift and others a small negative shift, effectively cancelling out any overall effect.

$$\Delta\lambda = \lambda_0 \frac{v}{c} \tag{7.43}$$

Furthermore, at an ablation altitude of approximately 80 km, the flow field is rarefied, with a high Knudsen number (ratio of mean free path to characteristic length) indicating minimal molecular interactions. This means that in this regime ablation products are expected to expand isotropically rather than forming a strongly directional plume, as would occur at lower altitudes where continuum flow dominates [110]. This justifies the experimental design choice of placing a fibre-optic sensor on each face of the CubeSat, enabling omnidirectional detection of spectral emissions. By covering all orientations, the setup ensures that material dispersal can be accurately characterised regardless of direction, which is crucial in a regime where ablated particles spread spherically due to the rarefied nature of the atmosphere.

The plasma in the shock layer is considered to be optically thin, meaning that the emitted radiation escapes without significant reabsorption or scattering. This allows direct use of Einstein coefficients to relate emission intensity to population differences in equation (7.40).

The assumption of a homogeneous shock layer in temperature, density, and composition within the measurement cone is made for this experiment. This assumption is justified as long as the shock layer is thin relative to the spatial resolution of the spectrometer, which is suitable for the scale of the CubeSat's re-entry dynamics. The spectrometer's resolution is sufficient to smooth out any variations in the shock layer, allowing for this simplification in the analysis.

8 Aerothermal Environment

8.1 Introduction - Claudio Vestini

The AeroThermal team's overarching goal is to ensure CubeSat's thermal environment allows for the correct functioning of all electronics, telemetry, and control systems throughout the mission's phases, and to reliably guarantee the complete demise of the satellite. The focus of this section of the report is the study of thermal environments to iteratively design CubeSats for testing commercial materials, with an emphasis on high-fidelity computational simulations of the heat fluxes and temperature distributions around the CubeSat throughout the mission. The analysis was simplified by separating simulations into two mission sections: the orbital and the re-entry phase. The stark differences in aerothermal environment dictate this decision: in orbit, the dominant thermal loading is that of incoming radiation from the Sun, whereas during re-entry, the thermal environment is dominated by the dissipation of the kinetic energy of the hypersonic air flow around the CubeSat.

The team developed a numerical solver for the orbital phase that predicts the transient temperature evolution across the CubeSat's walls, discussed in Section 8.2. In Section 8.3, re-entry aerothermal loading was estimated by mapping the trajectory conditions onto empirical hypersonic re-entry curves. Finally, in Section 8.4, the conditions of highest stresses were directly simulated through commercial software codes.

8.2 Orbital Phase - Claudio Vestini

8.2.1 Heat Equation and Geometry

The reference coordinate system adopted for this analysis is shown in Figure 8.1.

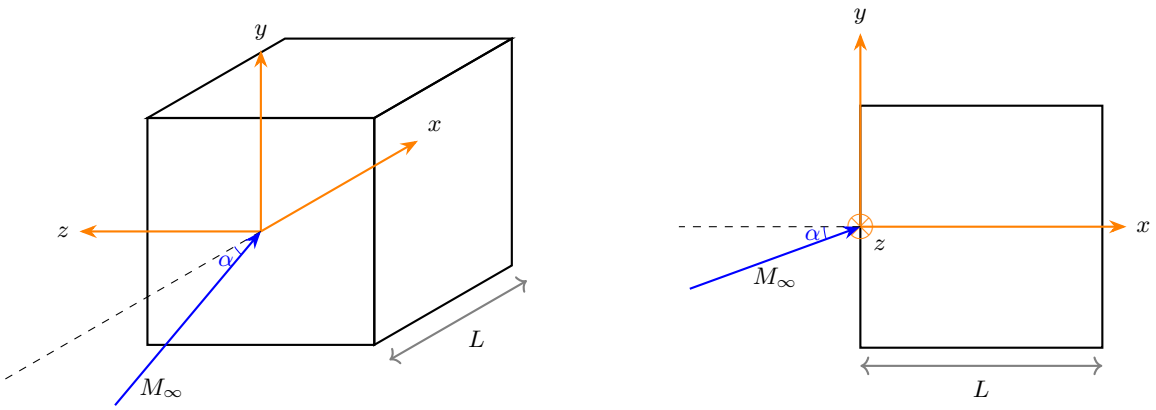

Figure 8.1: 3D (left) coordinate system for the CubeSat, where $L = 0.2$ m. A slice through the centre of the cube reveals the 2D (x, y) coordinate system (right), where z is the depth variable into the walls. $M_\infty := \frac{U_\infty}{a_\infty}$, with $a = \sqrt{\gamma R T_\infty}$ $[\mathrm{m\,s^{-1}}]$ (sonic speed), is the free-stream Mach number, and α is the in-xy-plane incidence.

The three-dimensional, convection-less, unsteady heat equation with internal heat generation is given by:

$$\frac{1}{\alpha}\frac{\partial T}{\partial t} = \nabla^2 T + \frac{G}{k} \tag{8.1}$$

where:

- $T(\mathbf{x}, t)$ is the scalar temperature field over the CubeSat's walls, with units [K].
- k is the material's thermal conductivity, with units [$\mathrm{W\,m^{-1}}$].
- α is the thermal diffusivity, given by $\alpha = \frac{k}{\rho c_p}$, where ρ is material density and c_p is specific heat capacity, and has units [$\mathrm{m^2\,s^{-1}}$].
- $G(\mathbf{x}, t)$ is the volumetric rate of internal heat generation (from electronics) within the walls' enclosed volume, with units [$\mathrm{W\,m^{-3}}$]. This value was assumed to be uniform and constant, and was estimated according to $G = \eta \times P_{\text{tot}}/L^3$, where P_{tot} is the peak total power consumption of electronics and η is the percentage of power dissipated as heat[11].

This equation was used as the system's Governing Equation (GE) for the numerical solver.

8.2.2 Flight Configuration and Assumptions

A sketch of relevant aerothermal factors during the orbital phase of our mission is shown in Figure 8.2.

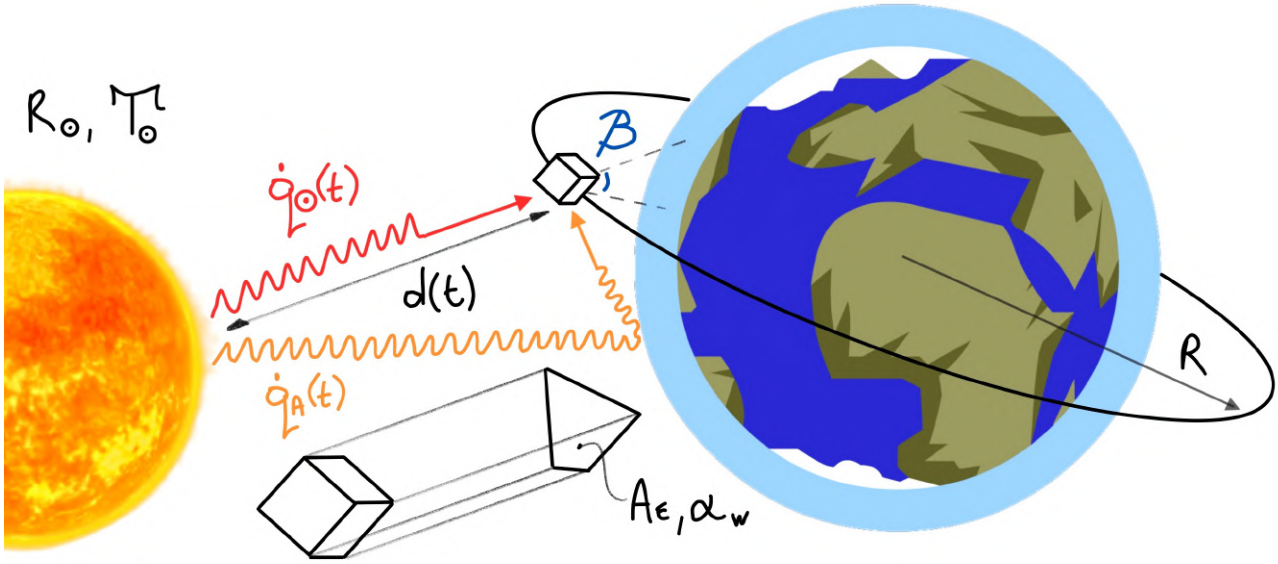

Figure 8.2: A sketch of CubeSat in orbit around the earth, with incoming direct radiation intensity $\dot{q}_\odot(t)$ and albedo radiation intensity $\dot{q}_A(t)$ [$\mathrm{W\,m^{-2}}$] (at the CubeSat's surface). $R_\odot$ and $T_\odot$ are the sun's radius [m] and surface temperature [K], respectively, whereas R is the orbital radius measured from the centre of the earth; that is: $R = R_e + R_{orbit}$. The sun-to-CubeSat distance is $d(t)$ [m], and β is the angle between the satellite's orbital plane around Earth and the geocentric position of the Sun. A_E is the effective thermal area of the CubeSat (geometric property), and α_w is the absorptivity of the outer walls (material property).

To solve for the wall transient temperature distribution $T(x, y, z = 0, t)$, the following assumptions are made:

- The orbital period can be divided into two sections: when the CubeSat is wetted by incoming sunlight, and when it is behind Earth's shadow. These are referred to as the "ON" and "OFF" periods, respectively. The illumination ratio is the fraction of the total period making up the "OFF" period: $f_e := \tau_{shadow}/\tau_{orbit}$.
- The orbital period τ_{orbit} is much greater than the time taken for the CubeSat to transition behind Earth's

[11] The value of η typically ranges from 0.7 to 0.9, and it was assumed to be 0.8 for this study.

shadow. This is justified as the dimensions of the CubeSat are negligible compared to those of the Earth, and the CubeSat travels at high velocity.

- The surface temperature of the sun is constant[12] at $T_\odot = 5772$ K, and its radius is $R_\odot = 6.9634 \times 10^8$ m.
- The distance d can be assumed to be constant. This is because $d(t) = d_0 + \delta d(t)$, with $d_o = 1\text{AU}$[13] and $\max \delta d(t) = (R_e + R_{orbit}) / \cos\beta \ll d_0$ (the maximum variation in distance δd_{max} is <0.001% of d_0).
- The effective thermal area A_E of the CubeSat is constant. It can be shown [111, 112] that, for any convex polyhedron illuminated by an infinitely-far-away light source, the average area of the shadow it casts on a two-dimensional plane is one-quarter of its surface area. Hence, for our CubeSat: $A_E = \frac{1}{4}(A_w)$.
- The effects of non-radiative heating factors (such as kinetic theory particle interactions) are negligible[14].

With the above assumptions, the incoming radiation density $\dot{q}_\odot(t)$ is found to be a square wave with "OFF" period equal to $f_e \tau_{orbit}$ and "ON" period $(1 - f_e)\,\tau_{orbit}$. The illumination ratio f_e is calculated [114] using:

$$f_e = \frac{1}{\pi} \cos^{-1} \left\{ \frac{\sqrt{R_{orbit}^2 + 2R_e R_{orbit}}}{(R_e + R_{orbit}) \cos\beta} \right\} \tag{8.2}$$

where $R_{orbit} = 400$ km is the orbital altitude and $R_e = 6371$ km is Earth's radius. Letting ϕ represent the azimuthal location of the CubeSat (ϕ spans $[0, 2\pi]$ for one orbit), the angles at which eclipse begins and ends are computed as $\phi_{e12} \in \{\pi(1 \pm f_e)\}$. Given the choice of trajectory discussed in Section 4, β can be assumed to be low for our orbit: $\cos\beta \approx 1 \implies f_e = 0.3898 \simeq 40\%$. Summertime conditions were selected for a worst-case estimate. To perform the heat balance, recall the Stefan-Boltzmann law:

$$\dot{q}_r = \epsilon_r \sigma T^4 \tag{8.3}$$

where ϵ_r is the emissivity of the surface and σ is the Stefan-Boltzmann constant, with a value of 5.670×10^{-8} [$\text{W m}^{-2}\,\text{K}^{-4}$]. Emissivity can range from 0 to 1, where $\epsilon_r = 1$ corresponds to a perfect black body (assumed for the sun). By Kirchhoff's law [115], emissivity ϵ_r and absorptivity α_r are equal.

The heat intensity at the satellite will depend on the view factor between the CubeSat and the Sun, given by $\frac{R_\odot}{d} F_\odot$, where $F_\odot$ is unity during the "ON" period and zero during the "OFF" period. Hence, the peak incident heat intensity at the CubeSat's surface is calculated as $\dot{q}_\odot = \alpha_w \left(\frac{R_\odot}{d}\right)^2 \left(\epsilon_\odot \sigma T_\odot^4\right) \simeq 1363.6\ \text{W m}^{-2}$ (with black body assumption $\epsilon_\odot = 1$). The evolution of radiation intensity is plotted in Figure 8.3 (solid red line). The albedo (reflected) radiation intensity $\dot{q}_A(t)$ is dependent on the direct intensity, with view factor equal to $F_a = F_\odot \cos(\beta) \left(\frac{1+\cos\phi}{2}\right)^2 \left[1 - \left(\frac{\phi}{\phi_{e1}}\right)^2\right]$ and peak value typically ranging from one to two fifths of the

[12] The Sun is considered a very stable star in terms of its energy output. Its total luminosity (total solar irradiance) varies by only about 0.1% throughout its 11-year solar activity cycle, which justifies the assumption.

[13] 1 Astronomical Unit (AU) = $1.495978707 \times 10^{11}$ m

[14] In practice, thermal loading of an orbiting satellite from sources other than the sun can represent 15 % of the total, with trapped particles in Earth's magnetosphere being the dominant contributor [113]. However, a comprehensive analysis to include these location-dependent effects was deemed beyond the scope of this design exercise. Earth's infrared contributions were also assumed to be negligible.

direct intensity. For a LEO orbit at 400 km, $\dot{q}_A$ was estimated to peak at a value of 29.8 % the value of $\dot{q}_\odot$, which corresponds to 407 $\mathrm{W\,m^{-2}}$, and its predicted distribution is shown in Figure 8.3 (dashed orange line).

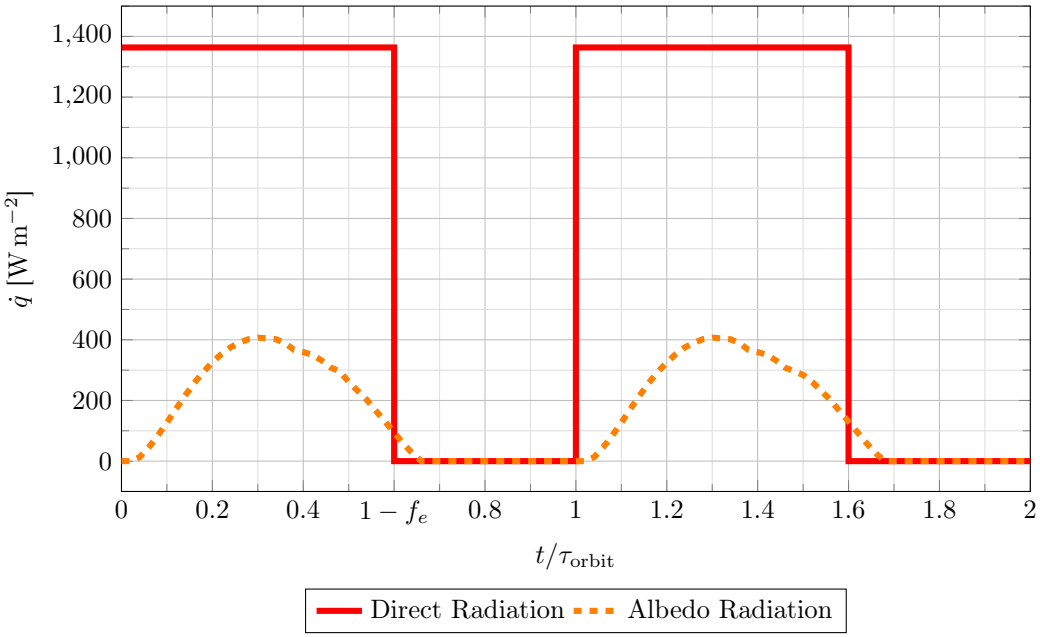

Figure 8.3: Radiation intensity profiles over dimensionless time. $t/\tau_{orbit} \in [0, 1 - f_e]$ corresponds to direct illumination ("ON" period), and $[1 - f_e, 1]$ represents the eclipse ("OFF" period). The orbital period is $\tau_{orbit} \simeq$ 92.5 min (computed for a circular orbit at an altitude of 400 km).

8.2.3 FTCS Solver

The temperature evolution through the walls of the CubeSat during its orbital phase is determined by coupling the material response of the heat shield with the known heat fluxes (taken as inputs) through a numerically solved transient heat conduction problem. A fundamental assumption made is that the internal and external surface temperature distributions are uniform. This simplifies the problem to one dimension. In reality, the temperature distribution will vary according to the transient orientation of the CubeSat in space. The above assumption is justified in this instance by consideration of the fact that the CubeSat undergoes induced tumbling, which will smooth out any localised heat flux concentrations.

The heat conduction problem is formulated and solved using a numerical Finite Difference[15] scheme, namely Forward-Time Central-Space (FTCS). Numerical schemes approximate the field variable of interest $\phi(z, t)$ as $\phi(z_l, t_n) \simeq \phi_l^n$ (where l and n represent the spatial and temporal indices, respectively) by partitioning the domains as a *stencil* of discrete locations. Finite Difference schemes are typically preferred in heat transfer problems due to the simplicity of computing the state update. For these, a choice of m neighbouring points considered to approximate the differential operators gives rise to an $(m-1)^{th}$ order scheme, which can be inferred from a direct comparison with the solution's Taylor series expansion [116]. FTCS is a suitable choice for the heat conduction problem due to its modularity, efficiency, and explicit nature. It has second-order accuracy in space and first-order accuracy in time. The heat shield is modelled as a one-dimensional multilayered domain representing an ablative sandwich structure composed of distinct thermal protection layers, each with known

[15] The three main categories of discretisation schemes are Finite Volume, Finite Difference, and Finite Element. Further differences between schemes within the same general category lie in the choice of the interpolating functions used.

thermal properties, and is shown in Figure 8.4. This is discretised spatially into M total nodes across L material layers, each with thermal conductivity k_j, specific heat $c_{p,j}$, density ρ_j, and thickness ΔL_j, according to equation (8.4), with domain bounds (z_F, t_F), and domain step sizes $(\Delta z, \Delta t) = (z_F/(M-1), t_F/(N-1))$:

$$(z_l, t_n) = (l\Delta z, n\Delta t); \quad (l, n) \in [0, (M-1)] \times [0, (N-1)] \in \mathbb{Z} \tag{8.4}$$

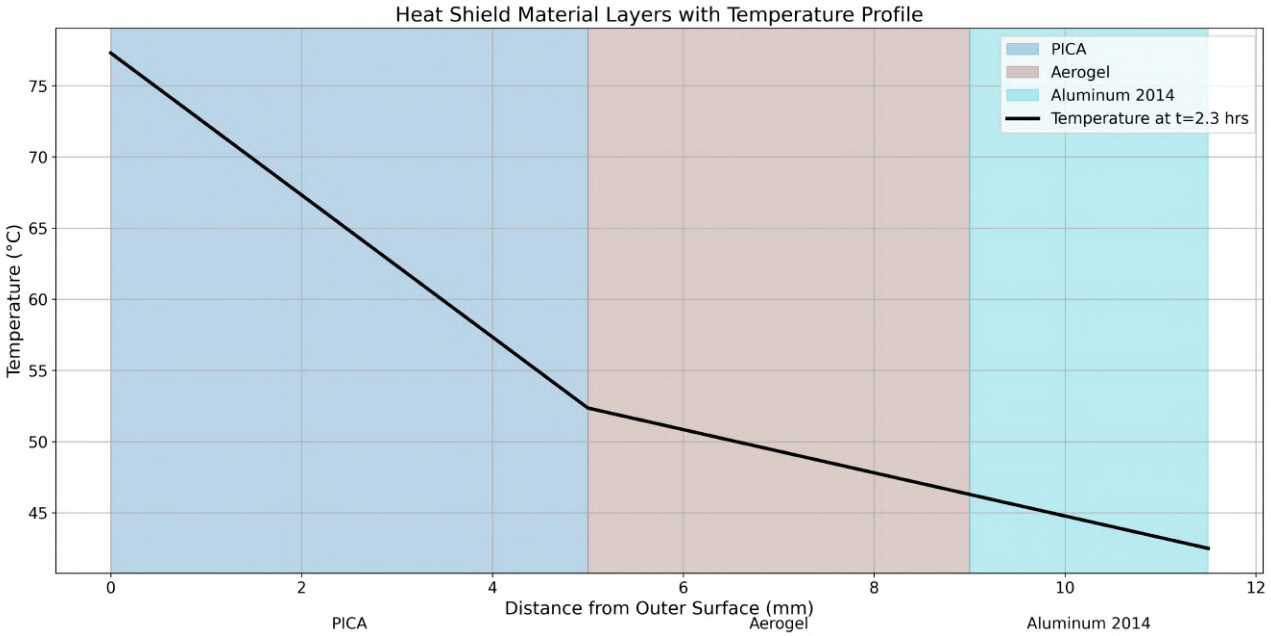

Figure 8.4: Schematic representation of the heatshield layers described in Table 8.1, each of which is itself discretised into several nodes (z_l, t_n), for a total of 1150 spatial nodes. Temperature at 2.3 hours is plotted.

An important parameter to describe discretisation resolutions lies in the dimensionless Courant number $C := c\frac{\Delta t}{\Delta z}$, which represents the ratio between the distance travelled by a disturbance over a time step and the size of the grid spacing (c is the characteristic speed, equal to thermal diffusivity α for this thermal analysis). For the heatshield simulation, the variable of interest ϕ is scalar temperature T, and the governing equation (GE) is the heat equation (8.1) given in Section 8.2.1. Discretising the GE using the FTCS scheme yields:

$$\frac{T_l^{n+1} - T_l^n}{\Delta t} = \frac{1}{\rho_l \, c_{p,l} \, \Delta z_l} \left[k_{l+\frac{1}{2}} \frac{T_{l+1}^n - T_l^n}{\Delta z_{l+\frac{1}{2}}} - k_{l-\frac{1}{2}} \frac{T_l^n - T_{l-1}^n}{\Delta z_{l-\frac{1}{2}}} \right] \tag{8.5}$$

To ensure conditional stability of the explicit scheme, the Courant number must satisfy the criterion (8.6) for the most diffusive layer (which is typically the innermost structural layer within the ablative structure) [116]:

$$\max_j C_j \;\leq\; \frac{\Delta z_j}{2}\,, \quad C_j = \alpha_j \frac{\Delta t_j}{\Delta z_j}\,, \quad \alpha_j = \frac{k_j}{\rho_j \, c_{p,j}} \tag{8.6}$$

Re-arranging equation (8.5), for interior nodes $l = 1, \ldots, M-1$, the multilayer FTCS update of the temperature field T is:

$$T_l^{n+1} \leftarrow T_l^n + \frac{\Delta t}{\rho_l \, c_{p,l} \, \Delta z_l} \left[k_{l+\frac{1}{2}} \frac{T_{l+1}^n - T_l^n}{\Delta z_{l+\frac{1}{2}}} - k_{l-\frac{1}{2}} \frac{T_l^n - T_{l-1}^n}{\Delta z_{l-\frac{1}{2}}} \right] \tag{8.7}$$

8.2.4 Boundary Conditions

At the external surface node $l = 0$, the known inward heat flux from radiation is imposed by:

$$T_0^{n+1} \leftarrow T_0^n + \frac{\Delta t}{\rho_0 c_{p,0} \Delta z_0} \left[k_{\frac{1}{2}} \frac{T_1^n - T_0^n}{\Delta z_{\frac{1}{2}}} + \dot{q}_{\text{net}}(t_n) \right] \tag{8.8}$$

where:

$$\dot{q}_{\text{net}}(t_n) = \dot{q}_{\odot}(t_n) + \dot{q}_A(t_n) - \dot{q}_w(t_n); \quad \dot{q}_w(t_n) = \epsilon_w \sigma (T_0^n)^4$$

Similarly, at the deepest interior node $l = M - 1$, internal heat generation is accounted for by imposing[16]:

$$T_{M-1}^{n+1} \leftarrow T_{M-1}^n + \frac{\Delta t}{\rho_{M-1}\, c_{p,M-1}\, \Delta z_{M-1}} \left[k_{(M-1)-\frac{1}{2}} \frac{T_{M-2}^n - T_{M-1}^n}{\Delta z_{(M-1)-\frac{1}{2}}} + G\, \Delta z_{M-1} \right] \tag{8.9}$$

Note that no ablation effects are considered in the scheme. This is justified as the wall temperatures during this mission phase will not be close to the ablation onset thresholds.

8.2.5 Initial Conditions

To compute an initial estimate for the surface temperature T_w, assume the heat absorbed by the CubeSat equals the heat it radiates away[17]. A simple heat balance yields:

$$\dot{Q}_{\text{in}} = \dot{Q}_{\odot} + \dot{Q}_A \simeq A_E \alpha_w \left(\frac{R_{\odot}}{d} \right)^2 \left(\epsilon_{\odot} \sigma T_{\odot}^4 \right) = \dot{Q}_{\text{out}} = \dot{Q}_w = A_w \epsilon_w \sigma T_w^4$$

Hence, the initial surface temperature will be:

$$T_w = T_{\odot} \sqrt[4]{\epsilon_{\odot} \left(\frac{A_E}{A_w} \right) \left(\frac{\alpha_w}{\epsilon_w} \right)} \sqrt{\frac{R_{\odot}}{d}} \approx \frac{T_{\odot}}{2\sqrt{2}} \sqrt{\frac{R_{\odot}}{d}} \simeq 139.2\,^{\circ}\text{C}$$

An initial internal wall temperature of $T_{in} = 20^{\circ}\text{C}$ is also assumed. This assumption is justified because the conditions immediately after orbit insertion are analogous to those just before launch, and it is assumed that the CubeSat will be thermally insulated by the launch vehicle until insertion. These conditions are then applied as $T_0^0 \leftarrow T_w$ at the outer surface, and $T_{M-1}^0 \leftarrow T_{in}$ at the inner surface, with a simple linear interpolation in between. It is noted that the steady-state temperature evolution over several orbital cycles was found to be independent of initial conditions, whose effect was limited to dictating the longevity of the transient response.

[16] The term $G\,\Delta z_{M-1}$ converts the volumetric heat generation due to dissipation by electronic components within the final layer into an equivalent heat flux [W m^{-2}] acting on node $M - 1$.

[17] This is equivalent to assuming no conduction initially occurs. Albedo radiation is also ignored for this computation.

8.2.6 Results

This scheme was implemented in a `MATLAB` modular codebase[18]. The direct heat conduction problem is solved using the FTCS update (8.7), which imposes boundary conditions (8.8)–(8.9) at each time step.

Results for a typical selection of wall material properties and thicknesses were computed as a test sample[19]. Reference values are given in Table 8.1. Temporal and spatial resolutions were chosen as $\Delta t, \Delta z = (0.1\text{s}, 0.01\text{mm})$; the most diffusive layer (Aluminum) has thermal diffusivity $\alpha_{\text{Al}} = 5.7 \times 10^{-5}\,\text{m}^2\,\text{s}^{-1}$, resulting in a threshold $\Delta t \leq 0.87$ s, thus satisfying criterion (8.6). The emissivity/absorptivity of the outer wall was assumed to be $\epsilon_w = \alpha_w = 0.85$, which is typical for black ablative materials like phenolic impregnated carbon ablators (PICA). An aerogel insulation layer is included for thermal shielding.

Layer	Material	Thickness (mm)	k ($\text{W m}^{-1}\,\text{K}^{-1}$)	ρ (kg m^{-3})	c_p ($\text{J kg}^{-1}\,\text{K}^{-1}$)	Max Service (Temp °C)
Outer	PICA	5.0	0.18	290	900	1650
Middle	Silica Aerogel	4.0	0.010	40	750	500
Inner	Aluminum 2014 T6	2.5	150	3000	870	210
Total		**11.5**				

Table 8.1: Example CubeSat Heatshield Design Specifications

The simulation was run from the initial conditions for several cycles. The steady-state temperature time series $\{T_0^n, T_{M-1}^n\}$ are plotted in Figure 8.5 over two orbital periods. Surface temperature T_0^n oscillates between -3.87 °C and 96.6 °C, which falls within a typical range (roughly -10 °C and 100 °C) for similar CubeSats which do not employ active cooling [117, 118, 119]. Internal wall temperatures T_{M-1}^n lie well within the threshold operational ranges of electronics discussed in Section 7.1. The findings confirm that the thermal requirements are met during the orbital phase. Future work should focus on experimental validation of these results.

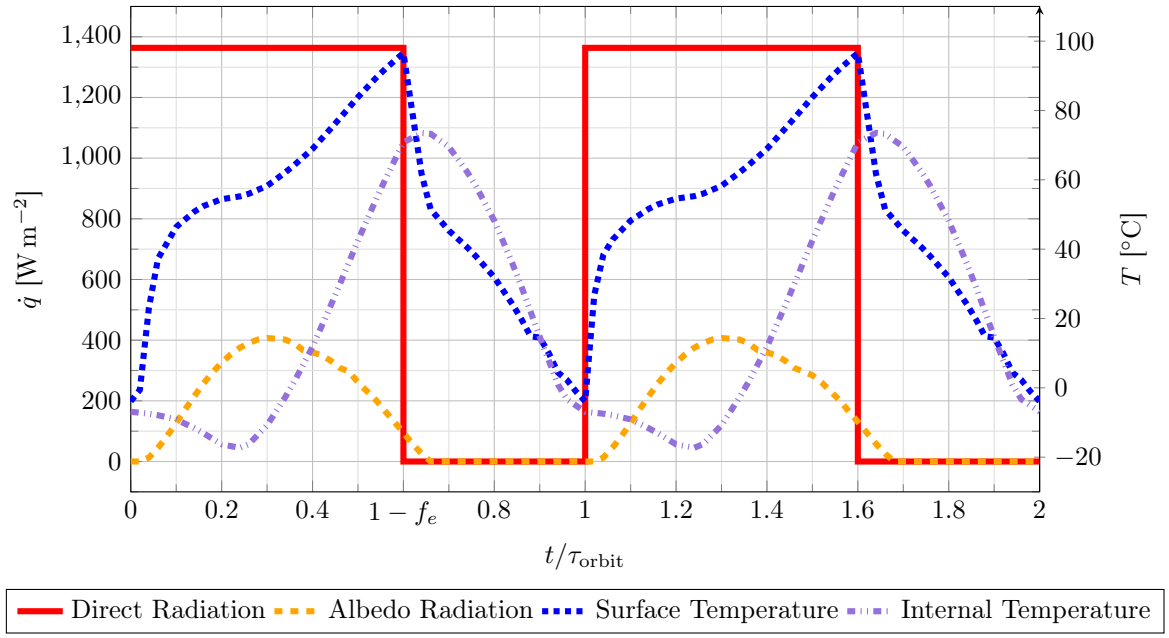

Figure 8.5: Plot of radiation intensities and temperature evolution over dimensionless time. Max radiation intensity $\dot{q}_{\odot,\text{max}}$ is 1363.6 W m^{-2}, and peak albedo radiation intensity $\dot{q}_{A,\text{max}}$ is 407 W m^{-2}. Surface temperature oscillates between -3.87 °C and 96.6 °C, while internal temperature ranges from -17.3 °C to 73.5 °C.

[18] The codebase was translated from a `Python 3.11` implementation, since the code provides mission-critical estimates.
[19] Each mission launch will require the customer to select a heat shield structure.

8.3 Re-Entry Phase - Claudio Vestini

This section aims to provide a top-level description of the aerothermal environment encountered by the CubeSat throughout the different stages of re-entry. The analysis is continued in Section 8.4 with high-fidelity simulations.

8.3.1 Flow Regimes

Flow conditions are categorised into separate regimes, depending on both the density of particles that make up the fluid, and how fast these are travelling relative to a fixed frame of reference. Firstly, a distinction is made between subsonic ($0 \leq M_\infty < 1$), transonic ($M_\infty \simeq 1$), supersonic ($1 < M_\infty \lesssim 5$), and hypersonic ($M_\infty \gtrsim 5$) Mach numbers. Whereas the difference between subsonic and supersonic flow behaviours is clear, and based on which direction information is permitted to travel, there is no obvious "transition" number to hypersonic regimes. These high-Mach conditions are characterised by the presence of strong shocks resulting in thin shock layers, entropy layers which interact with viscous boundary layers, extreme flow temperatures behind normal shocks and complex nonequilibrium thermochemical reactions [120]. Typical re-entry speeds for small uncontrolled satellites range from $M_\infty \in 25 \rightarrow 1$, with supersonic burn-up being most common.

A second distinction is made using Knudsen number[20]: at low Kn values, the flow behaves like a continuum; this regime is typical of the later stages of re-entry, as the atmosphere thickens and aerothermal loads on the CubeSat are greatest. At the opposite extreme, individual molecular kinetic interactions have to be considered, and the continuum model is no longer valid; this is known as the free molecular flow regime. In between, the flow conditions transition from one model to the other; this is the section of re-entry for which the least amount of both in-situ and experimental wind tunnel data is available, and theoretical understanding is still in development. An illustration of these flow regimes is given in Figure 8.6.

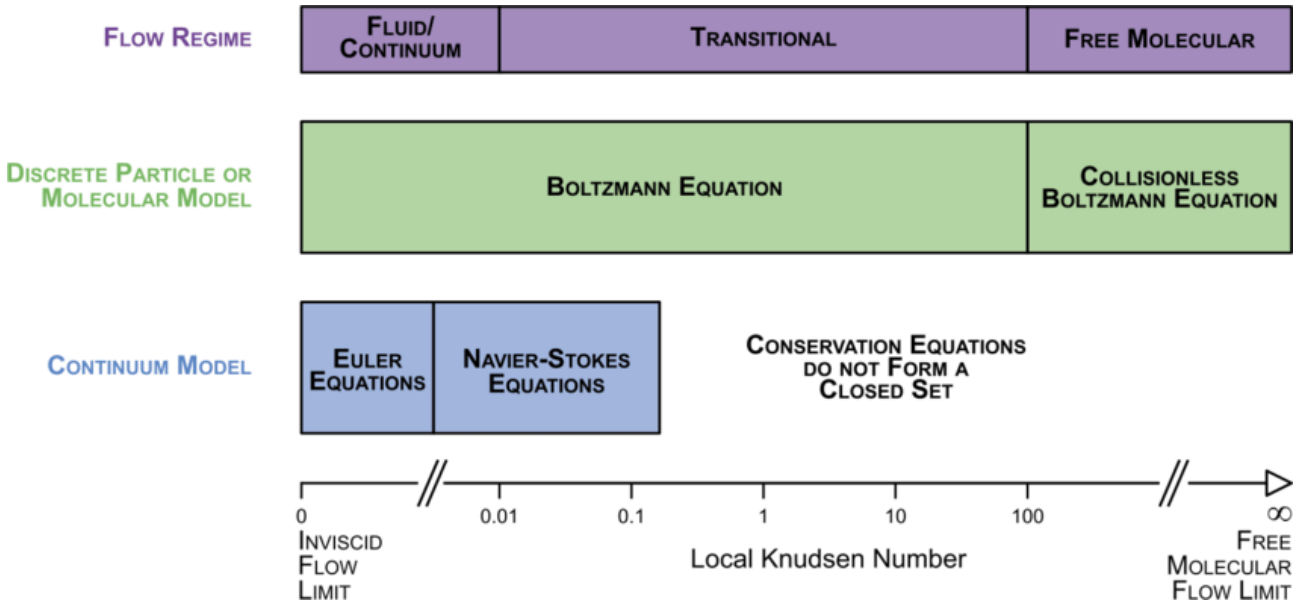

Figure 8.6: Illustration of flow regimes as a function of Knudsen number, as well as the intervals for which different models (continuum and discrete) are valid. From Marschall et al. (2020), adapted from Bird (1994).

[20]Knudsen number was first introduced in 1909 [121], and is defined as $\text{Kn} := \frac{\lambda}{L}$, where λ is the molecular mean free path length and L is the characteristic physical length scale of the system (sidelength of the CubeSat in this case).

8.3.2 Thermal Trajectory Analysis

A first-order analysis of the re-entry conditions the CubeSat will be exposed to was conducted by comparing the mission's trajectory, proposed in Section 4, to well-known results from the literature. As discussed, hypersonic flow distinguishes itself from classical supersonic regimes primarily due to the elevated temperatures reached in the shock layer behind strong shocks, which significantly alter the gas's chemical composition. Figure 8.7 summarises how these effects apply to the CubeSat mission at different altitudes.

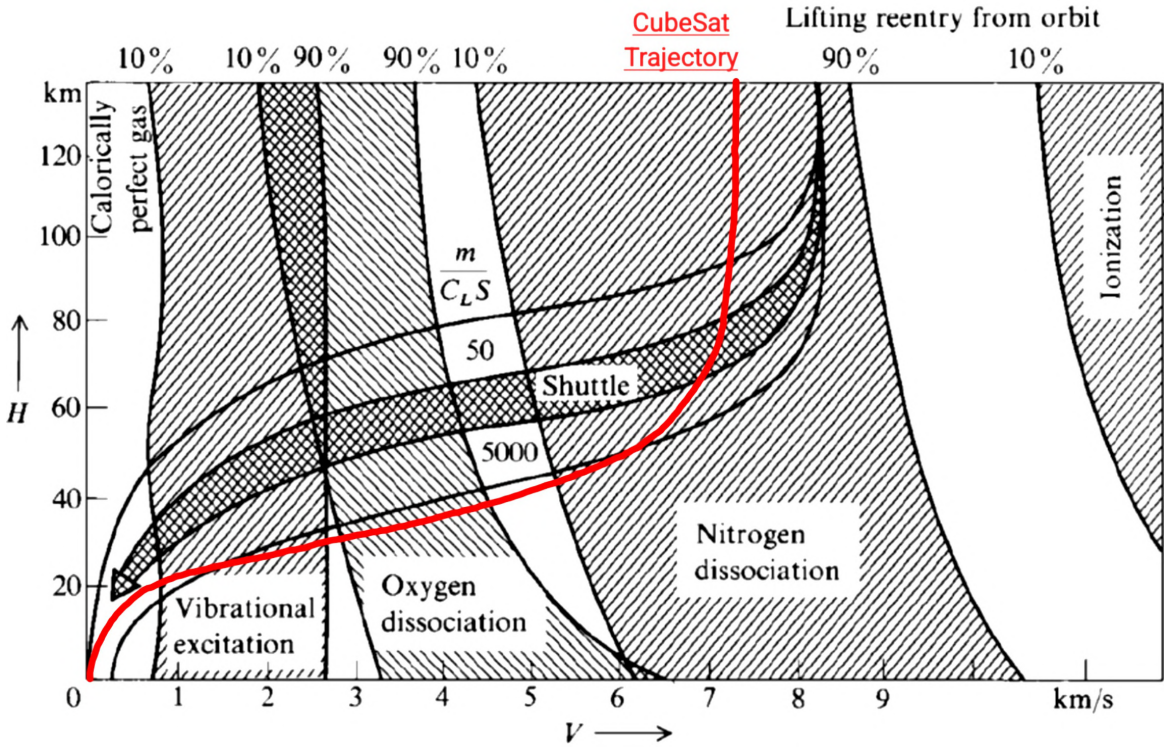

Figure 8.7: Thermochemical effects in hypersonic flow as a function of altitude and velocity during re-entry. The diagram highlights the onset of vibrational excitation, oxygen and nitrogen dissociation, and ionisation, overlaid with typical re-entry trajectories, including that of the NASA Space Shuttle. Superimposed is the trajectory of our CubeSat mission, in red (data from Section 4 - Trajectory). Adapted from Anderson (2006).

During the first stages of hypersonic re-entry, stagnation temperatures can exceed 800 K, activating vibrational modes in air molecules and leading to a temperature-dependent variation in specific heats (which occurs between 20 - 28 km altitude). These phenomena - along with the marked nonlinearity of thermodynamic properties at such temperatures - render classical ideal gas assumptions largely inadequate [120].

As the CubeSat re-enters through the upper layers of the atmosphere and temperatures behind the frontal shock reach approximately 2000 K, these excitations become sufficiently energetic to dissociate molecular oxygen (this happens at roughly 30 km altitude), and at 4000 K, the majority of O_2 has transitioned into its atomic form. These highly reactive atomic species initiate further thermochemical reactions, predominantly involving combinations of nitrogen and oxygen. At even higher temperatures, nitrogen molecules (N_2) begin to dissociate (the effect starts to become significant at 45 km altitude). Due to the strong triple bond in N_2, this process requires significantly more energy than the dissociation of oxygen and becomes relevant above approximately 8000 K [120]. The resulting atomic nitrogen contributes to a dense set of reactions in the shock layer, forming

additional species such as nitric oxide (NO) and further altering the thermal and chemical properties of the flow. These effects are especially relevant in the design of thermal protection systems, as the presence of atomic nitrogen increases the reactivity and overall energy content of the boundary layer.

Concurrently, radiation effects from both the boundary and shock layers become non-negligible, cooling the surrounding gas while heating the CubeSat's leading edge. The pronounced thermal gradients near the front faces of the CubeSat introduce considerable entropy differences into the system, resulting in a significantly thickened boundary layer on the streamwise edges downstream. Additionally, for many flight attitudes, the proximity between the shock front and the body (thin shock layers) causes direct interactions between the viscous boundary and the shock layers, further complicating both the physical structure of the flow and the associated thermochemical environments [120]. This is most relevant at angles of attack close to 45°, where the frontal shock is expected to be attached to the CubeSat's leading edge.

At even higher temperatures, ionisation processes would become significant, producing free electrons and giving rise to plasma formation in the surrounding flow [120]. However, the CubeSat is predicted never to encounter such extreme temperature environments during its re-entry mission, as shown in Figure 8.7.

8.4 CFD Simulations - Claudio Vestini

The analysis presented in this section aims to directly predict the aerodynamic and thermal loadings of hypersonic flow regimes around a cube via Computational Fluid Dynamics (CFD) simulations. Firstly, existing results from the literature are reviewed in Section 8.4.1. Secondly, simulation parameters and conditions are discussed in Sections 8.4.2 and 8.4.3, respectively, and the mesh used is introduced in Section 8.4.4. Finally, results and conclusions are presented in Section 8.4.5 and Section 8.4.6.

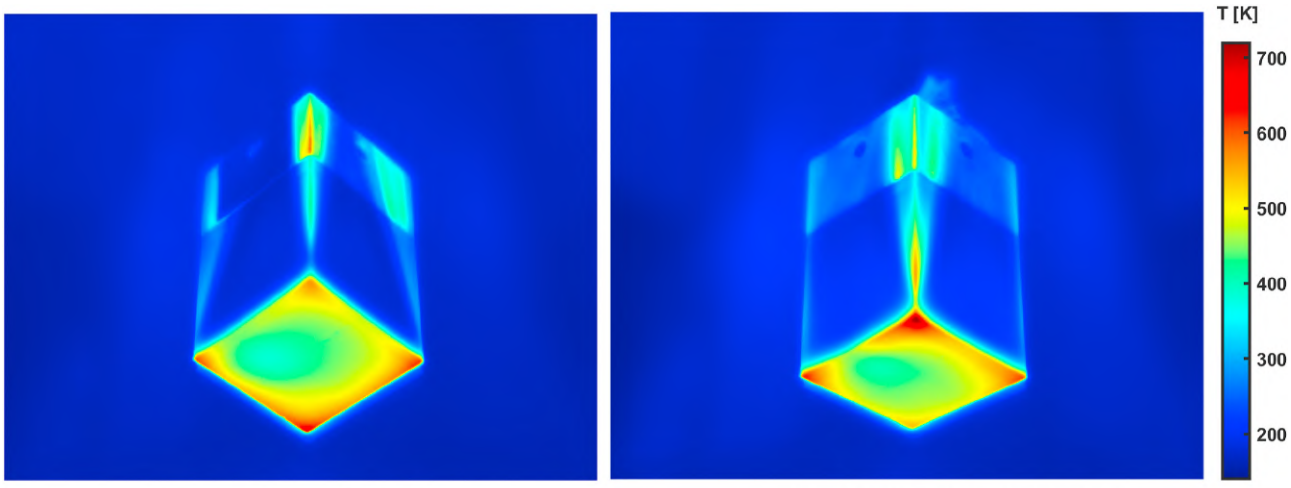

(a) +5° experiment (leeward side) (b) −5° experiment (windward side)

Figure 8.8: Experimental results of a Cube in Mach 5 flow at +5° incidence (a) and −5° incidence (b) performed at the University of Manchester's High SuperSonic Tunnel (HSST). Experiment and figure by Rees et al. (2021). The authors found that incidence had little influence over the maximum static temperature obtained at the corners. The experimental results are used to validate our predictions.

8.4.1 Cuboids in Hypersonic Flow: Literature

In general, very few simplifying assumptions can be made when simulating hypersonic flow regimes, and the overwhelming majority of publicly available literature focuses on simple geometries, such as spheres and flat-faced cylinders, which were extensively studied in the 1960s [125]. Often, re-entry simulation tools map aerodynamic and thermal correlations from these geometries to more complicated flow scenarios. Since most satellites are composed of faceted shapes, these mappings are often inadequate, as they largely underpredict effects such as boundary layer thinning-induced heating around corners.

Very few studies have been conducted on this class of aerodynamic bodies, and a limited number of research papers are available for validating hypersonic simulations of cubes. In particular, Rees analysed Stanton numbers for Mach 5 flows around a cube for small values of incidence in both 2D [126] and 3D [124] CFD simulations, which they validated against hypersonic wind tunnel experiments [127] (Figure 8.8). Seltner focused on aerodynamic coefficients at of Mach 7 flows around a cube [128]. Their Schlieren imaging results for critical hypersonic flow configurations around cube shapes are shown in Figure 8.9.

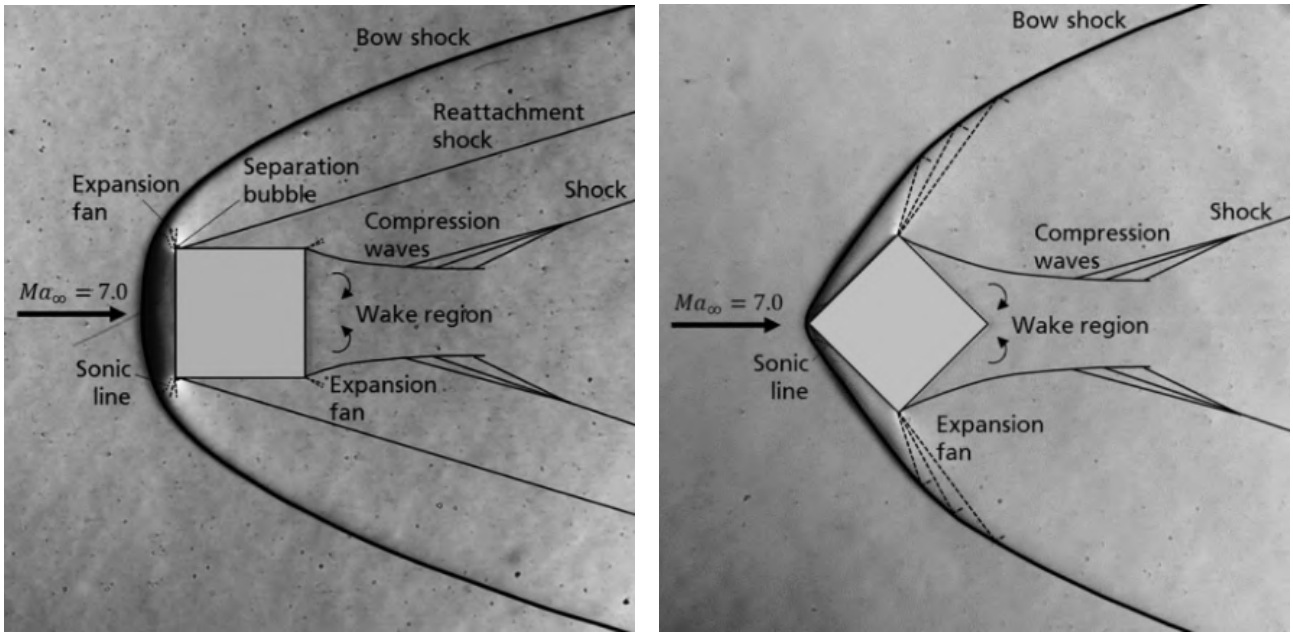

Figure 8.9: Critical flow configurations for a square in hypersonic flow, with $\alpha = 0°$ incidence (left) and $\alpha = 45°$ (right). Courtesy of Seltner, Willems, and Gülhan (2019).

The flow patterns at zero incidence predictably show a detached bow shock forming ahead of the CubeSat. Behind this strong shock, an entropy layer wets the CubeSat's walls. The region just behind the shock will be subsonic, where temperatures are expected to reach their highest values. The flow then accelerates around the CubeSat's corners via strong Prandtl-Meyer expansions, forming a separation bubble. It was shown in [126] that the presence of the bubble is strongly dependent on Reynolds number[21] but not Mach number, with separations forming for $Re_\infty > 5 \times 10^4$. The flow quickly reattaches to the top and bottom surfaces of the CubeSat through reattachment shocks. Not shown in Figure 8.9 (left), a weak compression wave was found to form about halfway

[21] Reynolds number is defined as $Re_\infty := \frac{\rho_\infty U_\infty L}{\mu_\infty}$, where variables have their usual fluid mechanics meanings.

down the top edge of the CubeSat in [126]. Simulations of the CubeSat presented in Section 8.4.5 also predict the existence of this Mach wave. The flow is then further expanded around the rear corners of the CubeSat, where a turbulent wake forms. At 45° incidence, the shock is attached to the stagnation corner of the CubeSat. With the absence of separations and reattachments on the frontal edges, the rest of the flow field is similar in nature to the 0° incidence case.

These experiments were used as validation cases for simulations conducted as part of this work.

8.4.2 Simulation Parameters

All relevant simulation parameters adopted in this study are summarised in Table 8.2.

Parameter	**Specification**
Software	ANSYS Fluent, Workbench, Post
Solver Type	2D, Density-based
Turbulence Model	k–ω SST
Solution Method	AUSM, implicit
Gradients	Green–Gauss Cell-Based
Fluid	Air (compressible, variable k, μ, c_p)
Spatial Resolution	Second-order upwind
Temporal Treatment	Steady-state
Mesh Type	Unstructured with AMR and inflation layers
Convergence Criteria	Residuals $< 10^{-4}$ for ≥ 50 iterations & MFI $< 2\%$

Table 8.2: Summary of CFD Simulation Parameters

The following paragraphs will provide some further explanation and justification behind these parameter choices.

ANSYS Fluent, a commercially available integrated CFD software package, was utilised in this project for the presented simulations. Fluent solves the two- or three-dimensional compressible Navier-Stokes equations:

$$\frac{\partial \rho}{\partial t} + \nabla \cdot (\rho \mathbf{V}) = 0 \qquad \text{(Continuity)} \tag{8.10a}$$

$$\frac{\partial (\rho \mathbf{V})}{\partial t} + \nabla \cdot (\rho \mathbf{V}\mathbf{V}^T + p\mathbf{I}) = \nabla \cdot \boldsymbol{\tau} \qquad \text{(Momentum)} \tag{8.10b}$$

$$\frac{\partial (\rho E)}{\partial t} + \nabla \cdot [(\rho E + p)\mathbf{V}] = \nabla \cdot (k \nabla T + \boldsymbol{\tau} \cdot \mathbf{V}) \qquad \text{(Energy)} \tag{8.10c}$$

The software uses either a pressure- or a density-based solver. The density-based solver was employed due to its ability to achieve convergence faster and with lower computational expense for supersonic simulations compared to the pressure-based solver. Fluent employs a Finite Volume discretisation method, which is particularly

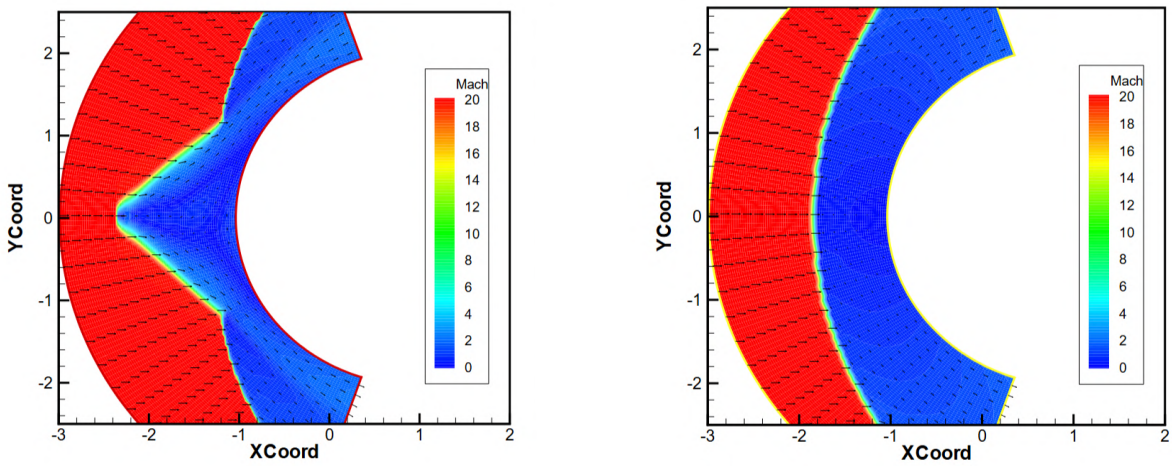

Figure 8.10: An illustration of the Carbuncle Phenomenon (left) compared to the stable solution for the same geometry (right). Figures from Ismail (2006).

advantageous because of its ability to process complex, unstructured meshes[22] [129]. We adopted the $k-\omega$ SST (Shear Stress Transport) turbulence model, as this is the industry standard for high-speed flows around sharp geometries[23].

A common challenge for hypersonic simulations is the misalignment of the stencil with flow solutions. This effect can cause spurious vorticity and shock-wave deformations, and it is known as the Carbuncle Phenomenon [130]. A demonstration of this phenomenon is shown in Figure 8.10, and an instance from the CubeSat simulations is shown in Figure 8.11. The nature of this phenomenon is poorly understood, and several cures have been proposed [131, 132, 133]. The Advection Upstream Splitting Method (AUSM) with implicit flux discretisation and vector splitting was implemented to help prevent carbuncles, resolving the issue shown in Figure 8.11.

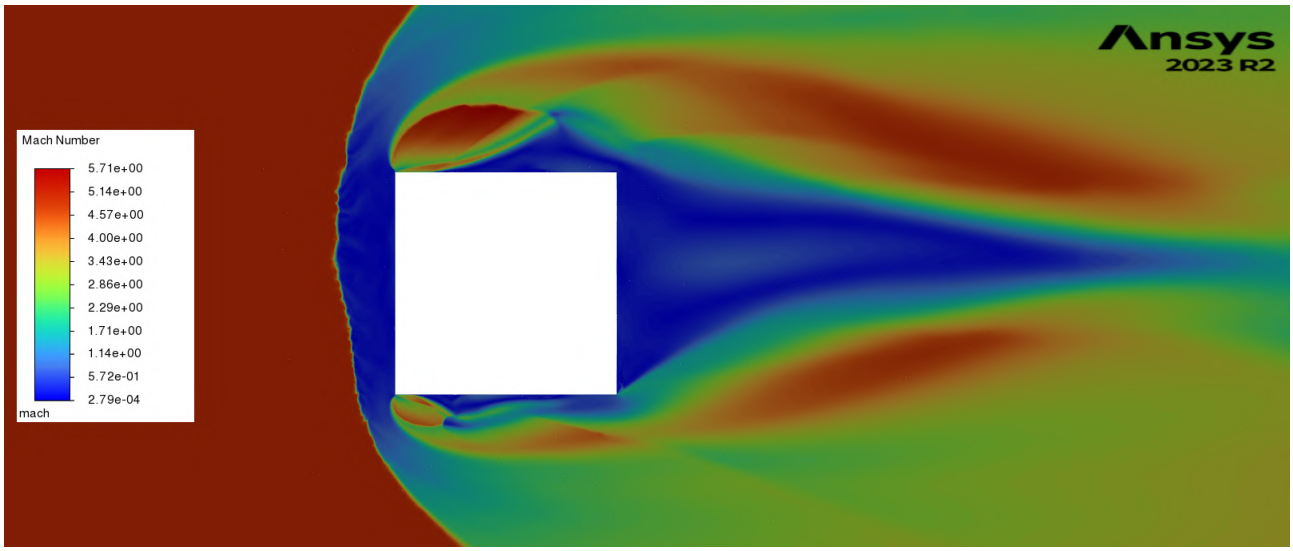

Figure 8.11: An instance of the carbuncle phenomenon. The plot shows contours of Mach number. It can be seen that the frontal shock behaves as if "punctured", and does not form the expected bow shape. It is also evident that this effect creates spurious asymmetries and nonphysical flow patterns after the shock.

[22] A mesh is said to be "unstructured" if its constituent polyhedra are not arranged in any orderly fashion.

[23] The software offers a wide range of turbulence models, including RANS (Reynolds-Averaged Navier-Stokes) models such as Spalart–Allmaras, $k-\varepsilon$ and $k-\omega$ (BSL or SST), and hybrid RANS-LES (Large Eddy Simulation) approaches such as DES (Detached Eddy Simulation) and SAS (Scale-Adaptive Simulation) [129].

Gradients were computed following the Green-Gauss Cell-Based method, and the fluid considered was compressible air, with Boltzmann-kinetic-theory specific heat c_p, Eucken-relation conductivity k, and Blottner-curve-fit viscosity μ. Fluent provides various discretisation schemes for both spatial and temporal resolutions, including first- and second-order accurate methods. Steady state solutions were considered, and second-order upwind methods were selected for flow and thermal computations to achieve high simulation fidelity.

Convergence was judged on flow residuals falling below 10^{-4} for ≥ 50 iterations, in addition to Mass Flow Imbalance, defined as MFI $:= 100(\dot{m}_{in} - \dot{m}_{out})/\dot{m}_{in}$, falling below 2% at the final iteration. This criterion is standard in high-fidelity simulations that do not have tight constraints on computational costs and runtimes.

8.4.3 Simulation Conditions

The three sets of simulation conditions for this report, Run 1, Run 2, and Run 3, are summarised in Table 8.3.

Parameter	**Variable Name**	**Run 1**	**Run 2**	**Run 3**
Mach Number	M_∞	5	5	17
Velocity ($\mathrm{m\,s^{-1}}$)	U_∞	1177	1177	5388
Angle of Attack (°)	α	0	45	0
Static Pressure (Pa)	P_∞	1584	1584	30000
Temperature (K)	T_∞	138	138	250
Reynolds Number	Re_∞	72,581	72,581	25,170,985
Knudsen Number	Kn	10^{-4}	10^{-4}	10^{-6}
Wall Thermal Condition	–	isothermal	isothermal	specified heat flux
Navier–Stokes	–	non-reacting	non-reacting	reacting
Air Model	–	ideal gas	ideal gas	5-species

Table 8.3: Summary of Boundary Conditions.

Given the nature of hypersonic atmospheric re-entry and the adoption of an attitude control system, the CubeSat is expected to tumble throughout the mission at rates of $\Omega \approx 1\,\mathrm{RPM}$. Since free-stream flow Mach numbers will be hypersonic for the entire mission, the Strouhal number, defined as $\mathrm{St}_r := \frac{\Omega L}{U_\infty}$, will remain very low: $\mathrm{St}_r \lesssim 10^{-5}$. Hence, the flow field can be assumed to always be fully developed in a quasi-steady state[24]. Transients are therefore neglected, and the flow can be studied for a specific value of Mach and incidence. For a perfect gas, the relationship between the Mach number, Reynolds number, and Knudsen number is given by:

$$\mathrm{Kn} = \frac{M_\infty}{Re_\infty}\sqrt{\frac{\gamma\pi}{2}} \tag{8.11}$$

All three cases fall within the continuum model regime and, therefore, run the two-dimensional, compressible Navier-Stokes equations. Run 3 considers reacting governing equations; Runs 1 and 2 have non-reacting[25] conditions to match Rees's papers [127, 126, 124].

Run 1 considers Mach 5 and zero incidence conditions for validation purposes. The thermal wall boundary

[24]Note that this assumption is very common for hypersonic re-entry simulations, as tumble rates are generally low compared to re-entry flow velocities.

[25]It is noted that, for these flow conditions, the maximum temperature recorded (behind the shock) did not exceed the 2000 K threshold for O_2 dissociation, which is a further justification for the choice of non-reacting physics.

condition is a non-slip, isothermal wall condition with a uniform temperature of $T_w = 300$ K. In practice, the flow is transient, and the wall temperature increases over time, approaching the adiabatic wall temperature [124]. Additionally, the temperature distribution across the surface will not be uniform due to elevated heat flux at the corners. These discrepancies are addressed[26] by reporting heat fluxes using the Stanton number, defined as $\mathrm{St} := \frac{q_w}{\rho U_\infty c_p (T_w - T_\infty)}$. Run 2 has the same conditions as Run 1, but at 45° incidence.

Throughout the CubeSat mission, far-field air density and composition, as well as Mach and Reynolds numbers, flow incidence, pressure, and temperature, will all vary continuously. Consequently, a vast spectrum of boundary conditions must be considered for testing. For commercial missions, the critical conditions—those that result in the highest aerothermal loadings—often receive the most scrutiny. This justifies the choice of flow conditions for Run 3, aimed at simulating typical re-entry conditions at an altitude of 40 km altitude, which is approximately the predicted location of maximum aerothermal loading[27]. For this run, the Mach number, pressure and temperature boundary conditions were taken from the Trajectory simulations to be $M_\infty = 17$, $P_\infty = 30\,000\,\mathrm{Pa}$ and $T_\infty = 250\,\mathrm{K}$. The Fluent models were altered to include reacting Navier-Stokes equations with 5-species air[28] (N_2, O_2, NO, N, O), and temperature-dependent viscosity μ and gas constant γ. The wall boundary condition is constant heat flux, informed by the Stanton number results of Run 1 (see Section 8.4.5). Note that no validation data were available for cube geometries at these conditions, so the results presented for Run 3 should be interpreted as indicative rather than definitive predictions.

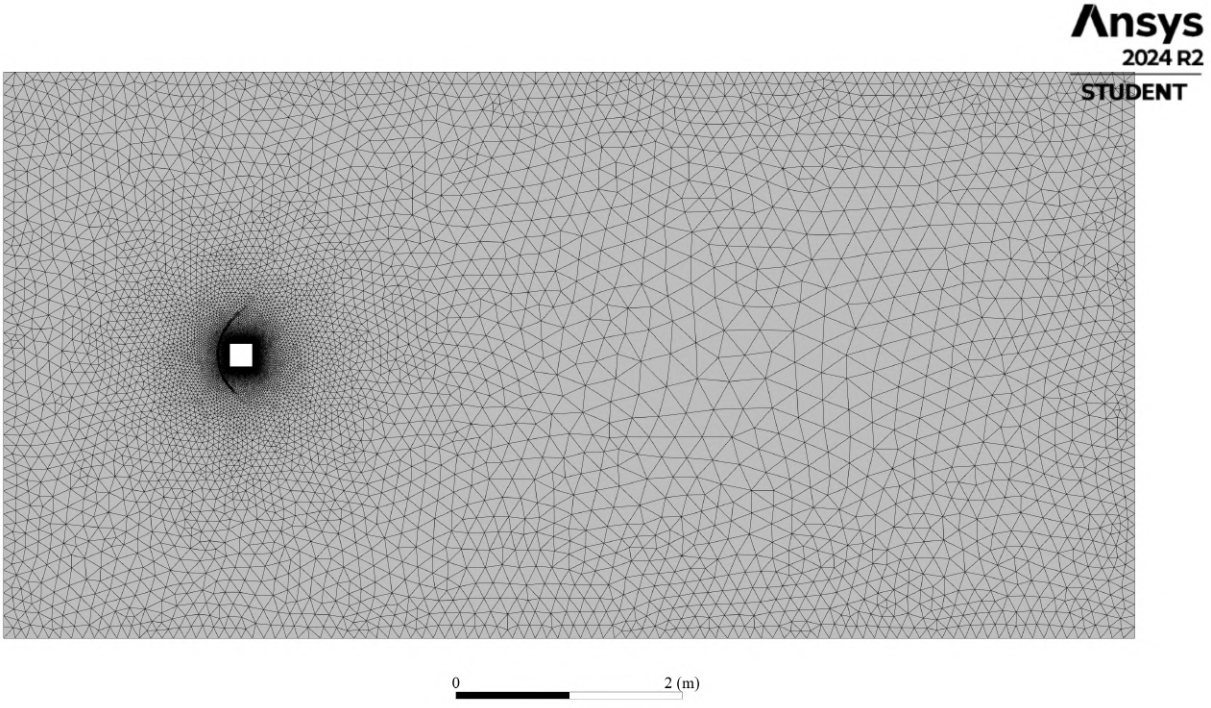

Figure 8.12: Domain Mesh for Run 1. Fluid domain dimensions are $5\,\mathrm{m} \times 10\,\mathrm{m}$, and CubeSat dimensions are $0.02\,\mathrm{m} \times 0.02\,\mathrm{m}$. Simulations were run on an ANSYS Professional license, and plotted via a Student license.

[26] This approach fails to account for thermal conduction through the geometry, particularly near the corners and edges. To properly simulate this phenomenon, we require an unsteady Fluent simulation coupled with a material thermal response model. At each step, the heat flux from the CFD solver is input into the thermal solver, which updates the wall temperature for the subsequent Fluent time step. The level of complexity in this kind of simulation is beyond the scope of this 3YP design project.

[27] This is common for many re-entry vehicles and capsules, such as SpaceX's Dragon [134, 135].

[28] For flight speeds ranging up to around 5 $\mathrm{km\,s^{-1}}$, a 5-species model is generally considered sufficient to accurately capture the effects of chemistry within a flow [136].

8.4.4 Mesh

The finalised mesh for Run 1 is shown in Figures 8.12 (domain view), and 8.13 (close-up views). Relevant mesh parameters are summarised in Table 8.4. Note that the same meshing process was used for all three runs.

Aspect	**Details**
Mesh counts	6.08×10^5 cells; 1.03×10^6 faces; 3.88×10^5 nodes
Cell types	Triangular (domain) + prismatic layers (near walls)
Boundary layers	20-cell inflation layer; $\Delta y_{\text{min}} = 10^{-4}$ m; GR = 1.07
Wall treatment	Fully simulated near-wall regions, with $y^+ < 1$
Refinement	Adaptive mesh refinement (AMR) on shocks and expansions
AMR	GCI study with 4 levels: coarse, medium, fine, extra-fine

Table 8.4: Mesh parameters and refinement details

For all simulations, the CubeSat was modelled as a simple square geometry of sidelength $L = 0.2$ m into a large rectangular domain of dimensions $5\,\text{m} \times 10\,\text{m}$. The large domain size enables the application of far-field boundary conditions and the capture of wake effects downstream of the CubeSat. This is a compromise in terms of computational cost. For this reason, and as good general CFD practice, mesh cell sizes are adapted to be finer near walls and shock waves, and coarser in the far field. In addition, the cell shape is adapted to capture the steep gradients of boundary layers: a prismatic inflation layer is adopted near the four walls, where prevalent gradients are aligned in the wall-normal direction, as visible in Figure 8.13 (right); polyhedral (triangular) cells are chosen away from walls for the remaining bulk of the fluid domain, which is visible in Figure 8.12.

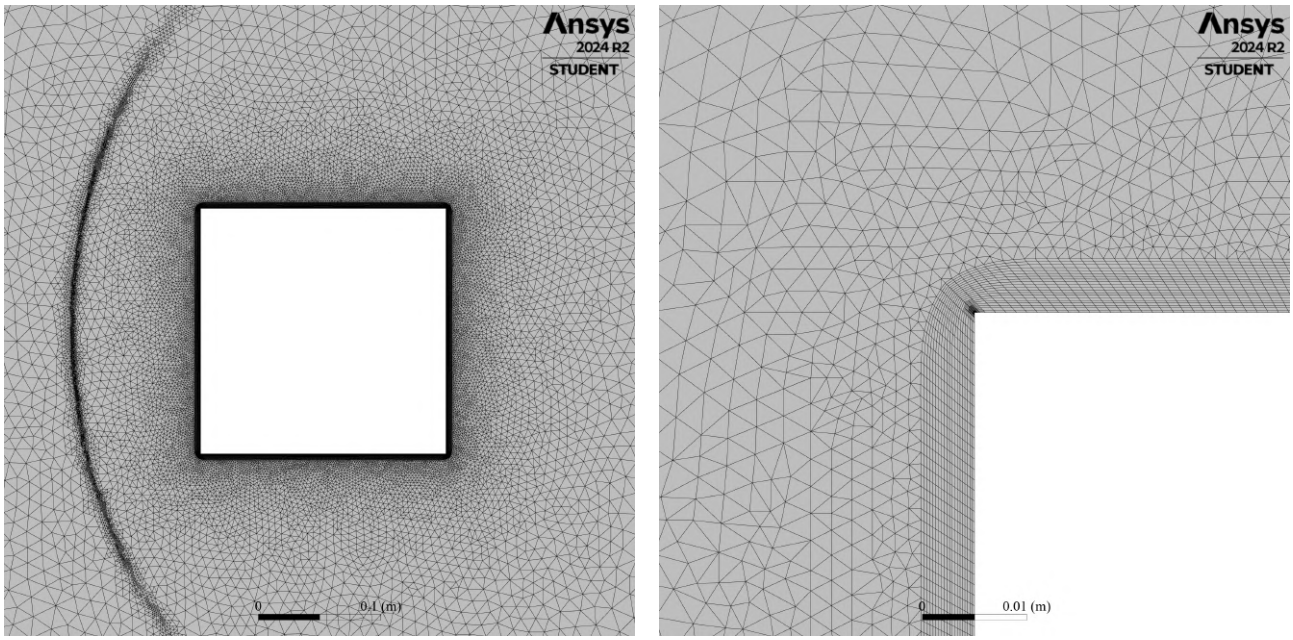

Figure 8.13: Detailed views of the CubeSat mesh for Run 1: zoomed view (left) and corner detail (right).

The impact of the inflation layer is measured[29] by analysing the dimensionless wall distance and velocity profile, y^+ and u^+, respectively, which are defined in terms of the friction velocity, u_τ, as:

$$u_\tau := \sqrt{\frac{\tau_w}{\rho}}; \qquad y^+ := \frac{\rho u_\tau y}{\mu}; \qquad u^+ := \frac{u}{u_\tau} \tag{8.12}$$

where y is the distance from the wall, μ the dynamic viscosity, ρ the fluid density and τ_w the wall shear stress.

The meshes for Runs 1, 2 and 3 were generated using the ANSYS Workbench Meshing program, with geometry imported from ANSYS Discovery. In all three cases, the prismatic inflation layer was created with $\Delta y_{min} = 10^{-4}$m for a total of 20 cells, and a moderate growth rate (GR) of 1.07 (the boundary layer was entirely contained within this inflation layer). As a result, for all three runs, the value of y^+ remained below 1 within all four viscous sublayers. Additionally, the maximum value of the first cell Reynolds number, defined as:

$$Re_{\mathrm{c}} = \frac{\rho_c a_c \Delta z}{\mu_c} \tag{8.13}$$

where ρ_c, a_c, μ_c are the local density, speed of sound, and viscosity of the fluid in the first cell, and Δz is the characteristic length scale of the cell (taken as the longest spatial dimension for structured meshes, or the cube root of cell volume for unstructured meshes), was recorded as 8.44. The first-cell Reynolds number serves as a standard criterion to ensure accurate prediction of the non-equilibrium chemical reactions and surface heat flux, guaranteeing that flow gradients within the viscous boundary layer near the wall are properly resolved. Values of Re_c on the order of unity can reliably simulate heat transfer rates to the wall [138].

The meshes were also refined around the bow shock and expansions, which is visible in Figure 8.13 (left). This was accomplished by using an Adaptive Mesh Refinement[30] (AMR) routine with four meshes (coarse, medium, fine, and extra-fine) based on a Grid Convergence Index (GCI) defined as:

$$GCI_{ij} = \frac{S_F|\varepsilon_{ij}|}{r^p - 1}, \quad \varepsilon_{ij} = \phi_j - \phi_i, \quad i \in 1:3, \quad j = i+1 \tag{8.14}$$

where the variable of interest ϕ_i was selected as Mach number on the stagnation streamline just ahead of the bow shock, $r = \Delta x_{coarse}/\Delta x_{fine} = 2$ is the refinement ratio, p is computed as $p = \ln(\varepsilon_{jk}/\varepsilon_{ij})/\ln r$ (with $k = j+1$), and $S_F = 1.25$ is a safety factor. A GCI of 0.037 was obtained beyond the second refinement (comparing an eight-fold versus sixteen-fold finer mesh), confirming mesh independence across the bow shock for $i \geq 3$. The refinement study for Run 1 is illustrated in Figure 8.14. Note that an analogous refinement routine was implemented for Runs 2 and 3.

[29] In some CFD simulations, it is possible to avoid simulating the boundary layer altogether. For this case, wall functions are used to bridge the wall-adjacent region without fully resolving the viscous sublayer, and the first mesh node is placed within the logarithmic layer ($30 < y^+ < 300$) [129]. On the other hand, to fully simulate the viscous boundary layer, it is necessary that $y^+ \lesssim 1$ near all walls [137]. This is the type of simulation we are running.

[30] This practice of Adaptive Mesh Refinement involves computing the rough position of high-gradient features using unrefined meshes at first, then increasing cell counts in those locations where the highest gradients are located.

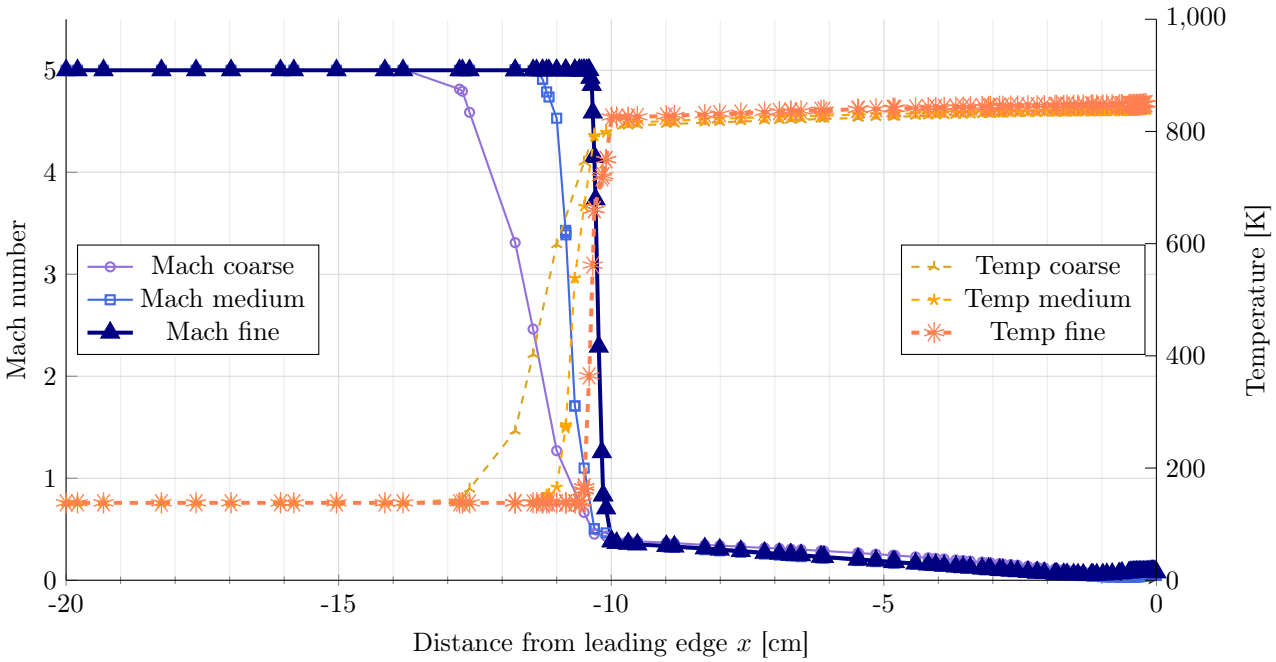

Figure 8.14: Run 1: Mach number and static temperature profiles across the frontal bow shock on the stagnation streamline for different grid refinements. The final mesh refinement (fine) is shown with a thicker line width.

8.4.5 Results: Run 1 and Run 2

Numerical Schlieren results for Runs 1 and 2 are shown in Figure 8.15, and a validation case in Figure 8.16.

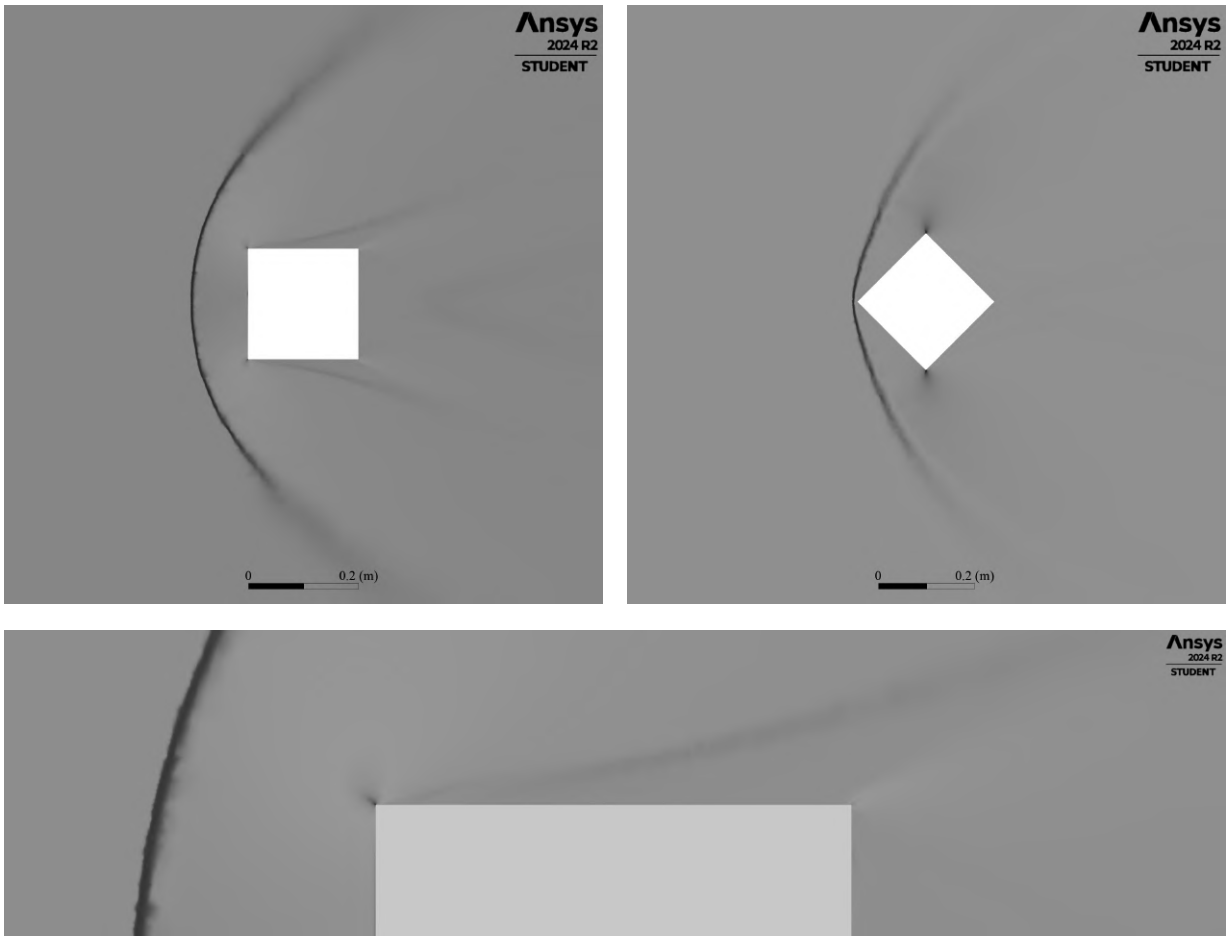

Figure 8.15: Schlieren (numerical) contours for Run 1 (top-left, bottom) and Run 2 (top-right).

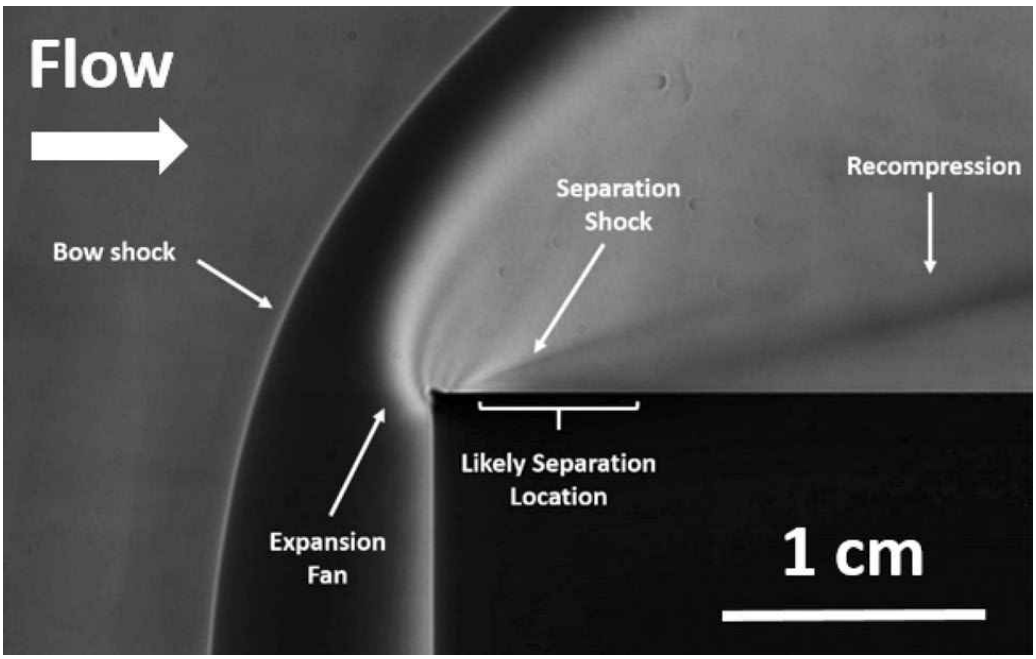

Figure 8.16: Labeled Schlieren for HSST wind tunnel test of a cube at $M_\infty = 5$ and $Re_\infty = 5.49 \times 10^5$. The same flow structures are simulated and labeled in Figure 8.17. Experiment and picture from Rees et al. (2020).

A bow shock (top-left) and a strong attached shock (top-right), as well as strong Prandtl-Meyer corner expansions, are all visible in Figure 8.15. As previously discussed, a weak compression wave appears in Run 1, which is also observed in [126]. This can be seen in Figure 8.15 (bottom), which gives a zoomed view of the top edge of the CubeSat for Run 1. The reattachment shock is also visible in this figure on the left side of the top edge, between the frontal corner expansion and the flow recompression. These results are validated by the HSST wind tunnel Schlieren results shown in Figure 8.16. Relevant flow structures in the Fluent simulations are labelled in Figure 8.17. These results show good qualitative agreement with the flow patterns described in Section 8.4.1.

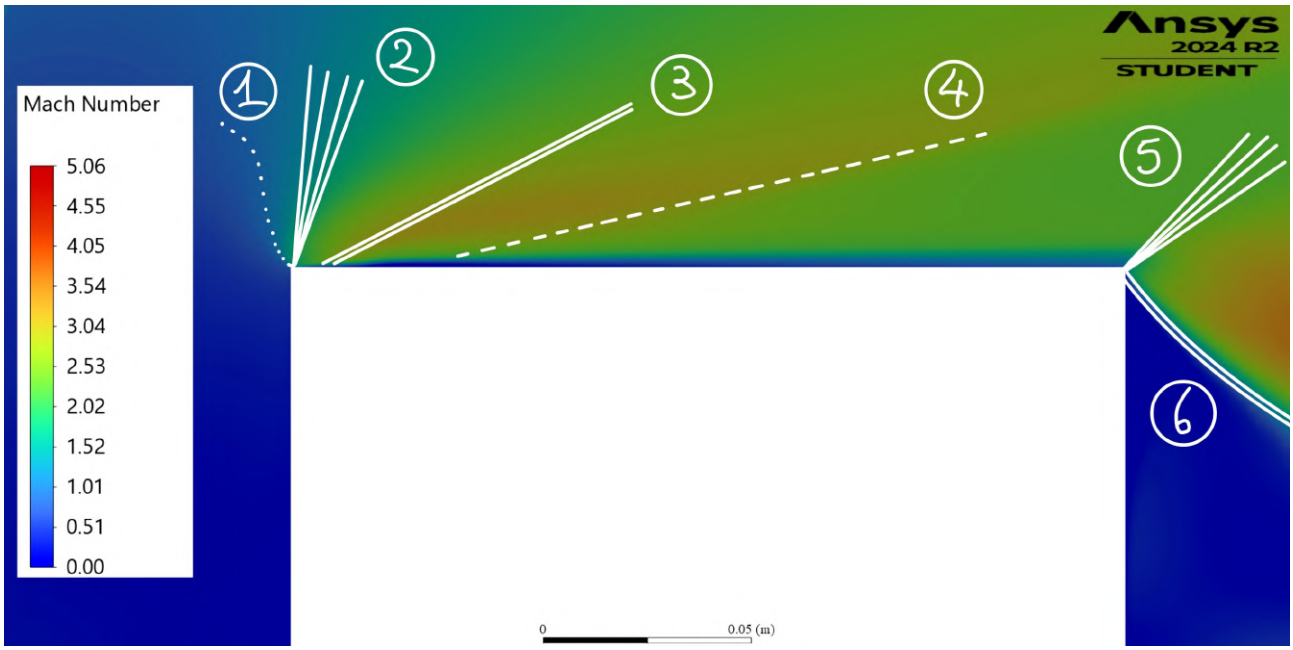

Figure 8.17: Run 1: detail of Mach number contours around the top half of the leading edge, top edge and top half of the leeward edge. Flow structures show the presence of: ① Sonic Line, ② Leading-Edge Expansion Fan, ③ Re-Attachment Shock, ④ Weak Compression Wave, ⑤ Trailing-Edge Expansion Fan, ⑥ Wake Shock.

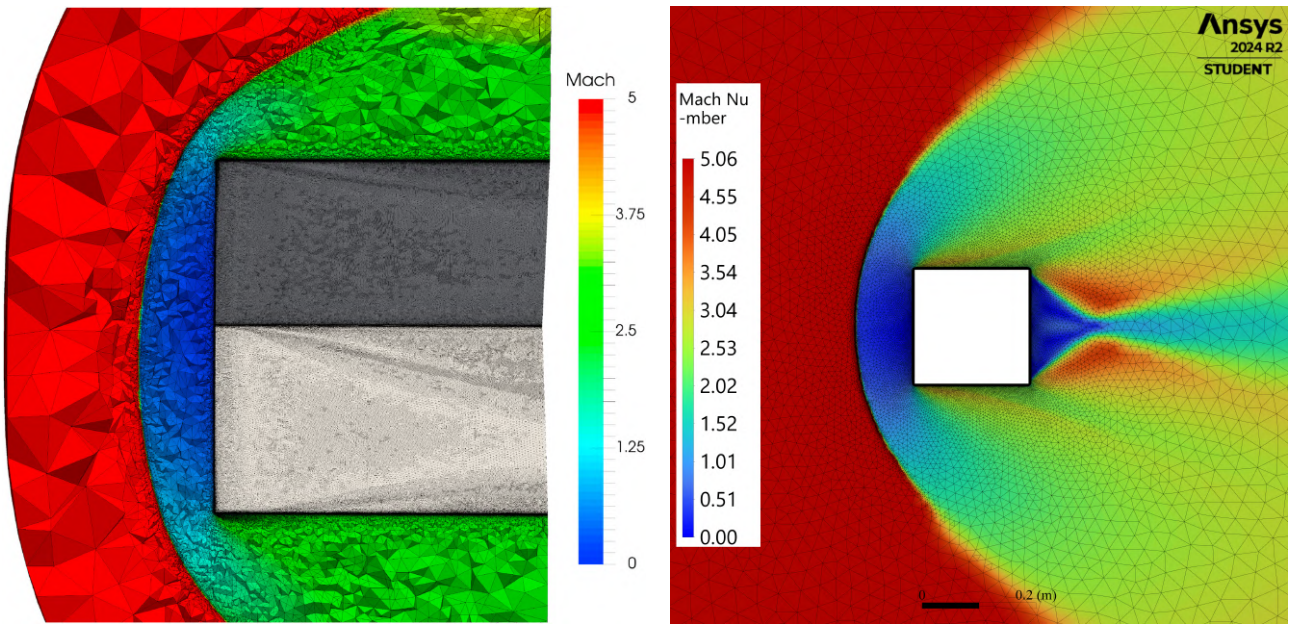

Figure 8.18: Comparison of Mach number contours between *Rees et al. (2021)* (left) and this report's Fluent Run 1 simulation (right). The results show good quantitative agreement.

Owing to the presence of shocks, expansions, separations, and strong heat fluxes, the boundary layer around the square requires careful definition. Here, the boundary layer height δ is taken as the point where the total enthalpy $H_0 = h + \frac{1}{2}|\mathbf{u}|^2$ recovers to the free-stream value $H_{0,\infty}$, thus capturing both thermal and kinetic viscous effects. For Run 1, the maximum height of the boundary layer on the streamwise edges was registered just after re-attachment at $x = 3$ cm as $\delta_{\max} = 2.38$ mm. The boundary layer thinning effect caused by the strong corner expansion is visible in Figure 8.17, and is consistent with [126]. This effect causes the sharp corner rise in heat flux to the wall, and consequently static temperature, as shown experimentally in Figure 8.8.

Results for Mach number (with literature comparison for validation) are shown in Figures 8.18. A bow shock is found to form at 10.6 cm ahead of the leading edge (right). The standoff distance for the bow shock in the CubeSat simulation is greater than in Rees, whose simulations are 3-dimensional and use the DLR TAU code [139]. This is a well-known phenomenon: 2D models restrict flow expansion to a plane, increasing pressure gradients near the body, which forces the shock wave to form farther from the surface compared to 3D simulations [140].

Distributions of static pressure and temperature for both Run 1 and Run 2 are shown in Figure 8.19.

As visible in Figure 8.19 (top-left), in Run 1, static temperature is found to sharply rise above the far-field value behind the bow shock, resulting in temperatures of upwards of 860.41 K[31]. The flow static temperature rises to values of about 550 K in the wake, which is significantly lower than the stagnation values as expected. The thermal loading experienced by the CubeSat in Run 2 is displayed in Figure 8.19 (top-right). Temperatures are found to be slightly higher at 45° incidence, with a maximum flow temperature of 871 K near the stagnation corner. This can be attributed to the enhanced proximity of the frontal shock[32].

[31] Note that the walls in Run 1 are isothermal at 300 K, so this peak value occurs a few cells away from the walls.

[32] However, the adiabatic wall temperature of the frontal corner in the 45° incidence case is expected to be comparable to that of the frontal two corners in the 0° incidence case, which is again due to the boundary layer thinning effect.

For Run 1, as seen in Figure 8.19 (bottom-left), static pressure rises behind the shock to a maximum value of 52.68 kPa at the stagnation point. A detailed examination reveals that static pressure drastically drops behind the first set of strong Prandtl-Meyer corner expansions to values as low as 0.21 kPa. The flow is then processed by the re-attachment shock and compression wave, and pressure rises to 2.36 kPa. As the flow recompresses, an adverse pressure gradient forms behind the re-attachment location (pressure reaches 3.73 kPa just before the trailing edge), which is consistent with the findings of [126], section IV-C. Displayed in Figure 8.19 (bottom-right) is the pressure distribution for Run 2, which shows zones of high pressure primarily concentrated near the frontal corner, with significantly lower pressure over the leading edges compared to Run 1. Overall, these results confirm the hypothesis that thermal loading on the CubeSat will far exceed aerodynamic loading, with fragmentation mechanisms driven by failure of fasteners and glues rather than failure of body panels [141].

For this reason, the results for Run 3 presented in Section 8.4.6 focus solely on thermal loading distributions.

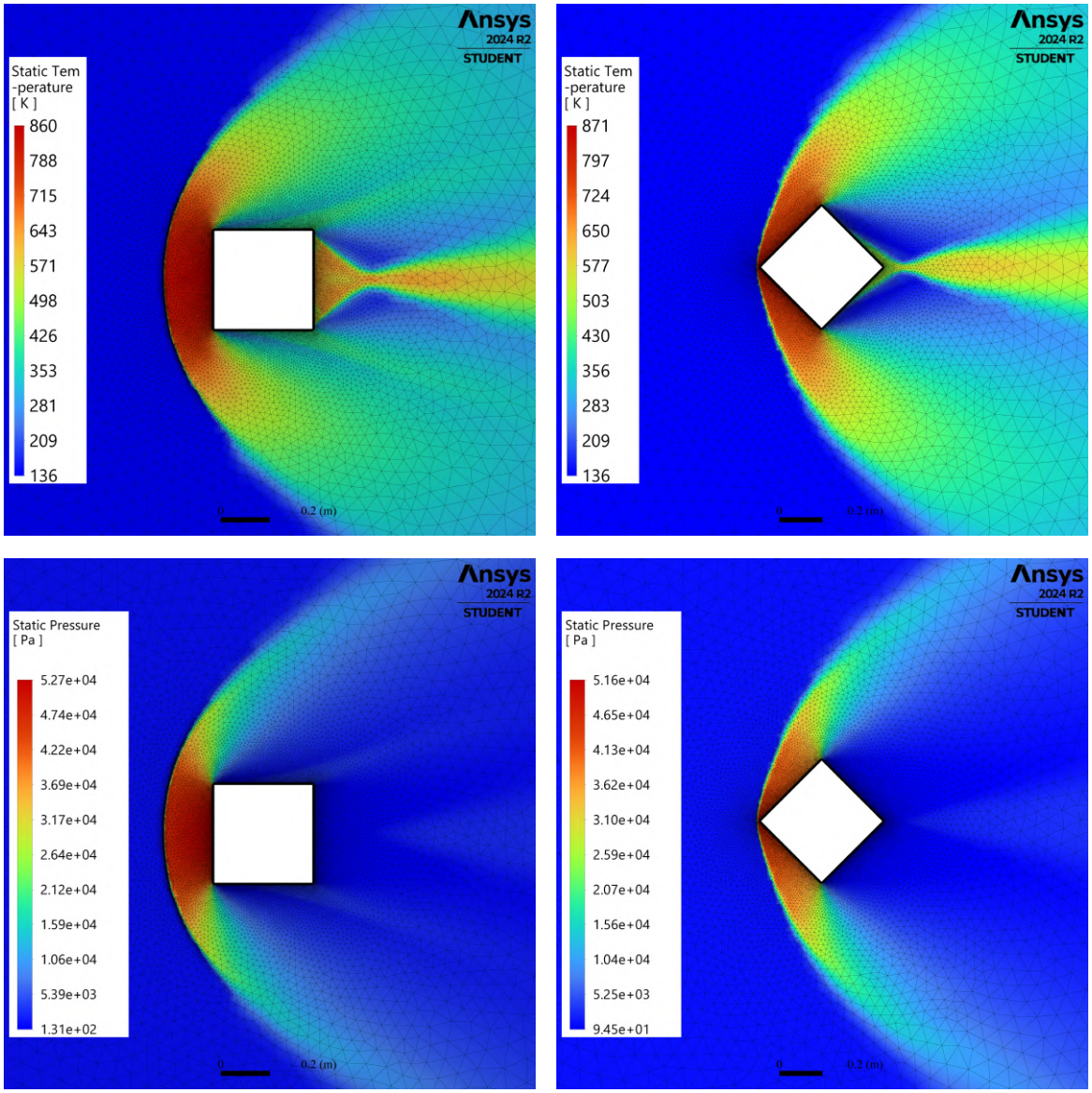

Figure 8.19: Static temperature contours for Run 1 (top-left) and Run 2 (top-right). Static pressure contours for Run 1 (bottom-left) and Run 2 (bottom-right). The distributions show interpolated nodal values.

8.4.6 Results: Run 3

Figure 8.20 shows distributions of static temperature increase, Stanton number and heat transfer coefficients along the leading and top edges. These results are normalised by the respective maximum values, in an attempt to generalise the findings beyond the specific simulation conditions of Run 3.

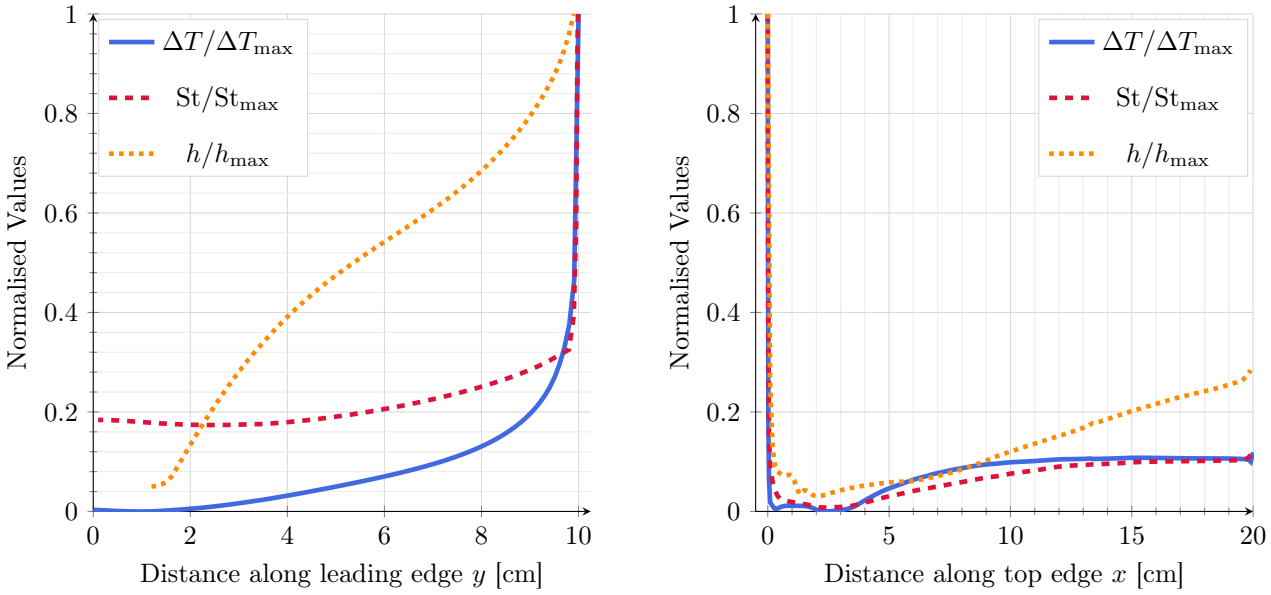

Figure 8.20: Normalised temperature increase above stagnation point temperature ΔT (Run 3), normalised Stanton number St (Run 1), and normalised y^+-based heat transfer coefficient h (Run 1) along the top half of the leading edge (left); Normalised static temperature increase above minimum top-edge static temperature ΔT (Run 3), normalised Stanton number St (Run 1), and normalised y^+-based heat transfer coefficient h (Run 1) along the top edge (right). The overall distributions are in agreement with the results of Figure 8.21.

For the Run 1 parameters, heat transfer coefficients were obtained as first cell, y^+-based values, and Stanton numbers were computed using the heat flux across the CubeSat's wall. The latter can be directly compared[33] to the experimental and numerical Stanton number results of [124], shown in Figure 8.21.

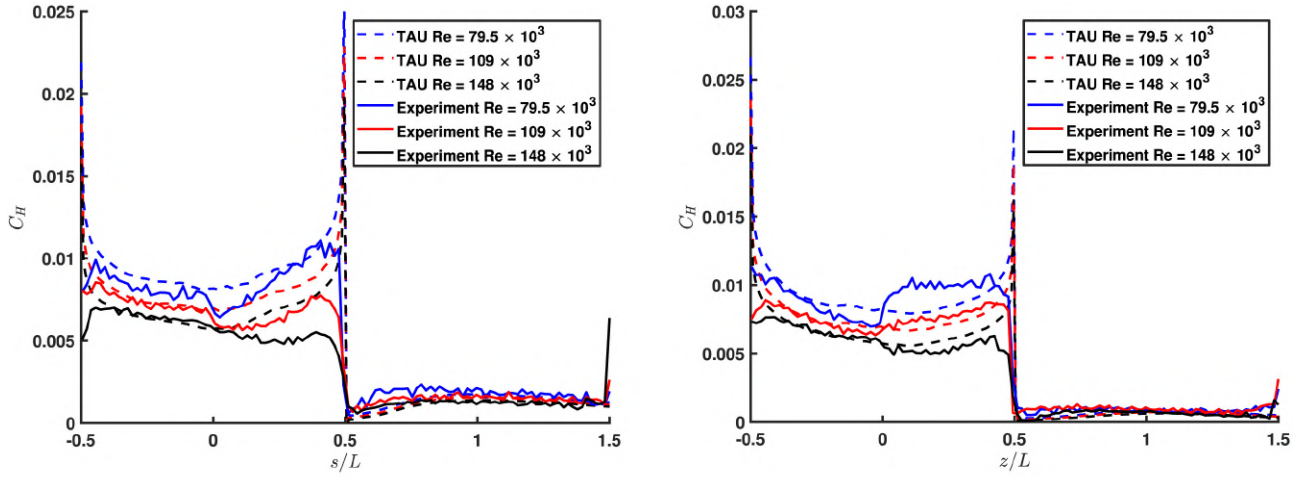

(a) Windward side at $z/L = 0$

(b) Leeward side at $s/L = 0$

Figure 8.21: Stanton number distribution along a 2D cross section on the windward side (a) and leeward side (b) from both experimental and numerical sources. Experiments, simulations and figures by Rees et al. (2021).

[33] Although the numerical and experimental results for these papers were run at 5° incidence, the authors reported that the small angle of attack had little effect on the results (and no other data was found at 0 incidence as of the writing of these results).

The Stanton number distributions show good agreement with the Rees data, with stagnation-point values constituting about 20 % of the maximum, with a sharp increase near the corners, as seen in Figure 8.20 (left). Stanton number drops after the strong corner expansions to a minimum of less than 1 % of its corner value, slowly increasing along the top edge to about 10 % near the leeward edge, as visible in Figure 8.20 (right).

The temperature increase data ΔT for Figure 8.20 were obtained from Run 3 (with non-isothermal wall conditions), where the maximum temperature increase (at the leading-edge corners) was found as $\Delta T_{\max} = 890\,\mathrm{K}$. The minimum static temperature value on the top edge, just before reattachment, was found to be 440 K.

Figure 8.22 shows the wall-normal temperature distribution within the boundary layer along the top edge. These profiles closely follow the typical hypersonic boundary layer distribution, where static temperature rises above wall temperature, then decays to its free-stream value (see [120] chapter 1.3-C). A maximum temperature of 1438 K is found to occur at $x = 3\,\mathrm{cm}$ away from the leading edge within the boundary layer.

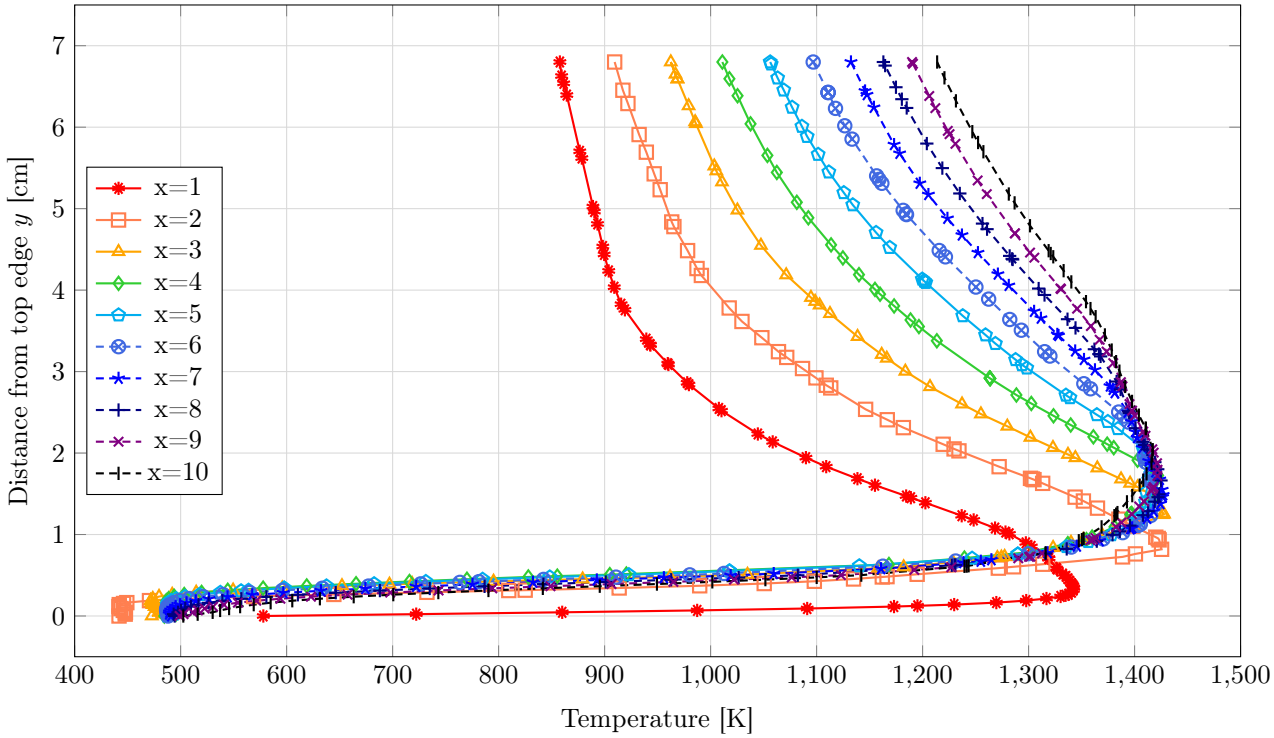

Figure 8.22: Run 3: temperature profiles within the viscous boundary layer at different streamwise positions (x-values, in cm) along the first half of the top edge of the CubeSat. Surface temperature is found to lie between 400 K and 600 K, with the highest surface temperature just after the frontal corner Prantl-Meyer expansion.

In Run 3, static temperature at the stagnation point was found to be 5049 K. This is much lower compared to an estimate from the ideal gas equation $T_0 = T_\infty \left(1 + \frac{\gamma-1}{2} M_\infty^2\right)$, which gives $T_0 = 14\,700\,\mathrm{K}$ for the conditions of Run 3. As described in Section 8.3.2, this is expected, as real gas phenomena such as O_2 molecular dissociation and temperature-dependent γ will result in much lower temperatures behind the bow shock. This highlights the importance of high-fidelity simulations for hypersonic environments, where accurate thermal predictions are critical. To verify the results, simulations were cross-checked against NASA's Langley Aerothermodynamic Upwind Relaxation Algorithm (LAURA, version 5.6), a structured-grid, finite-volume code specifically developed for simulating chemically reacting flows in hypersonic regimes. Unlike general-purpose CFD tools such as

ANSYS Fluent, LAURA is tailored for hypersonic flight conditions and has been extensively validated against experimental data. LAURA's output for the predicted stagnation temperature for the conditions of Run 3 was approximately 5100 K, differing by less than 1%. This confirms that the results of Run 3 are consistent with those of established hypersonic flow solvers, lending credibility to the predicted stagnation conditions despite the lack of experimental data for direct validation.

These results inform the customer's commercial design of an ablative heat shield, ensuring survival through the upper atmosphere, while also providing sufficient internal heating to ignite the thermite masses.

9 Budget - Alex Berresford

A budget estimate has been drawn up from the current understanding of the mission and design specifications. Figure 9.1 shows how this is broken down.

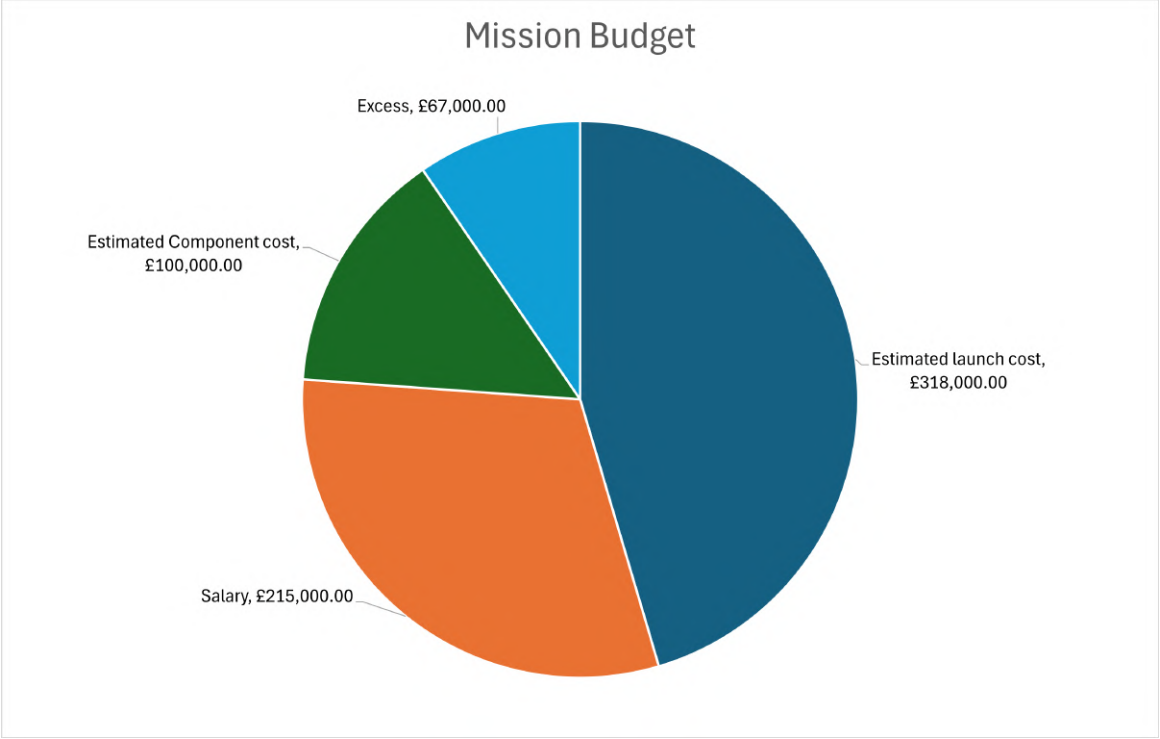

Table 9.1: Budget break down

The estimated required budget is £̃700,000 across the four main sections. The largest expense is launch cost, which has been estimated using an online tool developed by Endurosat to estimate mission costs based on their parameters [142]. This is expected to be an underestimate.

Salary has been approximated over a span from 04/25 to 01/27 for four graduate engineers on an average UK salary of £30,712 [143].

Component cost has been calculated from known component costs and estimates of those for which prices have not been located. This also includes the price of access to the iridium network.

Excess budget is to be used for one off costs such as transport and accommodation costs for the team assigned to the launch site. This also allows for the possible underestimate of either the launch of component costs.

10 Project Risks - Alex Berresford

A qualitative risk assessment of possible mission failure criteria has been completed to inform which areas to focus future development.See Table 10.1.

Table 10.1: Risk Matrix

Event	Liklihood	Consequence	Risk
Unable to meet target launch date (Dec 2026)	Low	Moderate	Medium/Low
Induced Spin Up Failure	Low	Insignificant	Low
Orbital Collision	Remote	Severe	Low
Reactivation system failure	Low	Severe	Medium
Satellite subsystem failure	Medium	Moderate	Medium
Thermite ignition failure	Low	Moderate	Medium/Low
Early Telemetry Failure	Medium	Severe	High

Early telemetry failure presents the greatest risk to the mission. If they fail, there is no way to recover data, resulting in a total mission failure. This risk is exacerbated by the relatively low antennae operational temperature range of -40 °C to 85 °C [49], making it very vulnerable to thermal damage. Due to this, internal thermal control will be a priority of future development.

Orbital collision and reactivation system failure both pose severe consequence of total mission failure, but are both very unlikely. Section 4.30 shows a collision risk of 0.00765% . Reactivation system failure has already been mitigated through the use of multiple RTCs to make the reactivation system more robust, as described in section 6.2.1.

Failure of other satellite subsystems poses a moderate risk to the mission that could result in partial failure. For example, early failure of a sensor array could result in missing results for one face of the CubeSat. Similarly to telemetry failure, this is most likely due to thermal damage and incentivises development of internal thermal management systems.

Thermite ignition failure poses no risk to data collection, but it risks ground impact and potential damage to structure or individuals. As the thermite ignites independently of any other systems at a design temperature, the risk of failure is incredibly low.

We are optimistic about our launch target date of December 2026, especially considering the flexibility of RocketLab. Delay may result in extra cost but otherwise has no downsides, especially if further key development is required to mitigate other risks.

11 Conclusion - Hani Moussa

This report has presented the design and method of a CubeSat re-entry mission developed to provide a commercial platform for live testing of ablative materials. The primary goal is to provide clients with a reliable test-bed for thermal protection system (TPS) development, recording material behaviour in realistic re-entry conditions. Additionally, this missions aims to analyse the corresponding changes in atmospheric conditions due to this ablation. The result is a cost-effective, repeatable mission that delivers practical data to support the improvement of heat shield manufacturing.

The mission begins with deployment at an orbital altitude of 400 km. Rocket Lab was selected as the launch provider due to its capability for low Earth orbit placement at this altitude. Their Electron rocket, which is partially reusable, offers consistent access to targeted altitudes through frequent deployments per launch. This allows for greater confidence in the applicability of our planned trajectory.

This mission's trajectory begins with a de-orbit burn following launch and ends with re-entry approximately 457 hours later. The deorbit burn consists of a retrograde impulse burn with cold gas thrusters, designed to work within the purview of the CubeSat's MPC system, and aiming to decrease the perigee to 140km. The atmospheric model incorporated the effect of the 11-year solar cycle on the thermosphere and ionosphere to accurately predict the trajectory. Density change with height was modelled piecewise with multiple space agency sources and MATLAB was used to simulate the density at each altitude down to 40km, at which point the satellite is assumed to have demised. This simulation was verified through use of GMAT, leading to only a 2.46% difference found. The chances of collision, additionally, were shown to be only 0.0765% through the use of the Poisson distribution.

The mechanical design of the CubeSat relies heavily on component selection and spatial constraints. Both mass and volume were carefully optimised to minimise launch costs and maximise utility. An 8U configuration was found optimal for this mission due to its size and regular shape. The latter is highly relevant to generating uniform exposure for each test material. The structural frame is constructed from Al 2014, selected for its suitable strength and density. Structural integrity was appraised for the produced model through the application of expected vibration and acceleration environments. To confirm full CubeSat demise, passive thermite charges are embedded into the frame at structural joints. This arrangement takes into account structural integrity and end-of-life responsibility whilst remaining within the purview of mission objectives.

The CubeSat's functions are managed by the Epik Sidekiq Z2, integrated into the ICEPS onboard computer. Whilst supplying the satellite with a pre-built electrical power system (EPS) and several regulated power rails, ICEPS also includes an I^2C network to dispatch commands to various subsystems. The Sidekiq board incorporates a software-defined radio to enable modulation of signals for transmission to the Iridium constellation. To improve reliability and maintain an acceptable link margin, the transmitted signal is split across four custom printed circuit boards, each introducing a calculated phase shift. This beamforming strategy creates a more directed signal, allowing more dependable data acquisition on the ground. This architecture enables data flow

from acquisition to transmission, maintaining consistent and reliable operation throughout re-entry.

A variety of instrumentation was selected to enable data capture and attitude control throughout the CubeSat's mission. The ablative sensing platform, with temperature, pressure, and recession sensors embedded within the test material, facilitates the primary objective. A spectrometer system was also implemented to provide spectral data to support these measurements. Attitude and altitude tracking is achieved through a combination of a magnetometer and inertial measurement unit. The sensors work with sensor fusion designed to maintain situational awareness. This data informs the model predictive control system, which induces a controlled tumble, allowing for uniformity of exposure across all six test surfaces. Together, these systems form an effective instrumentation system aimed at delivering practical data for post-mission analysis.

Aerothermal considerations were undertaken for the CubeSat to confirm intended function during orbital and re-entry periods. Adopting several simplifying assumptions, a one-dimensional heat conduction problem solver was constructed, in which the Forward-Time Central-Space (FTCS) scheme was implemented. Using an aerogel insulation layer in the heat shield, internal surface temperatures for the orbiting CubeSat were found to be within the operational ranges of the electronics. For the re-entry phase, the CubeSat was modelled as a 0.2m-sided cube, and CFD simulations were conducted on commercially available software to predict the aerodynamic and aerothermal loading experienced by the CubeSat at the critical conditions. Hypersonic speeds were found to contribute to high heating, with stagnation-point temperatures peaking at over 5000K. These result are to be used to inform future heat shield designs by customers. Calculating expected aerothermal effects also aids in the predictability of the mission's events.

This mission aims to provide a commercial platform for materials testing, and a reduced cost of producing the platform ensures a more competitive product. Overall, the required financial capital to attain launch was found to be around £700 000, including a margin for excess overhead. The vast majority of expense is due to launch costs, with the remainder originating from engineer salaries and component purchases. The result is a cost-effective CubeSat mission with practical data output and minimised risk.

The mission's risk has been carefully appraised and reduced through careful design decisions. The most severe risk with an above-low likelihood was found to be early telemetry failure. This eventuality, in which little or no useful data can be extracted from the CubeSat pre-demise, can be mitigated through thorough testing and built-in redundancy. Other risks, such as subsystem or thermite ignition failures, can be moderated in a similar fashion.

The design and analysis entailed in this report represents a strong foundation for CubeSat missions aiming to collect re-entry data. It has combined reliable subsystem architecture and consideration of environmental factors to result in a repeatable solution for commercial use. Future work could explore heating considerations or apply more detailed simulation conditions, thereby adding further to the mission's viability. This project suggests an approach that could establish a worthwhile avenue for live space materials research.

A Appendix

A.1 Other FEA results - Alex Berresford

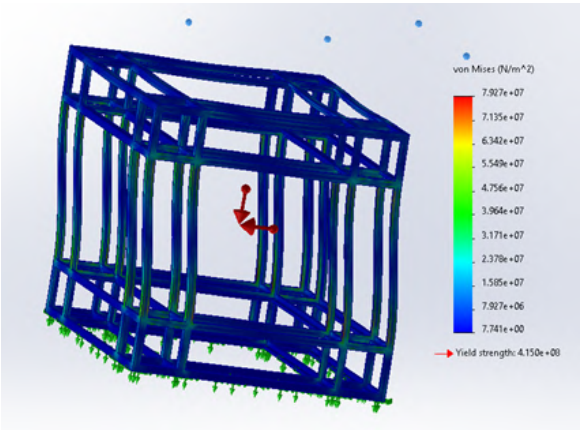

((a)) Stress with horizontal load perp. to side

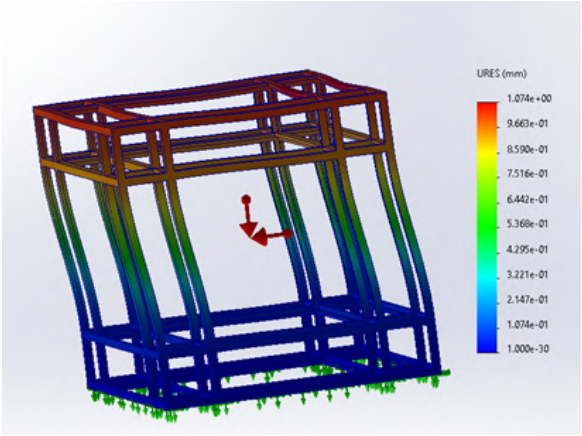

((b)) Displacements with horizontal load perp. to side

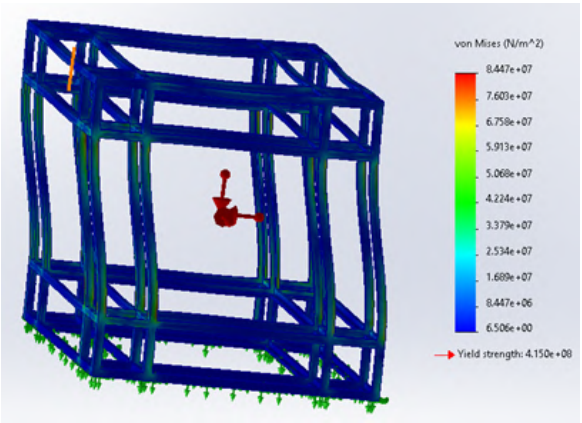

((c)) Stress with horizontal load 45 °to side

fig:img4[0.45] ((d)) Displacements with horizontal load at 45 °to side

Figure A.1: FEA heat maps for 2g axial and 3g horizontal loads

A.2 Kalman Filter - Fizza Naqvi

The Kalman filter is widely regarded as an optimal linear estimator in terms of minimising estimation error. The most common approach consists of two steps: prediction and measurement update [96]. The state-space model used for the Kalman filter is based on the linearised system equations, which relate the current state to the next state.

Initialisation The aim of the Kalman filter is to obtain an estimate of the state at the next time step $\hat{x}_{k+1|k}$ based on all the measurements taken up to the $(k+1)$th sample. To initialise this recursion, an estimate of $\hat{x}_{0|0}$ is required, which is taken to be:

$$\hat{x}_{0|0} = E[x_0]. \tag{A.1}$$

The covariance of the estimation error is:

$$P_{k|k} = E[(x_k - \hat{x}_{k|k})(x_k - \hat{x}_{k|k})^T], \tag{A.2}$$

which is initialised as:

$$P_{0|0} = E[(x_0 - \hat{x}_{0|0})(x_0 - \hat{x}_{0|0})^T]. \tag{A.3}$$

Prediction Step In the prediction step, the system's state is projected forward using the system dynamics.

$$\hat{x}_{k+1|k} = A_d\hat{x}_{k|k} + B_d u_k. \tag{A.4}$$

$$P_{k+1|k} = A_d P_{k|k} A_d^T + Q. \tag{A.5}$$

Measurement Update Step The update step incorporates new measurements from the sensors, adjusting the state estimate to account for noise and sensor errors. This process is repeated iteratively, allowing for continuous refinement of the altitude estimate.

$$L_{k+1} = P_{k|k-1}C_d^T(C_d P_{k|k-1} C_d^T + R)^{-1}. \tag{A.6}$$

$$\hat{x}_{k|k} = \hat{x}_{k|k-1} + L_{k+1}(y_k - C_d\hat{x}_{k|k-1}). \tag{A.7}$$

$$P_{k|k} = (I - L_{k+1}C_d)P_{k|k-1}. \tag{A.8}$$

Note that $L_{k+1} \in \mathbb{R}^{n\times p}$ is the Kalman gain.

References

[1] NanoAvionics. *How Many Satellites are in Space?* Accessed: 2025-04-20. 2023. URL: https://nanoavionics.com/blog/how-many-satellites-are-in-space/.

[2] J.-J. Dordain. *ESA/ADMIN/IPOL(2014)2 - Space Debris Mitigation for Agency Projects*. Tech. rep. ESA/ADMIN/IPOL(2014)2. Administrative Instruction of the ESA Director General, entered into force on 28 March 2014. Paris, France: European Space Agency, 2014.

[3] AA. VV. *ESA Space Debris Mitigation Requirements*. Tech. rep. ESSB-ST-U-007. European Space Agency, 2023.

[4] AA. VV. *IADC Space Debris Mitigation Guidelines*. 2020.

[5] AA. VV. *ESA's Annual Space Environment Report*. Darmstadt, Germany, 2022.

[6] Donald J. Kessler and Burton G. Cour-Palais. "COLLISION FREQUENCY OF ARTIFICIAL SATELLITES: THE CREATION OF A DEBRIS BELT." In: *J Geophys Res* 83 (A6 1978), pp. 2637–2646. ISSN: 0148-0227. DOI: 10.1029/JA083iA06p02637.

[7] J. Dobarco-Otero et al. "The Object Reentry Survival Analysis Tool (ORSAT) Version 6.0 and Its Application to Spacecraft Entry". In: *56th International Astronautical Congress*. Fukuoka, Japan, 2005.

[8] C. Martin et al. *DRAMA Final Report*. Tech. rep. European Space Agency, 2005.

[9] G. Koppenwallner et al. "SCARAB - A Multidisciplinary Code for Destruction Analysis of Spacecraft During Re-Entry". In: *5th European Symposium on Aerothermodynamics for Space Vehicles*. Cologne, Germany, 2005.

[10] P. M. Mehta et al. "An Open-Source Hypersonic Aerodynamic and Aerothermodynamic Modeling Tool". In: *8th European Symposium on Aerothermodynamics for Space Vehicles*. 2015.

[11] J. Annaloro et al. "Elaboration of a New Spacecraft-Oriented Tool: Pampero". In: *8th European Symposium on Aerothermodynamics for Space Vehicles*. 2015.

[12] Mckinsey and Company. *Space: The* $1.8 Trillion Opportunity for Global Economic Growth APRIL 2024. 2024.

[13] *Jonathan's Space Pages Starlink Statistics*. date accessed 22/04/2025. URL: https://planet4589.org/space/con/star/stats.html.

[14] United States Space Force (2025) – with major processing by Our World in Data. *Tracked objects in low Earth orbit, by type*. United States Space Force, "Number of objects in space" [original data]. Retrieved 22/04/2025. URL: https://ourworldindata.org/grapher/low-earth-orbits-objects.

[15] ESA. *Space debris by numbers*. date accessed 23/05/2025. URL: https://www.esa.int/Space_Safety/Space_Debris/Space_debris_by_the_numbers.

[16] Sangdi Gu and Herbert Olivier. *Capabilities and limitations of existing hypersonic facilities*. Feb. 2020. DOI: 10.1016/j.paerosci.2020.100607.

[17] NASA. *What are SmallSats and CubeSats*. date accessed 26/10/2024. URL: https://www.nasa.gov/what-are-smallsats-and-cubesats/.

[18] NASA. *SMD Rideshare 101*. 2020.

[19] SpaceX. URL: https://www.spacex.com/mission/.

[20] Spaceflightnow. URL: https://spaceflightnow.com/2025/05/26/live-coverage-spacex-to-launch-24-starlink-satellites-to-polar-orbit-from-california/.

[21] *RIDESHARE PAYLOAD USER'S GUIDE*. URL: https://storage.googleapis.com/rideshare-static/Rideshare_Payload_Users_Guide.pdf.

[22] SpaceX. URL: https://www.spacex.com/rideshare/.

[23] "Electron-Payload-User-Guide-7.0 - Rocket lab". In: (). URL: https://www.rocketlabusa.com/assets/Uploads/Electron-Payload-User-Guide-7.0.pdf.

[24] Lorenzo Casalino and Andrea Forestieri. "Approximate optimal LEO transfers with J2 perturbation and dragsail". In: *Acta Astronautica* 192 (Mar. 2022), pp. 379–389. ISSN: 0094-5765. DOI: 10.1016/J.ACTAASTRO.2021.12.006.

[25] George P. Sutton and Oscar Biblarz. *Rocket Propulsion Elements*. 7th. Hoboken, NJ: Wiley, 2017.

[26] *Orbits: the elliptical orbit | Rip's Applied Mathematics Blog*. URL: https://rip94550.wordpress.com/2010/06/14/orbits-the-elliptical-orbit/.

[27] Miguel C N Fiolhais et al. "Orbital decay in the classroom Orbital decay in the classroom Orbital decay in the classroom". In: (). URL: https://academicworks.cuny.edu.

[28] *Geomagnetic Indices | National Centers for Environmental Information (NCEI)*. URL: https://www.ncei.noaa.gov/products/geomagnetic-indices.

[29] *Solar Cycle Progression | NOAA / NWS Space Weather Prediction Center*. URL: https://www.swpc.noaa.gov/products/solar-cycle-progression.

[30] Australian Space Weather Agency. "Satellite Orbital and Decay Calculations". In: (). URL: www.ips.gov.au.

[31] *Earth Atmosphere Model - Metric Units*. URL: https://www.grc.nasa.gov/www/k-12/airplane/atmosmet.html.

[32] L. Zheng and X. Zhang. "Numerical Methods". In: *Modeling and Analysis of Modern Fluid Problems* (2017), pp. 361–455. DOI: 10.1016/B978-0-12-811753-8.00008-6. URL: https://linkinghub.elsevier.com/retrieve/pii/B9780128117538000086.

[33] David A. Vallado and David Finkleman. "A Critical Assessment of Satellite Drag and Atmospheric Density Modeling". In: *AIAA/AAS Astrodynamics Specialist Conference and Exhibit*. AIAA, 2008.

[34] *ERS-2 reentry – live updates – Rocket Science*. URL: https://blogs.esa.int/rocketscience/2024/02/05/ers-2-reentry-live-updates/.

[35] *General Mission Analysis Tool (GMAT) v.R2016a(GSC-17177-1) | NASA Software Catalog*. URL: https://software.nasa.gov/software/GSC-17177-1.

[36] *Space Environment Statistics · Space Debris User Portal*. URL: https://sdup.esoc.esa.int/discosweb/statistics.

[37] Newcastle University. "The Poisson Distribution 37.3". In: ().

[38] Kaman Sciences Corporation. "On-Orbit Collision Hazard Analysis in Low Earth Orbit Using the Poisson Probability Distribution (Version 1.0)". In: (Aug. 1992). DOI: 10.21949/1402715. URL: https://rosap.ntl.bts.gov/view/dot/12528.

[39] "Orbital Debris Management & Risk Mitigation". In: (). URL: www.nasa.gov.

[40] "Orbital Debris Quarterly News A publication of The NASA Orbital Debris Program Office". In: (2009). URL: www.orbitaldebris.jsc.nasa.gov.

[41] *Collision Velocity in LEO*. URL: https://www.spaceacademy.net.au/watch/debris/collvel.htm.

[42] CubeSat Market. *Cubesat OBC/EPS/Radio All-in-one card*. 2025. URL: https://www.cubesat.market/all-in-one.

[43] Gs-rw. *GranStal TM Reaction Wheels Solutions*. URL: https://satsearch.s3.eu-central-1.amazonaws.com/datasheets/satsearch_datasheet_ir72va_granstal_gs_rw.pdf?X-Amz-Algorithm=AWS4-HMAC-SHA256&X-Amz-Credential=AKIAJLB7IRZ54RAMS36Q%2F20250525%2Feu-central-1%2Fs3%2Faws4_request&X-Amz-Date=20250525T052716Z&X-Amz-Expires=86400&X-Amz-Signature=fb5a394cef69452b9df6b5cc0fa9106d03702a3b237d0e35a0fa863e3dc5de80&X-Amz-SignedHeaders=host.

[44] *CuSP Propulsion System | VACCO Industries*. URL: https://cubesat-propulsion.com/cusp-propulsion-system/.

[45] *AvaSpec-Mini2048CL - Avantes*. URL: https://www.avantes.com/products/spectrometers/compactline/avantes-spectrometer-mini-2048cl/.

[46] Cdr. Ronnie Nader, Jules Nader Drouet, and Gerard Nader Drouet. "ICEPS: Compact, all-purpose, USB 2.0 based small satellite system core". In: *2nd IAA Latin American Symposium on Small Satellites: Advanced Technologies and Distributed Systems*. Ecuadorian Space Agency (EXA). 2019.

[47] *Cosine Correctors - Avantes*. URL: https://www.avantes.com/products/fiber-optics/fiber-optic-accessories/cosine-correctors/.

[48] EXA. *BA01 High Energy Density Battery Array*. 2025. URL: https://catalog.orbitaltransports.com/ba01-high-energy-density-battery-array/.

[49] Helix Geospace. *Iridium IoT Certus 9704 Series Datasheet*. 2024. URL: https://helixgeospace.com/wp-content/uploads/2024/11/iridium-iot-certus-9704-series-datasheet-rev2.pdf.

[50] TE Connectivity. *Tip Sensitive Bearing Thermocouple Probe (Configurable Product)*. Configurable thermocouple sensor for industrial applications. 2025. URL: https://www.te.com/en/product-CAT-TCS0008.datasheet.pdf.

[51] AAC Clyde Space. $satsearch_datasheet_o7z8pc_aac_clyde_mm200$. URL: https://www.aac-clyde.space/wp-content/uploads/2021/11/MM200.pdf.

[52] Source of Aluminium alloy datasheets. URL: https://www.thyssenkrupp-materials.co.uk/properties-of-aluminium.

[53] A. M. Howatson, P. G. Lund, and J. D. Todd. *Engineering Tables and Data*. University of Oxford, 2009.

[54] Grant Gustafson. *5.8 Resonance*. 2010.

[55] A. Finazzi et al. "Thermite-for-Demise (T4D): Experimental analysis of heat transfer principles and preliminary sizing of an application". In: *International Journal of Heat and Mass Transfer* 220 (Mar. 2024). ISSN: 00179310. DOI: 10.1016/j.ijheatmasstransfer.2023.124957.

[56] A. Finazzi et al. "Thermite-for-Demise (T4D): Experimental analysis of heat transfer principles and preliminary sizing of an application". In: *International Journal of Heat and Mass Transfer* 220 (2024), p. 124957. DOI: https://doi.org/10.1016/j.ijheatmasstransfer.2023.124957.

[57] A. Finazzi et al. "Thermite-for-Demise Concept: from Material Selection to Test Campaign". In: *ESA-TRP SPADEXO project* (2024). Preprint.

[58] Isil Sakraker et al. "QARMAN: An Atmospheric Entry Experiment on CubeSat Platform". In: *8th European Symposium on Aerothermodynamics for Space Vehicles*. 2015.

[59] Ali Bostani. "KU Band vs. L Band Satellite Communication in Industry 4.0: Assessing IoT Connectivity Solutions with a Focus on Spread Spectrum Technology". In: *Zenodo* (2024). DOI: 10.5281/zenodo.11305839. URL: https://www.researchgate.net/publication/386699172.

[60] Mingyang Mao et al. "The propagation characteristics of low frequency radio waves in magnetized hypersonic plasma sheaths". In: *AIP Advances* 13.095019 (2023). Published Online: 20 September 2023. DOI: 10.1063/5.0163507. URL: https://doi.org/10.1063/5.0163507.

[61] Ryan P. Starkey, Mark J. Lewis, and Charles H. Jones. "Plasma Sheath Characterization for Telemetry in Hypersonic Flight". In: *International Telemetering Conference Proceedings*. International Foundation for Telemetering, 2003. URL: http://hdl.handle.net/10150/606733.

[62] Yusuke Takahashi, Kazuhiko Yamada, and Takashi Abe. "Prediction Performance of Blackout and Plasma Attenuation in Atmospheric Reentry Demonstrator Mission". In: *Journal of Spacecraft and Rockets* (2014). DOI: 10.2514/1.A32880.

[63] Wei Guo et al. "Polarization Characteristics Distortion for L-Band Fully Polarimetric Radar Subject to Magnetized Plasma Sheath". In: *Remote Sensing* (2024). DOI: 10.3390/rs16122061.

[64] Salvatore Esposito et al. “Non-equilibrium plasma distribution in the wake of a slender blunted-nose cone in hypersonic flight and its effect on the radar cross section”. In: *Aerospace Science and Technology* 155 (2024). Open access under CC BY license, p. 109699. DOI: 10.1016/j.ast.2024.109699. URL: https://www.sciencedirect.com/science/article/pii/S1270963824008289.

[65] Deschotelshop. *Buy Iridium Land Certus 350 / 700 satellite communications subscription*. 2025. URL: https://www.deschotelshop.nl/en/iridium-land-certus-350-700-volume-allowance-plans-per-month.

[66] MathWorks. *Link Budget*. 2025. URL: https://uk.mathworks.com/discovery/link-budget.html.

[67] Vincent J. Riot, Lance M. Simms, and Darrell Carter. “Lessons Learned Using Iridium to Communicate with a CubeSat in Low Earth Orbit”. In: *Journal of Small Satellites (JoSS)* 10.1 (2021). Peer-reviewed article, pp. 995–1006. URL: www.jossonline.com.

[68] Julien’s Lab. *Iridium Satellites Live Map*. 2025. URL: https://www.iridiumwhere.com/.

[69] Peter Delos, Bob Broughton, and Jon Kraft. “Phased Array Antenna Patterns—Part 1: Linear Array Beam Characteristics and Array Factor”. In: *Analog Dialogue* (2020). URL: https://www.analog.com/media/en/analog-dialogue/volume-54/number-2/phased-array-antenna-patterns-part-1-linear-array-beam-characteristics-and-array-factor.pdf.

[70] Kirt Blattenberger. *Cascaded Noise Figure & Noise Temperature Calculation Equation Formula*. 2025. URL: https://www.rfcafe.com/references/electrical/noise-figure.htm.

[71] All About Circuits. *Noise Figure and Noise Temperature Calculator*. https://www.allaboutcircuits.com/tools/noise-figure-noise-temperature-calculator/. 2025.

[72] Thomas A. Milligan. *Modern Antenna Design*. 2nd Edition. IEEE Press, 2005, p. 32.

[73] Craig Clark and Ritchie Logan. *Power Budgets for Mission Success*. AAC Clyde Space, 2011. URL: http://mstl.atl.calpoly.edu/~workshop/archive/2011/Spring/Day%203/1610%20-%20Clark%20-%20Power%20Budgets%20for%20CubeSat%20Mission%20Success.pdf.

[74] *Type K Thermocouple Reference Table*. Omega Engineering. URL: https://www.omega.co.uk/temperature/pdf/Type_K_Thermocouple_Reference_Table.pdf.

[75] Texas Instruments. *Temperature Compensation Using High-Accuracy Temperature Sensors*. Tech. rep. Texas Instruments, 2019. URL: https://www.ti.com/lit/ab/snoaa27/snoaa27.pdf.

[76] Jim Karki. *Understanding Operational Amplifier Specifications (Rev. B)*. Tech. rep. Texas Instruments, 2018. URL: https://www.ti.com/lit/an/sloa011b/sloa011b.pdf.

[77] Georg Herdrich et al. “MIRKA2: Small Re-Entry Demonstrator for Advanced Miniaturized Sensors”. In: *International Workshop on Instrumentation for Planetary Missions*. NASA Goddard Space Flight Center and University of Stuttgart. 2012. URL: https://www.researchgate.net/publication/351786281_MIRKA2_SMALL_RE-ENTRY_DEMONSTRATOR_FOR_ADVANCED_MINIATURIZED_SENSORS.

[78] Dr. George Vekinis. *ReWiG: A Resistive Wire Mesh TPS recession sensor*. Technical Report. ESA Contract 4000111843/14/NL/SC, ITI Phase A Study. European Space Agency (ESA), 2015. URL: https://nebula.esa.int/sites/default/files/neb_tec_study/2335/public/23690_FP.pdf.

[79] Nondestructive Evaluation Techniques. *Electrical Conductivity and Resistivity for Nickel and Nickel Alloys*. 2025. URL: https://www.nde-ed.org/NDETechniques/EddyCurrent/ET_Tables/ET_matlprop_Nickel.xhtml.

[80] *Ideal Rocket Equation | Glenn Research Center | NASA*. URL: https://www1.grc.nasa.gov/beginners-guide-to-aeronautics/ideal-rocket-equation/.

[81] AAC Clyde Space. $satsearch_datasheet_o7z8pc_aac_clyde_mm200$. URL: https://www.aac-clyde.space/wp-content/uploads/2021/11/RW400-1.pdf.

[82] COMAT space. *Reaction Wheels Long-lasting AGILITY*. URL: https://satsearch.s3.eu-central-1.amazonaws.com/datasheets/datasheet-comat-reaction-wheels-20-20-mnms-be8w1h.pdf?X-Amz-Algorithm=AWS4-HMAC-SHA256&X-Amz-Credential=AKIAJLB7IRZ54RAMS36Q%2F20250525%2Feu-central-1%2Fs3%2Faws4_request&X-Amz-Date=20250525T052344Z&X-Amz-Expires=86400&X-Amz-Signature=50794e9aff18de3a82ce333fe727cdd1312f58594456606f78287a22a3819803&X-Amz-SignedHeaders=host.

[83] C.Leibbrandt. *option-sheet-cubespace-gen2-cubewheel-cw1200-wq3ppo*. URL: https://www.cubespace.co.za/uploads/7007f7f5-f682-49d6-94d3-13d2cf3c5a93.pdf.

[84] William Lowrie and Andreas Fichtner. *Fundamentals of Geophysics*. 3rd ed. Cambridge University Press, 2020.

[85] Barbara M. Kreutz. "Mediterranean Contributions to the Medieval Mariner's Compass". In: *Technology and Culture* 14.3 (1973), pp. 367–383. ISSN: 0040165X, 10973729. URL: http://www.jstor.org/stable/3102323 (visited on 05/26/2025).

[86] National Centers for Environmental Information. date accessed 25/05/2025. URL: https://www.ncei.noaa.gov/products/world-magnetic-model/accuracy-limitations-error-model.

[87] A.A. Stepanenko, W. Lee, and S.I. Krasheninnikov. "Dynamics of sheath-connected plasma filaments in magnetic field with arbitrary geometry". In: *Nuclear Materials and Energy* 12 (2017). Proceedings of the 22nd International Conference on Plasma Surface Interactions 2016, 22nd PSI, pp. 887–892. ISSN: 2352-1791. DOI: https://doi.org/10.1016/j.nme.2017.03.011. URL: https://www.sciencedirect.com/science/article/pii/S2352179116300151.

[88] Gaoge Hu et al. "Robust Unscented Kalman Filtering with Measurement Error Detection for Tightly Coupled INS/GNSS Integration in Hypersonic Vehicle Navigation". In: *IEEE Access* 7 (2019), pp. 151409–151421. ISSN: 21693536. DOI: 10.1109/ACCESS.2019.2948317. URL: https://www.researchgate.net/publication/336662296_Robust_Unscented_Kalman_Filtering_With_Measurement_Error_Detection_for_Tightly_Coupled_INSGNSS_Integration_in_Hypersonic_Vehicle_Navigation.

[89] *What is Sensor Fusion? | Dewesoft.* URL: https://dewesoft.com/blog/what-is-sensor-fusion.

[90] Muhammad Asad Bashir et al. "Kalman Filter Based Sensor Fusion for Altitude Estimation of Aerial Vehicle". In: *IOP Conference Series: Materials Science and Engineering* 853 (2020). Proceedings of IOP Conf. Ser.: Mater. Sci. Eng., p. 012034.

[91] Richard F. Tinder. *Relativistic Flight Mechanics and Space Travel: A Primer for Students, Engineers and Scientists*. Extract of page 33. Morgan & Claypool Publishers, 2007, p. 33. ISBN: 978-1-59829-130-8.

[92] *Gyroscope - SparkFun Learn.* URL: https://learn.sparkfun.com/tutorials/gyroscope/all.

[93] Mangal Kothari. "Attitude Representation and Transformation Matrices". In: ().

[94] *Using the Accelerometer – HUSSTECH.* URL: http://husstechlabs.com/projects/atb1/using-the-accelerometer/.

[95] T. Ozyagcilar. *Implementing a Tilt-Compensated eCompass using Accelerometer and Magnetometer Sensors*. Tech. rep. Rev. 4.0. Freescale Semiconductor, 2015.

[96] Antonis Papachristodoulou. *B15 Optimal Control: Kalman Filtering*. Lecture notes. Accessed: 28 March 2025. 2024.

[97] Wei Tech Ang et al. "Physical Model of a MEMS Accelerometer for Low-g Motion Tracking Applications". In: (2004). URL: www.analog.com.

[98] Prof. Dr. Ulrich Thomas. *Transformation Matrices in Robotics*. https://www.tu-chemnitz.de/informatik/KI/edu/robotik/ws2017/trans.mat.pdf. Lecture Notes, TU Chemnitz, Department of Artificial Intelligence. 2017.

[99] Malcolm D. Shuster. "A Survey of Attitude Representations". In: *Journal of the Astronautical Sciences* 41.4 (1993), pp. 439–517. DOI: 10.1007/BF03256558.

[100] Mark Cannon. *C21 Model Predictive Control Lecture Notes*. https://markcannon.github.io/teaching. Lecture notes, Department of Engineering Science, University of Oxford. 2023.

[101] Idris Kempf et al. "Model Predictive Control for Electron Beam Stabilization in a Synchrotron". In: *2022 European Control Conference, ECC 2022*. Institute of Electrical and Electronics Engineers Inc., 2022, pp. 814–819. ISBN: 9783907144077. DOI: 10.23919/ECC55457.2022.9838467.

[102] *Multi-Furcated Fiber-Optic Cables - Avantes.* URL: https://www.avantes.com/products/fiber-optics/optical-fibers/multi-furcated-fiber-optic-cables/.

[103] *LED and Solid State Lighting Measurement.* URL: https://www.azom.com/article.aspx?ArticleID=11889.

[104] Ger Loop Avantes. "INTENSITY CALIBRATIONS IN SPECTROSCOPY AND RADIOMETRY Content". In: ().

[105] "Integrating Sphere Measurement Part I: Basics". In: (2014).

[106] "Atomic Spectra Database | NIST". In: (). DOI: 10.18434/T4W30F. URL: https://www.nist.gov/pml/atomic-spectra-database.

[107] S. Shukla et al. "Inverse-catalyst-effect observed for nanocrystalline-doped tin oxide sensor at lower operating temperatures". In: *Sensors and Actuators B: Chemical* 104 (2 Jan. 2005), pp. 223–231. ISSN: 0925-4005. DOI: 10.1016/J.SNB.2004.05.008.

[108] York University. "Boltzmann distribution in a nutshell". In: ().

[109] Robert C. Hilborn. "Einstein coefficients, cross sections, f values, dipole moments, and all that". In: *American Journal of Physics* 50 (11 Nov. 1982), pp. 982–986. ISSN: 0002-9505. DOI: 10.1119/1.12937.

[110] Jonathan M. Burt and Iain D. Boyd. "High Altitude Plume Simulations for a Solid Propellant Rocket". In: *https://doi.org/10.2514/1.30129* 45 (12 May 2012), pp. 2872–2884. ISSN: 00011452. DOI: 10.2514/1.30129. URL: https://arc.aiaa.org/doi/10.2514/1.30129.

[111] Augustin-Louis Cauchy. "Note sur divers théorèmes relatifs à la rectification des courbes et à la quadrature des surfaces". French. In: *Comptes Rendus de l'Académie des Sciences* 13 (1841), pp. 1060–1065.

[112] 3Blue1Brown. *A tale of two problem solvers | Average cube shadow area*. Accessed: 2025-03-24. 2021. URL: https://www.youtube.com/watch?v=ltLUadnCyi0.

[113] Insoo Jun et al. "A review on radiation environment pathways to impacts: Radiation effects, relevant empirical environment models, and future needs". In: *Advances in Space Research* (2024). ISSN: 0273-1177. DOI: 10.1016/j.asr.2024.03.029. URL: https://www.sciencedirect.com/science/article/pii/S0273117724003296.

[114] National Aeronautics and Space Administration. *LEO Satellite Illumination Analysis Report*. Technical Report NAS-2024-LEO-001. 2024. URL: https://ntrs.nasa.gov/citations/20240001234 (visited on 03/24/2024).

[115] Gustav Kirchhoff. "Über den Zusammenhang zwischen Emission und Absorption von Licht und Wärme". In: *Monatsberichte der Königlich Preussischen Akademie der Wissenschaften zu Berlin* (1860), pp. 783–787.

[116] Luca Di Mare. "Notes on Discretisation Schemes for CFD". Unpublished lecture notes. Course notes for Computational Fluid Dynamics (CFD) Coursework Module, University of Oxford. 2025.

[117] A. Kubade et al. "Transient Thermal Analysis of 1U Modular Cubesat Based on Passive Thermal Control Methods". In: *Archive of Mechanical Engineering* 4 (2023), pp. 1252–1253. URL: https://journals.pan.pl/Content/129628/PDF/AMM-2023-4-04-Kubade.pdf.

[118] KiboCUBE Academy. *Introduction to CubeSat Thermal Control System*. KiboCUBE Academy Pre-recorded Lecture 13. United Nations Office for Outer Space Affairs. 2021. URL: https://www.unoosa.org/documents/pdf/psa/access2space4all/KiboCUBE/AcademySeason2/On-demand_Pre-recorded_Lectures/KiboCUBE_Academy_2021_OPL13.pdf.

[119] R. Bevilacqua et al. "Thermal Modeling and Analysis of a Cube Satellite: Passive Thermal Coating Observatory Operating in Low Earth Orbit (PATCOOL)". In: *Journal of Small Satellites* 10.3 (2021), p. 1067. URL: https://jossonline.com/storage/2021/11/Final-Bevilacqua-Thermal-Modeling-and-Analysis-of-a-Cube-Satellite.pdf.

[120] J.D. Anderson. *Hypersonic and High-temperature Gas Dynamics*. AIAA education series. American Institute of Aeronautics and Astronautics, 2006. ISBN: 9781563477805. URL: https://books.google.com.sg/books?id=UgWmQgAACAAJ.

[121] M. Knudsen. "Die Gesetze der Molekularströmung und der inneren Reibungsströmung der Gase durch Röhren". In: *Annalen der Physik* 333.1 (1909), pp. 75–130. DOI: 10.1002/andp.19093330102.

[122] Raphael Marschall et al. *Cometary Comae-Surface Links: The Physics of Gas and Dust from the Surface to a Spacecraft*. Dec. 2020. DOI: 10.1007/s11214-020-00744-0.

[123] G. A. Bird. *Molecular Gas Dynamics and the Direct Simulation of Gas Flows*. Vol. 42. The Oxford Engineering Science Series. Oxford: Clarendon Press, 1994. ISBN: 978-0-19-856195-8.

[124] Thomas W. Rees et al. "Numerical and experimental studies of the hypersonic flow around a cube at incidence". In: *Acta Astronautica* 183 (June 2021), pp. 75–88. ISSN: 00945765. DOI: 10.1016/j.actaastro.2021.02.033.

[125] Donald M. Kuehn. "Experimental and theoretical pressures on blunt cylinders for equilibrium and nonequilibrium air at hypersonic speeds". In: *NASA Technical Report* R-117 (1963).

[126] Thomas W. Rees, Paul J.K. Bruce, and James A. Merrifield. "The effect of reynolds number on the hypersonic flow around faceted shapes". In: *22nd AIAA International Space Planes and Hypersonics Systems and Technologies Conference*. American Institute of Aeronautics and Astronautics Inc, AIAA, 2018. ISBN: 9781624105777. DOI: 10.2514/6.2018-5197.

[127] Thomas W. Rees et al. "Experimental characterization of the hypersonic flow around a cuboid". In: *Experiments in Fluids* 61 (7 July 2020). ISSN: 14321114. DOI: 10.1007/s00348-020-02975-x.

[128] Patrick M. Seltner, Sebastian Willems, and Ali Gülhan. "Aerodynamic coefficients of free-flying cubes in hypersonic flowfield". In: *Journal of Spacecraft and Rockets* 56 (6 2019), pp. 1725–1734. ISSN: 15336794. DOI: 10.2514/1.A34345.

[129] David Bacci. *B19 Nozzle Flow Lab Notes: Introduction to CFD Best Practices*. Lab notes for B19 lab at the University of Oxford. 2025.

[130] Farzad Ismail. *TOWARD A RELIABLE PREDICTION OF SHOCKS IN HYPERSONIC FLOW: RESOLVING CARBUNCLES W ITH ENTROPY AND VORTICITY CONTROL*. 2006.

[131] David I. Ketcheson and Manuel Quezada de Luna. "Numerical simulation and entropy dissipative cure of the carbuncle instability for the shallow water circular hydraulic jump". In: *International Journal for Numerical Methods in Fluids* 93.7 (2021), pp. 2250–2267. DOI: 10.1002/fld.5070.

[132] Simon Sangeeth and J. C. Mandal. "A cure for numerical shock instability in HLLC Riemann solver using antidiffusion control". In: *Computers & Fluids* 173 (2018), pp. 59–76. DOI: 10.1016/j.compfluid.2018.07.029.

[133] J. M. Powers, J. Bruns, and A. Jemcov. "Physical Diffusion Cures the Carbuncle Phenomenon". In: *53rd AIAA Aerospace Sciences Meeting*. American Institute of Aeronautics and Astronautics. Kissimmee, Florida, 2015.

[134] Loretta Trevino. "SpaceX Dragon Re-Entry Vehicle: Aerodynamics and Aerothermodynamics with Application to Base Heat-Shield Design". In: *6th International Planetary Probe Workshop*. Discusses computational aerothermal analysis of Dragon capsule at Mach 2-21, with altitude-specific heating profiles. Atlanta, Georgia, USA, 2008, pp. 1–8. URL: https://repository.gatech.edu/bitstreams/39f02e86-13a2-4066-a79d-2a87df7d2ccd/download.

[135] ANSYS Inc. *Reentry Capsule Analysis Using ANSYS Fluent*. Accessed: 2025-04-07. 2025. URL: https://ansyshelp.ansys.com/Views/Secured/corp/v242/en/flu_tg/flu_tg_reentry_capsule.html.

[136] Roop N. Gupta et al. *A Review of Reaction Rates and Thermodynamic and Transport Properties for an 11-Species Air Model for Chemical and Thermal Nonequilibrium Calculations to 30000 K*. NASA Reference Publication NASA-RP-1232, NAS 1.61:1232, L-16634. Accessed: 2025-04-22. Hampton, VA, United States: NASA Langley Research Center, 1990. URL: https://ntrs.nasa.gov/citations/19900017748.

[137] David C. Wilcox. *Turbulence Modeling for CFD*. 2nd. La Cañada Flintridge, CA, USA: DCW Industries, 1994.

[138] P.A. Gnoffo. "CFD Validation Studies for Hypersonic Flow Prediction". In: *Proceedings of the 39th Aerospace Sciences Conference*. Reno, NV, USA, 2001.

[139] Dieter Schwamborn et al. "Development of the DLR TAU-Code for Aerospace Applications". In: *International Forum on Aeroelasticity and Structural Dynamics*. Conference paper detailing TAU's architecture and capabilities. Bangalore, India, 2008, pp. 1–15. URL: https://elib.dlr.de/55519/1/INCAST_Schwamborn.pdf.

[140] Cyril Simon Wedlund et al. "A Fast Bow Shock Location Predictor-Estimator From 2D and 3D Analytical Models: Application to Mars and the MAVEN Mission". In: *Journal of Geophysical Research: Space Physics* 127.8 (2022). PMID: 36247834; PMCID: PMC9285960, e2021JA030200. DOI: 10.1029/2021JA030200. URL: https://www.ncbi.nlm.nih.gov/pmc/articles/PMC9285960/.

[141] T. Soares and J. A. Merrifield. "Characterisation of Tests of Structural Joints Behaviour During Re-Entry". In: *4th International Workshop on Space Debris Re-entry*. Darmstadt, Germany, 2018.

[142] Endurosat. URL: https://www.endurosat.com/configurator/.

[143] GlassDoor. URL: https://www.glassdoor.co.uk/Salaries/graduate-engineer-salary-SRCH_KO0,17.htm.